Molecular-Scale Effects of Additives on the Nucleation, Growth and Crystal Properties of Long-Chain Alkyl Methyl-Esters

Haiyang Jiang

In fulfilment of the requirements for the degree of
Doctor of Philosophy

The University of Leeds
Institute of Particle Science & Engineering

School of Process, Environmental and Materials Engineering

August 2012

The candidate confirms that work submitted is his own and that appropriate credit has been given where reference has made to the work of others.

Acknowledgements

I would like to thank my supervisors, Professor Kevin. J. Roberts and Dr. Robert B. Hammond as well as my industrial supervisors Dr Iain More and Dr Ken Lewtas from Infineum UK Ltd for giving me the opportunity to carry out this PhD study and for their constant support, much valuable advice and outstanding help.

I express my sincere gratitude to Dr. Vasuki Ramachaddran for her help with development of the systematic search program and discussion about the results from molecule modelling and and Dr Syarifah Abd Rahim for her assistance in the area of morphological simulation. I gratefully acknowledge Simon Lloyd for the build of the crash cool rigs. Very special thanks to Qassim Hussain, my partner involving the Infineum project for his assistance with the study of nucleation kinetics. I am indebted to Thai T. H. Nguyen who assisted me to analyze the images of crystals. I would like to thank to Dr Ken Lewtas, Dr Stuart Taylor for the build of the cold room and the assistance in taking the crystal images by Dr Stuart Taylor. I am grateful to Dr Graham Jackson who synthesised the commercial additives.

Abstract

Biodiesel is a diesel-related fuel manufactured from vegetable oils, recycled grease, or animal fats. It is technically competitive with, or offers technical advantages when compared to, conventional diesel fuel. However, the freezing and gelling behaviour of many biodiesel formulations are potentially limiting their applications. It is known that the use of additives is an efficient way to improve the cold flow properties of formulated, so it is very important to clarify the mechanism and effect of additives.

Molecular cluster modelling work has been explored to study the effect of additives on crystallization temperature, meta-stable zone width and solubility. A new method has been developed for the prediction of crystallisability through the comparison of structural variability of molecular clusters of pure naphthalene, pure biphenyl, and naphthalene in the presence of biphenyl and vice versa. The approach has been validated through the experimental determination of crystallization temperatures and meta-stable zone width.

The predicted growth morphologies of methyl stearate have been derived through attachment energy calculations and the resulting surface chemistry of the morphological habit faces characterized. Molecular simulations using grid search methods combined with experimental observed images were used to investigate the solvent-mediated effect on crystal habits of methyl stearate.

Tubidometric studies employing a 100ml batch crystallizer operating in a polythermal mode confirmed the change of crystallization temperature and the meta-stable zone width of methyl stearate with or without additives. Related crash-cooling studies enabled the characterization of crystallization kinetics with or without additives through examination of set points as a function of supersaturation.

List of Figures

List of Tables

Table of Contents

CHAPTER 1

Introduction

Summary:

The background perspective supporting this reseach and an overview of reseach progress are presented in this chapter. A whole area of the study, combined with a thesis route-map, is also provided.

1.1 Industrial Background

1.1.1 Biodiesel

Biodiesel can be obtained from transesterified vegetable oils or animal fats and is an alternative diesel fuel which can be used as a fuel in direct-injection compression-ignition engines. Biodiesel consists of a range of methyl esters (or ethyl ester depending on the use of methanol or ethanol in the preparation stage) from C_{10} to C_{22}, sometimes referred to as FAME (fatty acid methyl esters)[1-3]. The most common methyl esters are:

- Methyl Palmitate $C_{17}H_{34}O_2$
- Methyl Stearate $C_{19}H_{38}O_2$
- Methyl Oleate $C_{19}H_{36}O_2$
- Methyl Linoleate $C_{19}H_{34}O_2$
- Methyl Linolenate $C_{19}H_{32}O_2$

Important fuel properties such as viscosity, gross heat of combustion and cetane rating compare well between methyl esters and petroleum middle distillate [2, 4, 5].

Biodiesel fuel, it is made from used vegetable oil, methanol and sodium hydroxide. The vegetable oil is the feedstock, the methanol is used up in the convention of the molecules and the sodium hydroxide is the catalyst that makes the reaction happen. Vegetable oil is a triglyceride. Sources of triglyceride feedstocks that can be used in biodiesel manufacture include rapeseed oil, palm oil, sunflower oil, tallow, soybean oil, used kitchen oil, castor oil, jatropha oil and peanut oil. In Europe the main oil used is rape-seed oil, producing biodiesels known as rape-seed methyl ester (RME) or sunflower methyl ester. In Asia the main crop used for biodiesel production is palm oil and jatropha oil, whereas in USA corn is the main feedstock crop. Under steady-state conditions the combustion of methyl esters can significantly reduce exhaust emissions of smoke, particulates, unburned hydrocarbons, carbon dioxide and to a lesser degree carbon monoxide [6-8].

Methyl esters of fatty acids obtained from transesterified vegetable oils or animal fats are suitable for use as a fuel in direct-injection compression-ignition engines and therefore are an attractive alternative to the petroleum-based fuels traditionally used in such engines [1-3]. Important fuel characteristics such as viscosity, gross heat of combustion and cetane rating compare well between methyl esters and petroleum middle distillates [2, 4, 5]. Methyl esters have relatively high flash points in comparison to petroleum distillates, for instance the flash point of methyl soyate is 154°C whereas the flash point of petroleum diesel distillates is in the range of 52-96°C [9]. Thus methyl esters are easier to store than petroleum distillates.

Biodiesel is most commonly produced through reacting natural triglyceride oil (e.g. vegetable oil or animal oil) with a primary alcohol (most usually methanol) over an alkali catalyst. This process is known as transesterification and the products of the reaction are a mixture of methyl esters and glycerol which can be extracted as a valuable co-product. The structural formula equation for the reaction is given below:

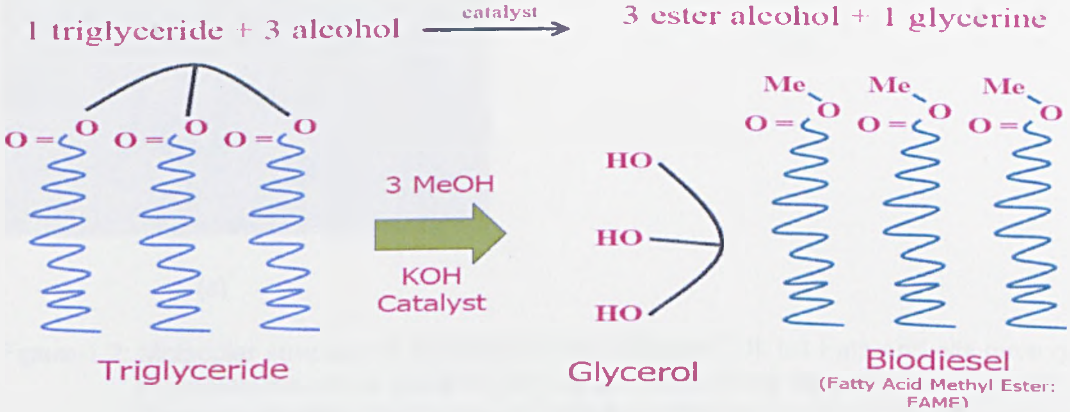

Figure 1.1: Transesterification Reaction [10]

Biodiesel is technically competitive with diesel fuels. Advantages of biodiesel include biodegradability, safer handling, inherent lubricity, reduction of most regulated exhaust emissions, renewability, domestic origin, and compatibility with the existing fuel distribution infrastructure. While many of the fuel properties of biodiesel are comparable to petroleum-based diesel fuel (hydrocarbon fuels), improvement of its low-temperature flow characteristics still remain one of the major challenges when using biodiesel as an alternative fuel for diesel engines. Therefore, the comprehension of crystallisation properties in the winterization processes, i.e. nucleation and growth kinetics, thermodynamics, morphology, habit and polymorph are very important to the development of technology to enhance fuel cold flow properties.

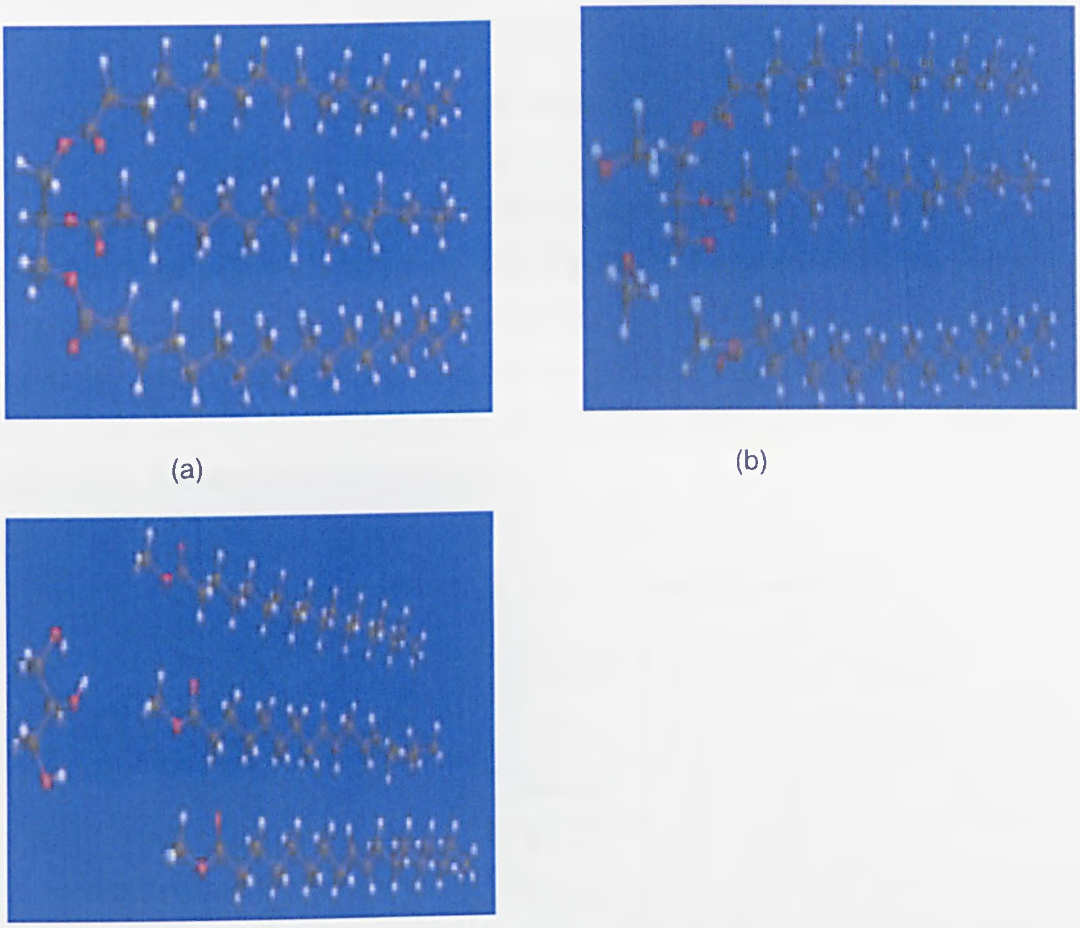

(a)

(b)

(c)

Figure 1.2: Molecular structure of triglyceride and biodiesel [10]. (a) Fats and oils have quite big molecules with a spinal of glycerol on which three fatty acids are bonded; (b) Transesterification: fatty acids are removed from the glycerol and each is bonded with methanol/ethanol; (c) Products are 1 mole glycerol and 3mol of fatty acid methyl ester [2]

The crystallisation process converts materials from a homogenous solution into three-dimensional crystals. The presence of chemical species in solution, in addition to the solvent, can have a pronounced effect on the crystallization kinetics and crystal habit even if present in trace amounts. This effect results from the differing effect the impurities have on the various crystallographic faces of a crystal [11]. The facial growth rates may be increased, decreased, or remain the same in the presence of additives [12, 13]. The effect of additives on crystallization kinetics can be viewed from experimental measurement of methyl esters with and without additives, and the effect on crystal habit can modelled via molecular modelling technique based on crystal structure information.

1.1.2 Cold flow properties of Biodiesel

In spite of its many advantages, the cold weather will impact the application of biodiesel in moderate temperature climates (see Table 1.1). Cold weather performance of diesel fuels is determined by measuring the tendency of a fuel to solidify or gel at low temperatures. Cloud point (CP) is defined as the temperature at which crystals in an oil or fuel appear [14]. At temperatures below the CP, crystals continue to grow and agglomerate eventually causing operability problems [14]. The cold filter plugging point (CFPP) test was developed to predict more accurately low-temperature limits [14].

Table 1.1 Cold flow properties of biodiesel (B100) derived from various feedstock lipids and alcohols[a] [14]

Lipid	Alcohol	CP (°C)	PP (°C)	CFPP (°C)	LIFT (°C)
Canola oil	Methyl	1	-9		
Coconut oil	Ethyl	5	-3		
High oleic (HO) sunflower oil[b]	Methyl			-12	
Linseed oil	Methyl	0	-9		
Olive oil	Methyl	-2	-3	-6	
Palm oil	Methyl	16	13		
Rapeseed oil	Methyl	-2	-9	-8	
	Ethyl	-2	-15		
Safflower oil	Ethyl	-6	-6		
Soybean oil	Methyl	0	-2	-2	0
	Ethyl	1	-4		
	Isopropyl	-9	-12		
	n-Butyl	-3	-7		
	2-Butyl	-12	-15		
Soybean oil/ tallow[c]	Methyl	2	1		
Tallow	Methyl	17	15	9	20
Tallow	Ethyl	15	12	8	13
Used cooking oil[d]	Methyl			-1	
Used hydrogenated soybean oil[e]	Ethyl	7	6		
Waste grease[f]	Ethyl	9	-3	0	9

Source: Clark et al., 1983; Dunn and Bagby, 1955; Foglia et al., 1997; Fukuda et al., 2001; González Gómez et al., 2003; Kalligeros et al., 2003; Lang et al., 2001; Lee et al., 1995;

Masjuki et al., 1993; Neto da Silva et al., 2003; Peterson et al., 2000; Peterson et al., 1987; Wu et al., 1998; Zhang and Van Gerpen. 1996.

[a] CP= cloud point; PP= pour point; CFPP= cold flow filer plugging point; LIFT= low-temperature flow test.

[b] Oleic acid content=77.9wt% before conversion of biodiesel.

[c] 4:1 v/v soybean oil methyl ester/tallow methyl ester.

[d] Total saturated fatty acid methyl ester content=19.2wt%.

[e] Hydrogenated to iodine value=65g I^2/100g oil.

[f] Free fatty acids ~9wt%before conversion to biodiesel.

Biodiesel made from feedstocks containing large concentrations of long-chain saturated fatty acids will have very poor cold flow properties [14]. FAME is found in the majority of biodiesel fuels, and is easy to gel around 0°C. Due to this disadvantage of biodiesel, many approaches were developed to improve the cold flow properties of biodiesel:

- Blend with petrodiesel: Cold flow properties of FAME and fatty ethyl esters in blends of petrodiesel can be improved and the higher the percentage of petrodiesel, the more FAMEs exhibit better cold flow properties.
- Carry out the transesterification of the oils or fats with long or branched alcohols.
- Reducing the total concentration of high melting components through the crystallization fractionation of the fuel.
- Through the use of cold flow improver additives.

In this study, the effect of cold flow additives on crystallization behaviour of methyl esters will be investigated, and the mechanism of cold flow additives will be explored.

1.2 Thesis Aims and Objectives

Due to cold flow properties of biodiesel mentioned above, the use of cold flow additives on clod flow behaviour will be assessed in this work. The aims of this PhD thesis centre around the following research questions: can molecular scale tools, such as molecular and crystallographic modelling and process analytical methods be used to assess the nucleation, growth and habit modification of long-chain methyl esters?

Answer above question, the effects of additives will be examined through the use of both experimental and molecular modelling techniques.

The objectives of this study were to determine the crystallization kinetics and crystal morphology of methyl esters with and without additives.

- The crystal nucleation kinetics of methyl esters will be confirmed with the measurement of meta-stable zone and induction time.
- The induction time and meta-stable zone of methyl esters will be measured under the condition of polythermal and isothermal cooling.
- The measurement of induction time of methyl esters with different additives will be used to appraise the effect of additives on nucleation and growth kinetics.

Prediction of crystal shape and modification of crystal shape with additives will be carried out using the HABIT98 [15] and SHAPE [16] programs.

- The effect of solvent on crystal morphology of methyl stearate will be examined using the SYST-SEARCH [17] program.
- Optical microscopy using in the cold room facilitated at Infineum will be used to investigate the modification of crystal morphology by solvents.

The mechanism of additives on habit modification will be investigated from the results of cluster modelling work. Cluster modelling work will be validated using two simple aromatic hydrocarbon materials: naphthalene and biphenyl.

1.3 Project Management

The PhD work was carried out at the University of Leeds, UK and Infineum Ltd, UK. The work was partly financially supported by Infineum and the Institute of Particle Science and Engineering at University of Leeds.

The PhD work was supervised by professor Kevin J. Roberts and Robert Hammond at University of Leeds, UK as well as Dr Iain More and Dr Ken Lewtas in Infineum Ltd.

The crystallization experiments were carried out using the equipments and the instruments of the crystallization laboratory in the Institute of Particle Science and Engineering at the University of Leeds. The observation of crystal images using the cold room was performed in Infineum and aided by Dr Ken Lewtas and Dr Stuart Taylor.

The habit modification of methyl stearate was performed using SYST-SEARCH with the help of Dr. Vasuki Ramachaddran at University of Leeds.

Turbidity probe for experiment designed and built in collaboration with Steve Caddick and Tarsem Hunjan etc.

1.4 Thesis Layout

The structure of this PhD thesis is summarised in Figure 1.3. The thesis contains 8 chapters.

This chapter (chapter 1) presents an overview of the manufacture, advantages and disadvantages of biodiesel as an alternative of fuels bring into focus the use of cold flow additives on improving cold flow behaviour of biodiesel and how this perspective leads to the research question and how the associated project is managed and delivered.

Chapter 2 discusses the fundamental knowledge of the nature of the crystallography, crystallization process notably nucleation and crystal growth, crystal morphology and habit modification by impurities, molecular modelling methods and characterization techniques.

Chapter 3 reviews the literatures related to the effects of inorganic and organic additives on nucleation, growth and crystal polymorphism transformation and cold flow additives on cold flow behaviour of diesel fuels and biodiesel.

Chapter 4 provides information about the materials, naphthalene, biphenyl, methyl stearate and synthesised additives together with computational and experimental methods used in this study.

Chapter 5 describes a molecular cluster modelling approach and the application of the methodology to crystallisability of naphthalene and biphenyl together with the experimental results of slow cooling crystallization of naphthalene and biphenyl. Chapter 6 details the intermolecular interactions and predicted morphologies in vacuum for both two polymorphs of methyl stearate and habit modification of methyl stearate in the presence of different solvents through experimental observation and molecular modelling method.

Chapter 7 provides details of the experimental nucleation kinetics measurements of pure methyl stearate in methyl oleate and examines the effects of synthesised additives on nucleation behaviour of methyl stearate in methyl oleate.

Finally, chapter 8 summaries the outcome from this work and makes suggestion for future development of this work.

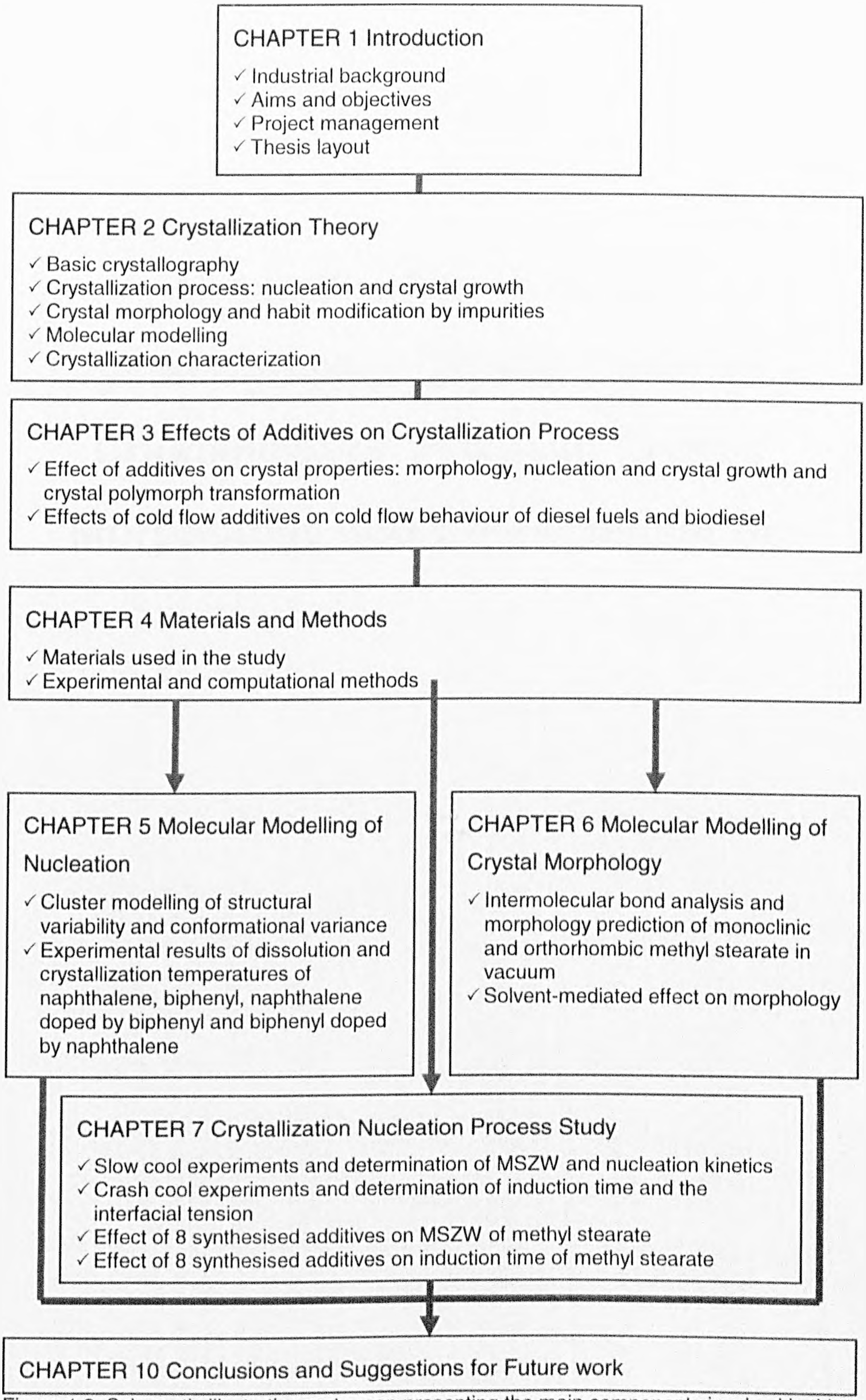

Figure 1.3: Schematic illustrative route-map presenting the main components involved in this thesis

CHAPTER 2

Crystallization Science: Crystallography, Crystal Chemistry, Crystallization Process, Crystal Morphology and Characterisation

Summary:

A summary of the fundamentals the nature of crystallography and crystal science supporting the formation of crystals and crystal growth is presented.

2.1 Introduction

This chapter focuses on the scientific and practical basis understanding the theory of crystallization in relation to the structure, crystallization and morphology of crystals. First of all, the study of the crystal lattice, unit cell is introduced. After describing the basis of crystals, crystal chemistry and space groups of different crystals are described. Following is the introduction of the fundamental theories on crystal nucleation and the crystal growth mechanism and crystal morphology. The next section covers the history and the method for crystallization modelling. Finally, the methods for characterizing crystallization process are given.

2.2 Crystals and Crystal Structures

Crystals are solids that possess long-range 3-D order. The arrangement of the atoms at one point in a crystal is identical (expecting localised mistakes or defects that can arise during crystal growth) to that in any other remote part of the crystals. Crystallography describes the ways in which the component atoms are arranged in 3-D within the crystals and how the long-range order is achieved.

2.2.1 Lattice, directions, planes and unit cells

Crystals are solids in which the molecules, atoms or ions are arranged in an ordered repeating pattern extending into three dimensions. This repeating pattern is known as ***lattice***. In two-dimensional design, the repeating pattern is a wallpaper pattern repeating in all directions [18]. The pattern in three-dimensions is correspondingly built up on space-lattice. The position of lattice point can be defined by the vector $P(uv)$:

$$P(uv) = ua + vb \tag{2-1}$$

where u and v are integers describing the position of other lattice points on the plane, vectors a and b specify the direction and magnitude of the translation from one point to the next along a row of points. The vectors (a and b) and the angle (γ) between them are termed lattice parameters (see Figure 2.1).

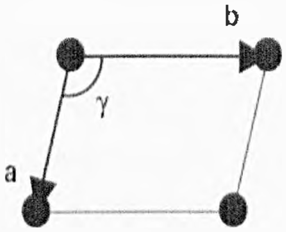

Figure 2.1: The unit cell and lattice parameters of the two dimensional pattern [19].

Three-dimensional lattices use the same nomenclature as the two-dimensional lattices described above. If any lattice point is chosen as the origin, the position of any other lattice is defined by the vector P (uvw):

$$P(uvw) = ua + vb + wc \tag{2-2}$$

where a, b, c are the basic vectors, and u, v and w are positive or negative integers or rational numbers.

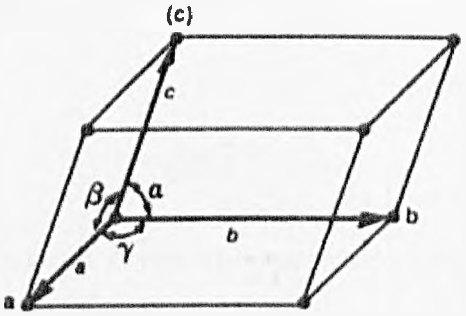

Figure 2.2: Three-dimensional unit cell, crystallography axes a, b, c and the lattice parameters a, b, c, α, β, γ [18].

The crystal axes form the edges of a parallelepiped which is known as a ***unit cell*** [20]. Each crystal consisted of a repetitive stacking of unit cells and each unit cell contained lattice parameters such as a, b, and c (shown in Figures 2.1 and 2.2).

The ***reciprocal lattice***, corresponding to the ***direct lattice***, is helpful to express the geometry of the three-dimensional patterns of scatter radiation diffracted for example by X-rays, electrons and neutrons. The direct lattice occupies real space, whereas the reciprocal lattice occupies the reciprocal space in which a vector within the reciprocal lattice is perpendicular to the crystal faces of the direct unit cell [19].

A notation [uvw] is needed to specify the ***crystal directions*** where the atoms locate in the crystal. Note that the symbol [uvw] includes all parallel directions, just as (hkl) specifies a set of parallel planes [19] see below. The directions specify three indices which define the coordinates of a point within the lattice. The index u gives the coordinates in terms of the lattice repeat a long the a-axis, and the same with the v and w. Negative values of u, v and w are written $\bar{u}$ (pronounced u bar), $\bar{v}$ (pronounced v bar), $\bar{w}$ (pronounced w bar) [19].

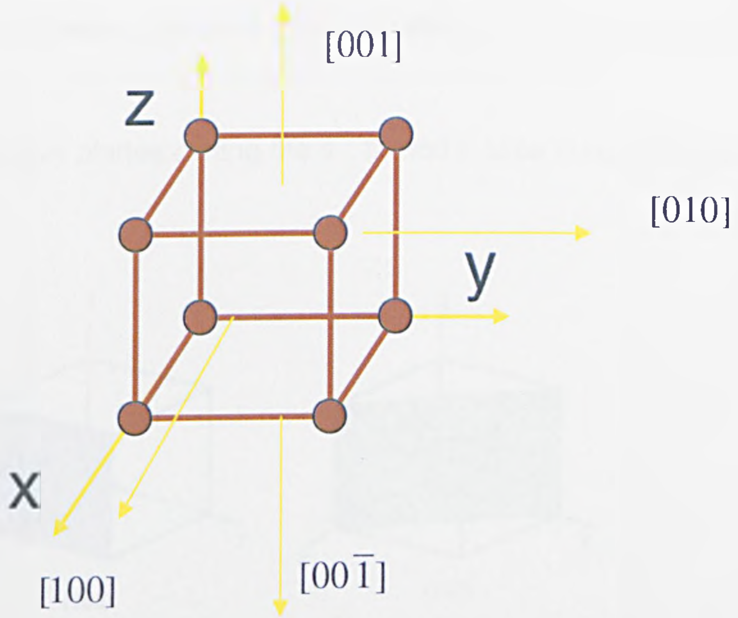

Figure 2.3: Crystallographic directions [19].

The notation <uvw> is another way to express a family of related directions. In cubic crystal the symbol <100> represents the six directions [100], [$\bar{1}00$], [010], [$0\bar{1}0$], [001], [$00\bar{1}$].

The faces of a crystal can be represented in terms of the axial intercepts. Miller indices are usually used as a system of notation for faces of crystal or planes within a crystal or a space lattice [20]. In 1839 W.H. Miller suggested that each face of the crystal could be represented by indices h, k, and l, defined by

$$h = \frac{a}{X}; \; k = \frac{b}{Y}; \quad l = \frac{c}{Z} \tag{2-3}$$

where X, Y, and Z are the intercepts of the intercepts of the plane on the axes x, y, z of the unit cell with length parameters a, b and c [21].

Miller indices, (hkl), represent not just a crystal face or lattice plane, but the set of all identical parallel lattice planes. The values of h, k and l are the reciprocals of the fractions of a unit cell edge, a, b and c respectively, intersected by an appropriate plane [19]. This means [20]:

(1) ***Pinacoids*** are forms in which each plane intersects a single axis and is parallel to the other two.

(2) ***Prism*** and ***domes*** each have planes cutting two axes and lying parallel to the third.

(3) ***Pyramids*** have planes cutting the a-, b- and c-axes (see in Figure 2.4)

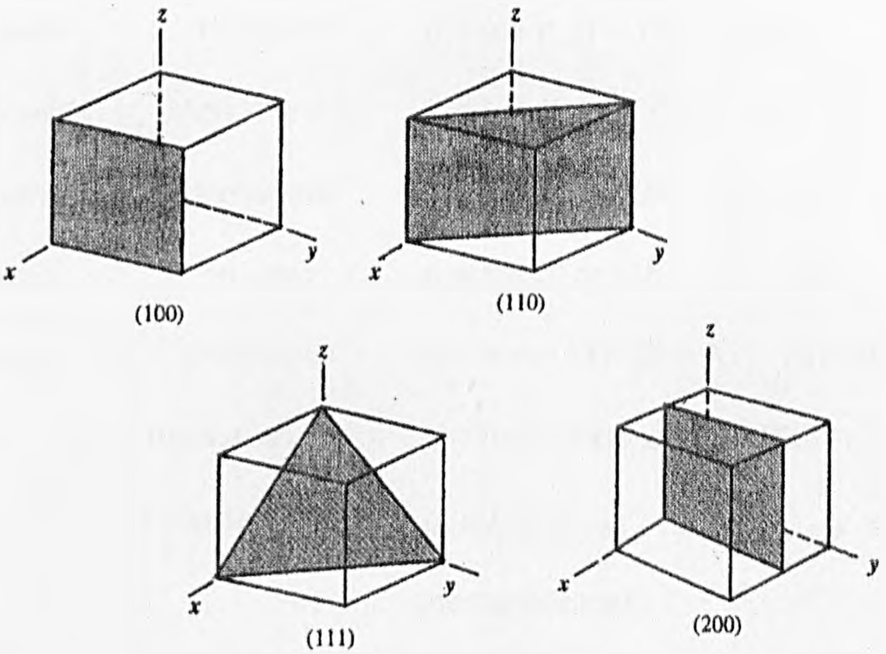

Figure 2.4: Some important planes in the cubic system along with their Miller indices [20].

2.2.2 Crystal system and Bravais lattice

To assign a given point in a lattice or atom in a structure, its coordinates are related to the crystal axes. The ***crystal systems*** are a series of crystal structures according to the axial system used to describe the lattice. Seven different crystal systems, each with specified equality or inequality of lengths and angles, have been used to describe the geometry arrangement.

The three reference axes are labelled a, b and c, and the angles between the positive direction of the axes are α, β, and γ, where α lies between +b and +c, β lies between +a and +c, and γ lies between +a and +b, (Figure 2.5). The angles are chosen to be greater or equal to 90° except for the trigonal system, as described below. In figures, the a-axis is represented as projecting out of the plane of the page, towards the reader, the b-axis points to the right and the c-axis points towards the top of the page. The arrangement is a right-handed coordinate system [19].

Table 2.1 The seven crystal system [19]

Crystal Family	Crystal System	Axial relationships
Isometric	Cubic	$a=b=c$, $\alpha=\beta=\gamma=90°$
Tetragonal	Tetragonal	$a=b\neq c$, $\alpha=\beta=\gamma=90°$
Orthorhombic	Orthorhombic	$a\neq b\neq c$, $\alpha=\beta=\gamma=90°$
Monoclinic	Monoclinic	$a\neq b\neq c$, $\alpha=90°$, $\beta\neq 90°$, $\gamma=90°$
Anorthic	Triclinic	$a\neq b\neq c$, $\alpha\neq 90°$, $\beta\neq 90°$, $\gamma\neq 90°$
Hexagonal	Hexagonal	$a=b\neq c$, $\alpha=\beta=90°$, $\gamma=120°$
	Trigonal or	$a=b=c$, $\alpha=\beta=\gamma=90°$ or
	Rhombohedral	$a'=b'\neq c'$, $\alpha'=\beta'=90°$, $\gamma'=120°$
		(hexagonal axes)

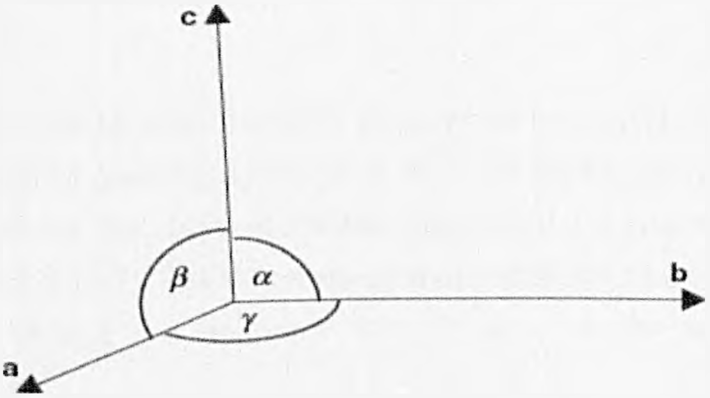

Figure 2.5: The reference axes used to characterise the seven crystal systems [19]

Fourteen possible three-dimensional lattices, called Bravais lattices, are pictured in Figure 2.6 [19], and listed in Table 2.2 [19]. Bravais lattices are sometimes called direct lattices. Bravais lattices are defined in terms of conventional crystallographic bases and cells. The rules for selecting the preferred lattice are determined by the symmetry of the lattice. In brief, the main conditions are [19]:

(i) The three basis vectors define a right-handed coordinate system, that is, a (or x) points out of the page, b (or y) points to the right and c (or z) is vertical.

(ii) The a, b and c basic vectors for a cubic lattice are parallel to the three four-fold symmetry axes.

(iii) The basis vector c for the hexagonal lattice parallel to the unique six-fold symmetry axis; a and b are along two-fold symmetry axes perpendicular to c and at 120° to each other.

(iv) The basis vector c for the tetragonal lattice is taken along the unique four-fold symmetry axis; a and c lie along two-fold symmetry axes perpendicular to each other and c.

(v) The basis vectors a, b and c for an orthorhombic crystal lie along three mutually perpendicular two-fold symmetry axes.

(vi) The unique symmetry direction in monoclinic lattices is conventionally labelled b; a and c lie in the lattice net perpendicular to b and include an oblique angle.

(vii) A rhombohedral lattice is described in two ways. If described in terms of a hexagonal lattice, c lies along the three-fold symmetry axis, with a and c chosen as for the hexagonal system. In terms of rhombohedral axes, a, b and c are the shortest non-coplanar lattice vectors symmetrically equivalent with respect to the three fold axis.

(viii) A triclinic cell is chosen as primitive.

From Table 2.2, it can be noted that if the lattice which has points only at corners is primitive, it should be given the symbol P. In the monoclinic system, there is a cell with a lattice point in the centre of the face opposite the c axis, then the cell is given the symbol C [20]. Cells with body-centred points are labelled I, and those with all faces centred are labelled F [20]. R as a symbol is given to the rhombohedral cell.

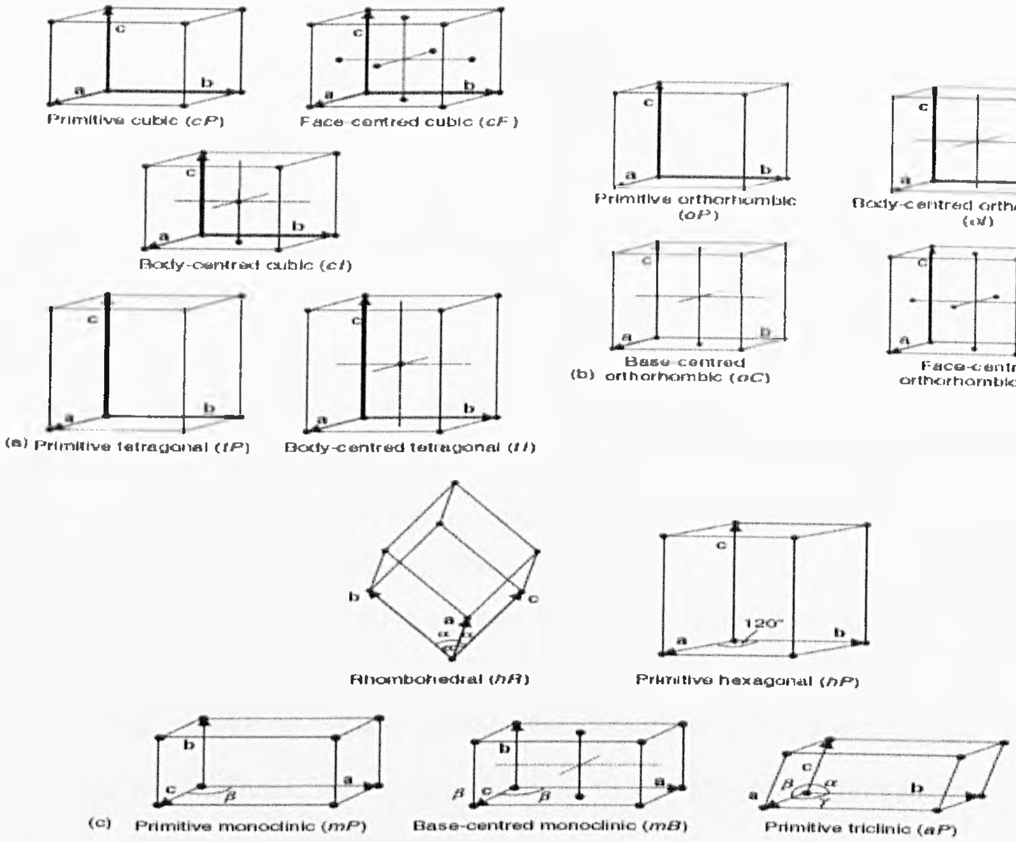

Figure 2.6: The 14 Bravais lattices. Note that the lattice points are exaggerated in size and are not atoms. The monoclinic lattices have been drawn with the b-axis vertical, to emphasise that it is normal to the plane containing the a- and c- axes [19].

Table 2.2 Bravias lattice [19]

Crystal system	Lattice symbol	Lattice parameters
Triclinic	aP	$a \neq b \neq c$, $\alpha \neq 90°$, $\beta \neq 90°$, $\gamma \neq 90°$;
Monoclinic primitive	mP	$a \neq b \neq c$, $\alpha = 90°$, $\beta \neq 90°$, $\gamma = 90°$;
Monoclinic centred	mC	
Orthorhombic primitive	oP	$a \neq b \neq c$, $\alpha = \beta = \gamma = 90°$
Orthorhombic C-face-centred	oC	
Orthorhombic body-centred	oI	
Orthorhombic face-centred	oF	
Tetragonal primitive	tP	$a = b \neq c$, $\alpha = \beta = \gamma = 90°$
Tetragonal body-centred	tI	
Trigonal (Rhombohedral)	hR	$a = b = c$, $\alpha = \beta = \gamma$ (primitive cell); $a' = b' \neq c'$, $\alpha' = \beta' = 90°$, $\gamma' = 120°$ (hexagonal cell)
Hexagonal primitive	hP	$a = b \neq c$, $\alpha = \beta = 90°$, $\gamma = 120°$
Cubic primitive	cP	$a = b = c$, $\alpha = \beta = \gamma = 90°$
Cubic body-centred	cI	
Cubic face-centred	cF	

2.2.3 Point symmetry and point group

All crystals can be classified in terms of the collection of symmetry elements that can be attributed to the shape. Besides the external symmetry of crystals, there is also an internal symmetry located around the atoms, on or around lattice points. The symmetry operators are described here by the International or Hermann-Mauguin symbols. The order in which the symmetry operators are written is governed by specific rules, given in Table 2.3. The places in the symbol refer to directions. The first place or primary position is given to the most important or defining symmetry element of the group, which is often a symmetry axis. Symmetry axes are taken as parallel to the direction described [19]. A solid can belong to one of an infinite number of general three-dimensional point groups. However, if the rotation axes are restricted to those that are compatible with the translation properties of a lattice, a smaller number, the crystallographic point groups are found. The operators allowed within the crystallographic point groups are: the centre of symmetry, $\bar{1}$, the mirror operator, m the proper rotation axes 1, 2, 3, 4 and 6, and the improper rotation axes, $\bar{1}$, $\bar{2}$, $\bar{3}$, $\bar{4}$ and $\bar{6}$ [19].

Table 2.3 The order of the Hermann-Mauguin symbols in point groups [19]

Crystal system	Primary	Secondary	Tertiary
Triclinic	–	–	–
Monoclinic	[010], unique axis b [001], unique axis c	–	–
Orthorhombic	[100]	[010]	[001]
Tetragonal	[001]	[100], [010]	$[1\bar{1}0]$, [110]
Trigonal, Rhombohedral axes	[111]	$[1\bar{1}0]$, $[01\bar{1}]$, $[\bar{1}01]$	
Trigonal, Hexagonal axes	[001]	[100], [010], $[\bar{1}\bar{1}0]$	
Hexagonal	[001]	[100], [010], $[\bar{1}\bar{1}0]$	$[1\bar{1}0]$, [120], $[\bar{2}\bar{1}0]$
Cubic	[100], [010], [001]	[111], $[\bar{1}\bar{1}1]$, $[1\bar{1}\bar{1}]$, $[\bar{1}1\bar{1}]$	$[1\bar{1}0]$, [110], $[01\bar{1}]$, [011], $[\bar{1}01]$, [101]

2.2.4 Space group

A combination of the translation inherent in the 14 Bravais space lattices with the symmetry elements present in the 32 crystallographic point groups, together with a new symmetry element, the screw axis, allows all possible three-dimensional repeating crystallographic patterns to be classified [19]. The resulting 230 combinations are the crystallographic ***space groups***. There is a different type of symmetry operation for the position of points, which is called ***translation symmetry***. Screw axes are rototranslation symmetry elements, formed by a combination of rotation and translation [19].

A screw axis of order n operates on an object by a rotation $2\pi/n$ counter clockwise and then translation by a vector n parallel to the axis [19]. If the rotation component of the operator is applied n times, the total rotation is equal to 2π , and the removal is represented by the vector nt simultaneously [19]. In order to maintain the lattice repeat, it should be expressed as [19]:

$$nt = pT \tag{2-4}$$

where p is an integer, and T is the lattice repeat in a direction parallel to the rotation axis [19]. Thus:

$$t = (p/n)T \tag{2-5}$$

The unique screw axes are list in Table 2.4 [19].

Table 2.4: Rotation, inversion and screw axes allowed in crystals [19]

Rotation axis, n	Inversion axis, $\bar{n}$	Screw axis, n_p				
1	$\bar{1}$ (centre of symmetry)					
2	$\bar{2}$ (m)	2_1				
3	$\bar{3}$	3_1	3_2			
4	$\bar{4}$	4_1	4_2	4_3		
6	$\bar{6}$	6_1	6_2	6_3	6_4	6_5

The space groups outline the total number of three-dimensional patterns, and each group can be termed as a unique symbol and number. The space group symbol contains two sections: (a) a capital letter, expressing the lattice that underlies the structure, and (b) a series of characters that represent the symmetry elements of the space group (see Tables 2.5 and 2.6).

Table 2.5 The crystallographic space group letter symbols [19]

Letter symbol	Lattice type	Number of lattice points per unit cell	Coordinates of lattice points
P	Primitive	1	0, 0, 0
A	*A*-face centred	2	0, 0, 0; 0, ½, ½
B	*B*-face centred	2	0, 0, 0; ½, 0, ½
C	*C*-face centred	2	0, 0, 0; ½, ½, 0
I	Body centred	2	0, 0, 0; ½, ½, ½
F	All-face centred	4	0, 0, 0; ½, ½, 0; 0, ½, ½; ½, 0, ½
R	Primitive (rhombohedral axes)	1	0, 0, 0
	Centred rhombohedral (hexagonal axes)	3	0, 0, 0; ⅔, ⅓, ⅓; ⅓, ⅔, ⅔ (obverse setting) 0, 0, 0; ⅓, ⅔, ⅓; ⅔, ⅓, ⅔ (reverse setting)
H	Centred hexagonal	3	0, 0, 0; ⅔, ⅓, 0; ⅓, ⅔, 0

Table 2.6 Symmetry elements in space group symbols [19]

Symbol	Symmetry operation	Comments
m	Mirror plane	reflection
a	Axial glide plane ⊥[010], [001]	Glide vector **a**/2
b	Axial glide plane ⊥ [001], [100]	Glide vector **b**/2
c	Axial glide plane ⊥ [100], [010]	Glide vector **c**/2
	⊥ $[1\bar{1}0]$, [110]	Glide vector **c**/2
	⊥ [100], [010], $[\bar{1}\bar{1}0]$	Glide vector **c**/2, hexagonal axes
	⊥ $[1\bar{1}0]$, [120], $[\bar{2}\bar{1}0]$ $[\bar{1}\bar{1}0]$	Glide vector **c**/2, hexagonal axes
n	Diagonal glide plane ⊥ [001]; [100]; [010]	Glide vector ½(**a**+**b**); ½(**b**+**c**); ½(**a**+**c**)
	Diagonal glide plane ⊥ $[1\bar{1}0]$; $[01\bar{1}]$; $[\bar{1}01]$	Glide vector ½(**a**+**b**+**c**)
	Diagonal glide plane ⊥ [110]; [011]; [101]	Glide vector ½(−**a**+**b**+**c**); ½(**a**−**b**+**c**); ½(**a**+**b**−**c**)
d	Diamond glide plane ⊥ [001]; [100]; [010]	Glide vector ¼ (**a**±**b**); ¼(**b**±**c**); ¼(±**a**+**c**)
	Diamond glide plane ⊥ $[1\bar{1}0]$; $[01\bar{1}]$; $[\bar{1}01]$	Glide vector ¼(**a**+**b**±**c**); ¼(±**a**+**b**+**c**); ¼(**a**±**b**+**c**)
	Diamond glide plane ⊥ [110]; [011]; [101]	Glide vector ¼(−**a**+**b**±**c**); ¼(±**a**−**b**+**c**); ¼(**a**±**b**−**c**)
1	None	–
2, 3, 4, 6	*n*-fold rotation axis	Rotation counter clockwise of 360°/*n*
$\bar{1}$	Centre of symmetry	–
$\bar{2}(=m)$, $\bar{3}$, $\bar{4}$, $\bar{6}$	*n*-fold inversion (rotoinversion) axis	360°/*n* rotation counter clockwise followed by inversion
2_1, 3_1, 3_2, 4_1, 4_2, 4_3, 6_1, 6_2, 6_3, 6_4, 6_5	*n*-fold screw (rototranslation) axis, n_p	360°/*n* right-handed screw rotation counter clockwise followed by translation by (p/n)**T**

2.2.5 Defects in crystal

In actual crystals, ***defects*** are always present and their nature and effects often play an important role in understanding the properties of crystals. There are several types of imperfections in metallic crystals [20]:

(1) when structures contain defects in all atomic sites of the structure, this defect is known ***point defect***. The point defects include vacancies, interstitials, schottky defects and fenkel defects in ionic crystals.

(2) If a plane of atoms enlarges half way through a crystal, the edge of such a plane is a defect in the form of a line, and is known as a ***dislocation***. There are two kinds of dislocation, one is called as edge dislocations and the other is screw dislocations. An edge dislocation [22] is illustrated in Figure 2.7, which is a cross section of a crystal lattice [23]. The dislocation is labeled at point A in Figure 2.7, half of a vertical row in the middle of the lattice is missing, and this row of atoms is missing in each plane of the lattice parallel to the page [23]. The other type of line defect is screw dislocation in three dimensions illustrated in Figure 2.8 [23]. The process of the screw dislocation can be imagined that the crystal was cut along the line BC going towards point A, and then the cut was pushed up until point B was displaced one lattice unit higher at the edge along the cut [23]. This resulted in a ledge running from A to B [23]. Because the screw dislocation is very important in crystal grow, it will be detailed in Section 2.6.

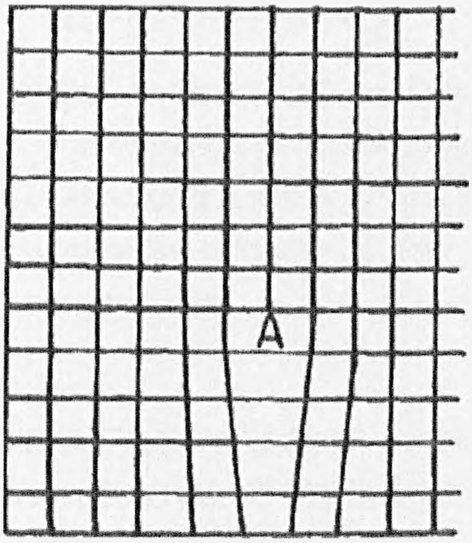

Figure 2.8: An edge dislocation in two dimensions [22].

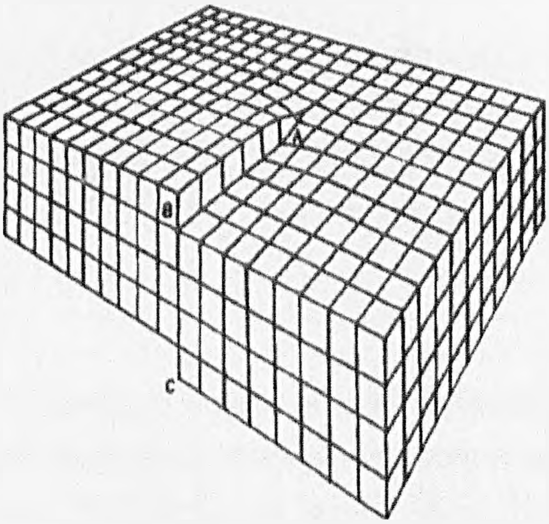

Figure 2.7: A screw dislocation in a simple cubic crystal. The screw dislocation AD is parallel to BC (D is not visible) [23].

2.3 Crystal Chemistry

2.3.1 Size and shape of molecule

The first of the molecular properties is atomic size which refers to the distance that the furthest electrons are from the nucleus. Each atom has a nucleus inside and electrons moving around the nucleus, so the size of an atom depends on the distance between the nucleus and outermost electrons, and the radii for the atom can be divided into the types of interatomic forces: ionic, covalent, metallic and van der Waals. Due to different strengths of bonding, the distance between electrons and nucleus will be varied [24]:

(1) Two factors affect the atomic size: electron repulsive force and covalent bond. For ionic atoms, the loss and attainment of electrons can determine the change of repulsive force, and greater repulsion means electrons move away from the nucleus and the size will increase. Due to type of force, the covalent radii are smaller than the ionic radii for the same elements. The reason for this case is that covalent bonds result in electron sharing.

(2) Because metallic atoms can be readily compressed by ligands in various directions and ionic charges are essentially absent in metals, also the atomic radii are very much larger than the ionic radii. The atomic size will decrease slight when the co-ordination is decreased.

(3) Van der Waals radii for atoms can be derived from molecular structures by determining the closest distance of approach between adjacent molecules. Although the radii are larger than covalent radii, Van der Waals radii can't be regarded as having the same degree of constancy as the ionic, covalent and metallic radii.

Atomic shape is also an important chemistry property. An atom consists of a nucleus and electrons zooming around the nucleus. The molecular orbit is used to describe where the electrons move. The shape of these orbital changes correspond to a principal quantum number, so although the total shape of the atom is round, different electrons in different shaped orbits is important to investigate how atoms can be put together by bonds.

2.3.2 Inter-atomic binding forces

As discussed above, the atomic sizes are varied with the type of inter-atomic bond. These forces can be divided into four distinct types [25]:

(1) The ionic, electrovalent, heteropolar or polar bond, the force of electrostatic attraction which operates between oppositely charged ions. First of all, due to different ionization potential, the ions of elements could be taken into account.

(2) The covalent or homopolar bond, the normal chemical valency bond between the two atoms which share the electrons in the molecules. In the covalent bond system, the atoms of the element can be the same or different, such as H_2, F_2, and CO2.

(3) The metallic bond, the inter-atomic force responsible for the cohesion of metal systems in the solid state. A metal can be regarded as an assemblage of positive ions immersed in a gas of free electrons. Attraction between positive ions and the electron gas provide the strength for the coherence of the structure, and a free mobility of this electron gas under the influence of the electrical or thermal stress is responsible for the high conductivity.

(4) The van der Waals or residual bond, a weak force of inter-atomic attraction operating between all atoms and ions in all solids. Because the van der Waals forces appear between the uncharged atoms or molecules, it is weak compared with the ionic, covalent and metallic bonds.

(5) The hydrogen bond is a special one-dimensional dipole-dipole interaction resulting from F-H, O-H and N-H dipolar covalent bonds. The formation of the hydrogen bond is due to the partially positive hydrogen attracting the partially negative atom such as F, O and N. The energy of a hydrogen bond is smaller than the energy of covalent and ionic bonds, but much larger than the energy of van der Waals bond.

It can be concluded that the molecular binding forces play an important role in the properties of molecular solids, i.e. atomic size, molecular structure and thermal and electrical conductivity.

2.3.3 Polymorph, solvates, co-crystal and salts

Because different inter-atomic bonds involved, there are some phenomenon happening for crystal form:

(1) Polymorph, means the solid materials have more than one crystal form or structure. Different polymorphs of a given material have identical chemistry properties, but will present different physical properties, i.e. solubility, melting

point. The different environmental conditions could be the main reason responsible for the formation of polymorphism, i.e. solvent effect, impurity involved in the growth of polymorphs, the level of supersaturation for the crystallization process. Dimorphous and trimorphous substances are commonly known [21], for example the polymorphs of calcium carbonate, carbon and silicon dioxide were shown in Table 2.7.

Table 2.7 Polymorph of calcium carbonate, carbon and silicon dioxide and the space group corresponding to these different polymorphs.

	Polymorph		
Calcium carbonate	Calcite (trigonal/rhombohedral)	Aragonite (orthorhombic)	Vaterite (hexagonal)
Carbon	Graphite (hexagonal)	Diamond (cubic)	
Silicon dioxide	Cristobalite (cubic)	Tridymite (hexagonal)	Quartz (trigonal)

(2) Solvate, which is a stable solute species with solvent molecules in the crystal lattice is formed by solvation, an interaction of the solvent molecule with solute molecules or ions of the solute. Because of the different type of molecule, the interactions are varied, i.e. hydrogen bonding, ion-dipole, and Van der Waals forces.

(3) Co-crystal is a crystal that contains two or more molecules corresponding to the different compounds in the crystal lattice. Compared with a pure form of crystal, the co-crystal exhibits different properties. The interaction in the co-crystal lattice is the hydrogen bond.

(4) Like co-crystals, salts are also defined as multicomponent crystals, but the characterization of degree of proton transfer is different from co-crystals [26]. It is reported that there is more or less complete proton transfer in salts, whereas little or none in co-crystals [26].

As discussed above, the main reasons for these different forms are different environmental crystallization conditions. The crystallization composition and processing variables are listed in Table 2.8 [27].

Table 2.8 Crystallization composition and processing variables [27]

Composition type		Process variables[a]				
Polymorph/ solvates	Salts/ co-crystals	Thermal	Anti-solvent	Evaporation	Slurry conversion	Other variables
■ Solvent/ solvent combinations	■ Counter-ion type	■ Heating rate	■ Anti-solvent type	■ Rate of evaporation	■ Solvent type	■ Mixing rate
■ Degree of supersaturation	■ Acid/base ratio	■ Cooling rate	■ Rate of anti-solvent addition	■ Evaporation time	■ Incubation temperature	■ Impeller design
■ Additive type	■ Solvent/ solvent combinations	■ Maximum temperature	■ Temperature of anti-solvent addition	■ Carrier gas	■ Incubation time	■ Crystallization vessel design (including capillaries, etc.)
■ Additive concentration	■ Degree of super-saturation ■ Additive type and concentration ■ pH ■ Ionic strength	■ Incubation temperature(s) ■ Incubation time	■ Time of anti-solvent addition	■ Surface-volume ratio	■ Thermal cycling and gradients	

[a] Applicable to all types of screens.

2.4 Crystallization Process

2.4.1 Solubility

Crystallization is a separation and purification method for manufacturing a large range of materials. Crystallization may be defined as a phase transition in which crystals are obtained from the solution. Solutions may be homogeneous mixtures of two or more substances. In general, solutions are normally liquids; however, solutions may include solids and even gases. Because solubility occurs under dynamic equilibrium, a variety of solubility models are all based on the equation of phase equilibrium.

A fundamental notion in thermodynamics is the state of a system, defined by the ensemble of state variables, such as volume, pressure, temperature, number of molecules, etc. Their functional dependence is called state function.

$$dy(x_1,x_2,\cdots,x_i,\cdots)=\left(\frac{\partial y}{\partial x_1}\right)_{x_2,\cdots,x_i,\cdots}dx_1+\left(\frac{\partial y}{\partial x_2}\right)_{x_1,x_3,\cdots,x_i,\cdots}dx_2+\ldots+$$

$$\left(\frac{\partial y}{\partial x_i}\right)_{x_1,x_2,\cdots,x_{i-1},x_{i+1},\cdots}dx_i+\ldots \tag{2-6}$$

is independent of the order of differentiation [28].

It can be readily shown that the Gibbs free energy of an ideal mixture (as in ideal gases) exceeds the value for the same unmixed material at constant T and p by an amount:

$$\Delta G = RT\sum_A n_A \ln x_A \tag{2-7}$$

Thus the chemical potential $\mu_A = \partial(\Delta G)/\partial n_A$ of species A is given by:

$$\mu_A = \mu_A^0 + RT\ln x_A \tag{2-8}$$

IF a mixture (or solution) exhibits non-ideal behaviour, the departure from ideality may be expressed in terms of the relative activity a_A which is defined by:

$$\mu_A = \mu_A^0 + RT\ln a_A \tag{2-9}$$

Comparison of equation (2-8) and (2-9) shows that, for an ideal mixture,

$$a_A = x_A \tag{2-10}$$

The conditions for a solution of material A to be ideal is that its chemical potential in the solution is the same as that of the pure substance in the solid state, so that

$$\mu_A(s) = \mu_A^0 + RT\ln a_A \tag{2-11}$$

Division by T and differentiation with respect to temperature gives:

$$\frac{\partial}{\partial T}\left[\frac{\mu_A(s)}{T}\right]-\frac{\partial}{\partial T}\left(\frac{\mu_A^0}{T}\right)=R\frac{\partial}{\partial T}\ln a_A \tag{2-12}$$

Now it is a familiar relation that [29]

$$\frac{\partial}{\partial T}\left(\frac{\mu}{T}\right)=\frac{-H}{T^2} \qquad (2\text{-}13)$$

So, if the solute and solvent did form an ideal solution, the solubility could be predicted from the van't Hoff equation[21]:

$$\ln x=\frac{\Delta H_f}{R}\left[\frac{1}{T_f}-\frac{1}{T}\right] \qquad (2\text{-}14)$$

where x is the mole fraction of the solute in the solution, T is the solution temperature (K), T_f is the fusion temperature (melting point) of the solute (K), ΔH_f is the molar enthalpy of fusion of the solute (J mol^{-1}) and R is the gas constant (8.134 J mol^{-1}K^{-1}) [21].

Also in an ideal solution, the equation holds [29]

$$\frac{\partial}{\partial T}\ln x_A=\frac{\Delta H_f}{RT^2} \qquad (2\text{-}15)$$

or

$$x_A=x_{\infty}\exp(-\Delta H_f/RT) \qquad (2\text{-}16)$$

If $\ln x_A$ is plotted against reciprocal temperature for an ideal solution, a straight line of slope ($(-\Delta H_f/R)$ is obtained with an upper limit of $\ln x_A=0$ at the melting point T_M.

Since:

$$\Delta H_f=T_f\Delta S_f \qquad (2\text{-}17)$$

The Equation (2-14) can be written,

$$\ln x=\frac{-\Delta H_f}{RT}+\frac{\Delta S_f}{R} \qquad (2\text{-}18)$$

Because the van't Hoff equation is used for ideal solutions, when the solution is non-ideal, the following equation could be used [21]:

$$\ln x = \frac{-\Delta H_D}{RT} + \frac{\Delta S_D}{R} \quad (2\text{-}19)$$

where ΔH_D is the molar enthalpy of dissolution, ΔS_D is the molar entropy of dissolution.

Also, the reformed van't Hoff equation for non-ideal solution can be expressed with introducing the activity coefficient:

$$\ln(x\gamma) = \frac{\Delta H_f}{R}\left[\frac{1}{T_f} - \frac{1}{T}\right] \quad (2\text{-}20)$$

The activity coefficient for real solution can be approximated using the UNIFAC method.

Broul [30] tested a number of polynomials in predicting the solubility of 70 solutes (inorganic salts) and proposed the solubility equation was:

$$\log x = A + BT^{-1} + C\log T \quad (2\text{-}21)$$

where: x is concentration expressed as a mass fraction

T is the solution temperature (K)

A, B, C are constants.

2.4.2 Supersaturation

Because solubility provides the concentration at which solid solute and the liquid solution are at equilibrium, the importance of solubility is that it can be used to calculate the maximum yield of product crystals. Ostwald [31] appears to be the first to specify this condition exactly by using the terms "meta-stable" and "labile". He points out that the principle is inherent in the reports of many other investigators. In effect, a supersaturated solution or supercooled melt will not adjust spontaneously to the equilibrium condition unless the supersaturation or supercooling exceeds certain more or less definite limits. This range of stability is designated as being "meta-stable". Beyond this limit lies the "labile" region where the meta-stable condition is relieved automatically by the spontaneous generation of nuclei of the proper crystallizing phase. Within this limit any appropriate "seed" will, of course, cause instantaneous crystallization. The supsaturation curve may be called the solubility curve of particles of critical size, while the solubility curve is that of particles of infinite radius. A schematic representation of these conditions is given in Figure 2.9 [32].

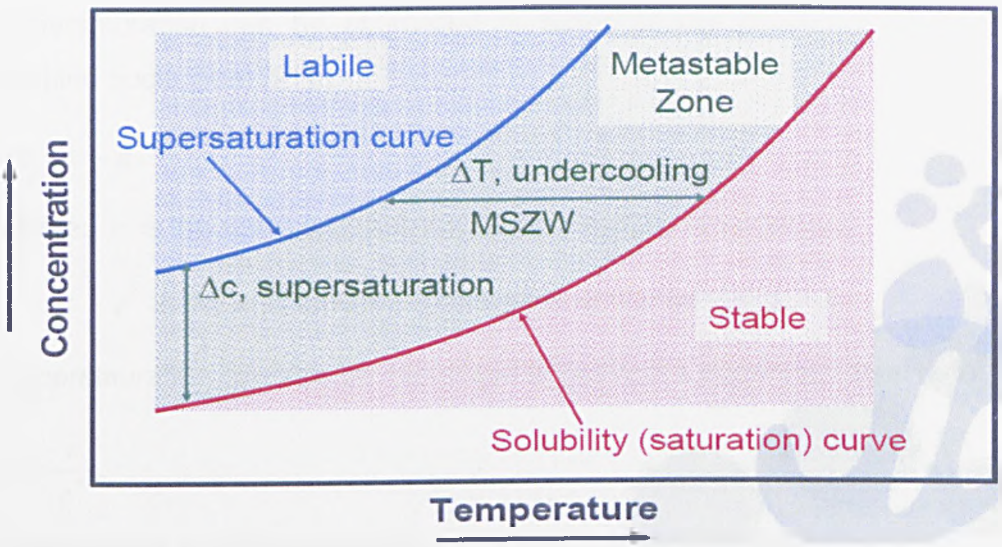

Figure 2.9: Supersolubility curve and regions [32]

Thus the phase diagram can be divided into three principle regions [21]:

- The stable zone, where solution is unsaturated and crystallisation is not possible.
- The meta-stable zone lies in between the solubility and supersolubility curve. Solution is supersaturated, but spontaneous crystallisation is improbable and the solution will remain supersaturated if left undisturbed. However, nucleation can be induced by seeding. At the limit of the meta-stable zone (supersaturated curve) crystallisation may occur spontaneously or may well be induced by seeding, agitation or mechanical shock.
- The labile zone is where the solution is supersaturated. Spontaneous crystallisation is probable but not inevitable.

Supersaturation is the driving force for the crystallization and can be expressed in dimensionless form as

$$\frac{\mu-\mu^*}{RT}=\ln\frac{a}{a^*}=\ln\frac{\gamma c}{\gamma^* c^*} \qquad (2\text{-}22)$$

where μ is the chemical potential, c is the concentration, a is the activity, γ is the activity coefficient, and * represents the property at saturation.

The solution supersaturation can be expressed in a variety of ways. Firstly the supersaturation can be expressed in terms of the concentration driving force (behind nucleation) [21]:

$$\Delta c = c - c^* \tag{2-23}$$

where: c is the solution concentration at a specific temperature,

c^* is the equilibrium concentration at that temperature.

Superstauration can also be expressed in terms of a supersaturation ratio:

$$S = \frac{c}{c^*}. \tag{2-23}$$

Alternatively, a relative supersaturation can be expressed as:

$$\sigma = \frac{\Delta c}{c^*} = S - 1. \tag{2-25}$$

The supersaturation property can also be expressed instead as supercooling, i.e. can be defined in terms of solution temperatures, θ as opposed to solution concentrations:

$$\Delta\theta = \theta^* - \theta. \tag{2-26}$$

Supercooling and supersaturation can then be related by:

$$\Delta c = \left(\frac{dc^*}{d\theta}\right)\Delta\theta \tag{2-27}$$

It is the free energy imbalance that is the result of supersaturation which is the driving force for crystal growth [33].

2.5 Nucleation

Gibbs [34] was the first to realize that the formation of the new phase requires as a necessary prerequisite the appearance of small clusters of building units (atoms or molecules) in the volume of the supersaturated ambient phase (vapour, melt or solution). He considered these nuclei as small liquid droplets, vapour bubbles or small crystallites, or in other words, as small complexes of atoms or molecules which have the same properties as the corresponding bulk phase with the only exception being their small linear sizes.

Crystallization from solution could be considered as a two-step process. Crystals are created, firstly when nuclei are formed (first step 'birth of new nuclei) and then grow to larger sizes. The driving force of nucleation and crystal growth is supersaturation, which can generally be obtained by a change in temperature (cooling in the case of a positive gradient dC^{*}/dv of the solubility curve or heating in the case of a negative gradient), by removing the solvent (usually by evaporation), or by adding a drowning-out agent or reaction partner [33]. Because a supersaturated solution is not at equilibrium, the system attempts to achieve thermodynamic equilibrium through nucleation and the growth of nuclei. If there is neither solid foreign particles nor crystals of its own type in the solutions, nuclei can be formed only by homogeneous nucleation. If foreign particles are present in the solutions, nucleation is facilitated and the process is known as heterogeneous nucleation. Both homogeneous and heterogeneous nucleation take place in the absence of solution-own crystals and are collectively known as primary nucleation [33]. This occurs when a specific supersaturation, known as the meta-stable supersaturation ΔC_{met}, is obtained in the system. However, in semi-commercial and industrial crystallizers, it has often been observed that nuclei occur even at very low supersaturation $\Delta C < \Delta C_{met}$ when solution-own crystals are present (e.g., in the form of attrition fragments or added seed crystals) [33]. Such nuclei are known as secondary nuclei. However, it should be noted that a distinction is made between nucleation resulting from contact, shearing action, breakage, abrasion, and needle fraction [35]. Figure 2.10 illustrates the dependence of supersaturation on several types of nucleation process plotted against solubility.

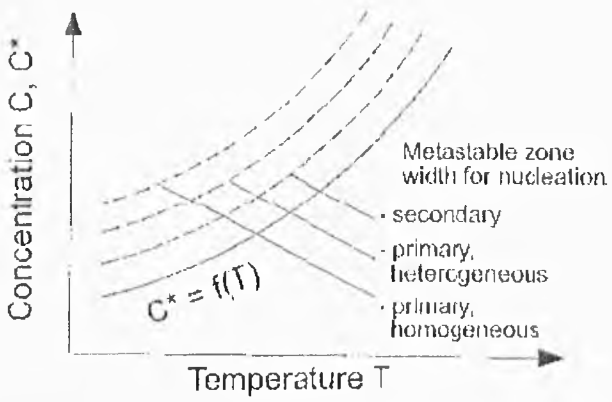

Figure 2.10: Meta-stable supersaturation against temperature for several types of nucleation process [33].

2.5.1 Homogeneous nucleation

The classical nucleation theory dates back to the work of Volmer and Weber [36, 37], who were the first to argue that the nucleation rate should depend exponentially on the reversible work of the formation of a critical cluster and was later extended by authors such as Becker and Döring [38], Farkas [39], Zeldovich [40], Frenkel [41], and others [42]. In order for a new phase to appear, an interface must be formed, which (in the absence of impurities or suspended foreign material) occurs by small embryos in the new phase being formed within the bulk meta-stable phase [33]. These embryos are formed due to spontaneous density or composition fluctuations, which may also result in the spontaneous destruction of such an embryo. Primary nucleation is believed to be initiated in a series of bimolecular collisions that forms an aggregate of embryos of the dissolved material.

$$A_1 + A = A_2$$

$$A_2 + A = A_3$$

$$\vdots$$

$$A_n + A \overset{k_A}{\underset{k_D}{\Leftrightarrow}} A_{n+1}$$

Embryos below a critical cluster size (r_c), are unstable and may detach, however embryos that exceed the critical cluster size may become stable nuclei and will grow [43-45].

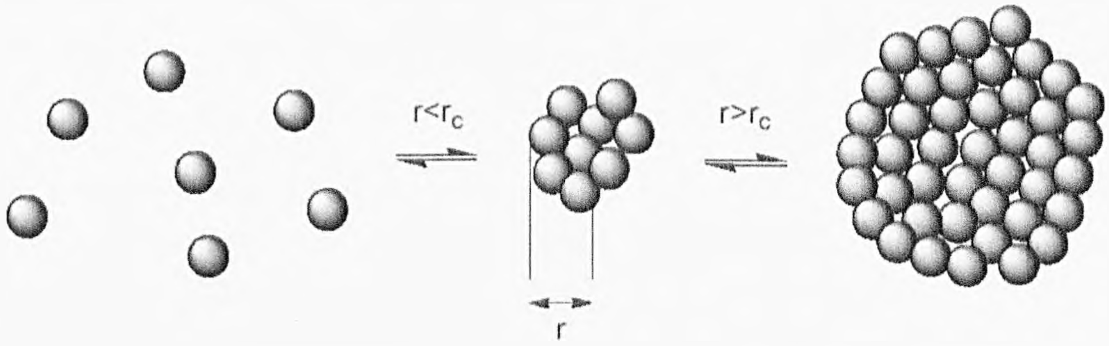

Figure 2.11: The process of nucleation from disorder molecules to embryos and then to nuclei [45].

That continues until the critical size. The rate of nucleus formation by this mechanism is given by an Arrhenius type of expression [23]:

$$B_0 = A\exp\left(-\frac{G_{cr}}{kT}\right) \tag{2-28}$$

Because there is no molecular association in the meta-stable solution and very few embryos, embryos can only grow or shrink as a result of single-molecule events, which can be described by the rate constants k_A and k_D. The value k_A is the rate constant of addition and k_D that of decay of units from a cluster. Because addition is a random process if supersaturation is sufficiently high, more and more elementary units can join together and create increasingly large nuclei known as clusters. The reversible work necessary to form such a cluster is given by a balance of the free enthalpy ΔG_V , that is gained (being proportional to the condensed matter and, thus, to the volume of the cluster) and the free-surface enthalpy ΔG_A needed to build the new surface. The change in positive free-surface enthalpy ΔG_A increases with the interfacial tension γ_{CL} between the solid crystal surface and the surrounding solution, as well as with the surface of the nucleus. The enthalpy is to be added to the system and is therefore positive. On the other hand, the change in free-volume enthalpy ΔG_V during solid phase formation is set free and is thus negative. The magnitude ΔG_V of this enthalpy is proportional to the volume of the nucleus and increases with increasing energy $RT\ln S$, where $S = a/a^*$ or in ideal systems, $S = C/C^*$, when the concentration C of the elementary units changes to the lower equilibrium concentration $C^* = C - \Delta C$ [33].

The free energy change of the formation of the new phase is the sum of the free energy change for the formation of the nucleus surface and free energy change for the phase transformation, thus:

$$\Delta G = \Delta G_s + \Delta G_v = \beta L^2 \sigma + \alpha L^3 \Delta G_v \tag{2-29}$$

Here, σ is the surface tension, and β and α are the area and volume shape factors, respectively. For a spherical nuclei, the area factor $\beta = \pi$, and the volume factor is $\alpha = \pi/6$ based on the diameter, d, of the nuclei. So Equation (2-29) for the spherical nuclei becomes:

$$\Delta G = 4\pi r^2 \sigma + \frac{4}{3}\pi r^3 \Delta G_v \tag{2-30}$$

From Figure 2.12, it is clear that for clusters of solute with a size smaller than critical size r_c to grow requires an increase in free energy. The critical size r_c is related to the surface tension σ and the free energy change ΔG_V

$$r_c = -2\sigma/\Delta G_V \tag{2-31}$$

r_c is critical size when $\dfrac{\partial G}{\partial r} = 8\pi r \gamma + 4\pi r^2 \Delta G_v = 0$

An expression for the critical nucleus size may be obtained by differentiating the above equation with respect to the size and setting the differential to zero at which point the critical cluster size with diameter D_c can be calculated, thus:.

$$D_c = \frac{2SSF}{3VSF}\frac{\gamma v}{k_B T \ln \sigma} \tag{2-32}$$

where VSF=0.52 and SSF=3.14 for spherical nucleus, γ is interfacial tension, k_B is the Boltzman constant, 1.3805×10^{23}, T is the temperature and σ is the solution supersaturation.

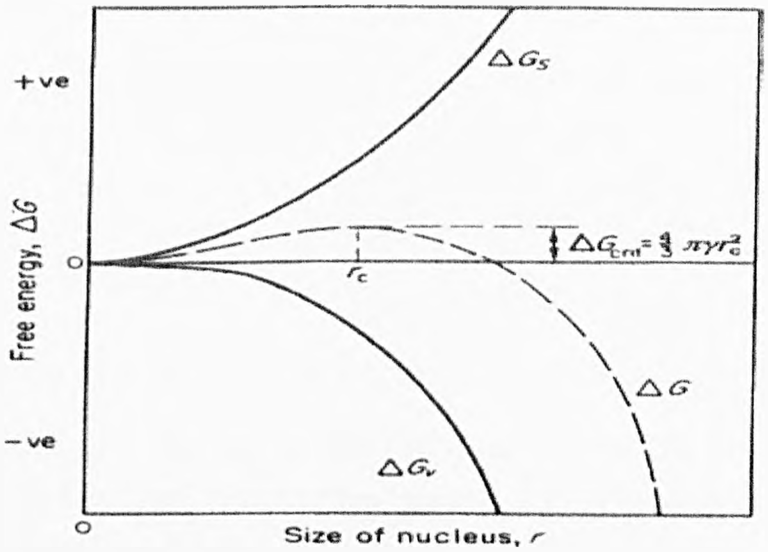

Figure 2.12: Free-energy change for homogeneous nucleation showing the relationship between nucleus and free energy [21].

Figure 2.13 shows the dependence of ΔG_{crit} on the relative supersaturation σ. As the supersaturation increases, both the energy barrier and the value of the critical size decrease. Finally, as the supersaturation increases, the valve of the energy barrier becomes so small that spontaneous and rapid nucleation happens. The rate of nucleation is defined as the rate at which clusters grow through the critical size and so become crystals [46].

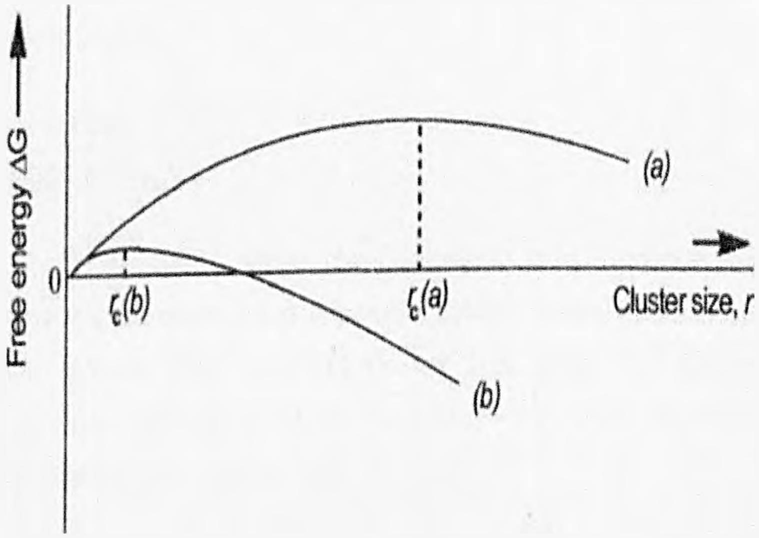

Figure 2.13: Free energy changes as a function of cluster size and supersaturation. Curve (a) at low supersaturation and curve (b) at high supersaturation [46].

2.5.2 Nucleation kinetics

The rate of nucleation, defined as the number of clusters that grow further than the critical size and so become crystals, is given by the equation:

$$J = J_0 \exp\left(\frac{-\Delta G^*}{k_B T}\right) \tag{2-33}$$

where ΔG^* is the critical free-energy change, k_B is the Boltzmann constant.

It has been observed that the solubility of small crystals varies with solution concentration. The resulting equation that represents this behaviour, known as the Gibbs-Thompson equation, is [35]:

$$\ln\left(C/C^*\right) = \ln S = 2\sigma v / kTr_c \tag{2-34}$$

From Equations (2-30) and (2-31):

$$\Delta G^* = \frac{16\pi\sigma^3}{3(\Delta G_v)^2} = \frac{4\pi\sigma r_c^2}{3} \tag{2-35}$$

Hence, from Equations (2-34) and (2-35):

$$\Delta G^* = \frac{16\pi\sigma^3 v^2}{3(kT\ln S)^2} \tag{2-36}$$

and from Equation (2-35):

$$J = J_0 \exp\left[-\frac{16\pi\sigma^3 v^2}{3k^3 T^3 (\ln S)^2}\right] \tag{2-37}$$

It is clear that three variables affect the nucleation rate, and the supersaturation (Figure 2.14) and temperature have a positive effect, however, the surface energy has a negative effect. The importance of the level of supersaturation is demonstrated by the calculation of the induction time [21] for the formation of nuclei in supercooled water (Table 2.9).

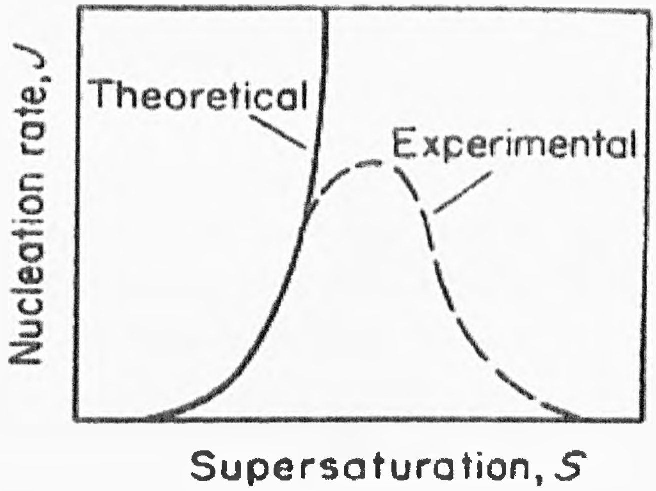

Figure 2.14: Effect of supersaturation on the nucleation rate [21].

Table 2.9 Induction time for nucleation of water vapour [23]

Supersaturation, S	Time
1.0	Infinity
2.0	10^{62} years
3.0	10^{3} years
4.0	0.1seconds
5.0	10^{-13} seconds

2.5.3 Heterogeneous nucleation

Because it is hard to remove all dust and extraneous material from the solution, and the supersaturation is always too high in the homogeneous nucleation, it is obvious that homogeneous nucleation is not ordinarily an important phenomenon in industrial crystallizers. Thus heterogeneouos nucleation and secondary nucleation are generally the most important contributors to new particle formation. Heterogeneous nucleation is termed as the crystallization of dust of solute on suspended dust particles or apparatus surface [35].

Nucleation in a heterogeneous system generally occurs at a lower supersaturation than a homogeneous system, the free energy barrier is lower in the case of a heterogeneous system [23]. Volmer [37] found that the decrease in free energy depended on the contact (or wetting) angle of the solid phase:

$$\Delta G_{\hom} = \varphi \Delta G_{het} \tag{2-38}$$

$$\varphi = \frac{1}{4}(2+\cos\theta)(1-\cos\theta)^2 \tag{2-39}$$

Thus, the supersaturation for nucleation in a heterogeneous system is lower than the homogeneous system. The shaped heterogeneously formed cluster on a solid substrate is often approximated by that of spherical cap with wetting angle θ, which is defined from 0 to 180^0 by the equation:

$$\cos\theta = \frac{\gamma_s - \gamma_{cs}}{\gamma_c} \tag{2-40}$$

in which γ_s and γ_{cs} are respectively the specific surface energies of the substrate/solution and cluster/solution. The limiting case of θ=0 is referred to as a complete wetting and at θ=180 one speaks for complete non wetting with the latter corresponding to cases of homogeneous nucleation.

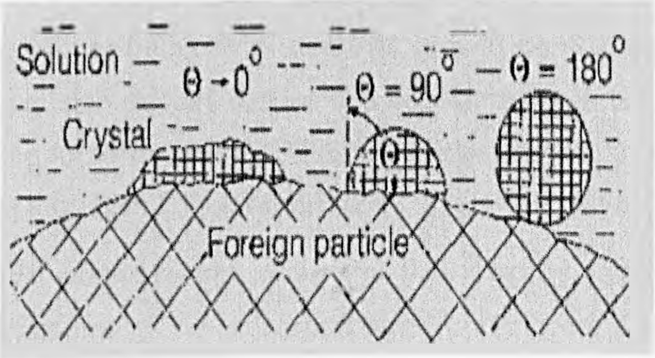

Figure 2.15: Nucleation on a foreign particle for different wetting angles [33].

Figure 2.15, which shows a foreign particle in a supersaturated solution illustrated a spherically shaped n-molecules sized crystalline cluster formed by homogeneously

2.5.4 Secondary nucleation

Secondary nucleation results from the presence of crystals in the supersaturated solution. Larson described secondary nucleation by six somewhat arbitrary mechanisms, one of which is by far the major source of nuclei in mixed suspensions [35].

Initial breeding as described by Strickland-Constable [47] results from crystalline "dust" adhering to large seeds introduced into batch crystallizers. This would occur only if the seeds were dry and were directly introduced into the crystallizer. Because this occurs only in seeded systems, we will not discuss it further [35].

Nucleation by some sort of ***fracture*** process occurs in systems that produce crystals that break easily, where the suspension is very dense, and where the suspension is subjected to violent agitation or high-velocity pumping. The crystalline product usually has a rounded appearance because of the high fracture and usually shows a deficiency of crystals in the large size range. The damage is usually done by impact with the impeller or sharp changes in the flow path. Fracture from crystal-crystal interactions probably does not occur [35].

Nucleation by ***attrition*** is merely fracture of a lesser degree and results from crystal-crystal interaction at high suspension densities as well as from crystal-apparatus contact. The crystal product may or may not exhibit obvious damage, but visible damage is usually slight. This and fracture nucleation can only be reduced by reduced agitation or pumping, by reduced suspension density, or by soft linings and covering on the crystallizer walls and impeller [35].

Needle breeding occurs because of dendritic growth on crystals. While reduced agitation and suspension density reduce this phenomenon, it is best controlled by reducing the driving force for growth. That is supersaturation, or using appropriate additive to change the crystal habit or tendency to form dendrites [35].

Nucleation by ***fluid shear*** results when the fluid velocity relative to the crystal velocity is large and some of the "adsorbed layer" is removed. The adsorbed layer, being nearly entirely solute, will nucleate if the clusters are sufficiently large. Sung, Estrin, and Youngquist [48] have shown shear produced nuclei must ordinarily be exposed to a much higher supersatuation than the one in which they were produced, in order to grow. As a consequence, it would not be expected that nucleation by fluid shear represents an important source of nuclei.

The most important source of nuclei in mixed suspension is the source that is described as contact nucleation, and results when crystals contact the agitator, pump, flow lines or other crystals [35].

2.5.5 Empirical approach for nucleation kinetics

A general theory for the prediction of nucleation rates does not exist, so several correlations based on the power model have been found to explain most of the experimental data satisfactorily by Nývlt [21]:

$$J = k_n \Delta c_{\max}^n \tag{2-41}$$

where the nucleation rate J is written in terms of the nucleation rate constant k_n and the maximum possible supersaturation $\Delta c_{\max}$.

Note that the solution is now cooled at a constant rate (r_1) and the temperature at which the first crystal appears is T_1. It can be assumed that the nucleation rate at the meta-stable limit can be approximated as:

$$J = \left(\frac{dc}{dt}\right) r_1 \tag{2-42}$$

The maximum supersaturation is given by:

$$\Delta c_{\max} = \frac{dc}{dt} \Delta t_{\max} \tag{2-43}$$

Combing the equations for nucleation and supersaturation rate and presenting the result in term of logarithms one gets an expression for dependence of the maximum under-cooling on the cooling rate.

$$\log(b) = (m-1)\log\frac{dc^*}{dt} + \log k_n + m\log \Delta t_{\max} \tag{2-44}$$

where b is the cooling rate ($-dt/d\tau$). Thus, a plot of the cooling rate and the maximum possible supercooling will give the apparent order m and the rate constant k_n. This method has been applied successfully on more than 25 substances [49].

2.5.6 Induction time

The rate of nucleation can also be determined by observing the time elapsed between the creation of supersaturation and the formation of a new phase. This time lag, generally referred to as an ‘induction period’, is considerably influenced by the level of supersaturation, state of agitation, presence of impurities, viscosity, etc. This time is a measure of the ability of the system to remain in meta-stable equilibrium.

The existence of an induction period in a supersaturated system is contrary to experience from the classical theory of homogeneous nucleation, which assumes ideal steady-state conditions and predicts immediate nucleation once superstaturation is achieved. The induction period may therefore be considered as being made up of several parts. For example, a certain 'relaxation time', t_r, is required for this system to achieve a quasi-steady-state distribution of molecular clusters. Time is also required for the formation of a stable nucleus, t_n, and then for the nucleus to grow to a detectable size, t_g. So the induction period, t_{ind}, may be written as:

$$t_{ind} = t_r + t_n + t_g \tag{2-45}$$

There are two methods for the theoretical determination of the induction time (τ) used so far and these two were proposed by Kashchiev [50]. The first one is based on the assumption that the event that brings the system out of its meta-stable equilibrium (mono-nuclear mechanism), whilst the second method depends on the presumption that the formation of a statistically large number of nuclei and their growth to detectable size are responsible for the breakdown of the meta-stable equilibrium (poly-nuclear mechanism). Kashchiev [51] proposed a general formula for determination of t_{ind} which is valid for any number of nuclei appearing and growing in the parent phase. This formula could be used for 1-D, 2-D or 3-D growth.

$$t_{ind} = 1/JV + \left(\alpha/\alpha_n JG^{n-1}\right)^{1/n} \tag{2-46}$$

where V is the nucleus volume, J and G are the nucleation and the growth rates, α is the ratio between the macroscopic volume of the new phase and the volume of the liquid phase, α_n is taking into account the shape of the nuclei. As seen, in the case of 3-D growth:

$$t_{ind} = 1/JV + \left(\alpha/\alpha_4 JG^3\right)^{1/4} \tag{2-47}$$

The induction period has frequently been used as a measure of the nucleation event, making the simplifying assumption that it can be considered to be inversely proportional to the rate of nucleation and therefore depends on the driving force, the temperature and the interfacial tension.

$$\ln\tau = -\ln B + \left(\frac{16\pi\gamma^3 v^2}{3k_B^3}\right).\left(\frac{1}{T^3(\ln\sigma)^2}\right) \qquad (2\text{-}48)$$

where τ is the induction time, γ is the interfacial tension, σ is the supersaturaion, v is the molecular volume, and k_B is the Boltzmann constant equal to 1.3805x10^{-23}J/K.

2.5.7 Ostwald ripening and the step rule

It was found long ago that when the new phase has several (at least two) modifications, one of which is thermodynamically stable and the others are meta-stable phases is often (but not always) observed first. A typical example is the crystallization of zeolites [52]. It appears that the first zeolite which crystallizes is not stable when it is left for some time in the reaction vessel in contact with the solution at the temperature of growth. After some time it dissolves into the mother solution and a new more stable type of zeolite crystallizes at the expense of the first one. The second type can also dissolve and a third type of zeolite nucleates and grows. These different forms are the polymorphs discussed in Section 2.3.

It was Wilhelm Ostwald [53] who first compiled the available observations which describe the evolution of an inhomogeneous structure over time and gave his famous empirical rule according to which the thermodynamically meta-stable phase should nucleate first. Then at a later stage the meta-stable phase should be transformed into a thermodynamically stable phase under given conditions (temperature and pressure). Thus the formation of the new stable phase should take place by consecutive steps from one phase to another with increasing thermodynamic stability. The first theoretical interpretation of this phenomenon which is known as Ostwald's step rule, was given by Stranski and Totomanow [54] in terms of the steady state nucleation rate. They showed that more often the meta-stable phase should have a higher nucleation rate provided the system has not been transferred very far below the transformation point.

2.6 Crystal Growth

The crystal, with its regular atomic construction, is the most commonly encountered state of solid materials. The three properties of a crystal, external form, perfection, and homogeneity, are directly related to how the crystal grows. Individual crystals of the same species and atomic construction may have different properties. The growth of crystals in a supersaturated solution is a very complex process that has not been well understood up to now. The reason for this is that many subsequent steps have to take place before a growth unit from the bulk solution is incorporated into the crystal lattice. Only a few of these steps are sufficiently understood to allow predictive calculation of growth rates. Moreover, a variety of growth units (atoms, molecules, ions, hydrated solute molecules, dimers, trimers, polymers, clusters, etc.) exists depending on the crystallizing system and the solvent, which complicates the situation even more. When dealing with crystal growth of an ionizing solute, the following steps can be distinguished according to Mullin [21]:

- Bulk diffusion of solvated ions through the diffusion boundary layer
- Bulk diffusion of solvated ions through the adsorption layer
- Surface diffusion of solvated or unsolvated ions
- Partial or total desolvation of ions
- Integration of ions into the lattice
- Counter-diffusion through the adsorption layer of the water released
- Counter-diffusion of water through the boundary layer

2.6.1 Two dimensional growth theory

When a crystal surface is exposed to a supersaturated environment, the flux of growth units (atoms, ions, molecules) to the surface exceeds the equilibrium flux so that the number of growth units joining the surface is greater than those leaving. This results in growth of the surface. The ability of a surface to capture arriving growth units and integrate them into the crystal lattice is, among other things, dependent upon the strength and number of interactions that can form between the surface and the growth unit [55]. The interfacial kinetic mechanisms of a particular crystal surface which is 'flat' rather than rough is described by steps. The critical step in the growth of crystals having perfect or nearly perfect surfaces is the formation of a cluster of atoms sufficiently large to constitute a stable nucleus which will grow to form a new layer [29]. One way to describe the birth of a step is to use what is called two-dimensional nucleation theory. The same logic and derivation can be applied to the nucleation of a two dimensional circular nucleus on a flat surface. Molecules will be continually absorbing on the surface diffusing and desorbing.

In two-dimensional growth, before grow can occur, a monolayer island nucleus, usually called a 'two-dimensional nucleus', must come into existence on an existing layer (Figure 2.16 (a)). This island becomes the source of new steps and kink sites at which additional units can join the surface. Subsequent crystal forming elements will tend to incorporate at sites where attractive forces are greatest, i.e. they will migrate towards the energetically favourable kink sites (Figure 2.16 (b)). The step-growth will advance until the whole plane is completed (Figure 2.16 (c)) and a new two-dimensional nucleus has to be generated before growth can advance. This two-dimensional growth mechanism is also known as the 'birth and spread' model; after nucleation ('birth') of a monolayer island it can grow ('spread') laterally across the surface. Two-dimensional growth is only expected to occur at relatively higher supersaturation since it is difficult to generate a nucleus on an already existing flat crystal surface.

If 2-D nucleation occurs on the surface it is treated as a cylindrical embryo of radius r and height a corresponding to one growth unit the critical nucleus size is:

$$r_s^* = \frac{\gamma_m a}{kT\sigma} \tag{2-49}$$

where γ_m is the energy per growing unit on the edge of the cylindrical nucleus and all the other parameters being the same as for bulk nucleation. Correspondingly, the change in the Gibbs free energy associated with the formation of the nucleus with critical size on the surface will therefore be:

$$\Delta G_s^* = \frac{\pi\gamma_m^2}{kT\sigma} \tag{2-50}$$

Once a surface nuclei is formed, there are two models explaining how the nuclei spread to form a complete layer. According to the mono-nuclear model it spreads across the surface at an infinite velocity and the surface must then await the formation of another surface nuclei. Since the rate-determining step is the formation of a surface nuclei, the growth rate will be expressed as [23]:

$$G = C_1 hA[\ln(S)]^{1/2} \exp\left[\frac{-C_2}{T^2 \ln(S)}\right] \tag{2-51}$$

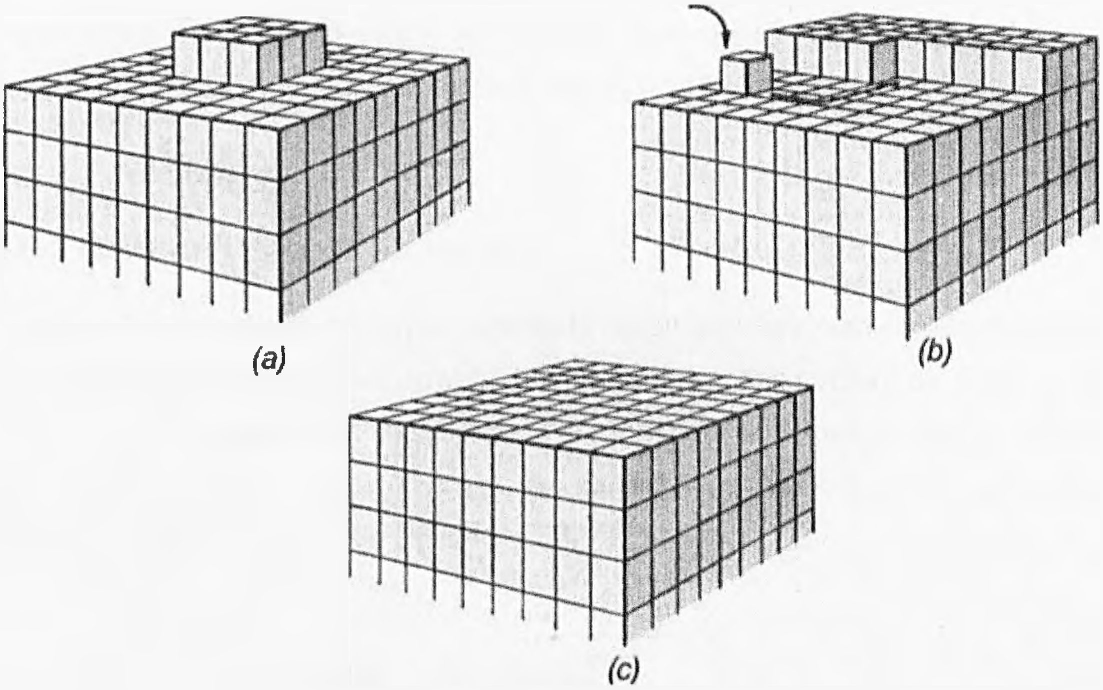

Figure 2.16: a-c Two-dimensional nucleation [21].

Equation (2-51) predicts the growth rate of a face is proportional to the area of that face. This model is known as the *mono-nuclear model.* This description suggests that larger faces grow faster than smaller faces, which is not consistent with experimental observation. If it is assumed that the two dimensional nucleus does not spread quickly and the growth layer is formed by formation of sufficient two-dimensional nuclei to give complete coverage of the surface. This theory, called the *poly-nuclear model,* predicts the growth rate will increase when the nucleation rate is increased. The growth expression would therefore be:

$$G = \left(\frac{C_3}{T^2[\ln(S)]^{3/2}}\right) \exp\left[\frac{-C_2}{T^2 \ln(S)}\right] \tag{2-52}$$

Between the extremes of the mono-nuclear model, in which the spreading velocity is infinite, and the poly-nuclear model, in which it is zero, is a model called the *birth and spread model* suggested by O'hara and Reid [56] which is:

$$G = C_4 (S-1)^{2/3} [\ln(S)]^{1/6} \exp\left[\frac{-C_5}{T^2 \ln(S)}\right] \tag{2-53}$$

It also assumes that nuclei can form at any location; including incomplete layers and that there is no intergrowth between the nuclei. Because all models depended on two-dimensional surface nucleation failed to predict growth taking place at low supersaturations this led Frank to propose that dislocations having a screw component act as a continuous source of layers on the surface of a crystal.

2.6.2 Continuous growth model

In molecular terms, assuming the surface is rough and has many kink sites [33], continuous growth may occur, provided that thermodynamic barriers do not impede it [33], so the growth unit will integrate at a site of the lowest energy for its orientation depicted in Figure 2.17. If the crystal surface, on a molecular scale, becomes smoother, it is more difficult for crystal growth.

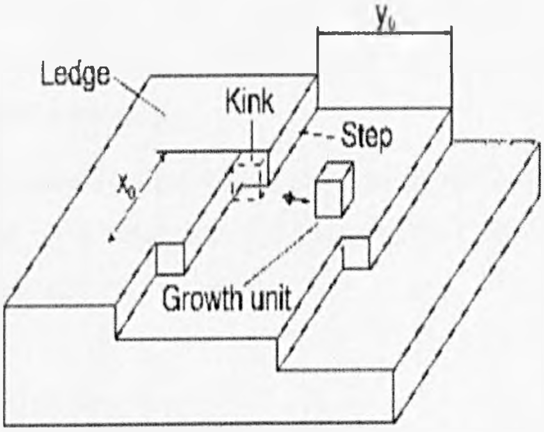

Figure 2.17: Attachment of a growth unit into a kink site [33].

2.6.3 Burton-Cabrera-Frank model

A crystal surface is, in particular for high surface energies, absolutely smooth and thus does not provide any integration site for an arriving growth unit. In practice, crystals have lattice imperfections preventing such ideally smooth surfaces. The basis for a model in which the steps are self-perpetuating was put forward by Frank

[57]. He assumed that the presence of spiral dislocations (see Figure 2.18), which end somewhere on the crystal surface, create steps know as a *screw dislocation*, and are thus a continuous source of favourable integration sites.

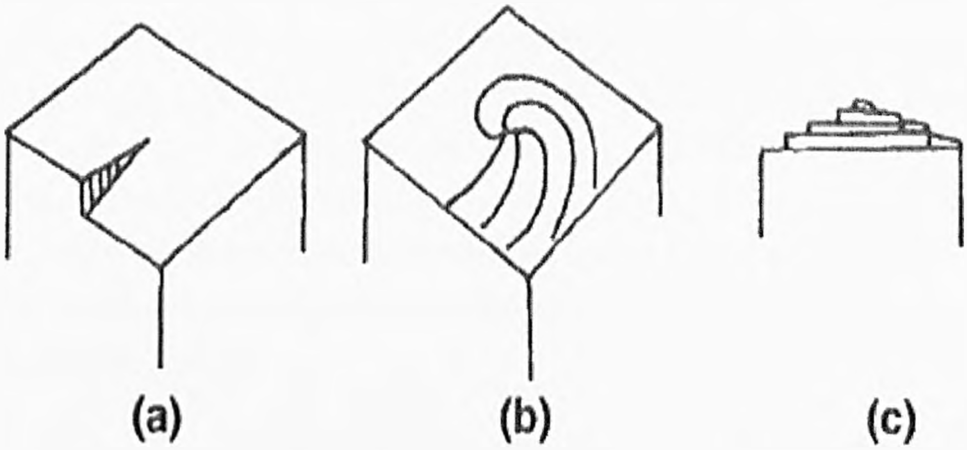

Figure 2.18: Development of a growth spiral from a screw dislocation [21].

Molecules adsorb on the crystal surface and diffuse to the top step of the two planes of the screw dislocation. The surface becomes a spiral staircase. After a layer is complete, the dislocation is still present; it is just a layer higher. The appeal of Frank's idea was that surface nucleation was not required for growth and that growth could occur at infinite rate at low supersaturation. Burton et al. [58] formularized this concept in a growth model in which surface diffusion was assumed to be the determining rate.

Descriptions and derivations of the Burton-Cabrera-Frank (BCF) growth equation can be found in Nývlt et al. [59]and O'hara and Reid [56]. The resulting kinetic expression is given below:

$$G = K_1 T(S-1)\ln(S)\tanh\left[\frac{K_2}{T\ln(S)}\right] \tag{2-54}$$

At low superstaturations, the equation reduces to a form in which the growth is proportional to the supersaturation to the second power while at high supersaturation, growth is linear with supersaturation. The BCF theory tells us that crystal growth rates vary from a parabolic dependence on supersaturation to a linear dependence as the supersaturation increases. This model is called the *BCF surface diffusion model* because diffusion on the crystal surface is considered to be the rate-controlling step. While this is true in vapour growth, it is often not true in solution growth where diffusion from the bulk solution to the crystal-liquid interface can often be the limiting rate step [23].

Bennema and Gilmer [60-62] revised the BCF theory with regard to growth from solutions, and their calculations confirm the role played by surface diffusion. One important result that is predicted by these types of models is that as the relative velocity between a crystal and the solution is increased, the growth will increase to a maximum value and then will remain the same. This maximum value is the value obtained when only surface diffusion limits growth. In the literature, this is known as *a growth limited by interfacial attachment kinetics.* When the crystal growth rate can be changed by changing the hydrodynamic conditions, it is known as a *mass transfer limited growth.*

2.6.4 Factors affecting crystal growth

The temperature of the system has a significant effect on the growth rate, as it can not only affect the relative rates of the diffusion and surface integration steps, but also the relationship between growth kinetics and temperature. High temperature is useful for diffusion-controlled growth, and high diffusion velocity will increase the mass transfer from the laminar sub-layer to the crystal surface. The rate of precipitation usually increases at high temperature, while the crystal size, shape and type can all change with temperature. Because the high agitation speed can increase the velocity of diffusion, the agitation speed should also be a factor in crystal growth rate.

Impurities usually cause a reduction in the growth rate of crystallization due to blocking of kink sites, thereby leading to smaller crystals than required. Although impurities can sometimes enhance growth rates, due to a reduction in interfacial tension, the impurities will also increase the surface nucleation rates. The mechanism of impurities on solute will be introduced in a later section.

The solvent effect can also lead to a change in crystal growth rates. One mechanism by which this may occur is as a consequence of the effects of solvent on mass transfer of the solute via changes in solution viscosity, density and diffusivity [63]. Another mechanism is via changes to the structure of the interface between crystal and solvent, as with some impurities [63]. The higher solubility in the solute-solvent system may result in a rougher interface and larger crystal growth rates.

2.7 Crystal Morphology

The external appearance of the crystals is also of great importance and is referred to as the crystal habit, crystal shape, or crystal morphology. These terms are often used interchangeably; however, crystal habit is used most often.

Crystal habit refers to the external appearance of the crystal. A quantitative description of a crystal means knowing the crystal faces present, their relative areas, the lengths of the axes in the three directions, the angles between the faces, and the shape factor of the crystal. Shape factors are a convenient mathematical way of describing the geometry of a crystal. If the size of a crystal is defined in terms of a characterization dimension L, two shape factors can be defined: the volume shape factor (α) and the area shape factor (β)

$$V = \alpha L^3 \tag{2-55}$$

$$A = \beta L^2 \tag{2-56}$$

Values of shape factors for common materials and geometries are available in the literature [21, 64]. Shape factors for common geometries are given in Table 2.10

Table 2.10 Shape Factors for Various Geometries [23]

Body	A	β	F= α/ β
Sphere	0.524	3.142	6.00
Tetrahedron	0.182	2.309	12.7
Octahedron	0.471	3.464	7.35
Six-sided prism	2.60	11.20	4.31
Cube	1.00	6.00	6.00
Prism	10.00	2.00	5.00
Platelet	0.20	2.80	14.00
Needle	10.00	42.00	4.20

2.7.1 Forms of polyhedral crystals

Polyhedral crystals bounded by flat faces can exhibit various Tracht and Habitus because they result from the interconnection of internal structural factors and the external factors involved during crystal growth. Among all of the various morphologies exhibited by crystals, it is the problem of variations in Tracht and Habitus exhibited by polyhedral single crystals that has attracted the deepest concern. Polyhedral single crystals are expected when crystals grow by the spiral growth mechanism under a driving force of $\Delta\mu/kT^*$. There are four approaches adopted to understand the polyhedral form of crystals.

The first is the prediction of the Habitus made from the characteristics of the crystal structure, entirely neglecting the effect of growth conditions. This is called the "structural form" or "abstract form". The second approach is to predict the Habitus thermodynamically when the crystal reaches the equilibrium state. This is called the "equilibrium form". The third is a method of analyzing the factors that may have an effect by correcting the Habitus and Tracht shown by real crystals and their growth conditions. Investigations of this type may be referred to as "growth forms". It should be noted that, whereas structural and equilibrium forms may be described as singular, growth forms are plural. The fourth method is to analyze the growth forms based on the observation of surface microtopographs of crystal faces, possible now that molecular information relating to growth form is available.

2.7.2 Equilibrium shape of a crystal

The equilibrium form of a crystal is that of its minimum energy. This is called the Wulff condition and indicates that the area of faces present will be such as to minimize the Gibbs free energy of the crystal. Gibbs [65] considered that a crystal, which has a regular structure for which anisotropy is the essential property, should, at equilibrium, take a form such that the total surface area times the surface free energy is at a minimum.

Gibbs [66] proposed that when the total surface energy times the surface area is at a minimum, the following concepts emerged: Curie's concept [67], which considered that the normal growth rates of crystal faces are proportional to the surface free energies; and Wulff's plot, indicating that the equilibrium form is obtained by connecting inscribed lines drawn at cusps on a raspberry-shaped polar diagram, on which points at distances proportional to the surface free energy from the center of a crystal are plotted. A Wulff plot is a polar plot of the surface free energy as a function of orientation, and a generalization for equilibrium form from the Wulff plot can be stated as:

$$\gamma_i / h_i = constant \qquad (2\text{-}57)$$

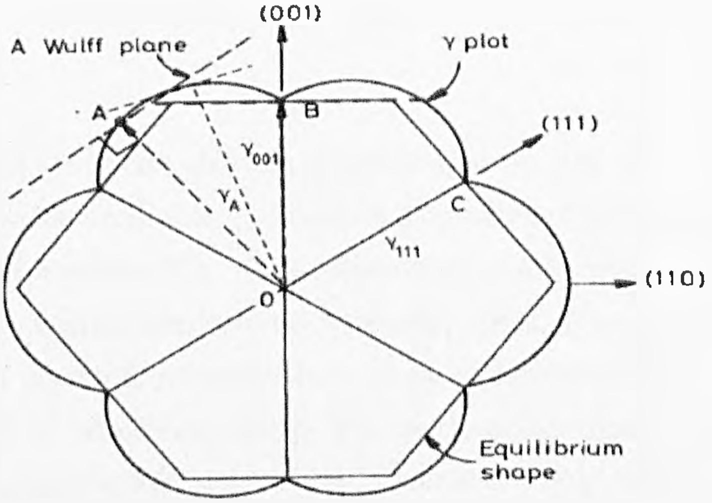

Figure 2.19: Representation of the equilibrium form of a crystal: the Wulff plot [68]

The equilibrium form is not just polyhedral in type, bounded by low-index crystal face [69], it may take a form bounded by flat and curved faces, depending on the given conditions. Unfortunately, the observed habit of crystals grown from solutions is often quite different from the prediction by the Wulff condition.

2.7.3 Structural form

The early investigation of crystals led to interest in the relation of crystal morphology with internal structure. A simple correlation was noticed by Donnay and Harker [70] between the interplanar spacing of a crystallographic plane, d_i, and its area on an average crystal. If the reticular densities of crystal faces are recalculated by expanding the symmetry elements involved in the thirty-two point groups to those in the 230 space groups, most of the discrepancies between the predicted forms determined from the Bravais empirical law and those that are actually observed disappear. This is an extension of the Bravais (Friedel) empirical law by Donnay and Harker [70], which is known as BFDH (Bravais-Friedel-Donnay and Harker) law. This approach assumes that the binding energy between crystal planes is inversely proportional to the interplanar spacing, i.e. the closer the molecules, the larger are their interaction energies. From this it follows that the growth rate v_{hkl} of the (hkl) face is proportional to the inverse of the distance between the (hkl) planes in the crystal structure, $1/d_{hkl}$. Thus, the relative growth rates of a series of faces can be assessed purely on the basis of the known crystal structure.

$$h_{hkl} \propto R_{hkl} \propto \frac{1}{d_{hkl}} \qquad (2\text{-}58)$$

Polyhedral crystal forms are defined by faces (planes) and edges (zones). One treatment that focuses mainly on the zones is the periodic bond chain (PBC) theory by Hartman and Perdok [71]. They developed a theory that related crystal morphology to its internal structure on an energy basis. They concluded that the morphology of a crystal is governed by a chain of strong bonds {called periodic bond chains (PBC)}, which run through the structure. The period of these strong bond chains is called the PBC vector. PBCs containing only an integer fraction of composition are partial PBCs, but these are not considered in HP (Hartman-Perdok) theory. Crystal faces are divided into three types:

1 K-faces (kinked), not parallel to any PBC vector;

2 S-faces (stepped), parallel to at least one PBC vector;

3 F-faces (flat), each of which is parallel to at least two PBC vectors.

A K face corresponds to a rough interface, an F face to a smooth interface, and an S face to a face having an intermediate nature between that of the K and F faces. Further, a K face grows by the adhesive-type growth mechanism, an F face grows either layer-by-layer or a spiral growth mechanism, and an S face appears by the piling up of growth layers advancing on the neighbouring F face. Therefore, an F face develops to a large size in order to control Habitus and Tracht in a real crystal, the K face will disappear from the crystal surface, and the S face will be characterized by striations only, if it appears on a crystal.

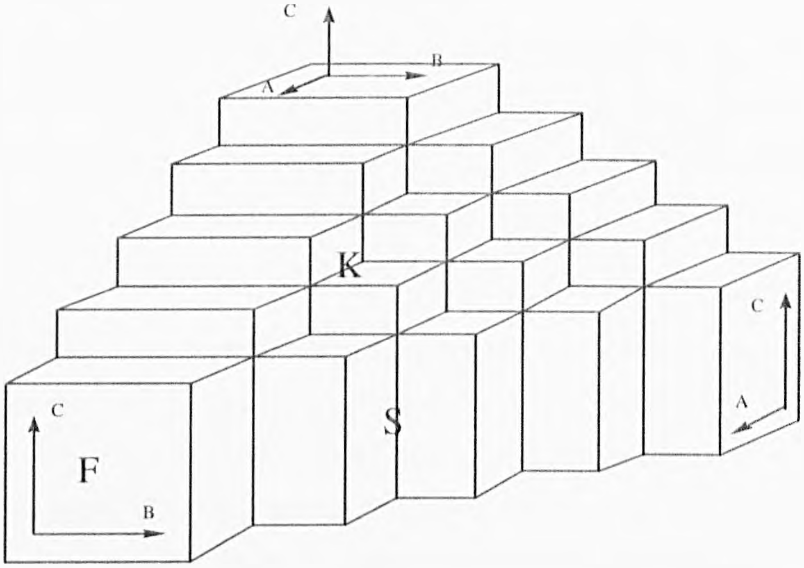

Figure 2.20: PBCs (solid arrows, A, B, and C) and an F face {100}, an S face {110}, and a K face {111} in PBC (HP) theory [72].

Another advantage of the *PBC* theory is its ability to predict not only the bulk morphology of a polyhedral crystal, but also the morphology of growth layers developing on F faces. When growth layers are polygonal, the step direction is assumed to be defined by the PBC. These predictions cannot be made by the BFDH law, and also sometimes the results from BFDH model are different from that observed.

The attachment energy of a crystal face is the difference between the crystallization energy and the slice energy. For an F face the attachment energy can also be expressed as the bond energy of bonds belonging to the PBC's that are not parallel to the face. The attachment energy of an S face will require the formation of at least one stronger bond than an F face and a K face will require at least one stronger bond than an S face. The *attachment energy model* (AE) was developed by Hartman and Bennema [73] on the basis of the PBC model. The concept of the AE model requires the determination of the lattice and slice energies (energy released upon the formation of a slice of thickness d_{hkl}) in Equation (2-59) for calculation of the attachment energy in each important crystallographic direction.

$$E_{att} = \frac{1}{2}\left(E_{cr} - E_{slice}\right) = \left(-\Delta H_{subl} + 2RT\right) - \frac{1}{2}E_{slice(hkl)} \qquad (2\text{-}59)$$

The assumption is made that the attachment energy is proportional to the growth rate (R) and that the larger attachment energy will lead to larger growth rate and hence less important face in the morphology. This assumption has been shown to be valid for a number of growth theories [15].

A major weakness in the calculations described above is that they can only be used to represent vapour grown crystals. In crystals grown from solution, the solvent can greatly influence the crystal habit as can small amounts of impurities. Several investigators [74, 75] accounted for discrepancies between observed crystal habit and those obtained using attachment energies by assuming preferential solvent (or impurity) adsorption on crystal face. The impurity (or solvent) can slow the growth rate of a face by stearically hindering the attachment of additional molecules.

2.7.4 Growth forms

The Tracht and Habitus exhibited by real crystals vary greatly depending on the perfection of the crystals and the growth environment and conditions [33]. The structural and equilibrium forms of crystals are predicted assuming that the crystal is perfect and that the ambient phase is isotropic. It is possible to analyze what sorts of growth environment and conditions may influence crystal forms using the structural form and the equilibrium as criteria. Growth forms are used to describe real crystals containing lattice defects growing in a real ambient phase. The growth forms of polyhedral crystals appear as a result of different normal growth rates R of different crystal faces or among different, crystallography equivalent, faces. Crystal face with large R will disappear; only those with small R will survive. There are four factors which may affect the growth forms [33]:

- The structure of the ambient phases, i.e. the differences in the melt phase, solution phase, and vapour phase, and the difference of the solute-solvent interaction energies in solution growth.
- The factors inducing anisotropy into the ambient phase: flows in solution, such as laminar or turbulent flow, convection induced by temperature difference, concentration difference, or difference in surface tension.
- Anisotropy in interface roughness and in a roughness transition.

- Anisotropy distribution of active centres for growth, such as lattice defects, which contribute to growth.

It is known that the relative growth rates of different crystal surfaces can be particularly susceptible to the conditions prevailing in the growth medium. Crystal growth is a thermally activated process in which growth rates increase with temperature according to a Arrhenius relationship. One consequence of this is that growth tends to become diffusion controlled with increasing temperature. In addition to these global kinetic effects, specific morphological changes can occur in both solution and melt growth due to the selective adsorption of non-crystallizing components on a particular crystal surface. So in order to control the crystal habit, we should focus on the solvent, impurities, and the growth mechanism of growth.

2.8 Habit Modification by Impurities

In many instances, small amounts of impurities have dramatic effects on crystal growth, morphology, and nucleation. In industrial crystallization operations in particular, the presence of impurities, synthesis by-products, and corrosion products can influence the crystallization process, negating improvements that can be made using normal operating parameters such as temperature, supersaturation, and residence time. Because of the complexity of the process, however, the exact mode of operation of these impurities on the molecular level is still, by and large, obscure. In this chapter, the effect of impurities on crystal morphology and habit will be presented.

The presence of chemical species in solution, in addition to the solute and solvent, can have a pronounced effect on the crystallization kinetics even if present in trace amounts. Indeed, the solvent itself can have the marked effect [35]. The presence of impurities is detrimental to the desired objectives of a crystallization process, but some times the presence of impurities is essential. The classic example is the crystallization of gypsum from phosphoric acid in the wet phosphate acid process. Here some of the impurities present in the phosphate rocks are essential in order to obtain the desired crystal size and habit. As crystallization is essentially a molecular recognition process occurring on a grand scale; impurity influence can be rationalized in terms of intermolecular interactions. Since the interactions of impurities at the interface play a role in all aspects of crystallization, emphasis is placed on describing the structure and environment at the interface, and explaining its impact on crystal shape. In particular, emphasis is placed on utilizing theories of crystal growth and adsorption to understand how impurities affect the growth process.

2.8.1 Adsorption on crystal surface

The shape of a crystal is determined by the relative growth rates of individual faces of a crystal, and could be influenced by the presence of impurities. The mechanism of the action of impurities on the growth occur when they are adsorbed on the crystal faces.

Impurities can form in a wide range of substances with adsorbate on the crystal varying from ions, atoms, molecules and from macromolecules to clusters.

For non-ionic impurities, the adsorption may be described using the Langmuir isotherm; the loading θ, depends on the Henry coefficient, He_{im}, of the impurity and its mole fraction, y_{im}^*, in the mother liquor [33]:

$$\theta = \frac{(He_{im})y_{im}^*}{1+(He_{im})y_{im}^*} \tag{2-60}$$

or

$$\frac{\theta}{1-\theta} = (He_{im})y_{im}^* \tag{2-61}$$

The change of crystal morphology is based on the difference in adsorption energies on different faces. The molecules of impurities will be adsorbed on the crystal surface into kinks, steps and faces (see Figure 2.21).

Davey [76] has summarized and recalculated data for several organic and inorganic impurities on a variety of crystals, pointing out the different adsorption locations and disturbances of growth kinetics.

The action of ionic impurities is different from the non-ionic impurities, because two additional obstacles to adsorption have to be taken into account. The crystal habit in an electrolytic solution is charged when the pH or the stoichiometry of the lattice ions is varied. At a glance, with the multicomponent adsorption of H^+, OH^-, and the surplus lattice ion, there is a positively or negatively charged crystal face depending on the solution conditions and an electrical double layer is formed [33]. When the impurities come up against such a charged interface, additional action due to the electrostatic repulsion or attraction has to be overcome.

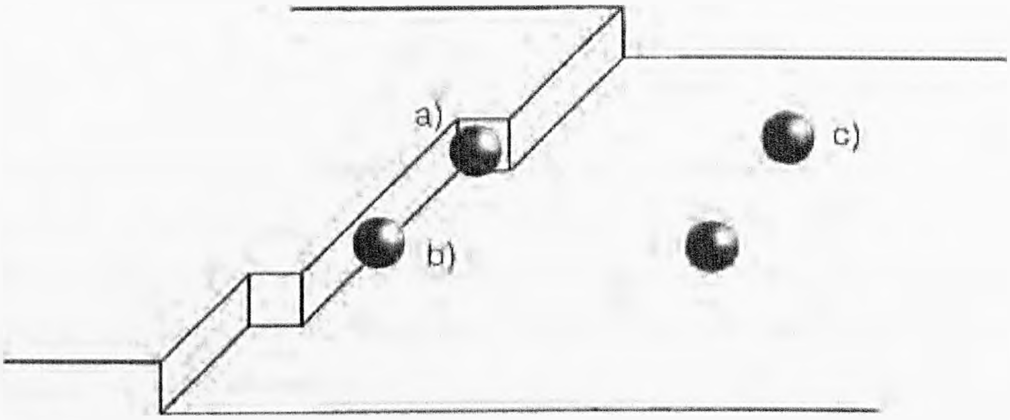

Figure 2.21: Distinct adsorption sites for additives and impurities: (a) kink, (b) step, (c) ledge [33]

2.8.2 Impact on thermodynamics and kinetics

The adsorbed impurities on crystal growth can influence the thermodynamics and kinetics, so the impact of impurities can be investigated from the thermodynamic and kinetic changes. Because the adsorption and crystal growth are both highly specific to the single faces of a crystal, the impurity may influence every single face, too. In general, an impurity can accelerate, decrease or totally suppress the growth of a crystal face. In addition, the impurity has an impact on the growth mechanism, so it is important to learn which of these contrary effects predominates from the considerations which of the thermodynamic and kinetic effects prevails.

2.8.2.1 Impact on thermodynamics

The important thermodynamic parameter in the BCF, B+S, and PN model, which is altered notably through the adsorption of an impurity, is the interfacial energy, γ_{CL} [33]. Setting up the Gibbs adsorption equation in such a way that the excess of the solvent is zero, the effect of the adsorbing species on the interfacial energy $\gamma_{CL,im}$, with the coverage Γ in moles per unit area of the surface, reads [33]:

$$\gamma_{CL,im} = \gamma_{CL,0} - \int \Gamma_{im} d\mu_{im} \tag{2-62}$$

When the Langmuir adsorption isotherm is applied with the maximum coverage of impurities, Γ_{max}, Equation (2-62) becomes [33]:

$$\gamma_{CL,im} = \gamma_{CL,0} - \Re T \Gamma_{max} \ln\left(\frac{1}{1-\theta}\right) \tag{2-63}$$

The equation shows that the interfacial energy decreases with increasing the impurity adsorbed, thus, the rate of growth increases. The reduction in the interfacial energy causes a decrease in the Gibbs free enthalpy to form nuclei, so that at a given supersaturation, the number of nuclei in the polynuclear and birth and spread models increases.

2.8.2.2 Impact on kinetics

Based on the location of the adsorbed impurity, different models describe the growth kinetic effects that result in an impeded step velocity. For the reversible adsorption on kink sites, Blisnakow and Kirkova [77] have proposed a model for the growth rate of a crystal face:

$$v_{imp} = v_0(1-\theta_k) + v_{imp,\infty}\theta_k \tag{2-64}$$

With θ_k the loading of the impurity on available kink sites and v_{imp}, v_0, and $v_{imp,\infty}$ the face growth rate in the presence, in the absence, and in the case of complete coverage with impurity, respectively [33]. The model will be valid, if the impurities incorporated into the crystal lattice as is the instance for “tailor-made” additives or if the mobility on the surface decreases with increasing molecular mass of the adsorbate. Due to the crystal habit modification by impurities, it is important to investigate the mechanism of impurity for habit modification from the change of thermodynamics and kinetics.

2.9 Molecular Modeling

A molecule may be defined as a collection of atoms linked by bonds. Molecules are always moving, modifying shape and, sometimes, losing and gaining pieces through rearrangement and reaction. However, due to the complexity and levity of molecules, it is hard to obtain the molecular information in the real circumstance. In some ways, molecular modelling is a useful tool which can be used to obtain information about molecules. The behaviour of molecules can be investigated with the molecular energy which is calculated using simple mechanical models. There are some ways to calculate energy such as conformation searching, molecular dynamic simulation and molecular orbital theory, but they are all time consuming and limited.

2.9.1 Force fields

Because it is hard to calculate the free energy G directly, the molecular mechanics model gives a value for 'energy' by adding up strain in all of the bonds and the Van der Waals and Columbic interactions of all the atoms [78]. This quantity can be called E_{MM}, the molecular mechanics energy which can be reflected by the internal energy of a molecule U [78].

The standard equations of thermodynamics for energy can be defined as [79]:

$$H = U + PV \tag{2-65}$$

For a simple molecular mechanics model without external pressure, the equation can be simplified,

$$\Delta H \approx \Delta U \approx \Delta E_{MM} \tag{2-66}$$

Based on the Equation (2-65) for free energy and $\Delta S \approx 0$, the change in molecular mechanics energy, ΔE_{MM}, equals approximately the change in free energy.

$$\Delta G = \Delta H - T\Delta S \tag{2-67}$$

The molecular mechanics energy, E_{MM} is made up of a number of components [78].

$$E_{MM} = E_{bonds} + E_{angles} + E_{vdw} + E_{torsion} + E_{ch\arg e} + E_{miscellane\ ous} \tag{2-68}$$

E_{bonds} - the energy in every bond

E_{angles} - the energy in every angle

E_{vdw} - the energy of all the Van der Waals interactions

$E_{torsion}$ - the energy of torsion angle

These equations, together with the data (parameters) required to describe the behaviour of different kinds of atoms and bonds, is called a "force field". The molecular mechanics "force field" relates the motions and energies of motions of atoms within the molecule. The force field is used to govern how the parts of a molecule relate to each other, that is how each atom or group of atoms is affected by its environment, and how these forces contribute to the structure of the molecule. Force fields provide an empirical way of calculating E_{MM}, especially best for 'organic' systems.

2.9.2 Minimisation

The energy can be removed from a molecule, driving it to a low energy conformation. This process is called energy minimization, which can give unstrained conformations. Minimisation is the process of making small adjustments to a molecule geometry [78]. The process of minimisation is illustrated for a diatomic molecule in Figure 2.22.

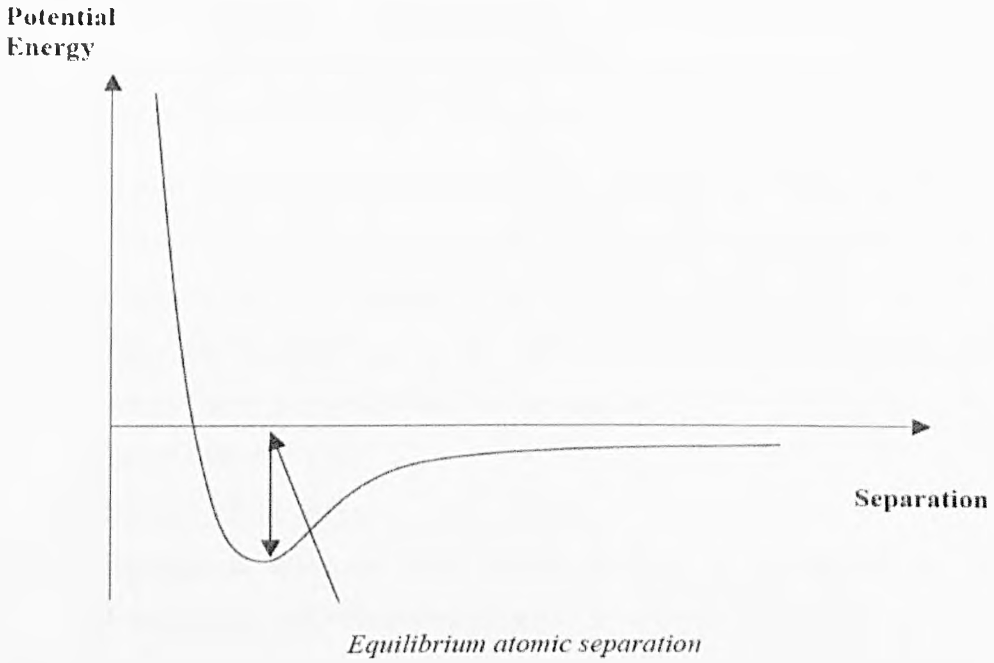

Figure 2.22: The relationship between lowest energy and equilibrium atomic separation [78].

The process of movement of position will continue until all possible small changes to the structure increase the energy of the structure. However, this process becomes quite complicated due to the large degree of freedom which a molecule will have, and the decision to move the direction is important in the process of minimisation. Different characteristics of molecules and force fields will use different minimisation algorithms to solve the problem, and can be divided into non-derivative and derivative methods. If a molecule is rigid, then there may only be one minimum in the potential energy surface, and so minimisation is all that is required to get an idea of its properties [78]. However, most molecules have a measure of flexibility and so some form of conformation searching is essential to obtain meaningful results [78].

2.9.3 Conformation searching

It is very important to find out which conformation has the lowest energy of all in the molecular modelling work and this problem may be solved by conformation searching.

Conformation searching is a crucial step in most molecular mechanics studies. Because it will not confirm the conformations of a molecule which is under consideration to represent the lowest energy, without the conformation search. Some automated methods of searching conformation were used to determine the low energy conformations [78]:

- Systematic Search: check through all possibilities - reliable, but slow.
- Monte Carlo Search: make use of information gathered as the search proceeds much faster and is often the method of choice.
- Molecular Dynamics: not an ideal method for conformation searching, unless many experimental data are available.
- Genetic Algorithms.
- Distance Geometry.
- Rule-based Methods: very rapid method of generating a reasonable structure, but not necessarily the global minimum.

2.9.4 Molecular orbital theory

Due to the complexity of the equations which describe the molecular structure, quantum mechanics is involved in the calculation of the energy minimisation. The molecular orbital is made up of the parts of the atomic orbitals which can be classified as one-electron atoms and multi-electron atoms. So the basis for the molecular orbital theory is the atomic orbital theory.

The molecular properties are based on the knowledge that the atoms can be calculated with Ab initio molecular orbital methods (GAUSSIAN, CADPAC, GAMESS, Spartan, etc.), only used for fairly small systems [78]. Semi-empirical molecular orbital methods (MOPAC) are faster than ab initio but less accurate [78]. AM1 and PM3 are the most sophisticated models in general use, superseding MNDO, MINDO/3,CNDO and numerous others [78].

2.9.5 Molecular cluster modelling

Over the recent years, it has become possible to glean information about crystal nucleation and growth of crystals by a variety of experimental and computational techniques at nanometre scale. Computational methods being developed, such as molecular dynamics, have obtained some results on the aggregation of solute molecules and molecular clustering in solution. Most experimental studies [80, 81] of structures of supersaturated solutions at the onset of crystallization support the existence of molecular clusters. Experiments have yielded some information on cluster size and structure [82-84] and modelling by molecular simulations has been conducted [84]. Hence, clusters provide a way to envisage the nucleation mechanism, and the molecular behaviour during nucleation and growth of the new phase can be investigated directly and in detail.

Compared with conventional approaches for measuring nucleation rates, the advantages of the study of clusters modelling are that the problem of heterophase contaminants can be avoided. Besides, in the condition of small volumes and rapid cooling rates, this method can be applicable to solid-state transformation at high nucleation rate. The existence of clusters was pointed out by Davey et al. [85] and the molecular clusters were observed in systems such as methanol and ethanol as shown experimentally using neutron scattering data. The birth of molecular clusters, reported by some recent theoretical results, has resulted in the combination of Coulomb repulsion and attraction [86-88].

The existence of clusters in the solution prior to the formation of crystals [89], although classic homogenous nucleation theory assumes the formation of clusters takes place before nucleation. Hence, a general hypothesis is assumed that molecular clusters in supersaturated solutions assemble as the various forms of shapes and arrangements [90], with clusters existing with the molecular packing mirroring the crystal packing for corresponding polymorphs in the system [85].

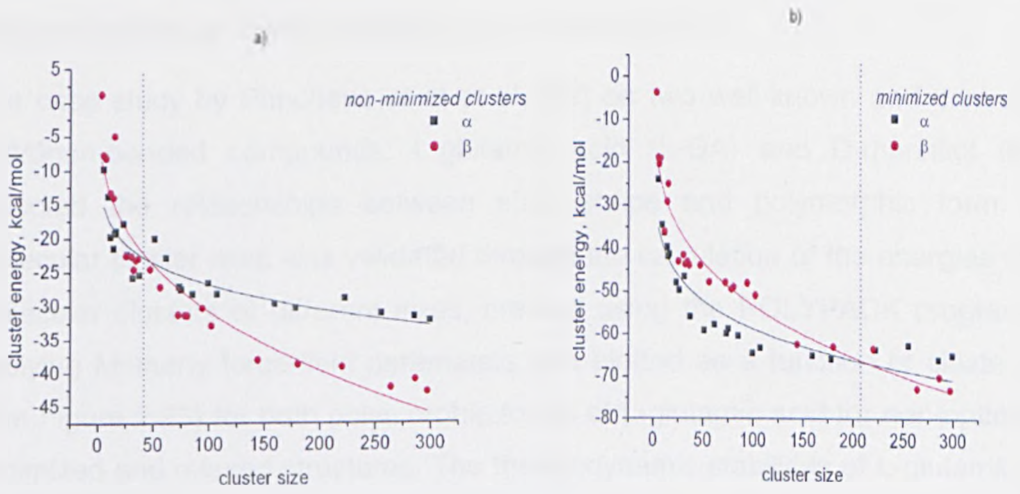

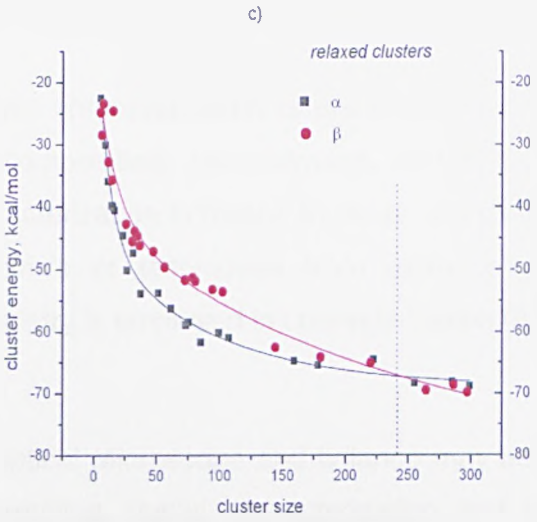

Figure 2.23: Energy minimization of facetted molecular clusters for α and β polymorphic forms of L-glutamic acid showing that the meta-stable form is more stable at small cluster size (a) non-optimized structures; (b) minimized structures;(c) optimized structures [91].

This hypothesis was used by Pencheva et al. [91] to create clusters of molecules which initially are representative of the molecular organisation within the bulk of a fully crystalline, solid form of the material in question. Hence in the approach adopted here the underlying hypothesis is that the molecular organisation within clusters of solute molecules, which form in solution during fluctuations leading to nucleation events, is similar to that in the solid phase that emerges from the solution via crystallization. However, there is another hypothesis describing the shape of molecular cluster as spherical in shape [80, 81].

The case study by Pencheva et al et al. [91] on two well-known and contrasting hydrogen-bonded compounds: L-glutamic acid (L-GA) and D-mannitol (D–M) reflected the relationships between size, shape and polymorphic form. The molecular cluster work was validated through the calculation of the energies of the molecular clusters of different sizes, created using the POLYPACK program, by applying Momany force-field parameters and plotted as a function of cluster size (see Figure 2.23) for both polymorphic forms of L-glutamic acid for non-optimized, minimized and relaxed structures. The thermodynamic stabilities of L-glutamic acid corresponding to different polymorphs which can be determined; hence the polymorph selection can be confirmed during the nucleation process.

2.10 Crystallization Characterization

Crystal characterization refers to the physical and chemical properties of crystal, i.e. composition, concentration, morphology and structure. To learn the crystal characterization is helpful to study and control the crystallization process. A whole spectrum of techniques from exotic physical methods to classical analytical chemistry is employed in characterization [92].

An optical microscope and balance may be the most fundamental instruments for determining crystal characterization and besides these, the following methods could be used for crystal characterization in this research:

- Turbidimetric method

The turbidimetric method can be used to detect on-set of crystals in the solution through the detection of the reduction in light transmittance. The light came from the LED photosensing diode in turbidity probe illustrated in Figure 2.24, and was reflected back via a mirror at the bottom. This method has been widely used to measure the nucleation and dissolution temperatures and induction time [52, 93, 94].

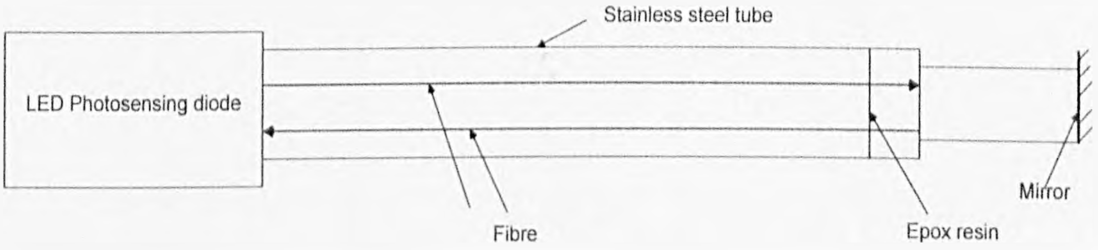

Figure 2.24:Schematic structure of turbidity probe.

- Thermal methods

The phase transfer will lead to generation or absorption of heat, so thermal analysis can be used to assess this change. In this project, differential scanning calorimeter (DSC) was used to measure the heat of diffusion.

2.11 Conclusions

This chapter has discussed and reviewed the fundamentals underpinning crystal science, especially basic crystal structure and crystallography, crystallization process, methods for simulating crystal morphology and techniques characterizing the crystallization. This chapter reviewed the molecular modelling method combined with the historical work on cluster modelling.

CHAPTER 3

Effect of Additives on Crystallization Process

Summary:

Literature review of the effects of additives on crystallization process: nucleation, growth and polymoph transformation and cold flow additives on clod flow behaviour of diesel fuels and biodiesel.

3.1 Introduction

In this chapter, a selection of previous research work into the effect of additives on the crystallization process is presented. This included both inorganic and organic system and particular attention is given to studies of crystallization with conventional and biodiesel fuels.

3.2 Effects of Additives on crystallization properties

3.2.1 Effect of additives on crystal morphology

The morphology of crystals grown from solution could be changed if appropriate additives are added. There is so much work to indicate the effect of the additives on the habit, in spite of inorganic or organic additives.

3.2.1.1 Inorganic additives

After an addition of small amount of $CdCl_2$ as additive, the shape of NaCl crystal grown from the solution changed, and the (111) faces became the dominant face instead of the normal (100) morphology (see Figure 3.1) [95]. From the optical microscopy, atomic force microscopy and surface X-ray diffraction (SXRD) observation, it can be seen that the (111) surface became smooth without surface reconstruction. Optical and AFM observations showed that the growth of octahedral crystal faces proceeds by monomolecular and higher steps. Steps originate from 2D nucleation starting from the edge of the crystal as well as from spiral growth. In situ SXRD observation showed the (111) NaCl surface was similar to its bulk face truncated along the (111) plane.

Figure 3.1: Ex situ optical DICM images of {111} NaCl crystal surfaces grown from a water solution with $CdCl_2$ added as impurity: (a) typical {111} surface; (b) ex situ DICM optical image of a {111} surface showing bunch patterns close to the edges of the face. These undulated steps are not observed at the centre of the crystal surface [95].

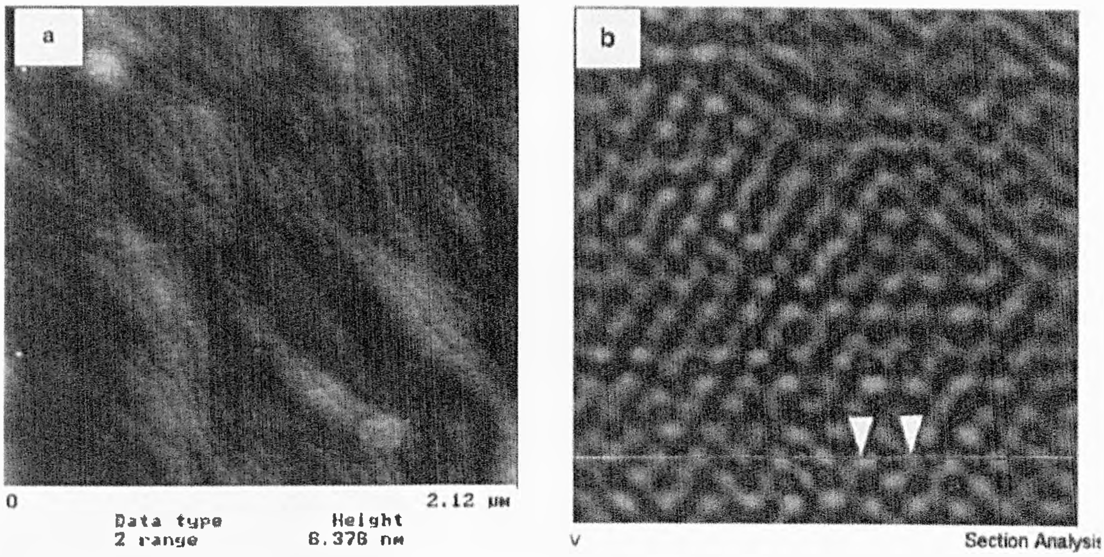

Figure 3.2: AFM images of (111) NaCl crystal surfaces grown from an aqueous NaCl solution with $CdCl_2$ added as impurity, showing: (a) monomolecular steps; the step height is about 0.3 nm. Each monomolecular step consists of one Na+ layer plus one Cl- layer; (b) atomic resolution structure. The oriented patterns of the single bright spots refer to the positions of single ionic species. The observed interatomic distances are 0.4 nm [95].

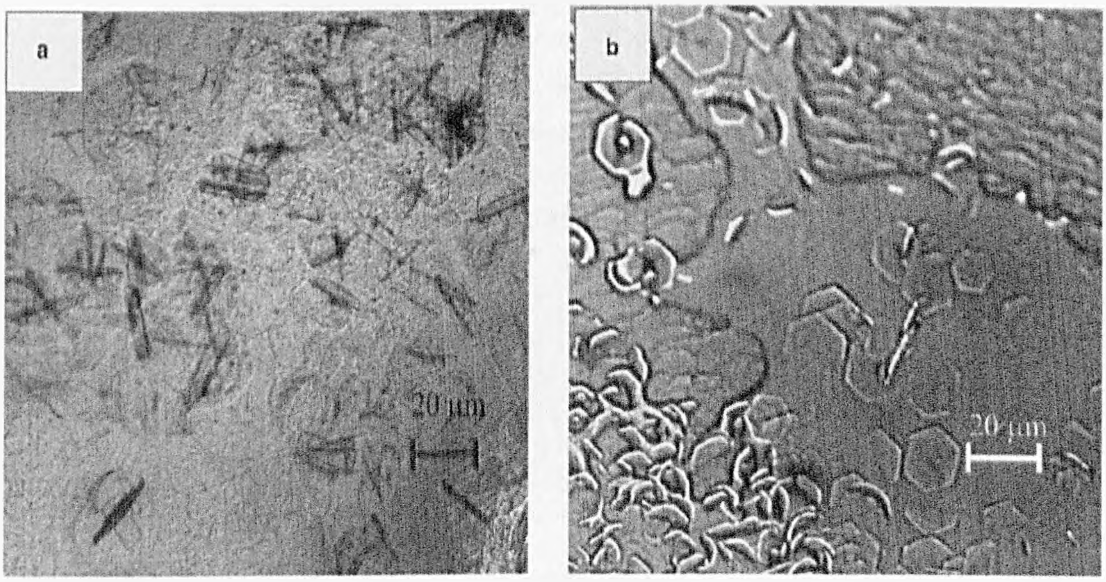

Figure 3.3: Optical image of epitaxial $CdCl_2{\cdot}2NaCl{\cdot}3H_2O$ crystals: (a) needle-like patterns, assigned as a twin pair (macle) consisting of a (non-visible) crystal with its basal(0001) plane parallel to the (111) substrate surface and a (visible) twin inclined with respect to that plane; (b) hexagonal plates presenting non-twinned $CdCl_2{\cdot}2NaCl{\cdot}3H_2O$ crystals with their basal (0001) plane parallel to the (111) NaCl surface [95].

The effects of additive (acetic acid, 1.15%) on the habit modification of $NaBrO_3$ crystals have been investigated (see Figure 3.4) [96]. The plot in Figure 3.5 (named morphodrome) of growth temperature against supersaturation showed that the additive influences on the shape changes were more important in the low supersaturation range than in the high supersaturation range.

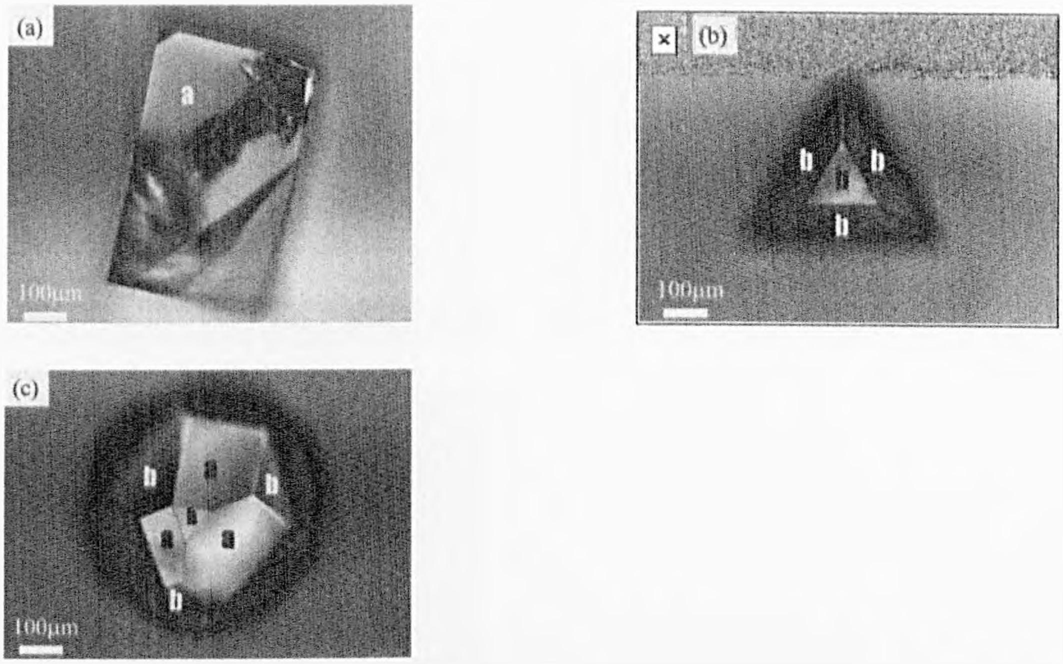

Figure 3.4: Typical examples of three growth shapes of NaBrO3 crystals grown from the solutions doped with acetic acid (1.15mol %). (a) {100} (cubic habit), after growth of 17min. (a) indicates {100}. A growth temperature is 33°C, $\ln(C/C_e)=0.14$. (b) {111} (tetrahedral habit), after growth of 24min. (b) indicates {111}. Growth temperature is 30°C, $\ln(C/C_e)=0.09$. (c) {100} and {111} (intermediate habit), after growth of 8h (a) and (b) indicated {100} and {111}, respectively. Growth temperature is 50°C, $\ln(C/C_e)=0.01$ [96].

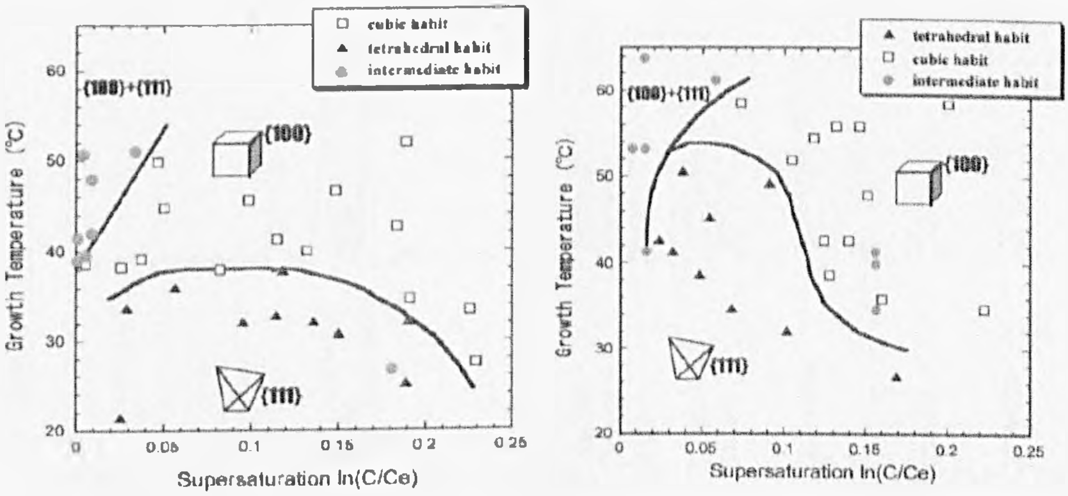

(a) (b)

Figure 3.5: Morphodrome of $NaBrO_3$ (a) grown from pure solution; (b) in the presence of acetic acid of 1.15mol% [96]

The effect of inorganic Co (II) and organic (urea) impurities on the properties and crystalline perfection of tri (thiourea) copper (I) chloride (TCC) single crystals grown at 30°C using slow evaporation grown technique (SEST) is investigated [97]. The photographs of TCC, Co (II) and urea-doped as grown crystals are shown in Figure 3.6 [97].

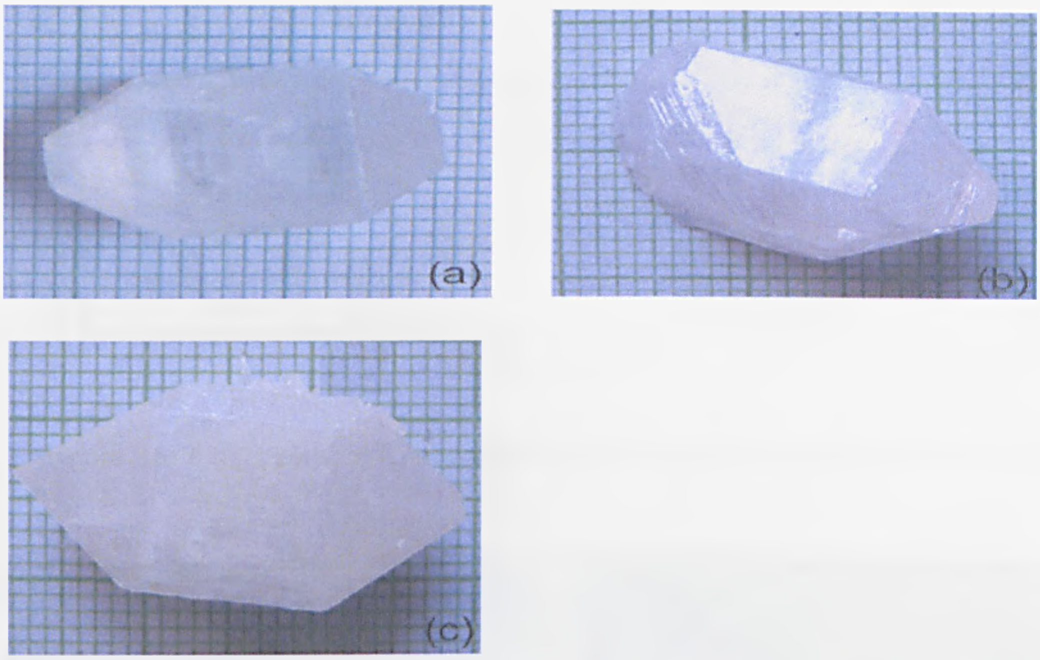

Figure 3.6: Photographs of TCC as-grown crystals: (a) pure (b) 10 mol% Co(II)-doped and (c) 5mol% urea-doped [97].

The powder XRD and FT-IR (Figures 3.7 and 3.8) results indicate the additives caused a small change in intensity and vibration patterns, respectively. SEM (see Figure 3.9) reveals a defect structure and the presence of Co in the doped TCC crystal results in more scatter centres than of the undoped specimen.

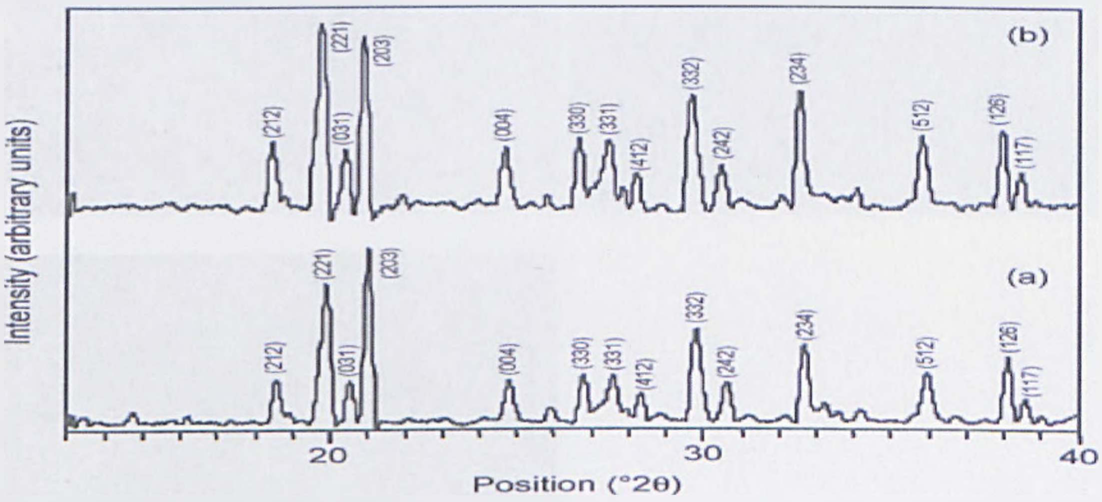

Figure 3.7: Powder X-ray diffraction curves of TCC crystals: (a) pure and (b) 10mol% Co(II)-doped [97].

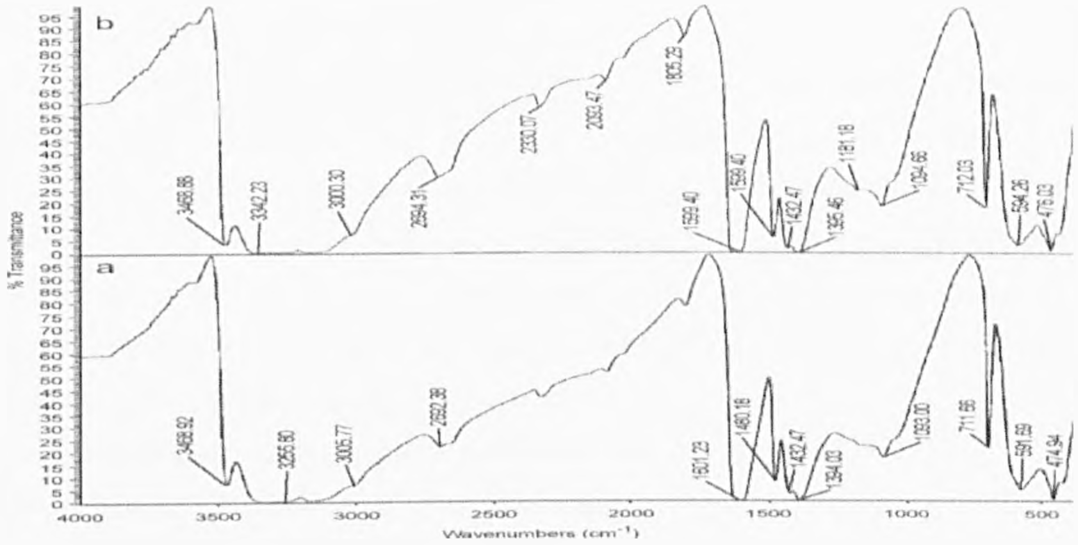

Figure 3.8: T-IR spectra of TCC crystals: (a) pure and (b) 10mol% Co (II)-doped [97].

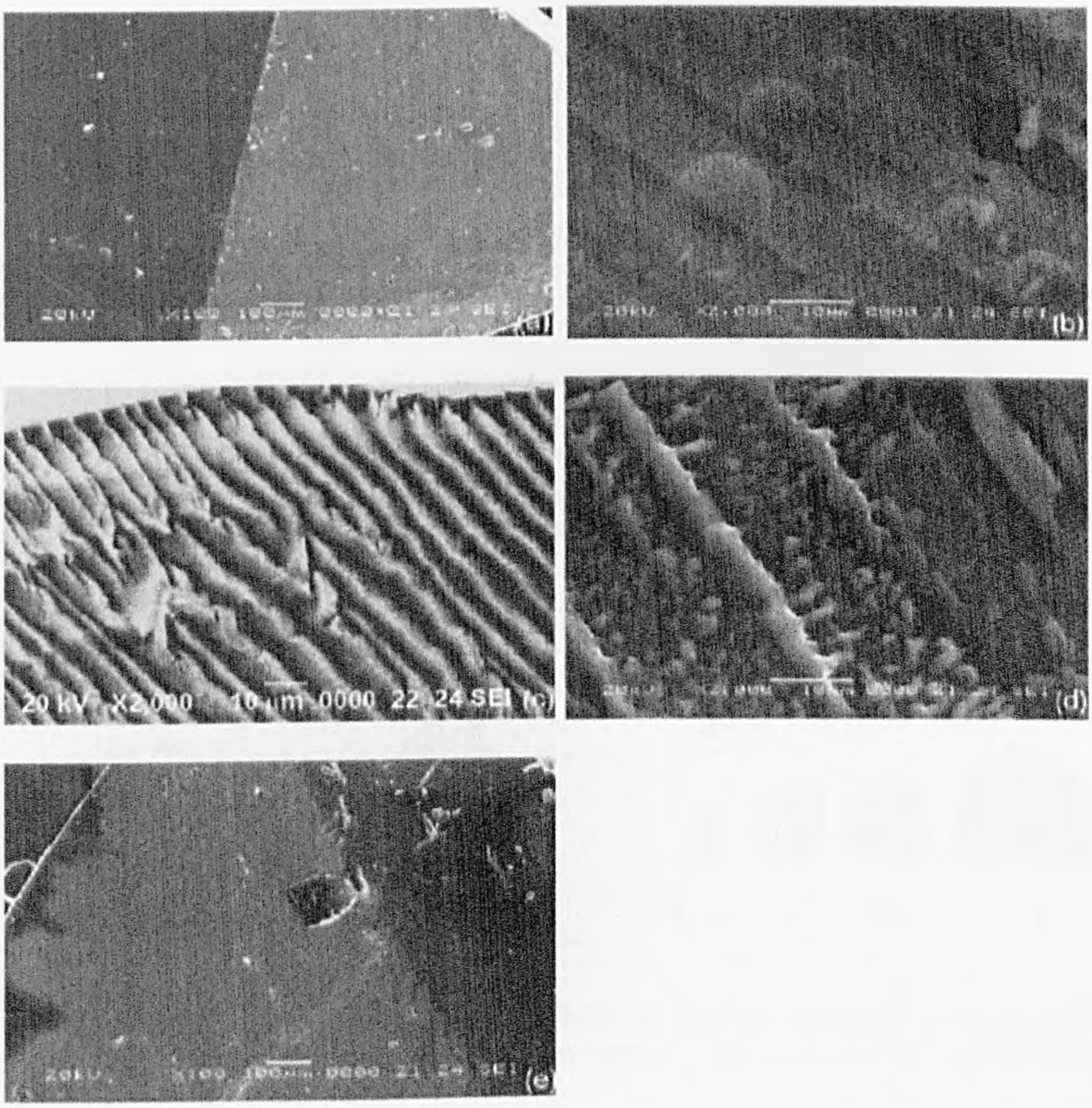

Figure 3.9: SEM of TCC crystals: (a) pure, (b) 1mol% Co(II)-doped, (c) 5mol% Co(II)-doped, (d) 10mol% Co(II)-doped and (e) 1mol% urea-doped [97].

3.2.1.2 Organic additives

After an addition of six structurally related additives, four additives led to significant morphological changes. Among the six structurally related additives tested in the study, sucrose and β-glucuronamide were shown to have no effect on the crystal shape of alpha-lactose (Lα-H_2O), whereas the other additives (α-galactose and β-cellobiose) proved to be habit modifiers (see Figure 3.11). In the presence of α-glucosamine-HCl, crystals became strongly elongated (see Figure 3.12), due to the larger length increases along the b direction. By contrast, the use of maltitol, α-galactose or β-cellobiose induces that "flattened" morphologies to be obtained, in connection with the dominant length increases along the direction. Depending on the nature of the additive from molecular simulation in Figures 3.14 and 3.15, crystal habit varies from "elongated" along the b direction or "flattened" along the axis [98].

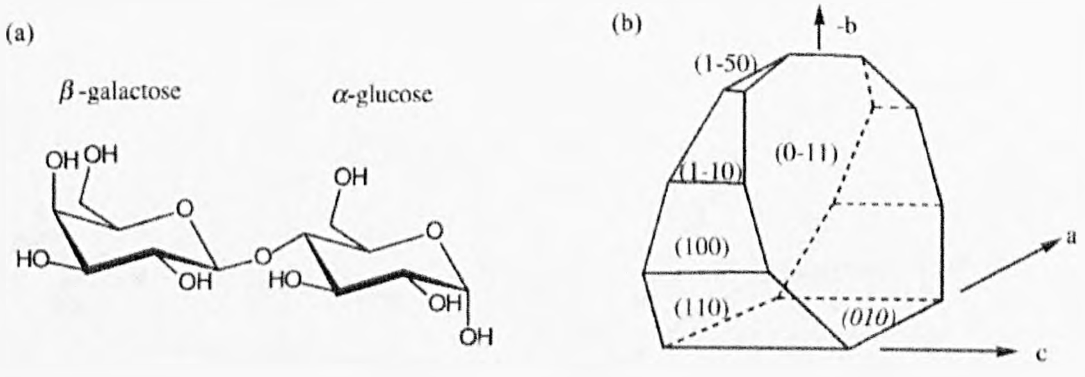

Figure 3.10: Molecular formula of α-lactose (a) and representative habit of single crystal obtained from water (b) [98]

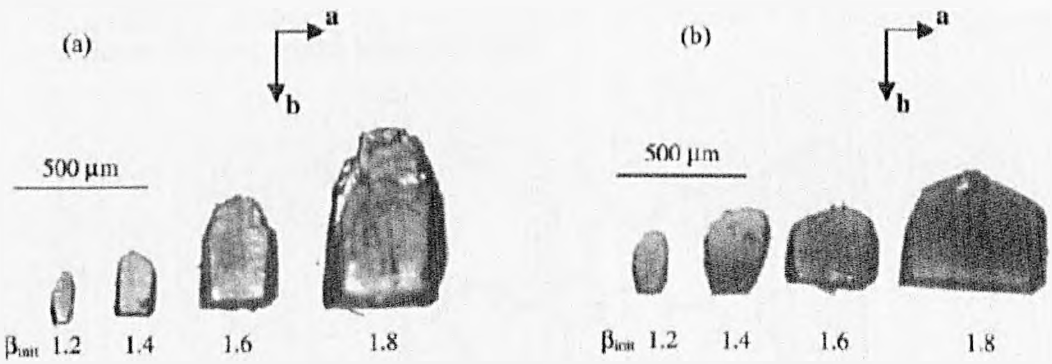

Figure 3.11: Photographs of representative Lα-H2O crystals with increasing supersaturation in the absence of (a) and in the presence of (b) 10% (w/w) of a structurally related additive (β-cellobiose) [98]

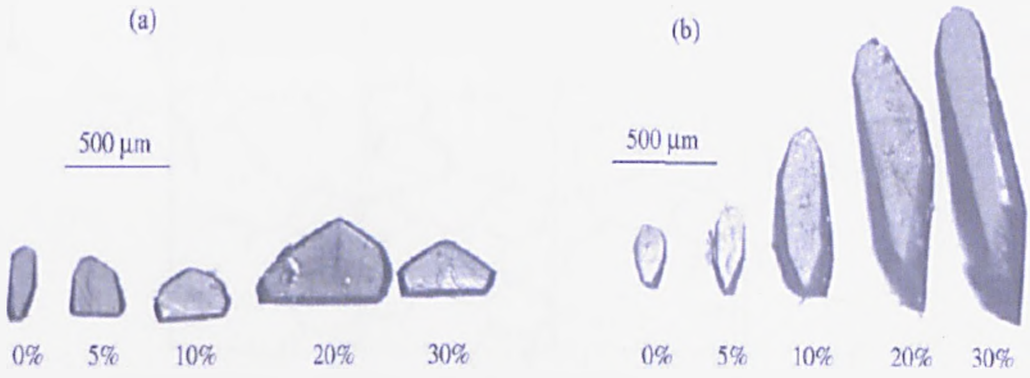

Figure 3.12: Photographs showing the evolution of the crystal habits as a function of the proportion of structurally related additives: β-cellobiose (a) and α-glucosamine hydrochloride (b), with corrected; $\beta_{init} = 1.4$ [98].

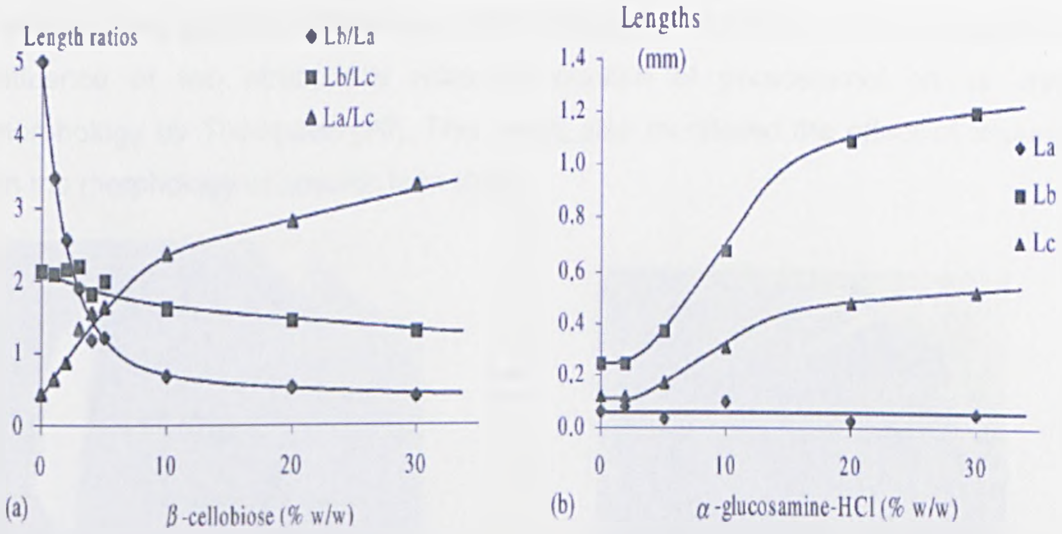

Figure 3.13: Evolution of the crystal lengths along the 3 main axes as a function of the proportion of structurally related additives: β-cellobiose (a) and α-glucosamine hydrochloride, crystal length (b) [98].

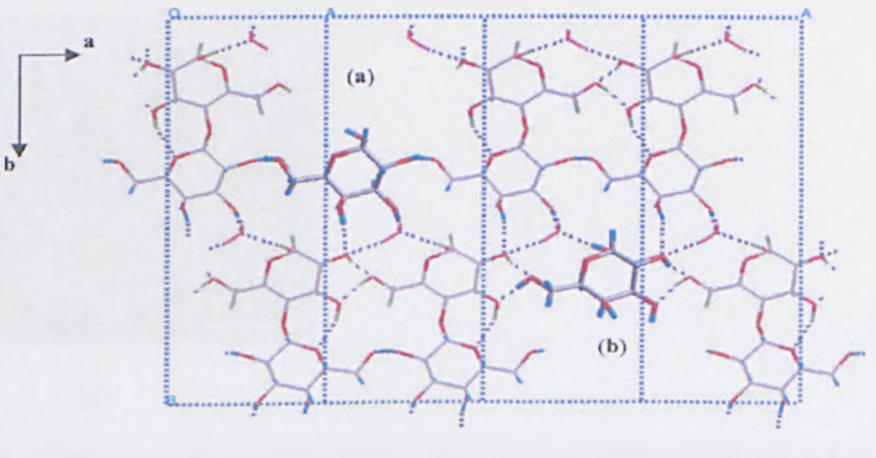

Figure 3.14: Hypothetical substitution of a α-galactose molecule in the structure of Lα-H2O simulating the probable adsorption mechanism along b and –b directions [98].

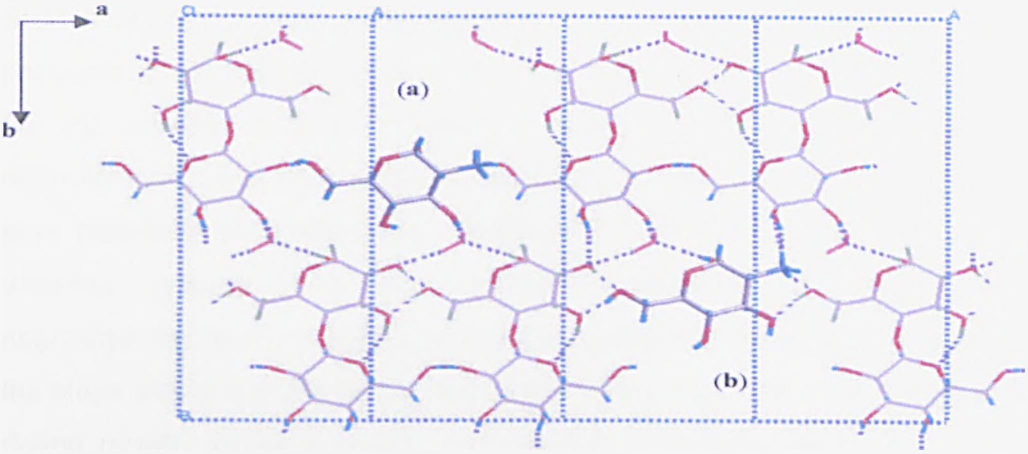

Figure 3.15: Possible adsorption of a glucosamonium unit in the crystal structure of Lα-H2O by replacement of galactose unit (a) or the glucose unit (b) [98].

The effect of additives on the morphology of paracetamol crystal has been investigate by Thompson [99] and Hedriksen [100]. Atomic force microscopy (AFM) and scanning electron microscopy (SEM) (Figure 3.16) are used to investigate the influence of two structurally related impurities of paracetamol on its crystal morphology by Thompson [99]. Their work also monitored the effect of impurities on the morphology of specific face (001)

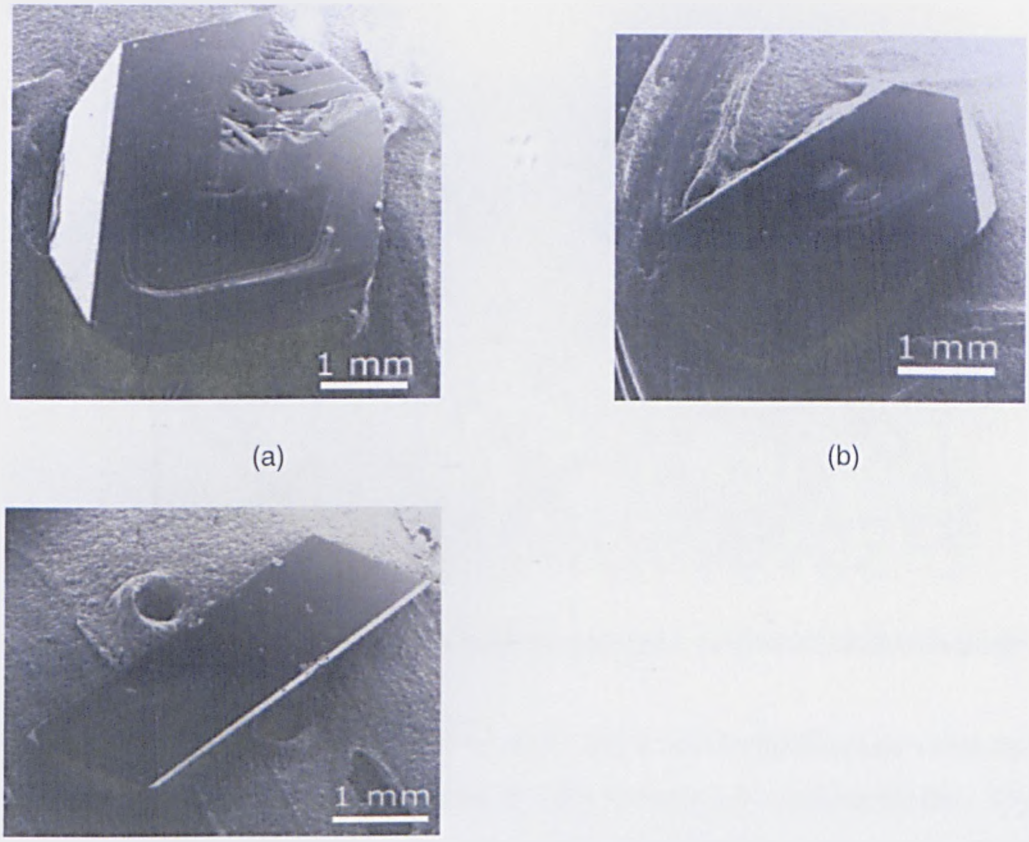

(a)

(b)

(c)

Figure 3.16: SEM images of a parecetamol crystal: (a) pure parecetamol; (b) in the presence of 4 mol% acetanilide; (c) in the presence of 4 mol% metacetamol [99].

SEM images in Figure 3.16 indicated the characteristic tabular habit of pure paracetamol crystals was only moderately altered by the presence of acetanilide, but the crystals adopted a columnar habit when grown in the presence of metacetamol. On a microscopic level, AFM revealed that the surface features of pure paracetamol crystals were steps ranging from 1 to 21 nm in height [99], whereas crystals grown with acetanilide possessed thin, branched steps of approximately 20 nm in height, so it is suspected that the branched appearance of the steps was due to the adsorption of acetanilide molecules onto terraces or steps during growth, causing pinning and bending of growing steps. The presence of metacetamol during growth resulted in steps of approximately 15 nm in height interspersed with holes, and also induced the formation of the defects in the crystal surface [99].

The crystal structural approach [100] was used to explain the observed additive uptake, the morphological changes and the inhibition of nucleation. The crystal structure of pure axetaminophen displays a hydrogen bonded network, from which is derived a mechanistic interpretation of the abilities of additive molecules to influence crystal growth [100].

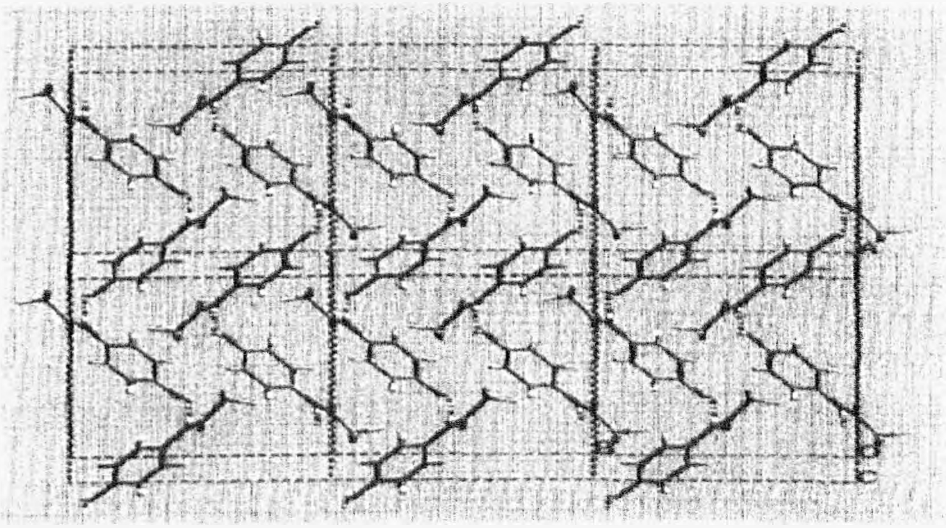

Figure 3.17: Representation of the crystal structure of paracetamol (acetaminophen) [100]

From the Table 3.1 and Figures 3.17 and 3.18, it can indeed be seen that hydrogen bonding plays a significant role in the crystal structure of acetaminophen. The inter-atomic bonding strengths and atom-atom contributions were calculated using HABIT. Based on the analysis of the molecular structure with additives, the effects of the additives are interpreted by considering the ability of each additive to dock on to the crystal surface by adsorption, to block the uptake of paracetamol molecules on the crystal surface and/or the crystal lattice [100].

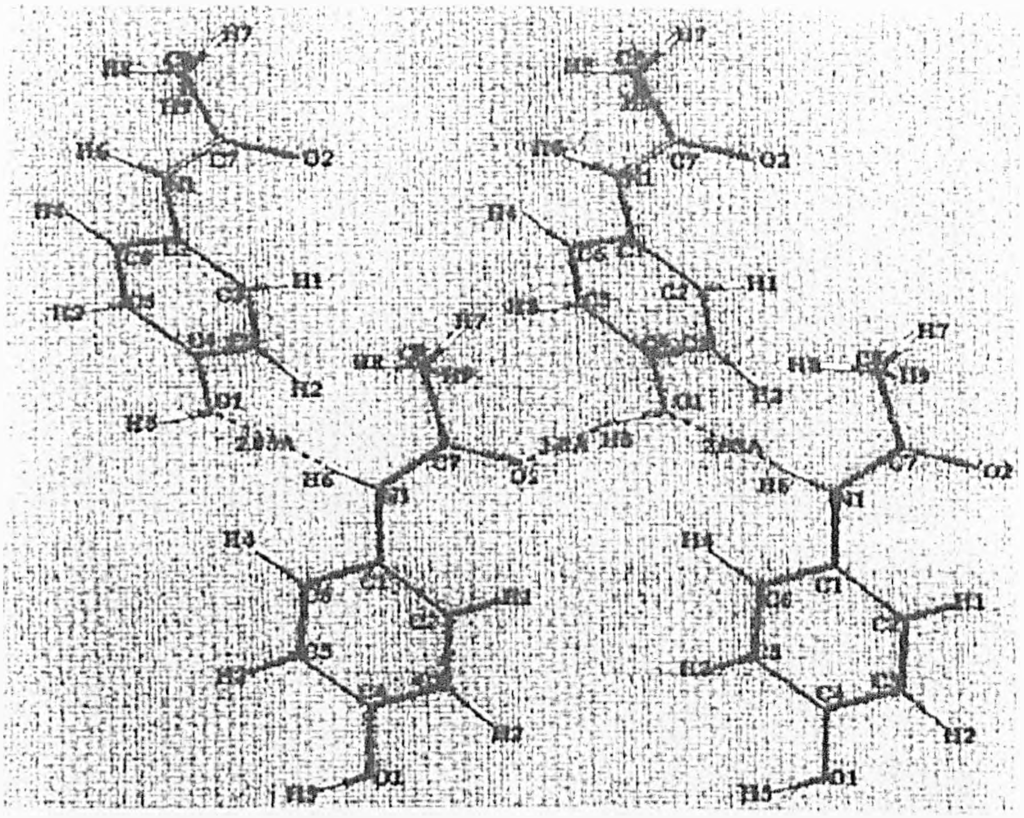

Figure 3.18: Illustration of the interactions with origin paracetamol (acetaminophen) molecule and the molecule defined by the symmetry operator "$x+\frac{1}{2}$, $\frac{1}{2}-y$, z" [100]

Table 3.1 Ranking of inter-atomic hydrogen bonding interactions for paracetamol. The calculated lattice energy was -27.91kcal mol^{-1} [100]

U	V	W	Z	Atom A	Atom B	Distance $(\dot{A})$	Energy (kcal mol^{-1})
-1	0	-1	4	O2	H5	1.8	-5.76
-1	0	0	4	O1	H6	2.05	-2.55

Note: 'Distance' is the intermolecular distance between the interacting atoms A and B for the intermolecular interaction between atom A on the central molecule [0001] and atom B in the molecule defined by [UVWZ], where U,V,W are multiples of the unit cell dimensions and Z refers to the symmetry number defining the molecule in the unit cell. Here $Z = 4(x + 1/2, 1/2 - y, z)$.

The effect of crystallizing phenytoin (5.5-diphenylhydantoin; DPH) from methanol under defined conditions in the presence of various concentrations of additive, 3-propanoyloxymethyl-5, 5- diphenylhydantoin (PMDPH; a cited prodrug of DPH) was investigated [101]. The presence of 3gl^{-1} (8.9mmol^{-1}) or more of PMDPH in the crystallization media caused the DPH crystals to develop into long, thin plates (Figure 3.19), the extent of which depended on the PMDPH concentration. Concomitant with the habit thinning of DPH crystals was a slight decrease in mean particle size and an increase in specific surface area of crystals (Figure 3.20).

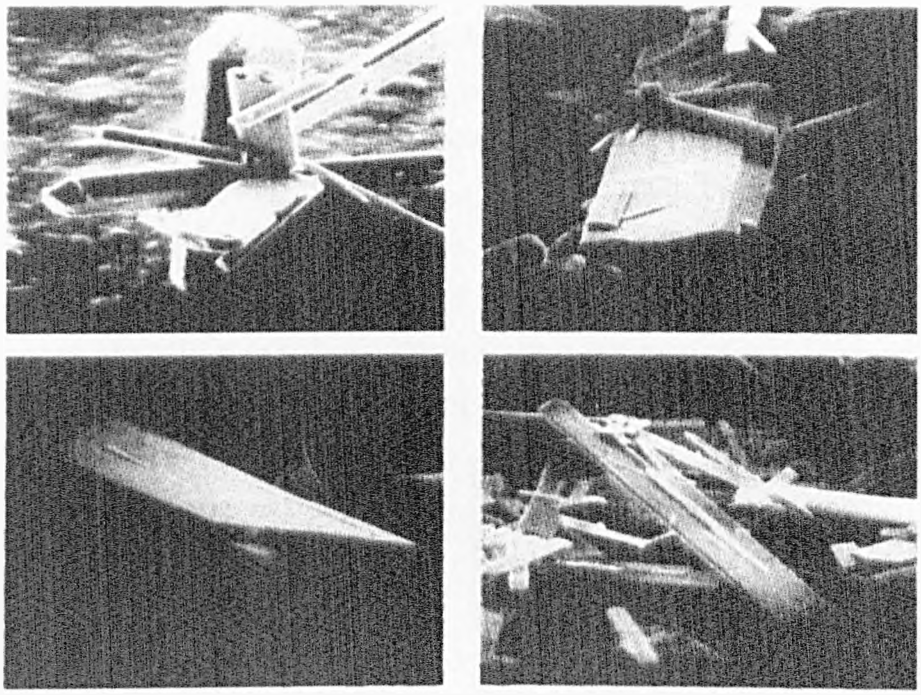

Figure 3.19: Scanning electron photomicrographs of DPH crystallized from methanol in the presence of the following concentrations of PMDPH: upper left, $0 gl^{-1}$; upper right, $1 gl^{-1}$; lower left, $5 gl^{-1}$; lower right, $7 gl^{-1}$ [101].

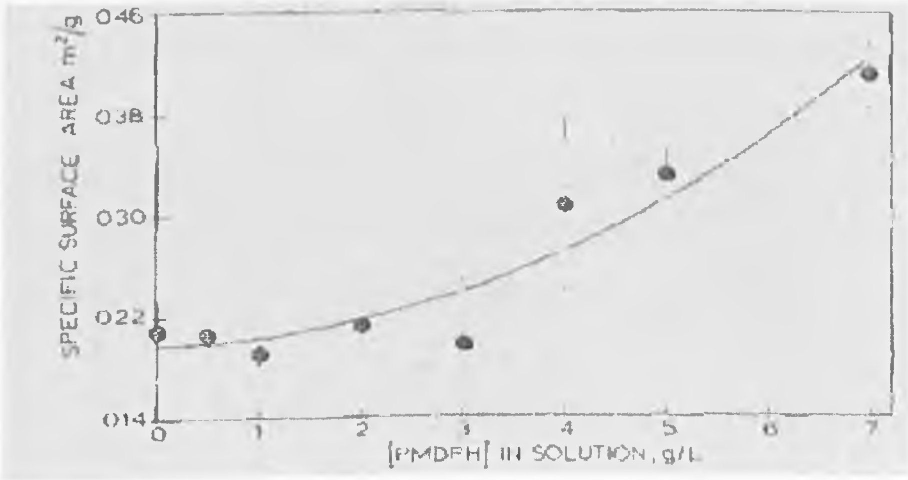

Figure 3.20: Specific surface areas of DPH crystallized from methanol containing various concentrations of PMDPH. Each data point is the mean value of two separate batches [101].

3.2.2 Influence on nucleation and crystal growth kinetics

The evaluation of the effects of additives on the nucleation and crystal growth kinetics is very important for the control of the crystal form and crystallization process.

Rauls investigated the influence of additives on the crystallization kinetics of ammonium sulphate [12]. Figure 3.21 presented habit modification and change of growth rate in the presence of Al^{3+}.The meta-stable zone of ammonium sulfate with impurities became wider than the pure ammonium sulphate (see Figure 3.22). All crystal additive systems investigated had an optimal concentration where growth rate and crystal size had a maximum and the nucleation rate a minimum. Further the increases of additive concentration above this optimal value decreased growth rates and crystal size at increasing nucleation rates [12].

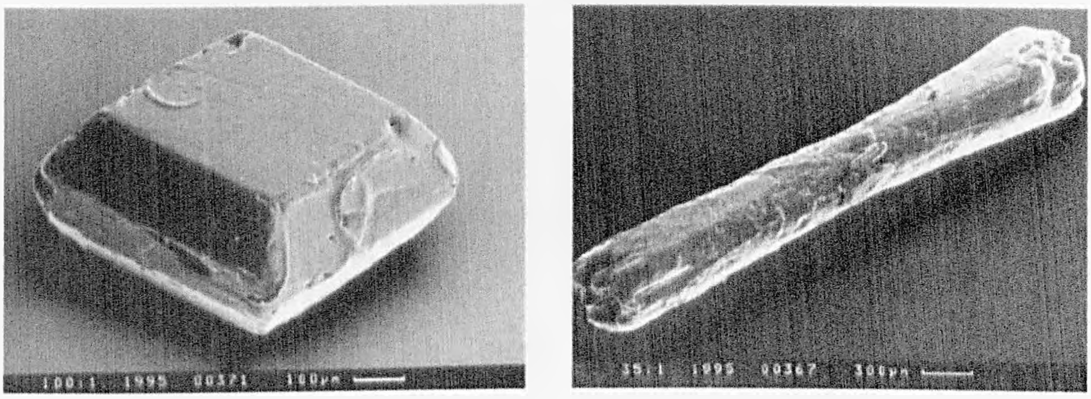

Figure 3.21: SEM images of ammonium sulphate crystals obtained in low-temperature experiments from pure solution (left) and in presence of 100ppm Al^{3+} (right) [12]

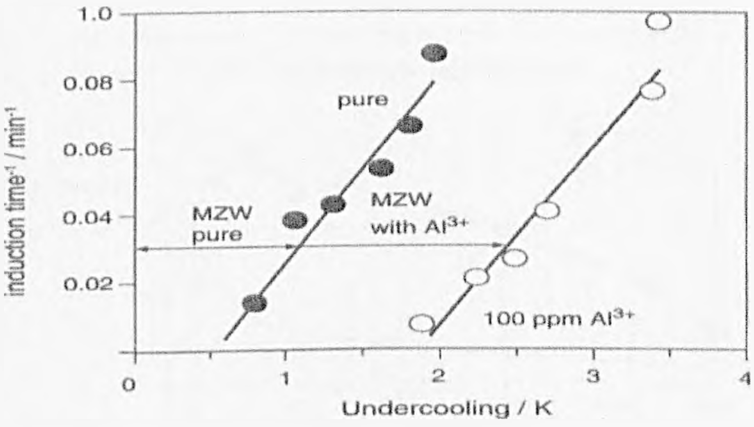

Figure 3.22: Induction times for secondary nucleation for pure ammonium sulphate solutions and in presence of aluminium ions [12]

The results from Figures 3.23 and 3.24 indicated that all impurity levels in the system reduce kinetic coefficients for crystal growth and suppress nucleation by adsorption on the crystal surface [12]. The retarding effect of aluminium on two faces of ammonium sulphate are presented in Figure 3.25, and finally the effects of additives on nucleation and growth kinetic parameter can be seen in Figure 3.26.

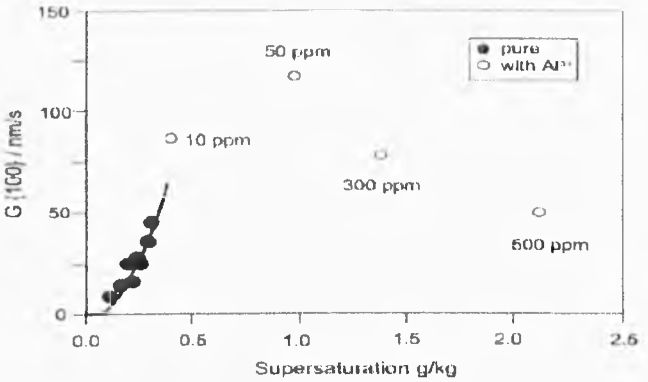

Figure 3.23: The growth kinetics of ammonium sulphate – in pure solution at different residence times and in the presence of Al^{3+} at 2h residence time [12].

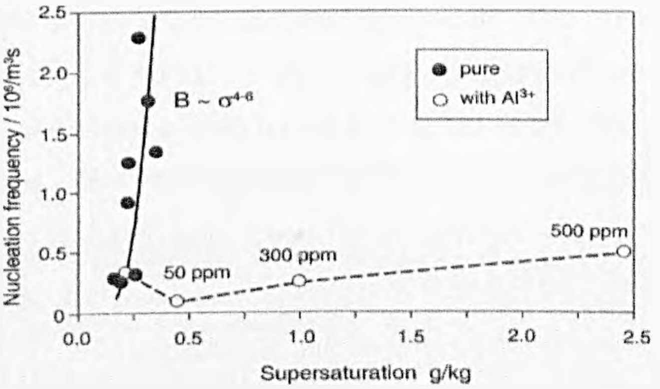

Figure 3.24: Nucleation rates measured in the pure and impure system [12]

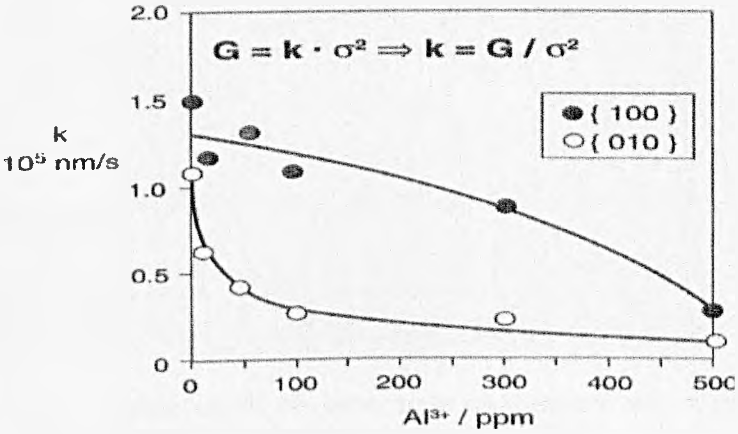

Figure 3.25: The growth-retarding effect of impurities on the crystallization kinetics of ammonium sulphate [12]

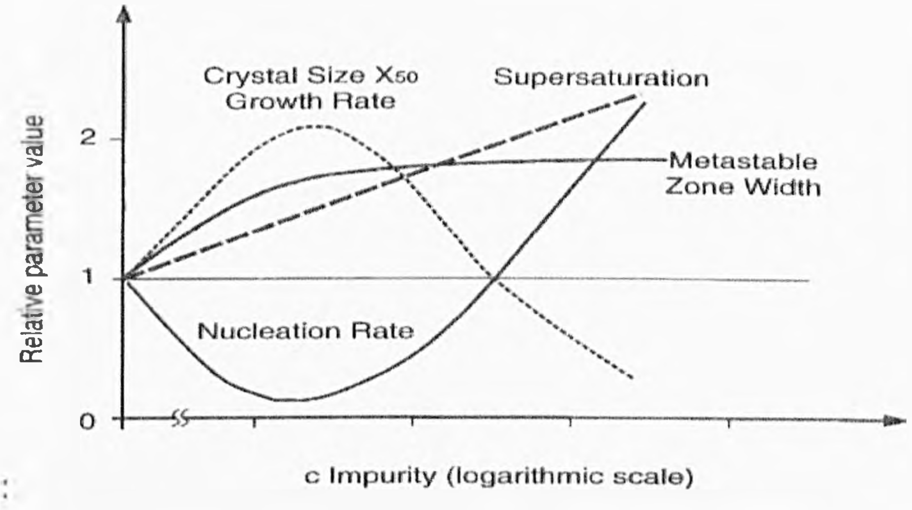

Figure 3.26: Simplified scheme of the general relationship between relevant crystallization parameters [12].

The growth kinetics of PE in aqueous solutions appear to be strongly affected by the presence of some additives (see Figure 3.27) [13]. In particular, the growth rate of highly pure crystals may be up to three orders of magnitude higher than that of the pure grade (98 wt. % purity) commercial product. The presence of additives, absorbed on the crystal surface, may cause complete blocking of the growth process for supersaturation values below the critical value. The inhibiting effect of additives decreases with temperature, the adsorption process being obstructed.

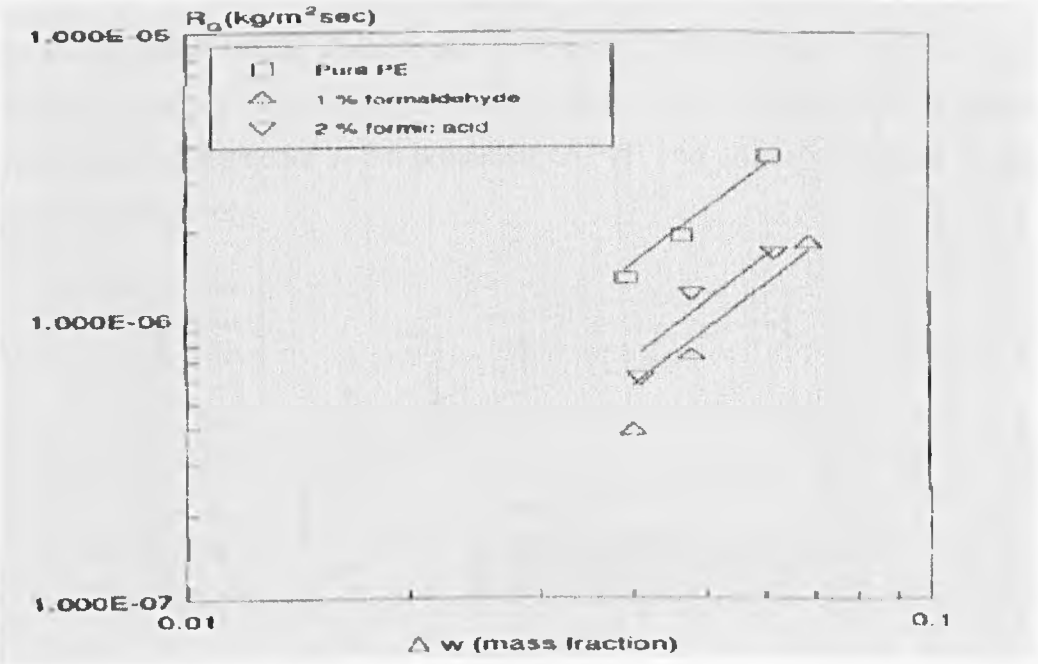

Figure 3.27: Growth kinetics of PE in pure aqueous solution and in aqueous solution containing formic acid from batch runs at 30°C [13].

Experimental growth kinetics of the most important F forms of sucrose crystals, has been investigated at T=40°C in the presence of varying raffinose concentrations [102].

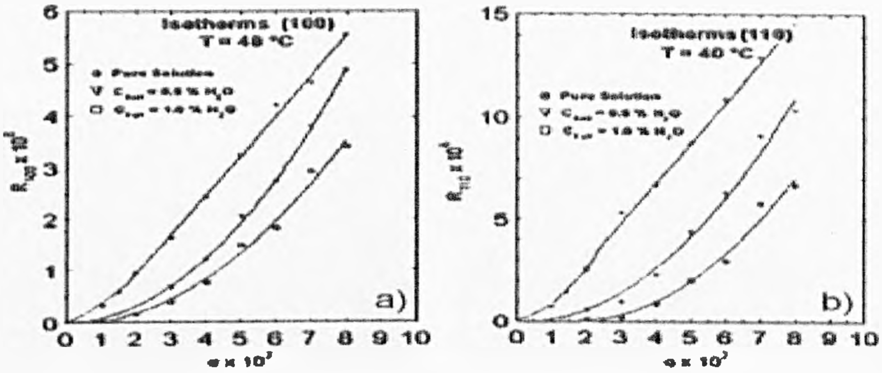

Figure 3.28: Growth isotherms of {100} (a) and {110} (b) forms of sucrose crystals in pure and raffinose doped solutions [102].

The isotherms (Figure 3.28) obtained from pure and impure solutions ($C_{raff} = 0.5$ and 1.0%) clearly show that raffinose not only dramatically slows down the growth rate of the first three forms, but also spreads the parabolic law over the whole explored σ range. Moreover, only {100} isotherm does not show dead zones.

Carbamazepine (CBZ) crystals were grown from pure ethanol solutions containing various impurities [103]. The results in Figure 3.29 indicated that the highest dissolution rate and the lowest dissolution rate were obtained for the samples recrystallized from alcohol in the presence of PVP and untreated cambamazepine particles, respectively.

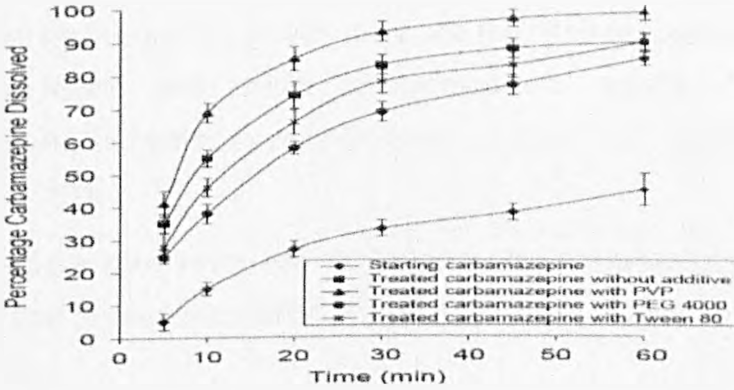

Figure 3.29: The dissolution profiles of untreated carbamazepine sample and carbamazepine crystals obtained from alcohol solutions in the absence or presence of various additives [103].

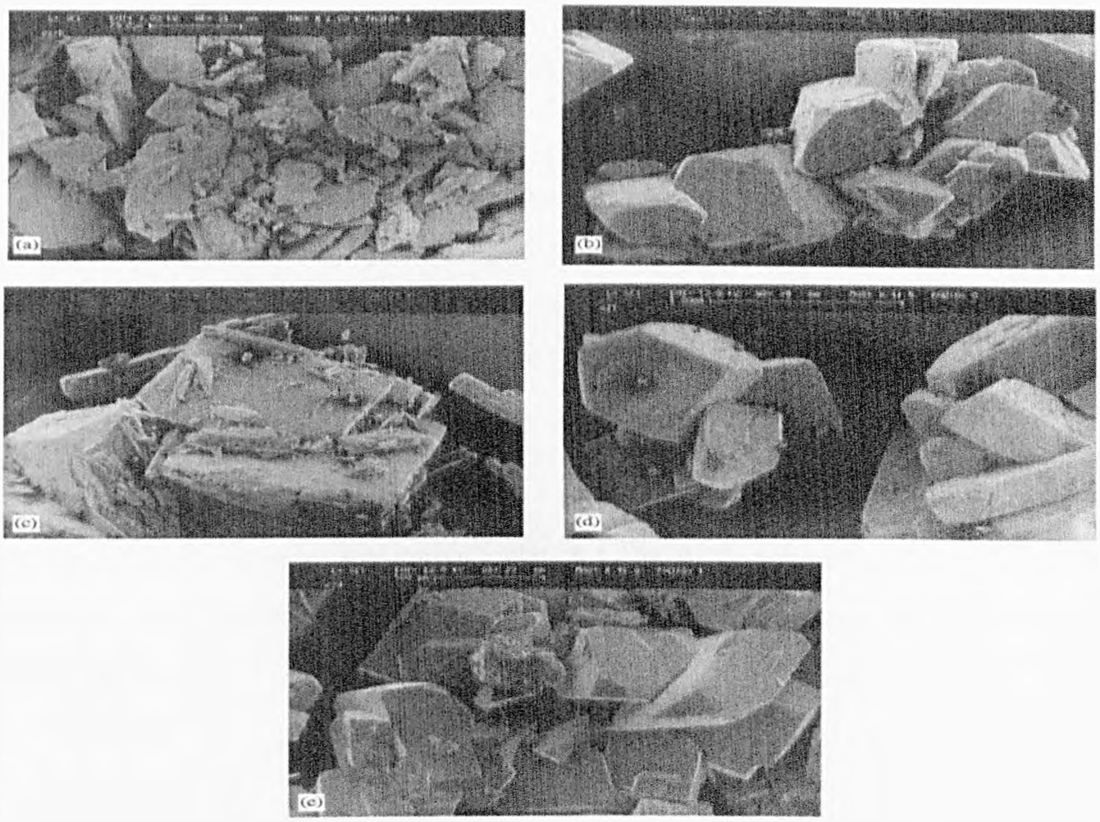

Figure 3.30: SEM of (a) untreated cambamazepine, and those grown in alcohol in the presence of (b) no additive, (c) 0.1%w/v PEG4000, (d) 0.1% w/v PVP K30, (e) 0.1%w/v Tween 80 [103].

The scanning electron micrograph (SEM) (Figure 3.30) studies showed that the presence of the additives in the solutions growth medium affected the morphology and size of carbamazepine [103]. It exhibited different shapes corresponding to the different additives involved in the cambamazepine, and it seemed that the shape was modified by PEG400.

The solubility of hydroquinone, growth rates and the habit of hydroquinone crystals and the meta-stable zone width of hydroquinone solutions were studied experimentally with and without pyrogallol as an additive. The following conclusions may be derived [104].

(1) The meta-stable zone width was increased by the presence of pyrogallol. This suggests that primary nucleation of hydroquinone is reduced by the presence of pyrogallol.

(2) The longitudinal and lateral growth rates increased linearly as the relative supersaturation was increased. The longitudinal growth rate (see Figures 3.31and 3.32) was reduced by the presence of pyrogallol and the ratio of

reduction did not depend on supersaturation. The lateral growth rate (see Figures 3.33 and 3.34) did not seem to be affected by the additive.

(3) The effect of pyrogallol on the longitudinal growth rate was reasonably explained by the Kubota-Mullin model. According to the Kubota-Mullin model, the crystal growth rate in the presence of impurity (or additive) is decreased by the pinning effect caused by the additive species adsorbed on the step lines at kink sites. The growth rate in the presence of additive is described as a function of additive concentration, C_{im} as, $G_1 = G_{10}\left(1-\frac{\alpha K C_{im}}{1+KC_{IM}}\right)$

where G_{10} is the longitudinal growth rate for the pure solution, α is the impurity (additive) effectiveness factor, and the K is the Langmuir constant for additive adsorption.

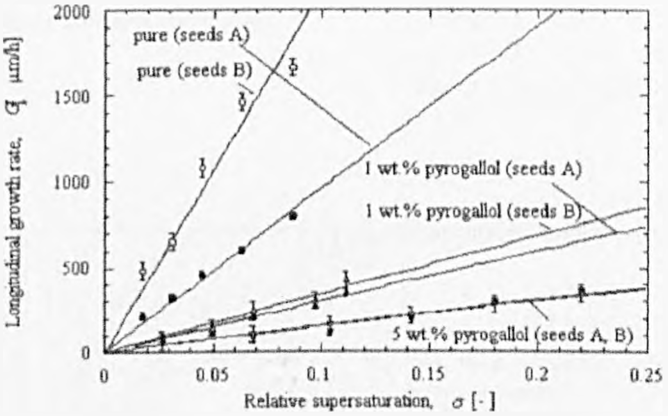

Figure 3.31: Longitudinal growth rates as a function of supersaturation at different additive concentrations. Vertical bars indicate standard deviations [104] .

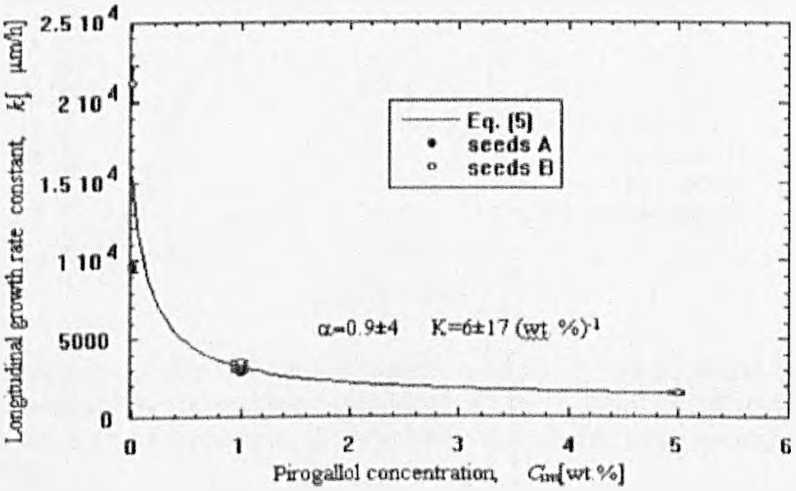

Figure 3.32: Longitudinal growth rate constant vs additive concentration. Vertical bars indicate standard errors estimated when applying a least-square fit to the longitudinal growth rate data. The datum point for seeds A at 5 wt% was completely the same as that for seeds B [104].

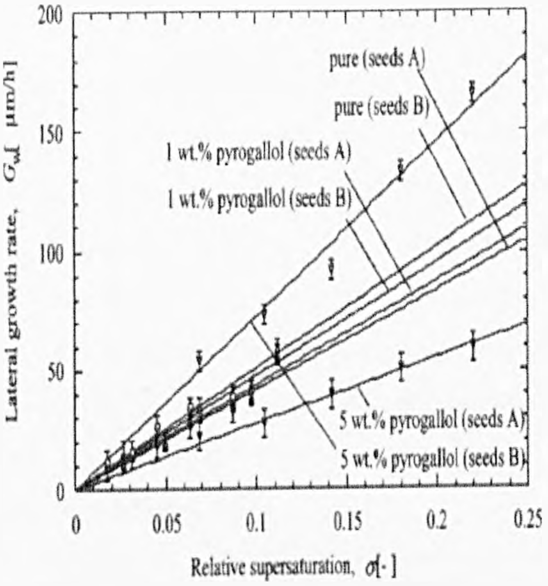

Figure 3.33: Lateral growth rates as a function of supersaturation at different additive. Vertical bars indicate standard deviations g [104].

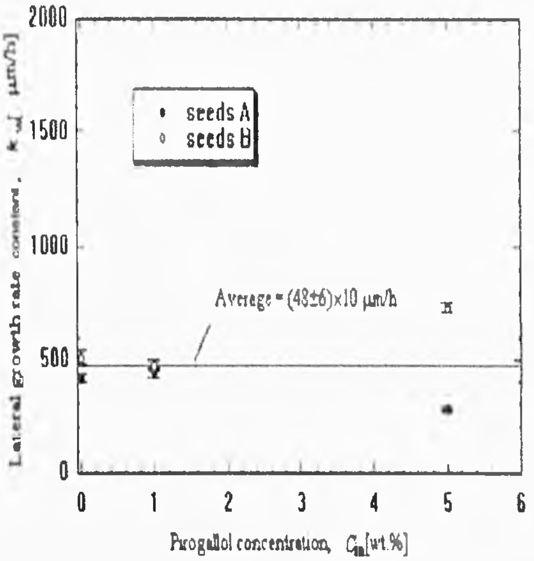

Figure 3.34: Lateral growth rate constant vs additive concentration. Vertical bars indicate standard errors estimated when applying a least-squares fit to the lateral growth rate data in Figure 3.34 [104].

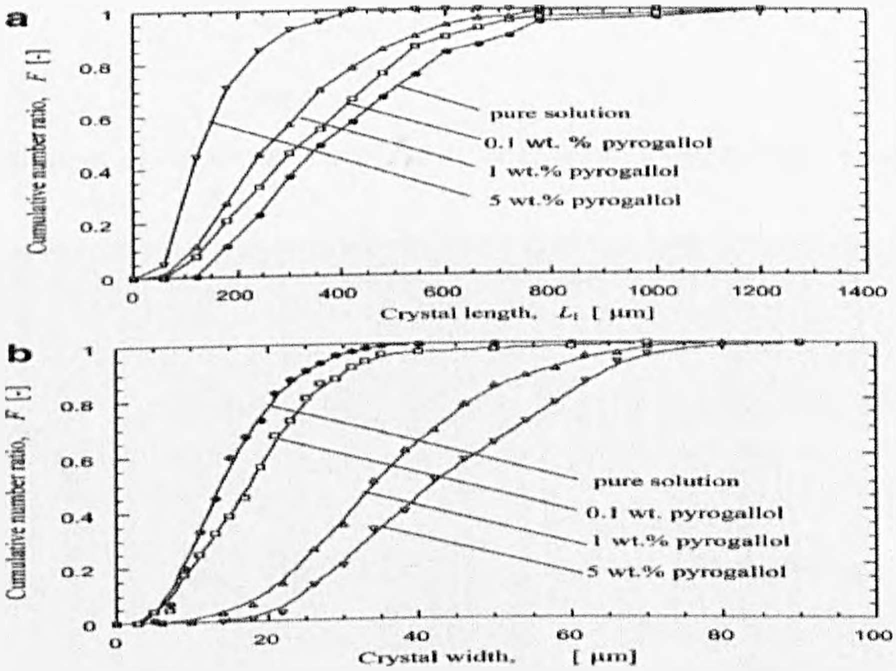

Figure 3.35: Longitudinal distributions of product crystals of hydroquinone obtained form unseeded batch cooling crystallization. (b) Lateral distribution of product crystals of hydroquinone obtained form unseeded batch cooling crystallization [104].

3.2.3 Influence on the transformation of polymorphic crystals

The solution-mediated phase transformation of the meta-stable A form of an active pharmaceutical ingredient (1) to the stable B form is investigated in 2-propanol. The studies show that the rate of transformation is sensitive to the tailor-made additives and that the presence of certain inhibitors reduced the rate of transformation in Figure 3.38 [105]. Molecular modelling studies are undertaken to investigate the incorporation of these structurally related additives into the crystal lattice, and it is observed in Figure 3.37 that the build-in approach used in morphology predictions for additive-host systems can be applied to evaluate the extent of additive incorporation [105].

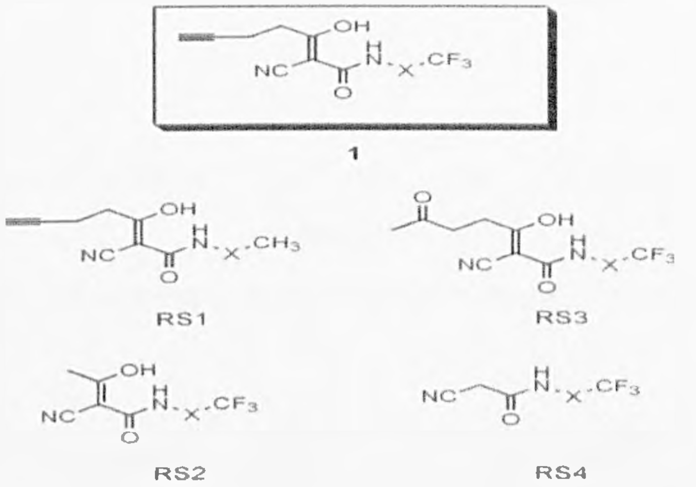

Figure 3.36: Molecular structures of compound 1 and the structurally related additives [105].

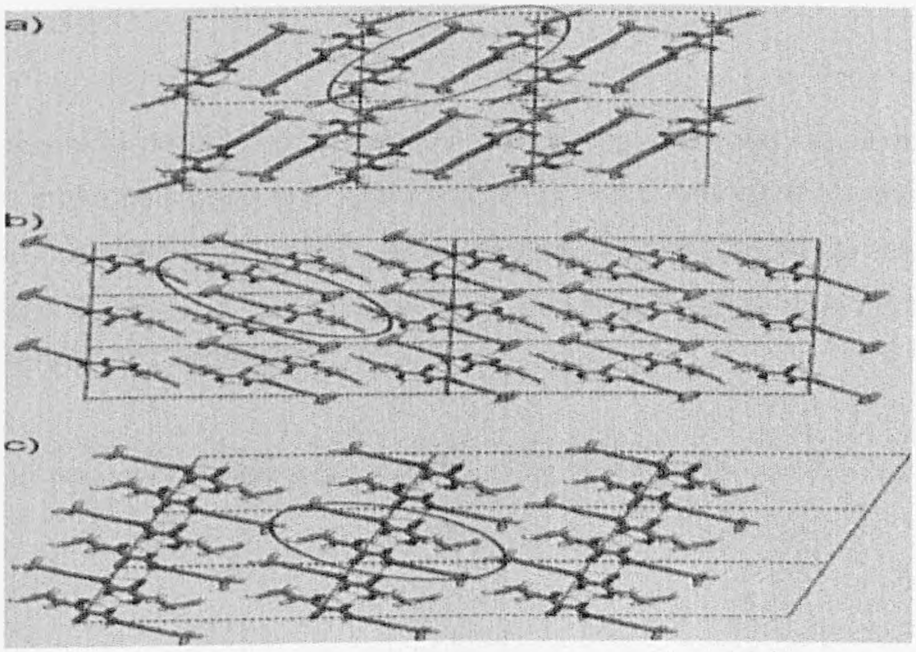

Figure 3.37: Crystal packing of compound 1 polymorphs: (a) form A viewed along the c-axis; (b) form B viewed down the b-axis; and (c) form C viewed parallel to the c-axis. Hydrogen bonds are represented by the aqua dashed lines. The circled areas indicate the growth units of each form [105].

In Figure 3.38, it can be seen that both impurity RS1 and RS4 slightly reduced the transformation rate, while the transformation of compound 1in the presence of RS2 and RS3 of the meta-stable A form to the stable form is hindered, particularly RS2, where a trace amount of form B is observed after 30 h [105].

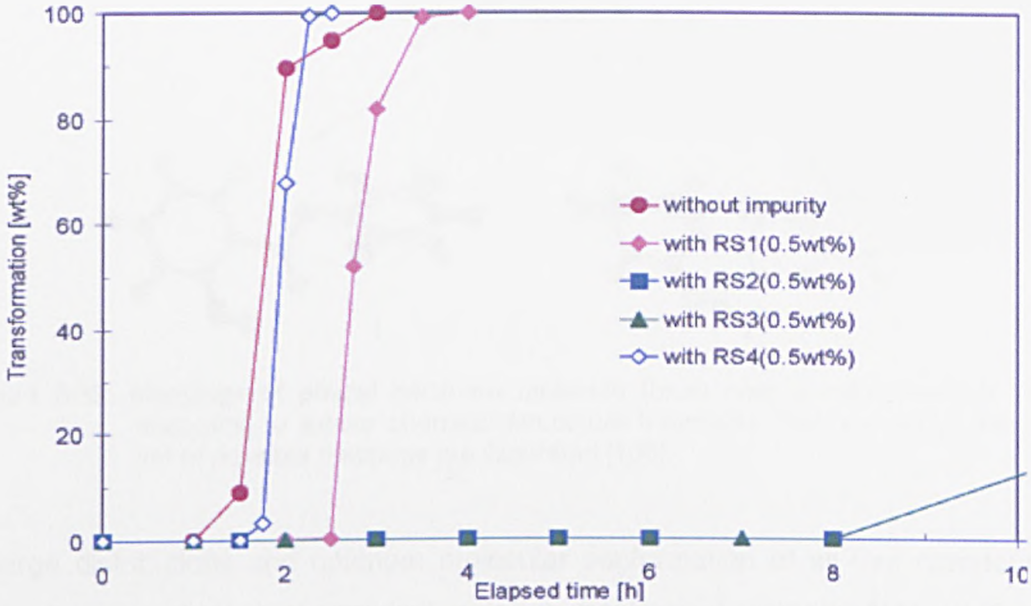

Figure 3.38: Influence of additives on the transformation behaviour of compound 1 at 30°C [105].

3.2.4 Molecular modelling study on the effect of additives

Computational work of atomistic simulation is utilized to model the crystal and evaluate the effect of the additives on the crystal morphology, nucleation and growth kinetics.

A new model to predict crystal morphology that depends upon concentration of additives in the bulk liquid was developed [106]. In this method, the procedure of adsorption of additives on crystal surfaces were simulated to predict the crystal morphology of salol in the presence of three different impurities: phenyl benzoate, benzophenone and benzhydrol.

Table 3.2 Lattice energies calculated from sets of charge distribution and force fields[a] [106]

QM method	force field	E_{latt} (kcal/mol)
PM5	Dreiding	−27.35
	Universal	−38.04
AM1	Dreiding	−25.88
	Universal	−38.90
	COMPASS	−27.26

[a] The force field parameters were applied as implemented in Cerius^2.

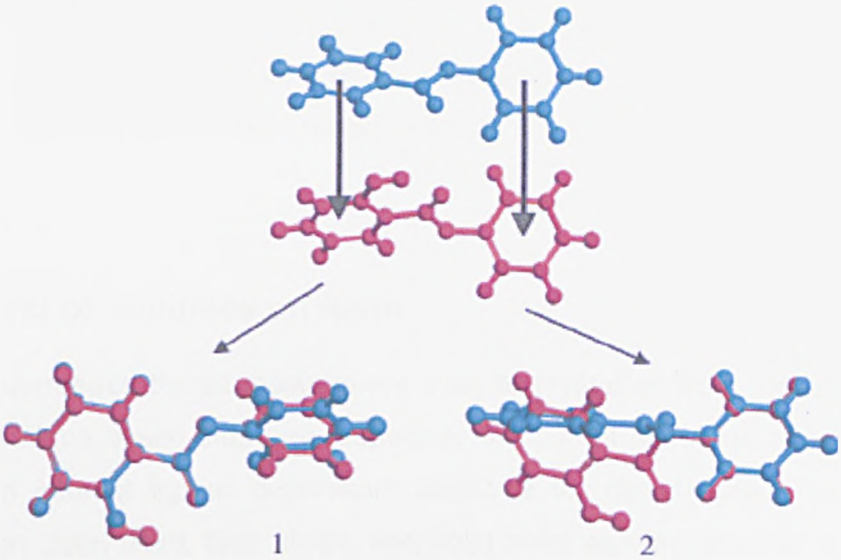

Figure 3.39: Mappings of phenyl benzoate molecule (blue) onto a salol molecule (red) according to similar chemical strucuture fragments. Two examples from the set of possible mappngs are illustrated [106].

Charge distributions and optimum molecular conformation of all four compounds were determined by semi-empirical quantum mechanical methods AM1, PM5, and MNOd. The smallest error was found when the PM5 method was used, so the PM5 optimized molecules were favoured [106]. The new approach was based upon the concept of adsorption sites, and Figure 3.39 illustrated the mapping of phenyl benzoate onto salol, indicating that a set of possible mappings for each impurity molecule exists [106]. The model was successfully applied to predict the ratio of growth rates of the faces (020) and (111) with the additives of phenyl benzoate, benzophenone, and benzhydrol.

3.3 Cold flow Improver Additives

As a method to improve the cold flow properties of petrodiesel, cold flow improver additives have been recognized for more than 40 years. Many additives can affect the wax crystal nucleation, growth, or agglomeration. Exact chemical structures are very important to additives and the most effective additives are often composed of low molecular weight co-polymers or long chain function groups similar in melting point to the n-alkanes found in petrodiesel. These additives include a variety of polymers such as ethylene vinyl acetate co-polymers, fumarate vinyl acetate co-polymers, carboy-containing interpolymers, styrene-maleic anhydride co-polymers, polyoxyalkylene compounds, and co-polymers with long chain alkyl groups from fatty alcohols as pendant groups [14]. Cold flow improver additives mitigate the effect of wax crystals on diesel fuels by changing the shape, size, froth rate and degree of agglomeration of the crystals produced.

3.3.1 Effect of additives on fuels

At low temperatures the oil mixtures are easy to crystallise from the liquid phase, so the technique based literature, especially the patent literature, shows a rather widespread interest inpour depressant additives for diesel fuels. The effect of additives on cloud point, filter ability, and solid point was investigated by Lebedev and Berezina [107].

Table 3.3 Low-temperature characteristics of diesel fuels in relation to chemical structure of additive [107]

Fuel composition	Temperature, ^{0}C		
	cloud point	filter-ability	solid point
Fuel from medium-sulfur crudes			
Without additives	-1	-1	-6
with unsaturated naphthalene-ester (600 mol.wt.)	-2	-10	-40
with copolymer of ethylene and vinyl acetate (1800 mol.wt.)	-1	-11	-32
with polyoxypropylenediol (500 mol. wt.)	-1	-1	-5
with polyoxypropylenediol (2000 mol.wt.)	-1	-2	-5
with polyoxypropylenediol (750 mol.wt.)	-2	-1	-6
with polyoxypropylenediol (3000 mol.wt.)	-1	-2	-7
with polyoxypropylenediamine (1000 mol.wt.)	-3	-1	-5
Fuel from low-sulfur crudes			
Without additives	-4	-9	-10
with unsaturated naphthalene-ester (600 mol.wt.)	-6	-27	Below -60
with copolymer of ethylene and vinyl acetate	-5	-20	-35
with polyoxypropylenediol (2000 mol.wt.)	-3	-9	-11
with polyoxypropylenediol (3000 mol.wt.)	-4	-9	-11
with polyoxypropylenediamine (1000 mol.wt.)	-4	-10	-12

The data in Table 3.3 indicated that the depressant additives can decrease the crystallization temperature of fuels at low temperatures and the type of additives used for improving cold flow properties.

The additives can decrease the crystallization temperature and increase the dissolution temperature (see Figures 3.40, 3.41 and 3.42), and the mechanism of the additives worked was explained by Hennessy et al [108]. This work was supported with optical turbidometric methods and in-situ combined small and wide-angle X-ray scattering (SAXS/WAXS) techniques [108].

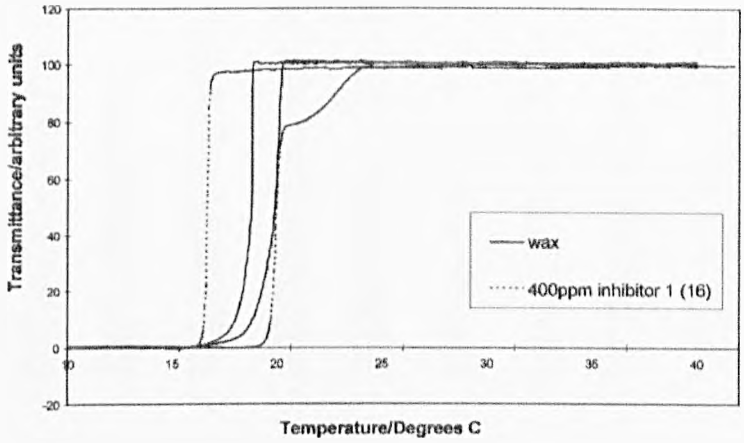

Figure 3.40: The turbidity plot for wax and inhibitor 1(C16) mediated wax solution at 0.1°C/min, showing T_{cryst} and T_{diss} [108].

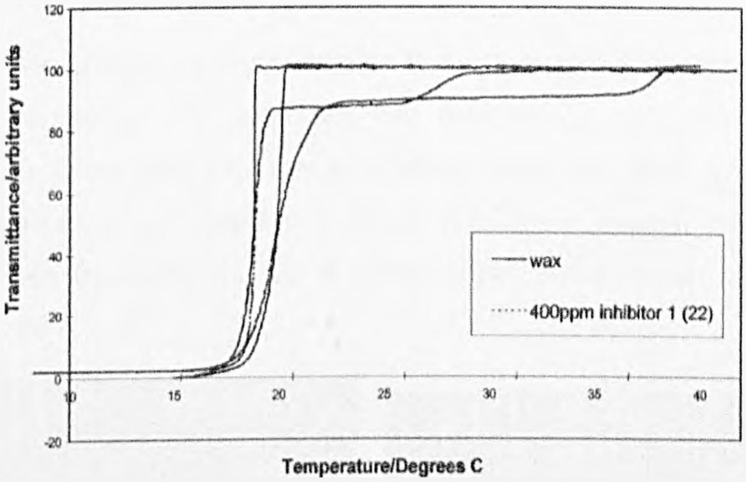

Figure 3.41: The turbidity plot for wax and inhibitor 1(C22) mediated wax solution cooled at at 0.1°C/min, showing T_{cryst} and T_{diss} [108].

In Figures 3.40 and 3.41, the crystallization temperatures of wax crystal were decreased through the addition inhibitor 1 (16), while there was no effect on crystallization temperatures of wax crystals with inhibitor 1 (22). The effects of additives on crystallization temperatures and MSZW were presented in Figure 3.42, it can be found that inhibitors 2 decreased the crystallization temperatures of model oil significantly. The c-axis of the wax is determined by the longest chain length of the crystallizing wax mixture, the a and b axes were determined by the inhibitor family used and the inhibitor efficiencies were determined by the chain lengths of the alkyl chains protruding from the inhibitor backbone [108].

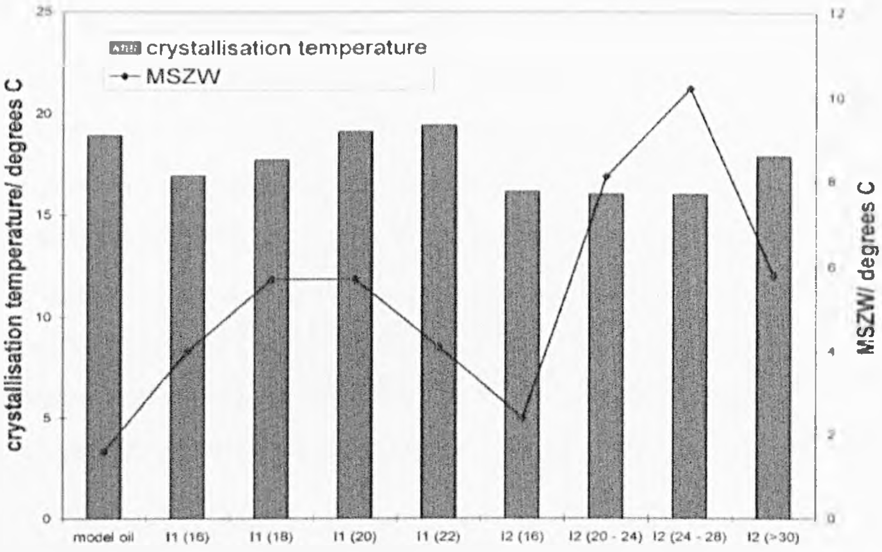

Figure 3.42: The effect of inhibitor alkyl chain length on crystallization temperature and MSZW. The inhibitor family is represented by inhibitor 1 and inhibitor 2, with the chain length in parentheses [108].

In addition to decreasing the crystallization temperature of wax, inhibitors can alter the crystal morphology. For example, the morphology has been observed to change from the usual plate-like shape to highly branched microcrystalline meshes with additives, this was observed by Hutter [109]. These mesh forms were defined as bands formed by nucleation via a meta-stable phase ahead of the inhibition growth front [109].

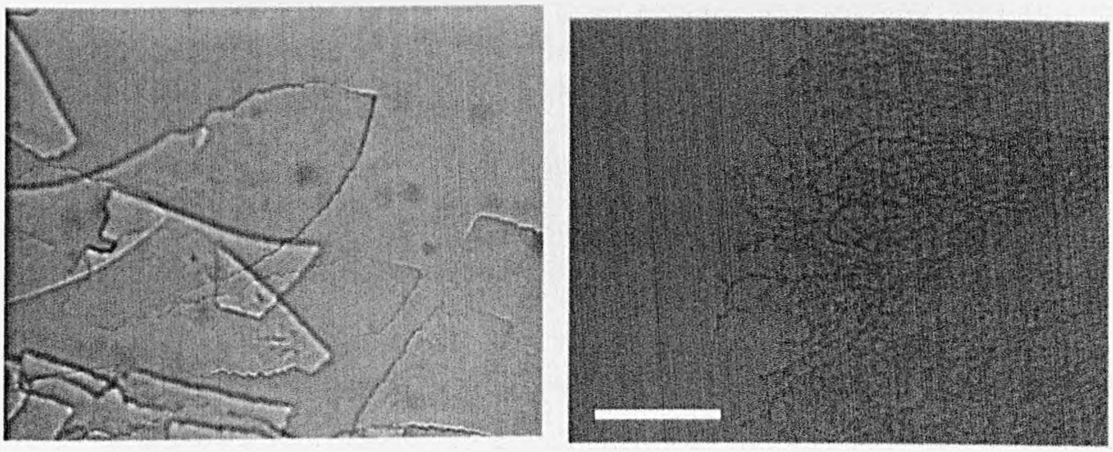
(a)
(b)

Figure 3.43: Optical micrographs of C_{23} precipitates. (a) Precipitate formed from a solution with C_{23} mole fraction of 0.344. Crystals consist of thin, overlapping plates. (b) Precipitate formed from a 0.344 molar fraction of 7.0×10^{-3} PA-18. Here, the crystals form a highly branched tree-like structure. The scale bar spans 100μm and applies to both images [109]

Molecular dynamic simulations have be used to model the nucleation and growth of methane hydrate from a liquid water film together with the suppression of the growth through the addition of polyvinyl pyrrolidone [110]. The All simulations were performed with the package named DL_POLY, and this method was applied to predict the activity of polymers [110]. The layer of alkane molecules was added on top of the inhibitors (see Figure 3.44), then the average energy of the added molecules were calculated to compare the effectiveness of inhibitors. A high value for the average energy represented that little energy was released when the layer is added, ans so should indicate slow crystal growth [110].

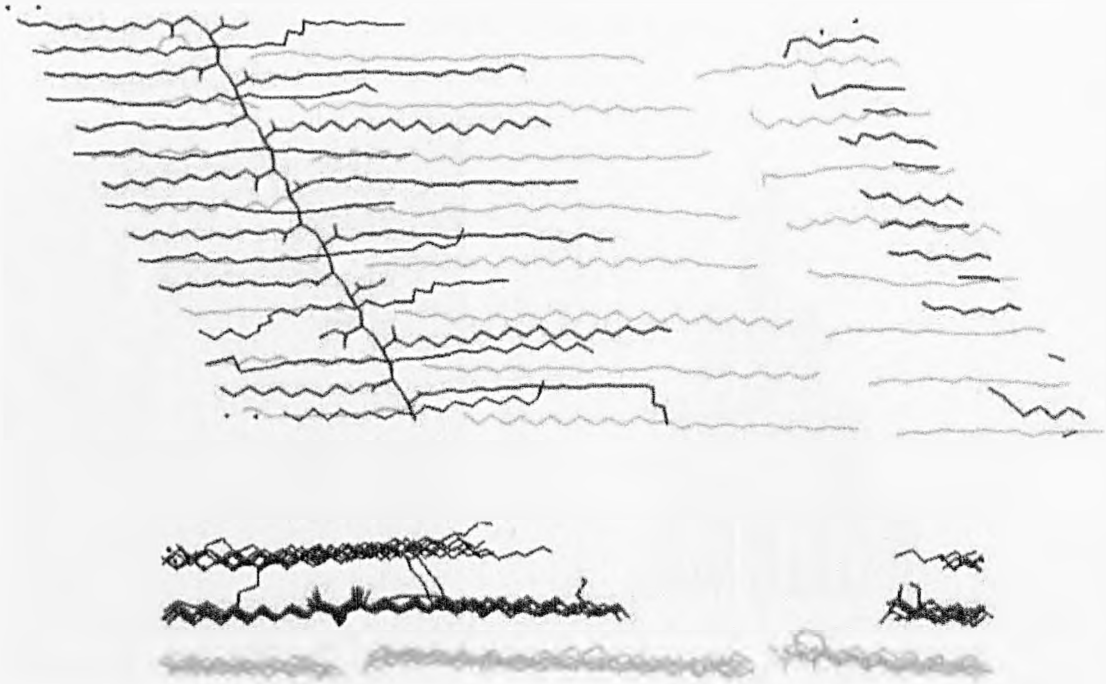

Figure 3.44: Top and side views of the final configuration from a simulation of eight C_{28} molecules (black) adsorbed onto a random PA1 (19%)/PA18 (81%) copolymer (blue), which is in turn adsorbed onto the (010) surface of a C_{28} crystal (surface layer depicted in grey) [110].

The crystallization behavior of n-alkanes has been well investigated with and without additives [111]. The crystal morphology of pure n-alkanes exhibit different forms based on the length and evenness: monoclinic (even-carbon n-alkanes with n>26), triclinic (even-carbon n-alkanes with n<26), or orthorhombic (odd-carbon n-alkanes) structure. n-alkane mixtures crystallize as orthorhombic or hexagonal phase. The cooling rate can also determine the shape of crystals and fast cooling rate will induce needle-shape crystals, whereas slow cooling rates will induce plate-shaped crystals. The effect of additive ethylene-vinyl acetate co-polymer (EVA) on wax crystallization has been concluded [111] and the important results of these experiments are as follows [111]:

(1) In ethylbenzene the EVA co-polymer enters the growth sites with the same probability as the n-alkane units, whereas in kerosene there is a preference for EVA co-polymer to enter the growth site over the n-alkane units.

(2) The n-alkane crystals grown from pure solutions were found to be needle-shaped with a length of about 5mm, but addition of EVA was found to lead to the formation of platelets associated with a log-normal crystal size distribution (Figure 3.45)

(3) The mean crystal size decreased with increase of the concentration of additive (Table 3.4) and the mechanism of additive action differed between the two solvents studied.

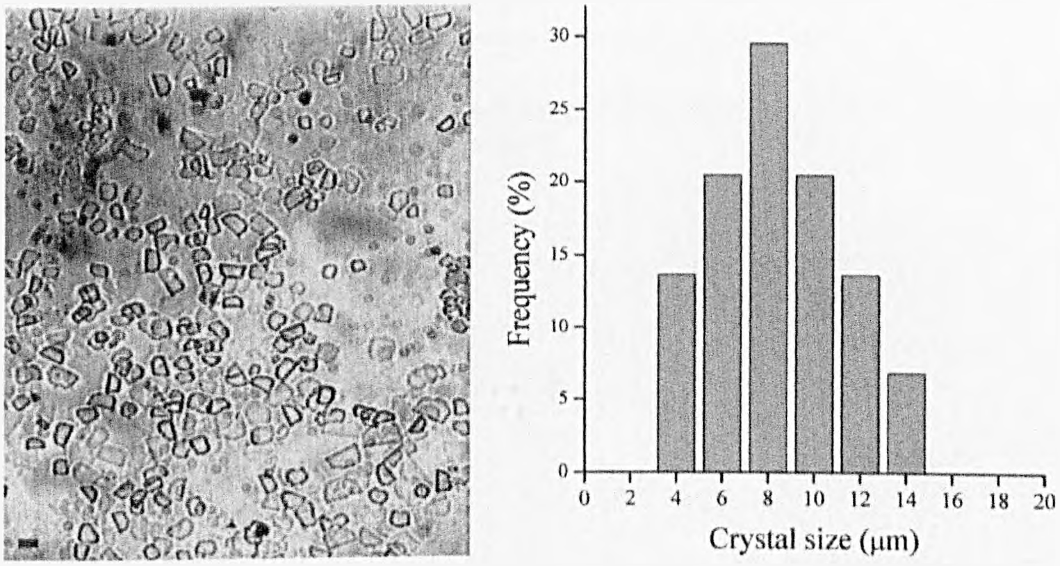

(a) (b)

Figure 3.45: (a) n-alkane crystals obtained from K2 solution containing 500ppm EVA. (b) crystal size distribution corresponding to the crystals of (a) [111].

Table 3.4 Crystal size as obtained from optical microscopy pictures [111]

Paraffin solutions	Mean crystal size (μm)	Standard deviation (μm)
E1 + 100 ppm of EVA	11	3
E1 + 250 ppm of EVA	14	3
E1 + 500 ppm of EVA	8	3
E1 + 1000 ppm of EVA	17	8
K2 + 250 ppm of EVA	7	3
K2 + 500 ppm of EVA	9	3
K2 + 750 ppm of EVA	5	2
K2 + 1000 ppm of EVA	4	1

3.3.2 Effect of additives on biodiesel

2-ethylhexyl-2ethylhexanoate (EHEH) mixed with FAME was demonstrated to lower the crystallization temperature from tests carried out several different methyl hexadecanoate (Figures 3.8 and 3.9) [112].

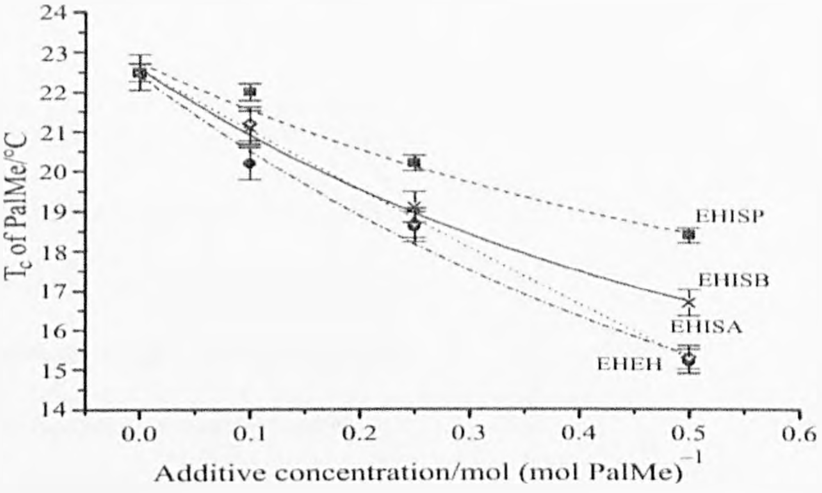

Figure 3.46: Effect of esters synthesized from 2-ethyl hexanoic acid (EH) and branched alcohols on the T_c of Palme [112].

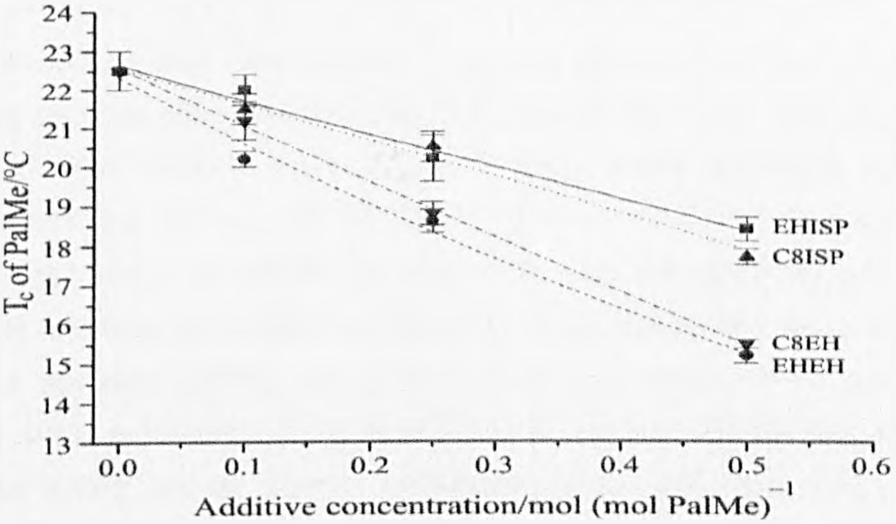

Figure 3.47: Comparative effect between linear and branched acids having 8 carbon atoms (C8 and EH) with two different branched alcohols on T_c of Palme [112]

Twelve polymers and surfactants were used to investigate the effect of additives on the pour point of palm oil methyl esters. Seven out of the twelve compounds tested were found to be miscible in palm FAME due to the similar polarities of the solute and biodiesel (Table 3.5). Poly (maleic anhydride-alt-1-octadecene) was found to be able to improve the PP of palm oil methyl esters from 12 to 6°C when 2 wt-%

was added. The cloud point was reduced from 12.9 to 8.1°C, and the cold filter plugging point was reduced from 12 to 7°C [113].

Table 3. 5 PP of polymeric compounds miscible with palm oil methyl esters [113]

Additives	**Percentage of additive [wt-% of methyl esters]**	**PP [°C]**
Polyoxyethylene(2) cetyl ether	0	12
	1	12
	2	12
Polyoxyethylene(10) cetyl ether	0	12
	1	12
	2	12
Poly(styrene-co-maleic anhydride)	0	12
	1	12
	2	12
Poly(ethylene glycol) distearate	0	12
	1	12
	2	12
Poly(octadecyl methacrylate)	0	12
	1	12
	2	12
Poly(1-decene)	0	12
	1	12
	2	12
Poly(maleic anhydride-*alt*-1-octadecene)	0	12
	1	9
	2	6

Eight palm oil samples were studied to test the effect of cold flow additives on improving cold flow behaviour, including palm olein (POo), super olein (SOo), palm oil methyl esters (POME), palm kernel oil methyl esters (PKOME), mixture of POME and POo at 2:1 ratio (POMEPOo), mixture of POME and SOo at 2:1 ratio (POMESOo), mixture of PKOME and POo at 2:1 ratio (PKOMEPOo), and mixture of PKOME and SOo at 2:1 ratio (PKOMESOo). The additives used were Tween 80, dihydroxy fatty acid (DHFA), acrylated polyester pre-polymer (APP), palm-based oligomer (PP), a mixture of DHFA and PP at 1:1 ratio (DHFAPP), castor oil ricinoleate (COR) and an additive synthesized using DHFA and 2-ethylhexanol (DHFAEH). All the additives used showed satisfactory results, with greater reduction in the pour points and cloud points in POME, PKOME, POMEPOo, POMESOo and PKOMESOo. The biggest reduction in pour point was found to be about 7.5°C (addition of 1.0% DHFA to POMEPOo) and the biggest reduction in cloud point was found to be about 10.5°C (addition of 1.0% DHFA and 1.0% PP to POME). It is suggested that the additives, particularly DHFA and PP, could be used to improve the cold flow stability of palm oil products and hence be effective additives [114].

Co-polymers have also been produced to lower the pour point of biodiesel. For example, a methacrylate copolymer has been devised to be a cloud point depressant of FAMEs by Majerczak [115].

A patent has presented a co-polymer additive for improvement of the low-temperature behaviour, especially of the cold filter plugging point, of fatty acid esters of monohydric alcohols, especially of rapeseed oil methyl ester. As an example, the target was to lower the CFPP from -15°C to -22°C in the case of rapessed oil methyl ester [116].

The following additives were used to test the effect on CFPP of rapeseed methyl ester[117]:

A: an ethylene/vinyl acetate co-polymer having a vinyl acetate concentration of about 37wt% and a number average molecular weight of about 2,700;

B: a 3:1(wt:wt) mixture of additive A and an ethylene/vinyl acetate co-polymer having a vinyl acetate concentration of about 13.5 wt% and a number average molecular weight of about 5,000;

C: a mixture containing the same compounds as B but where the wt: wt ratio is 13:1.

Additive A, B and C were each dissolved in samples of the same rapeseed methyl ester fuel and the cold filter plugging point (CFPP). The results are shown in Table 3.6.

Table 3. 6 The CFPP of Rapeseed Methyl Ester with Additives A, B and C [117]

Additive	CFPP(°C) Treat Rate (ppm Al)	
	500	1000
A	-14	-16
B	-13	-14
C	-15	-18

Note: "ppm Ai" refers to the active ingredient of the cold flow additive in ppm by weight, i.e., without regard to any amount of carrier solvent

In comparison, the CFPP of the untreated fuel was -9°C. It is therefore seen that additives A, B and C each improved the filterability of the fuel as measured by the CFPP test [117].

Several investigations have been carried out to improve the low-temperature flow properties of neat biodiesel prepared from different vegetable oils by using chemical additives [118-120]. The stabilization factor, induction period, increases with increasing additive concentration between 0.01 and 0.1% by weight (Figure 3.48) [121]. The role of the additive molecules is to bind the saturated ester components, thereby suppressing the onset of three-dimensional nucleation.

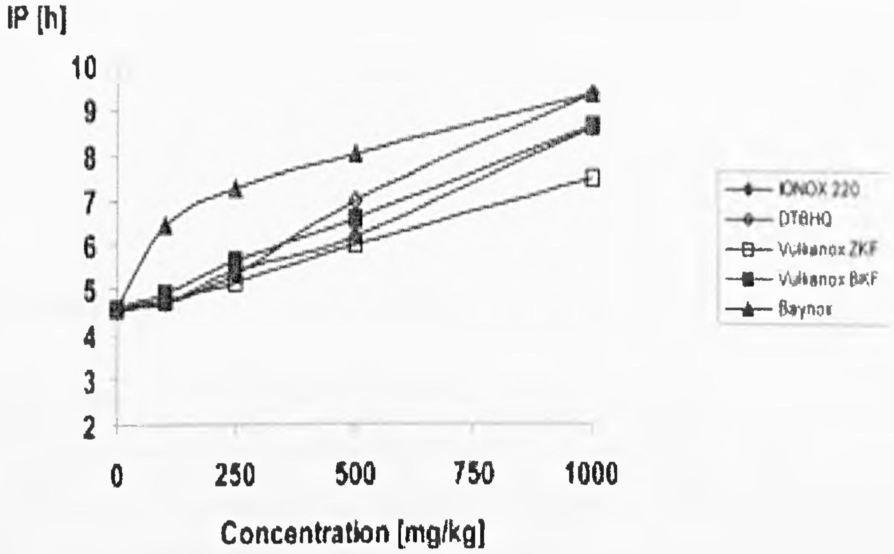

Figure 3.48: Dependence of induction period for instability (as determined by pour point) of rapeseed oil methyl ester on the concentration of some selected additives [121].

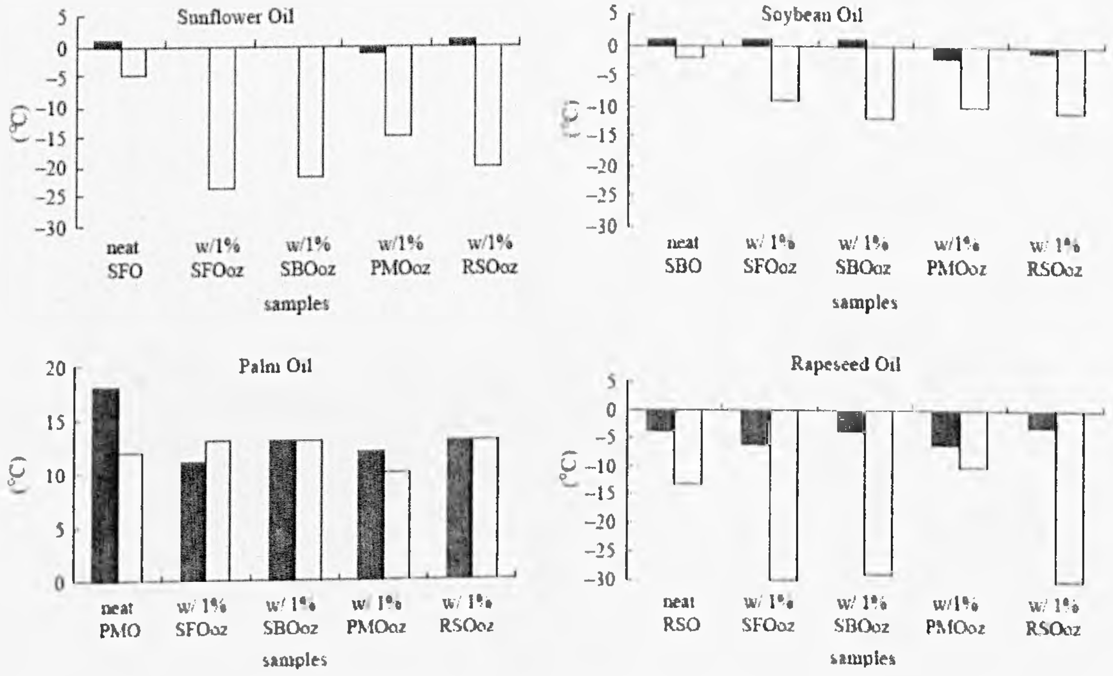

Figure 3.49: Effect of ozonized vegetable oils on cloud point (■) and pour point (□) of biodiesel prepared from different vegetable oils [122]

The protruding polar groups was found to be the main reason for the pour-point depressants to improve cold flow properties for conventional diesel fuels. However, vegetable oils and their FAMEs do not have polar groups. Therefore, to design effective pour-point depressants for biodiesel, polar structures ideally need to be introduced into their structure. Scoriano et al. [122] investigated the effect of 1% (by weight) of ozonized sunflower oil, soybean oil, palm oil and rapeseed oil on the cloud points and pour points of biodiesel prepared from different vegetable oils (Figure 3.49). The data reveals that these additives are effective in decreasing the pour point.

3.4 Conclusions

This chapter reviewed the effect of additives on crystallization process: nucleation, crystal growth, morphology and phase transformation including inorganic and organic additives. This chapter also detailed the effect of additives on crystallization temperatures of petrodiesel and biodiesel. However, it can be seen that the use of monomer cold flow additives have not been studied in much detail, so the effect of that kind of additive will be explored in this thesis work.

CHAPTER 4

Materials and Methods

Summary:

The crystal and molecular structures of the materials studied in this thesis work, together with an overview of the experimental and computational methods used are highlighted.

4.1 Introduction

This chapter describes the materials examined in this research and the methodologies used for their examination. The former were: naphthalene, biphenyl, methyl stearate methyl palmitate and eight additives used for improving cold flow properties of methyl stearate. Naphthalene and biphenyl were selected carefully as illustrative systems for the development of the molecular cluster work since they do not manifest intermolecular hydrogen bonding as is the case for methyl stearate. Because methyl stearate is one of the main components in biodiesel, it was used as a model material to study the effect of additives on nucleation behaviour such as crystallization, dissolution temperatures and induction time. The additives selected for the nucleation study have a similar alkyl chain length to methyl stearate. Both methyl stearate and methyl palmitate were selected to study the effects of solvents (toluene, dodecane and methyl oleate) on crystal size and morphology.

All the compounds excluding additives used for case studies in this work were molecular crystals, in which the crystal chemistry is dominated by van der Waals interactions and for which there are no strong columbic interactions. The crystal structures of all the compounds except for methyl palmitate were available in the Crystal Structure Database (CSD).

4.2 Materials

4.2.1 Methyl stearate

Methyl stearate ($C_{19}H_{38}O_{2,}$ M.W. = 298.51) normally occurs in the form of a colourless crystal. It melts at 39°C; it is insoluble in water, but can dissolve in organic solvents such as toluene and methyl oleate. Because methyl stearate crystals tend to agglomerate at low temperatures, there is very little literature reporting the crystal shape of methyl stearate.

The crystal structure of methyl stearate was first analyzed by Aleby [123], and then another form of methyl stearate was reported by Macgillavry [124]. The crystal structure information is shown in Table 4.1.

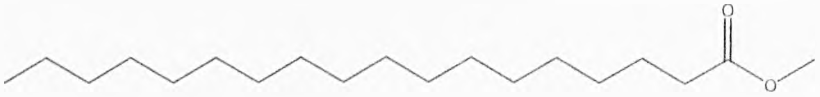

Figure 4.1: Formula of methyl stearate

Table 4.1 Crystallographic Data of Methyl Stearate

Name	Space group	Space group number	Length a (Å)	Length b (Å)	Length c (Å)
Methyl stearate 1	A2/a	15	5.61	7.33	106.6
Methyl stearate 2	Pnab	60	5.61	7.35	95.15
Name	Angle α	Angle β	Angle γ	Cell volume ($Å^3$)	polymorph
Methyl stearate 1	90°	116.78°	90°	3910	Monoclinic
Methyl stearate 2	90°	90°	90°	3930	Orthorhombic

The materials used for experimental purposes were purchased from the Sigma-Aldrich Co Ltd., having purity of 96% or 97%. The solvent, methyl oleate was purchased from the Alfa Aesar Co Ltd, having a purity of 75%.

4.2.2 Methyl palmitate

Methyl palmitate ($C_{17}H_{34}O_2$, M.W. = 270.45) is also a colourless crystal. It melts as 35°C; it is insoluble in water, but can be dissolved in methyl oleate, toluene and doecane.

The crystal structure of methyl palmitate has not been reported so far. Due to similarities between the molecular structures of methyl stearate and methyl palmitate, we have studied the crystal structure of methyl palmitate based on that of methyl stearate.

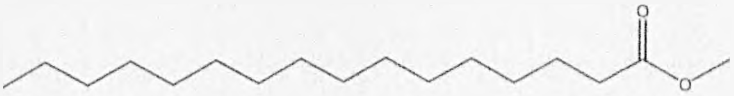

Figure 4.2: Formula of methyl palmitate

The material for the experiments was purchased from the Alfa Aesar Co Ltd, having a purity of 97%.

4.2.3 Ethyl stearate and monostearin

Ethyl stearate ($C_{20}H_{40}O_2$, M.W. = 312.53), and monostearin ($C_{21}H_{42}O_4$, M.W.=358.56) were used as additives to decrease the crystallization temperature of methyl stearate.

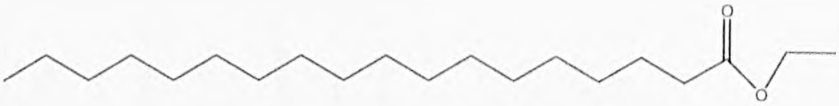

Figure 4.3: Formula of ethyl stearate

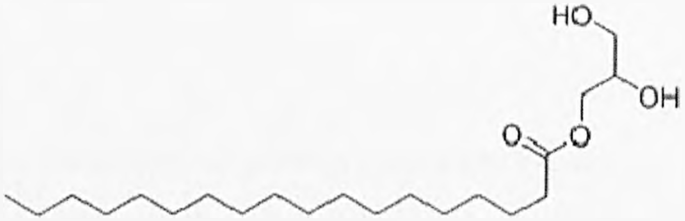

Figure 4.4: Formula of monostearin

The ethyl stearate was purchased from Avocado Research Chemicals Co. Ltd, having a purity of 99%; and the monostearin was purchased from TCI.UK having a purity of 65%.

4.2.4 Synthesised additives

There were six dialkyl additives molecule were synthesised based around to different core motif using dialkyl (A) and salt link (B) respectively by Infineum. Ltd. The name of these additives are: 16A16, 16A18,18A18, 16B16, 16B18 and 18B18, the formula corresponding to each synthesised additives were shown in Figure 4.5. Here, 16 means the number of carbon in this alkyl group is 16.

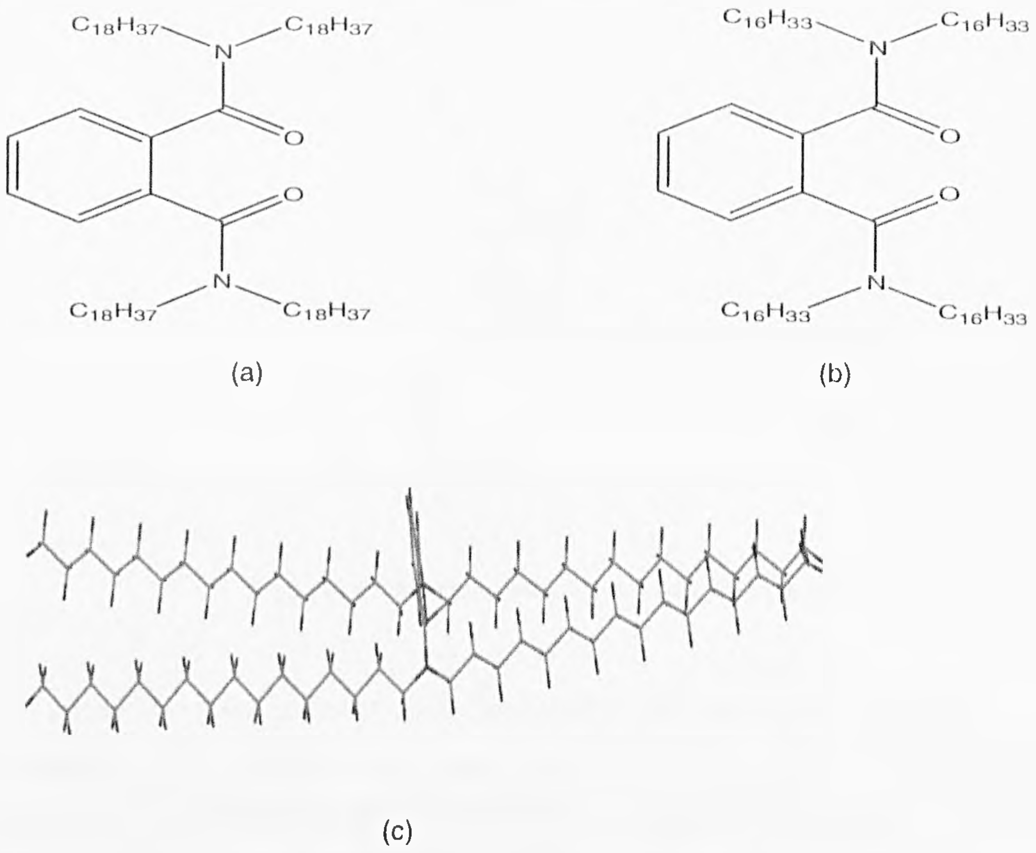

(a)

(b)

(c)

Figure 4.5: 2D molecular diagrams of additives produced by Infineum, (a) 18A18; (b) 16A16; (c) 16B16

4.2.5 Naphthalene

Naphthalene ($C_{10}H_8$) is a simple polycyclic aromatic hydrocarbon (see Figure 4.6), and conformationally rigid. The crystal structure of naphthalene was sourced from CSD (ref code NAPHTA[125]). Naphthalene (M.W. =128.17) normally occurs in the form of white flake like crystals with a strong odour of coal tar. It melts at 80.26°C and the solubility of naphthalene is about 32.91% (mole fraction) in toluene at 30°C, about 14.15% in n-hexane and 18.25% in cyclohexane at 30°C[126].

Table 4.2 Crystallographic information of Naphthalene cell parameters

Name	Space group	Space group number	a (Å)	b (Å)	c (Å)
naphthalene	$P2_1/a$	14	8.235	6.003	8.658
Z	Angle α	Angle B	Angle γ	Cell volume (Å^3)	polymorph
2	90.00°	122.92°	90.00°	360.656	Monoclinic

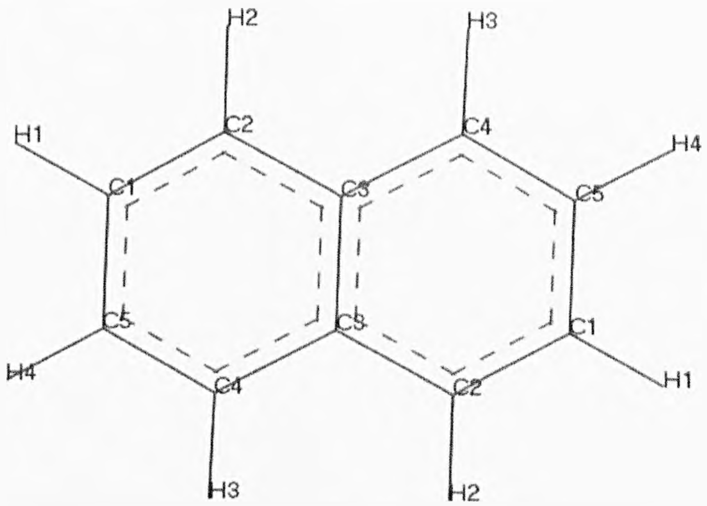

Figure 4.6: Molecular structure of naphthalene [127]

As one of the most common materials used in the manufacture of plastics, resins, fuels and dyes, naphthalene has been studied in many aspects by many researchers. The simulation of naphthalene properties such as crystal morphology [128] and the modified morphology in the presence of biphenyl [129] has been carried out.

The material used for experimental purposes was purchased from Fisher Scientific Ltd., having a purity of 99.0%. The solvent, toluene, used for re-crystallization of naphthalene was purchased from the Sigma-Aldrich Co Ltd, having a purity of 99.3 vol. %.

4.2.6 Biphenyl

Biphenyl ($C_{12}H_{10}$) shown in Figure 4.7 is an aromatic hydrocarbon which crystallises in the monoclinic space group $P2_1/a$. The crystal structure of biphenyl, sourced from CCDC (ref code BIPHEN[130]), is shown in Table 4.3. Biphenyl (M.W. =154.21) forms colourless crystals. It melts at 69.2°C, and the solubility of biphenyl is about 16.08% (mole fraction) in n-hexane at 30°C, about 39.56% in carbon tetrachloride and 24.71% in cyclohexane at 30°C [126]. The molecular structure of biphenyl is flexible, and the equilibrium angle in the gas phase with the lowest energy was 44.4±1.2° found by Almenningen et al [131].

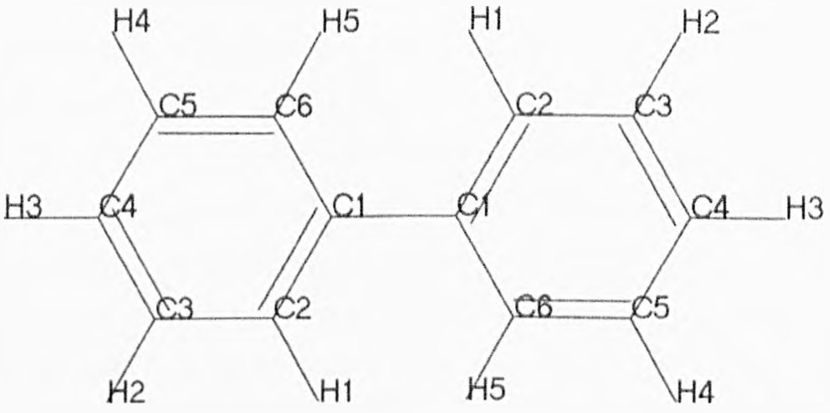

Figure 4.7: Molecular structure of biphenyl

Table 4.3 Crystallographic Data on unit cell parameters of biphenyl [130]

Name	Space group	Space group number	a (Å)	b (Å)	c (Å)
Biphenyl	$P2_1/a$	14	8.120	5.640	9.470
z	Angle α	Angle B	Angle γ	Cell volume (Å^3)	polymorph
2	90.00°	95.40°	90.00°	431.771	Monoclinic

Biphenyl is used mainly in the chemical industry, in the manufacture of textiles and dyes and of other chemicals. It is also used as a heat transfer agent and to produce PCBs. The material used for experimental purposes was purchased from Fisher Scientific Ltd., having a purity of 99.0%.

4.3 Experimental and Computational Methods

4.3.1 Experimental methods

4.3.1.1 Development of a 100ml automated crystallization system

This rig (in Figure 4.9) is mainly used for carrying out the crash cool experiments, and it can also be utilised for slow cool experiments. The equipment employed includes a 100ml reactor and two Julabo water baths. The two water baths were placed at the same level, one was heating water bath, the temperature of the other one can be controlled by the Julabo computer program. Behind the reactor, there are many metal pipes with electronic valves which were utilised to decide which bath would be used, and the valves were controlled with an electronic box which was switched manually. When the solutions in the reactor needed to be heated, the hot water bath was run, and the fluid from the hot water bath flowed through the pipe, at the same time, the temperature in the cooling water bath decreased to around 0°C. At this point the hot bath was switched off and the cooling bath switched on after the temperature of solution was stable, and when the fluid in cooling bath flowed through the pipe to reactor, the temperature of the solution in the reactor decreased rapidly.

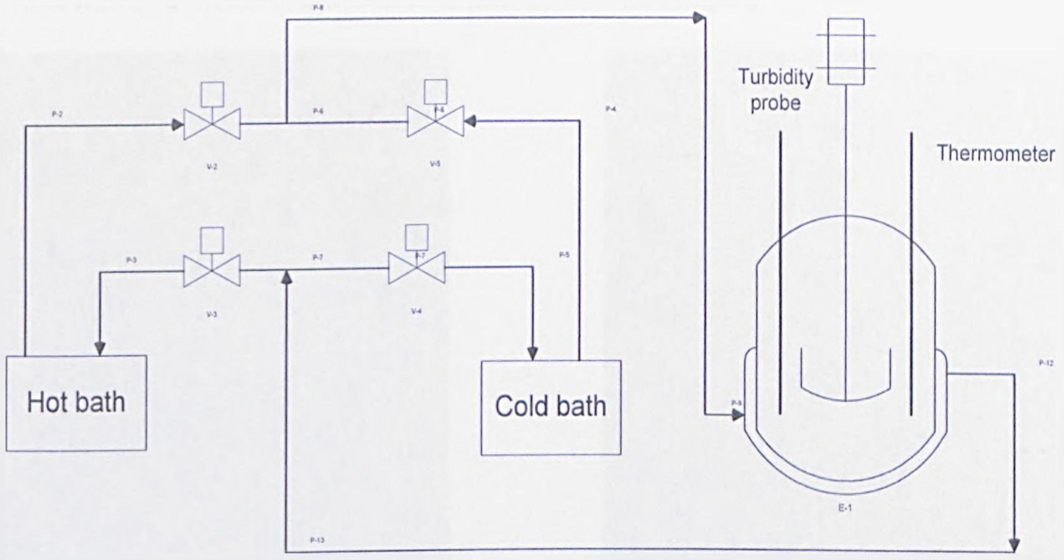

Figure 4. 8: Schematic flow diagram of the flow system

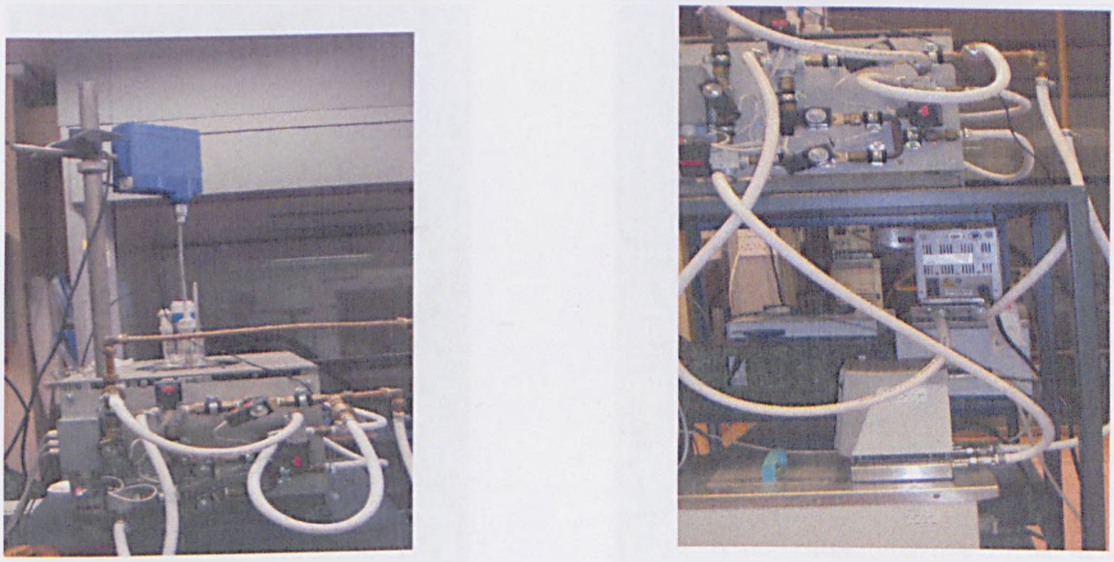

(a)

(b)

Figure 4.9: Photographs of the connection of pipes with water bath and distribution of pipes: (a) Photograph of pipes behind reactor; (b) Photograph of the connection of pipes with bath.

Control of the reactor temperature was achieved by using the Julabo computer program which monitored reactor temperature. A turbidity probe was employed within the reactor to measure the solution turbidity and hence crystallization and dissolution on-set points, and the LABVIEW computer program was used to monitor the turbidity.

However, the original turbidity probe used (in Figure 4.10 a and b) was somewhat fragile and tended to be easy to break and could corrode due to the plastic fibre, so a new turbidity probe (Figure 4.10 c and d) was developed.

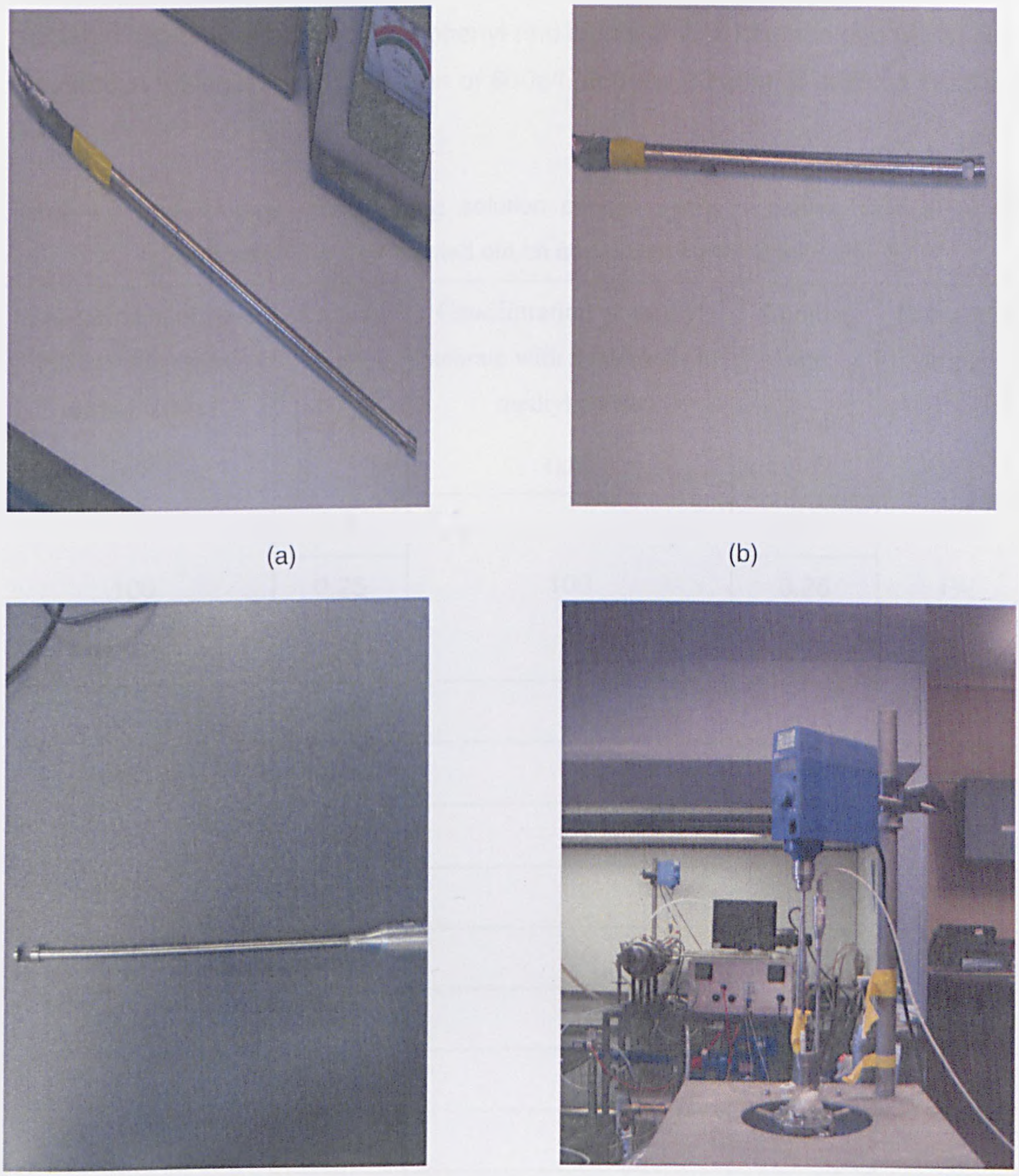

(a) (b)

(c) (d)

Figure 4.10: Photographs of old and new turbidity probes: (a), (b) old turbidity probes; (c), (d) new turbidity probe used in the experiments.

4.3.1.2 Slow cool procedure

A solution was prepared by adding the appropriately weighed solute and solvent, using a balance with accuracy of +/- 0.01g, to the crystallizer before heating the mixture to approximately 10°C above the saturation temperature and the temperature maintained constant for 30 minutes in the crystallizer to ensure that all the crystal embryos had been fully dissolved. The concentration of methyl stearate in methyl oleate was chosen at:100g/l, 150g/l, 200g/ and 250g/l, and the content of 8 additives in the solute is from 0.5% to 5.0%.

Besides the system of methyl stearate, four solutions of pure naphthalene, pure biphenyl, naphthalene doped by biphenyl and biphenyl with naphthalene were also prepared in toluene at concentration of 600g/l, and the content of additive in solute is 1%.

Table 4.4 Experimental matrix giving solution concentrations x cooling rate at which crystallisation run were carried out on all solution systems tested

Concentration of pure methyl stearate in methyl oleate (g/l)	Cooling rate (^{0}C/min)	Concentration of methyl stearate with 8 additives in methyl oleate (g/l)	Cooling rate (^{0}C/min)	Content of additives
100	0.1	100	0.1	0.5%
	0.25		0.25	1%
	0.5		0.5	2%
150	0.1			5%
	0.25			
	0.5			
200	0.1			
	0.25			
	0.5			
250	0.1			
	0.25			
	0.5			

The solution was then cooled down with various cooling rates to a temperature at which the crystals begin to form. The beginning of the of crystallization process of crystallization and hence the temperature of crystallization was determined from the sudden rise of the turbidity readings. The dissolution temperature is expected to be approximately constant at different cooling rates as it is a thermodynamic system-dependant parameter. However, it could also be evaluated from the turbidity data as a drop in the turbidity readings. The experiment was repeated with cooling rates of 0.1, 0.25, 0.5^{0}C/min. The dissolution (T_{diss}) and crystallization (T_{cr}) temperature as a function of the cooling rate enables determination of the meta-stable zone width (MSZW) as the difference (T_{diss}- T_{cr}) at cooling rate approaching zero as it is the minimum possible difference between these two temperatures. The experiment was repeated with different starting concentrations. To assess the error from the operation in the process, the slow cooling experiments for each solution were repeated more than three times, and the standard deviations of dissolution and nucleation temperatures calculated.

4.3.1.3 Crash cool procedure

Once the meta-stable zone width had been determined using the slow cool crystallization technique, crash cool studies were performed so that the lower temperature to which the solution was cooled down to fall within the meta-stable zone. The solution was prepared in the same way as described in the slow cool procedure, cooled down to a certain lower temperature and maintained at this temperature until the crystallization started. The beginning of the crystallization process was detected using turbidity measurements. The elapsed time between achieving a level of supersaturation and the first appearance of crystals was measured. This time is called the induction time. The induction time was measured for different end temperatures and hence different supersaturations. The induction time data were then used to determine the interfacial tension between the crystal and the mother liquor.

4.3.1.4 Development of the inverse microscope

Due to low crystallization temperatures, the dense solution of methyl stearate in methyl oleate and associated problems of solid/liquid separation, it can be very difficult to observe ex-situ the crystal shape of methyl stearate in the solution.

Hence, an inverse microscope system was developed to observe the shape of crystals in-situ within mother liquid and at the low temperatures associated with their formulation.

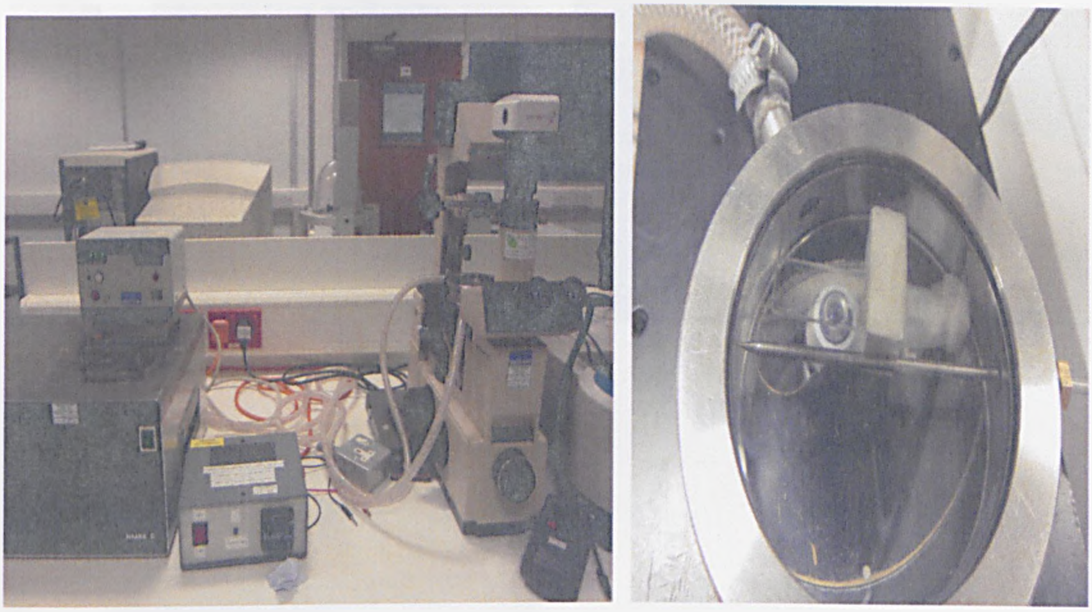

Figure 4.11: Prototype cell for observation of methyl stearate in methyl oleate

The crystallization set-up employed in this study includes an Olympus optical polarizing microscope integrated with a CCD camera, a PC using image capture and analysis software, a 0.5 μl 2mm patt length sealed UV cuvette crystallization cell and Haake F3 re-crystallizing temperature controlled water bath. Using this crystals appear during solution cooling and settle at the bottom of the cell. A CCD Lumenera Infinity 3.3 megapixel camera, 2080 x 1536 resolutions, 1/1.8" CCD Colour Chip was used for this crystallization set-up. The image capture and analysis system was used to capture crystal images and record video clips during the crystallization process. The UV cuvette crystallization cell was submerged in a shallow tank of water whose temperature was accurately controlled using the water bath.

4.3.1.5 Observation of crystals in cold room

Pictures of methyl stearate and methyl palmitate crystals were also taken in the cold room at Infineum. The cold room was almost $10m^2$ in flow area and has the capability to decrease its temperature to -20°C. Crystals of methyl stearate and methyl palmitate were formed in a sample bottle as the temperature decreases.

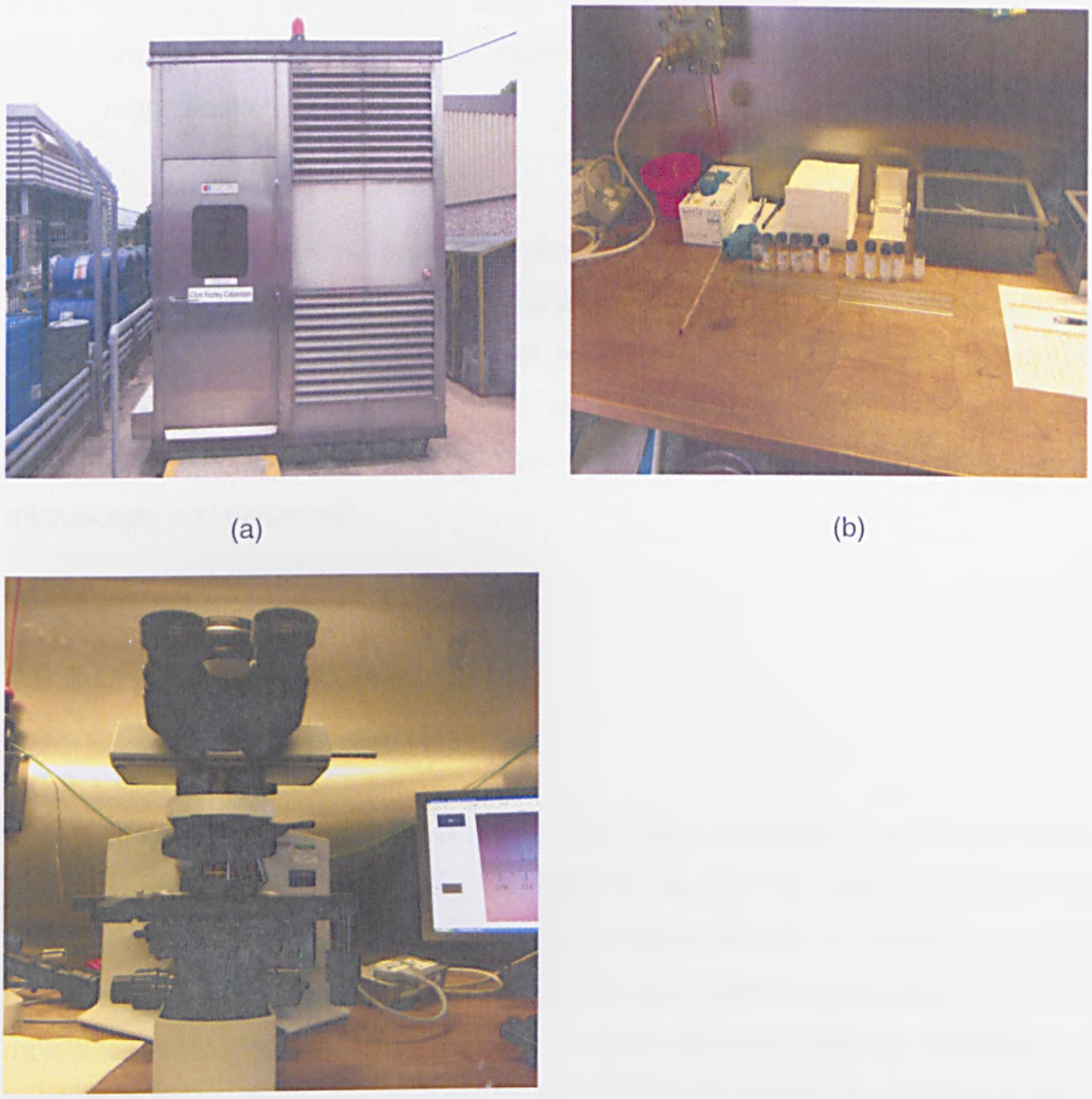

(a)

(b)

(c)

Figure 4.12: Photographs of the cold room facilities at Infineum used to observe the crystals of methyl stearate and methyl palmitate: (a) external view; (b) sample preparation area; (c) microscope for observing crystal habit

The microscope (see Figure 4.12 (c)) used for this observation is an Olympus BX51 with a digital imaging capability. The specifications of the microscope are shown below:

- centering telescope for phase contrast diameter 30mm;
- 360° rotatable analyzer slider (U-AN360-3);
- polarizer slider for reflected light illuminator with U-AN360-3 connection parts;

- 5 megapixel colorview IIIu digital camera with analysis docu software and imaging workstation. The objective lenses used are 10x and 20x magnification.

Methyl stearate and methyl palmitate were dissolved in toluene, methyl oleate and dodecane. The concentrations of solutions were from 5% to 50%. The temperature was decreased from 10°C to -10°C at the cooling rate of 1°C. The crystals of methyl stearate or methyl palmitate were crystallized with the decrease of temperature, and the crystals were taken from the bottle to the cell, placed on the microscope and examined.

4.3.2 Computational methods

4.3.2.1 Morphological prediction

The simulation of crystal morphology from first principles data is a routine procedure (Figure 4.13) involving the use of several computer programs. The program HABIT98 [15] employs of a structural description of the crystal that makes use of the atom-atom approximation method to determine the interactions between molecules within the crystal. The program uses atomic-coordinate information to build up a three dimensional model of the molecular crystal by applying a list of symmetry operators from the appropriate space group. The atomic coordinates of the crystal which have been minimized can be obtained from constructing the molecule using Materials Studio [132]. The molecular geometry obtained from crystallographic data can be used to calculate the partial atomic charges using the semi-empirical quantum mechanics program MOPAC [133]. A number of faces which are most likely to be dominant in the crystal morphology was selected using the software Materials Studio [132] based on the geometrical BFDH principle [134] which states that the larger the inter-planar spacing d_{hkl}, the more morphologically important the crystal (hkl) face will be. The lattice energy (E_{latt}) was calculated from the 3D periodic model of the crystal structure by atom-atom summation of the interactions between a central molecule and all the surrounding molecules out to a distance where the intermolecular interactions become negligible using a particular force-field function. Given that there were n atoms in the central molecule and n′ atoms in each of the N surrounding molecules then the crystal lattice energy (E_{cr})was calculated using the expression [135]:

$$E_{cr} = \frac{1}{2}\sum_{k=1}^{N}\sum_{i=1}^{n}\sum_{j=1}^{n'} V_{kij} \tag{4-1}$$

where V_{kij} is the interaction energy between atom i within the central molecule and atom j in the kth surrounding molecule. The interaction energy between two non-bond atoms i and j was calculated through the atom-atom method using a number of intermolecular potential functions such as the Lennard-Jones 6-12 potential.

$$V_{ij} = -\frac{A}{r_{ij}^{6}} + \frac{B}{r_{ij}^{12}} + \frac{q_i q_j}{D r_{ij}} \tag{4-2}$$

where A and B are parameters specific to particular atom-atom interaction, q_i and q_j are the fractional charges on atom i and j separated by distance r and D is the dielectric constant. The potential function of Momany was chosen [136] because it is suitable for the calculation of lattice energy of hydrocarbons, carboxylic acids, amines and amides.

The atom-atom method used considered each interaction to be a sum of constituent atom-atom interactions. The applicability of the potential function for the particular system studied was tested through comparison of the calculated value of E_{cr} with the experimental lattice energy calculated from the enthalpy of sublimation and given by:

$$V_{\exp} = \Delta H_{sub} - 2RT \tag{4-3}$$

where $V_{\exp}$ represents the experimental lattice energy, ΔH_{sub} is the enthalpy of sublimation and 2RT represents a correction factor for the difference between the gas phase enthalpy and the vibrational contribution to the crystal enthalpy.

The attachment energy (E_{att}) is related to the E_{cr} through the slice energy (E_{sl}) which is the energy released upon the formation of a slice of thickness d_{hkl}. The relative (hkl) surface growth rate was predicted from the assumption the slowest growing face was the one with lowest attachment energy. The resulting predicted crystal morphology was simulated using the Wulff classical polar plot by assuming the growth rate is directly proportional to the attachment energies.

$$E_{cr} = E_{att} + E_{sl} \tag{4-4}$$

$$R \propto E_{att} \tag{4-5}$$

The slice and attachment energies were calculated using HABIT98 [15] by summing pair-wise the potential energy involved in the intermolecular interactions between a central molecule and all molecules within and outside the slice, respectively, a slice of thickness d_{hkl}, as shown in Figure 4.14.

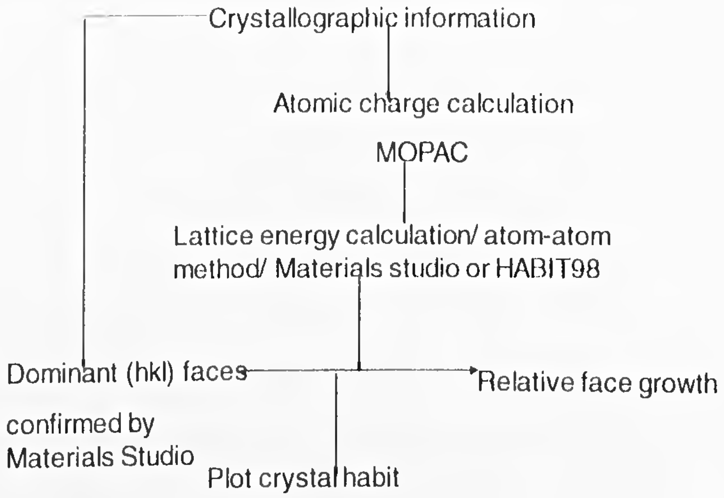

Figure 4.13: The procedure describing the formalism associated with the crystal morphology prediction from basic crystallographic principles.

These calculations have been successfully used to predict the crystal morphology of a wide range of organic crystals revealing reliable correlation between observed and simulated crystal shape [128, 137, 138].

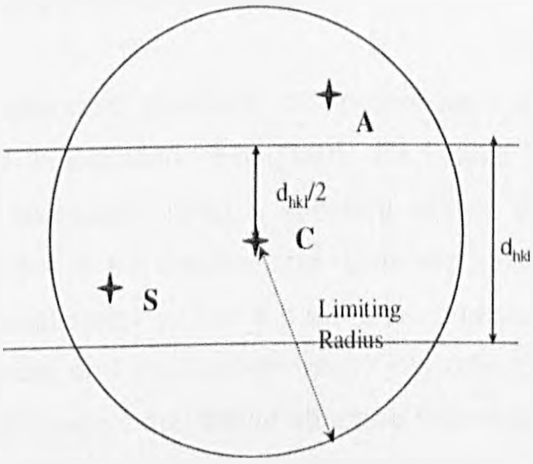

Figure 4.14: Schematic diagram showing how the lattice energy can be partitioned between the slice and the attachment energies within a limiting spherical zone: C is the central molecule, A is a molecule outside the slice and S is a molecule inside the slice [128, 137, 138].

4.3.2.2 Molecular cluster modelling

The early stages of the crystal growth process were modelled using crystal cluster calculations. The methodology used is summarized in Figure 4.15. Molecular clusters for pure naphthalene, biphenyl, naphthalene doped in biphenyl and biphenyl doped in naphthalene can be constructed and analyzed using this approach. One molecule of biphenyl was substituted for a molecule of naphthalene at the centre of the molecular cluster using INTERCHEM [139], then molecular clusters of naphthalene doped by biphenyl were constructed. The molecular clusters of biphenyl doped by naphthalene were constructed as the same procedure with the creating of molecular clusters of naphthalene doped by biphenyl.

The modelling was based on the assumptions below:

- Inter-molecular and intra-molecular geometry optimization molecules, clusters can be modelled using empirical force fields and the atom-atom method based on in-vacuo simulations at 0K.
- The shape of the molecular clusters can be assumed to be as the spherical clusters.
- Solution environmental effects are ignored.

Spherical molecular clusters of different sizes were constructed using HABIT 98 [15] and the optimized structures of clusters were created using the Materials Studio [132] molecular modelling software.

The original and optimized structures of clusters were used to calculate an Rwp parameter defined in Equation (4-6) [140], the values of Rwp as a function of cluster size were calculated using a specially written visual Basic in Excel into which the coordinates of the original and optimized clusters were imported. Rwp originated from crystallography, and it is a measure of the agreement between the crystallographic model and the experimental X-ray diffraction data. In this study, it is used to assess the extent the cluster structure has change after optimizationThe R_{wp} parameter calculated as a function of the number of step-shifts calculated using a specially written visual Basic in Excel from the centre of the molecular clusters was used to model the change of the cluster's atomic coordinates from the original crystallographic positions.

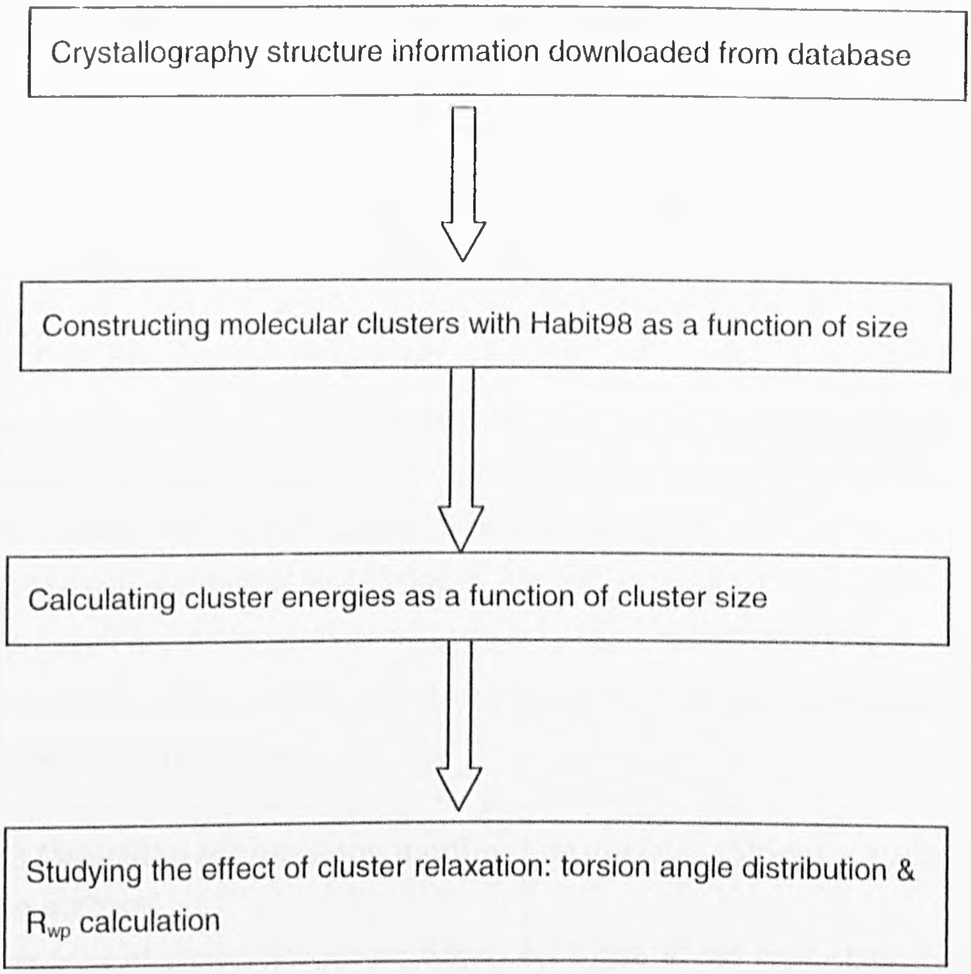

Figure 4.15: Schematic representation of the methodology for cluster modelling used.

$$R_{wp} = \sum_{i=1}^{N} \frac{1}{N} \sqrt{\left(x_i - x_i^{opt}\right)^2 + \left(y_i - y_i^{opt}\right)^2 + \left(z_i - z_i^{opt}\right)^2} \tag{4-6}$$

where x,y and z are the coordinates of all cluster atoms, N is the number of atoms, the optimized atomic coordinates are marked with superscript 'opt'. The R_{wp} parameter was expected to be close to zero for structures which did not undergo a significant change in terms of atomic position when optimized This change reflects the degree of the return of the perturbed system into equilibrium, so this parameter can be used as a measure of the crystallinity for the structure of the relaxed cluster and can be related to the ability of the system to crystallize. . It is well understood, at least intuitively, that the change after optimization will not be homogeneous in the entire cluster structure, especially for lager cluster sizes. The bulk of the structure will most probably behave differently from the surface layer and the latter, of course, will differ depending on the cluster size. The results from the calculations can be used to assess the ease or otherwise of the crystallization process.

For conformational flexible molecules the degree of conformational disorder was also assessed through the calculation of variance parameter defined in Equation (4-7) and given below:

$$VAR = \frac{\sum_{i=1}^{N}\left(T_i - T_{crystal}\right)}{N-1} \tag{4-7}$$

where T_i is the torsion angle within the cluster, $T_{crystal}$ the torsion angle of a molecule within the bulk of the crystal structure, N is the number of molecules in the cluster. A higher value of the VAR parameter means a higher degree of disorder within the relaxed cluster. The coordinate of each atom within the optmized molecular cluster was imported into the Excel, then each of the torsion angles T_i corresponding to individual molecule was calculated using a specially written visual Basic program in Excel according to the atomic coordinates of the molecules within the clusters.

4.3.2.3 Modelling morphology modified by solvent using the systematic search method

The influence of growth solvent on crystal habit due to the interactions between solute and solvent at surfaces of the crystals was predicted using systematic (grid-based) search method [78, 141], as shown in Figure 4.16. The overall approach involves the modelling of heterospecies binding on 2-D crystal habit surfaces related to solvent binding. The interaction energy of different solvent molecule types on the crystal surfaces associated with crystal grown form solution was calculated using the method developed for the prediction of solvent-mediated growth morphology [142] study a computer program developed by Hammond [17] was used to assess In this, the competitive interaction between the methyl stearate solute and various growth solvent was predicted and the solvent-mediated growth morphologies calculated.

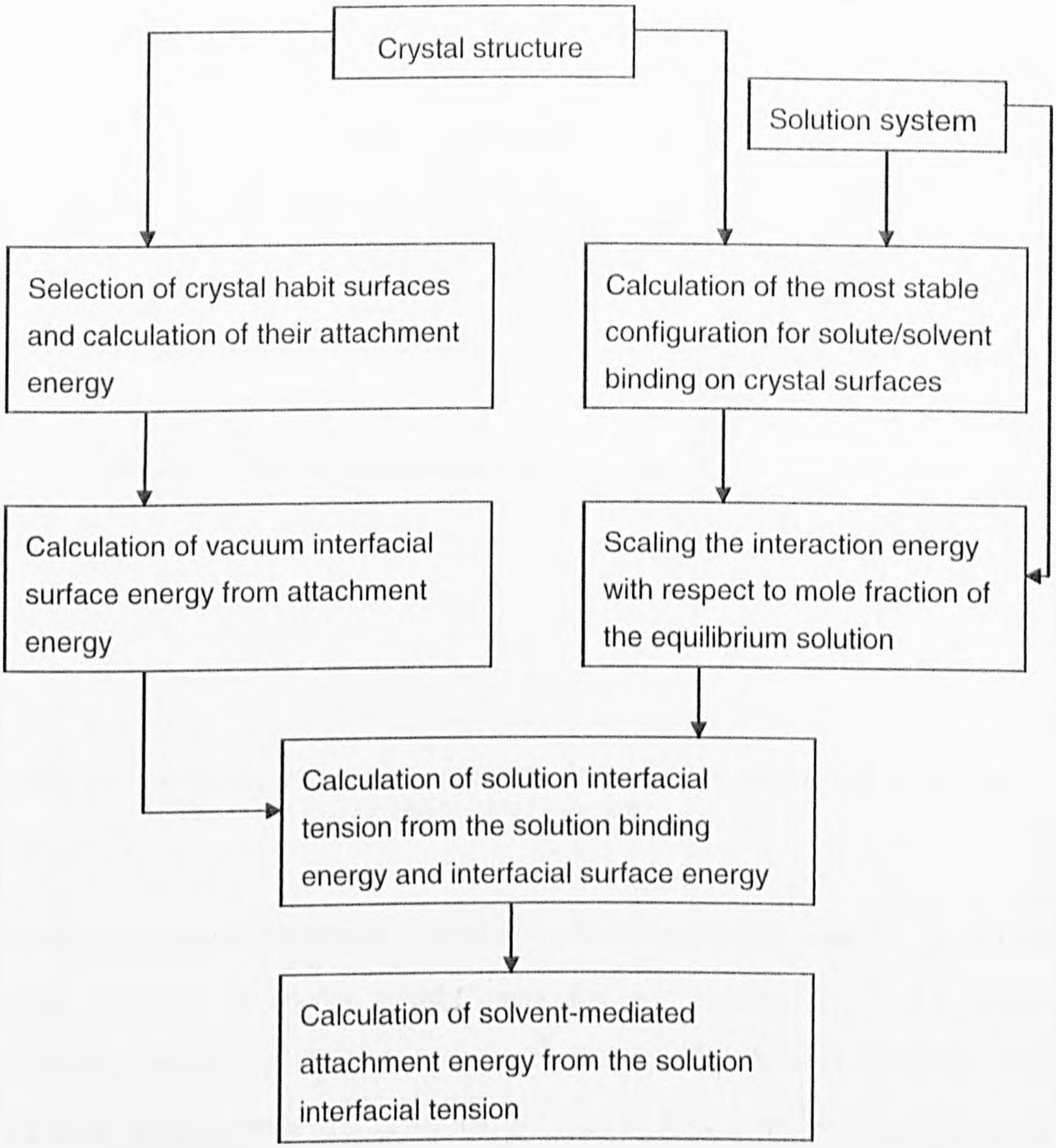

Figure 4.16: Schematic diagram summarizing the overall approach used to calculate specific surface energies of crystal surface in the presence of solution.

In this approach, a selected crystal surface was cleaved from the bulk crystallographic structure (see Figure 4.17), and then the solvent or host molecule was arranged in the position on the cleaved surfaces, and translated in two dimensions, with a step size equal to 1.0Å for both the host molecule and solvent molecules and oriented by rotation about principal axes with an angular step size of 20°. Then the binding energies of the solute and solvent molecule to the selected surfaces were calculated by treating the interfacial probe molecules (either a methyl stearate solute molecule or toluene/dodecane solvent molecule). There are two in-plane translations in the cleaved surface and a third translation perpendicular to the cleaved surface. For the two in-plane translations the step size is selected in fractional coordinates. For the translation perpendicular to the surface the translation step is specified in angstrom units.

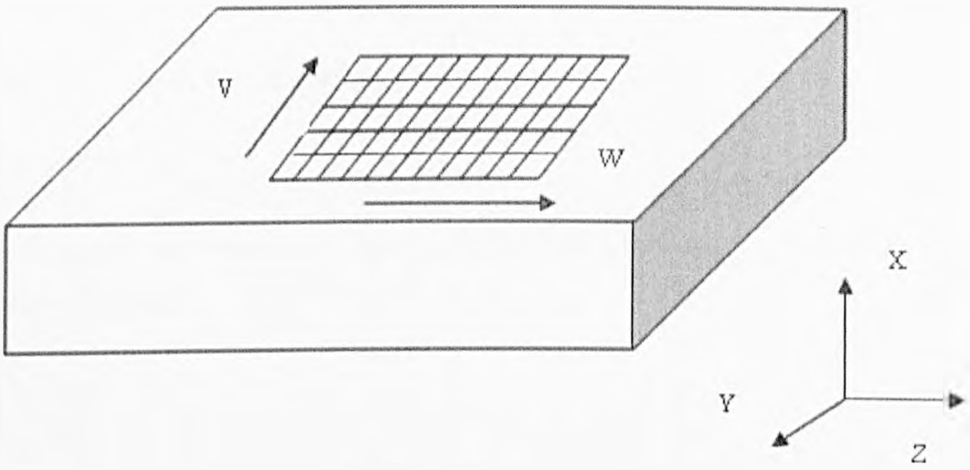

Figure 4.17: Schematic diagram presenting initial step of system search method, cleaving surface from bulk crystallographic structure.

Finally, the specific interaction energies of solvent for per unit area, $U_{solvent}$, for the probe dodecane or toluene solvent molecules, and similarly, U_{solute}, the specific interaction energies of solute for the probe solute molecule were calculated from the most stable energies ($\overline{U}_{solvent}$) and ($\overline{U}_{solute}$) derived from the output file of the systemmatic search method using equation (4-8):

$$U_{solvent} = \frac{Z_R^{hkl} U_{solvent}}{S_R^{hkl} N_A} \quad \text{where } S_R^{hkl} = \frac{V_{cell}}{d_{hkl}} \qquad (4\text{-}8)$$

In this, Z_R^{hkl} is the number of solvent molecules per reticular area, V_{cell} is the volume of the unit cell, d_{hkl} is the d spacing and N_A is Avogadro's number.

These two specific surface energies were used to calculate the total interaction energies for the solutions using Equation (4-9) together with the mole fraction (n) of each component in the system:

$$U_{solution} = n_s U_{solvent} + n_h U_{solute} \tag{4-9}$$

The final solution binding energy ($U_{solution}$) for each face was used to reduce the vacuum specific surface energy (γ_{hkl}^{vacuum}), and then the crystal/solution interfacial energies, $\gamma_{hkl}^{solution}$, was calculated via

$$\gamma_{hkl}^{solution} = \gamma_{hkl}^{vacuum} - U_{solution} \tag{4-10}$$

Numerical values of surface energies can be estimated using attachment energy calculations [73] thus,

$$\gamma = \frac{ZE_{att} d_{hkl}}{2V_{cell} N_A} \tag{4-11}$$

So the attachment energy ($E_{att}^{solution}$) modified by solvent can be derived,

$$E_{att}^{solution} = E_{att}^{vacuum} - \frac{2V_{cell} N_A}{Zd_{hkl}} U_{solution} = E_{att}^{vacuum} - \frac{2Z_R^{hkl}}{Z} \overline{U}_{solution} \tag{4-12}$$

In this equation, Z is the number of solute molecules in the unit cell. The modified attachment energy can be used to predict the solution-mediated crystal growth morphology.

4.4 Conclusions

This chapter provides a general description of the crystal and molecular structures of the materials used in this PhD thesis. The chapter summaries all the experimental and computational methods used in the work. The experimental crystallization kinetic studies involved both slow and crash-cool runs resulting in the determination of the MSZW, induction time and critical nucleus size. The methodologies for observing the crystal habit of methyl stearate and methyl palmitate are also described. The basic computational method for crystal morphology prediction using attachment energy method is summarized here together with the simulation method of molecular clusters for studying the structural stability and variability. Finally, details about the systematic search method for investigating of solvent-mediated effects on crystal morphology are presented.

CHAPTER 5

Development and Validation of a New Molecular Modelling Methodology for Predicting the Influence of Additives on Nucleation and on the Early Stages of Crystal Growth

Summary:

This chapter describes a development and validation of a novel methodology for predicting the influence of additives on the nucleation and early stages of crystal growth for naphthalene, biphenyl, naphthalene with biphenyl and biphenyl with naphthalene, involving the examination of structural stability and variance.

5.1 Introduction

In this chapter a methodology to predict the influence of additives on nucleation and early stages of crystal growth was described. This has been validated against experimental studies on the crystallization of a model system: naphthalene, biphenyl and the when in the presence of each other as impurity synthesis. This section of the work programme is designed to address the following issues: to validate molecular cluster modelling work using naphthalene and biphenyl as model materials and to investigate the relationship between the change of atomic positions and MSZW for pure solute and solute doped by additives.

In this work, two well-known bicyclic aromatic compounds: naphthalene and biphenyl are used as model materials to test the simulation work and the measurements of nucleation and dissolution temperatures of naphthalene and biphenyl are used to validate the cluster modelling work.

5.2 Modelling Studies

5.2.1 Molecular modelling of pure naphthalene and naphthalene in the presence of biphenyl

5.2.1.1 Structural analysis and morphological prediction of naphthalene

The configurations from Figure 4.6 shows that the molecule of naphthalene is rigid due to no torsion within the molecule of naphthalene. So the conformation did not change after energy minimization, with the lowest total energy of the naphthalene molecule shown in Figure 5.1.

The result of crystal lattice energy, -19.89kcal mol^{-1}, calculated using HABIT98 was consistent with calculated lattice energy -19.4kcal mol^{-1}, from the literature [129]. The morphology simulated was the same as the predicted morphology which has been published [129]. It was found that (001) is the dominant face. The results of slice energy and attachment energy corresponding to different important faces were shown in Table 5.1, and the predicted shape of naphthalene was presented in Figure 5.2.

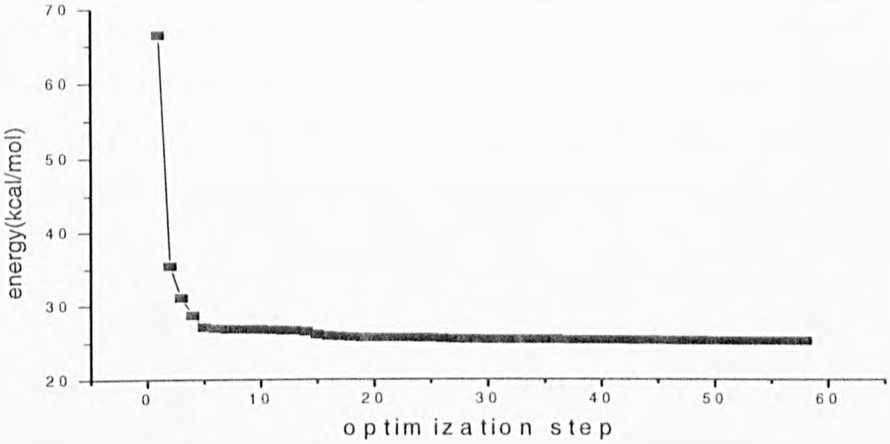

Figure 5.1: Energy minimization using the module of geometry optimization in Material Studio

Table 5.1 Slice energy and attachment energy for the important habit faces of naphthalene based on attachment energy calculations

Face	d_{hkl} (Å)	Slice energy (kcal mol^{-1})	Attachment energy (kcal mol^{-1})
(0 0 1)	7.14	-13.93	-5.96
(1 1 -1)	4.63	-7.29	-12.60
(1 1 0)	4.44	-7.80	-12.09
(2 0 -1)	4.02	-6.90	-12.99

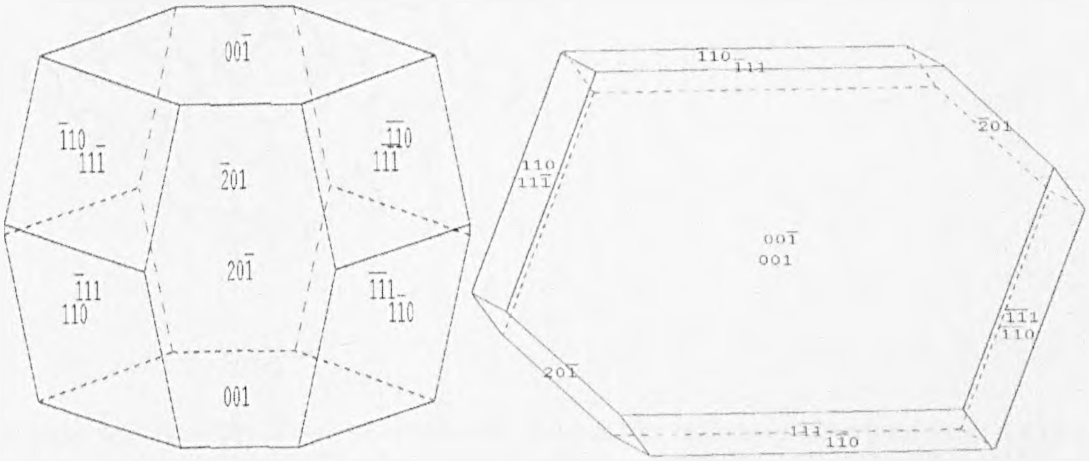

Figure 5.2: Different projections of predicted morphology of naphthalene based on attachment energy calculations

5.2.1.2 Cluster construction and calculation of R_{wp}

Molecular clusters of naphthalene and naphthalene with biphenyl constructed as a function of cluster size using HABIT98 [15] based on the approach shown in Figure 4.15, the molecular packings in three different sized clusters are shown in Figures 5.3 and 5.4. The clusters were constructed with the increasing radius from the central molecule, so the clusters are approximately spherical, and the molecular cluster size is expressed as the number of molecules within the cluster.

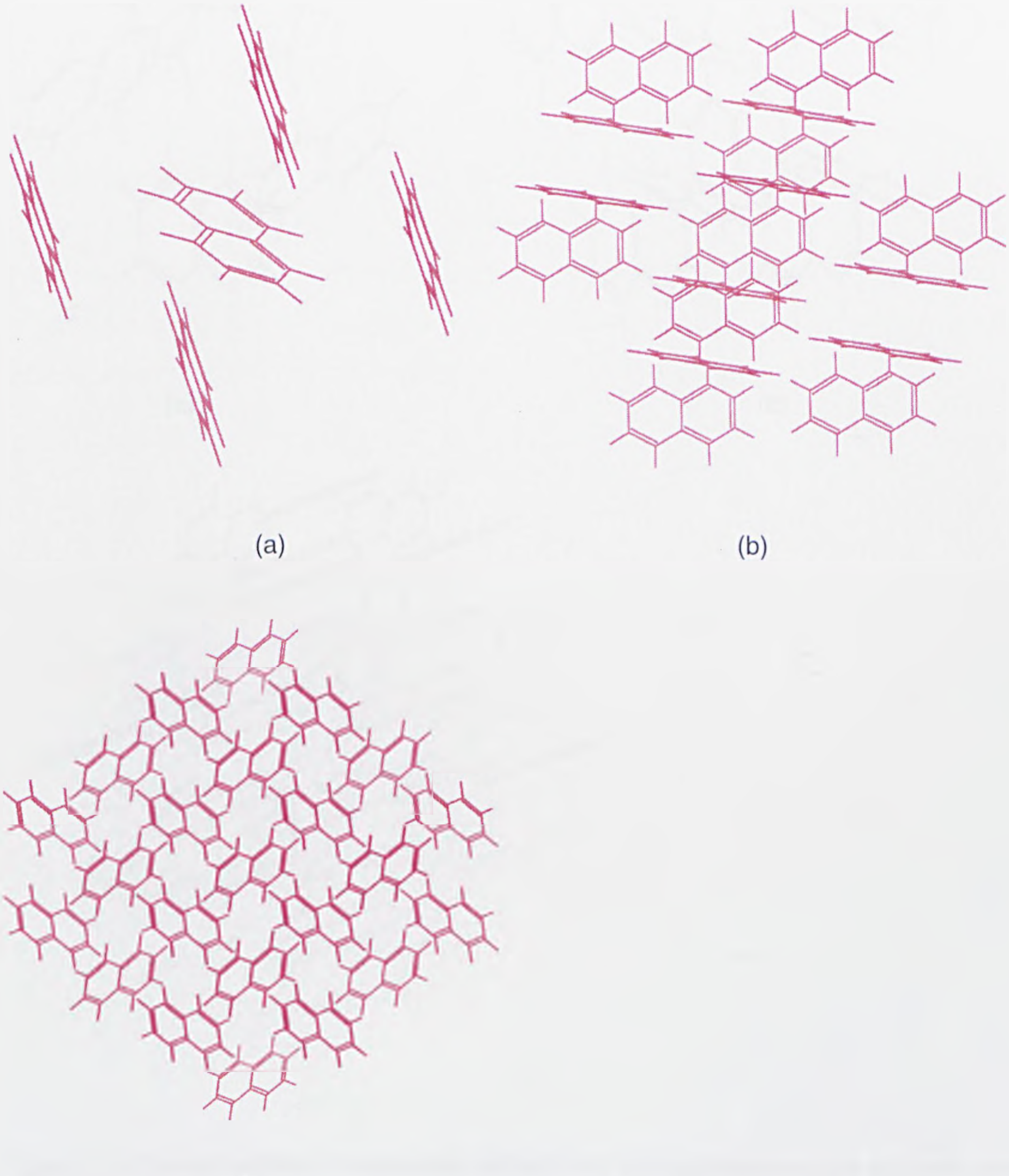

(a) (b)

(c)

Figure 5.3: Conformations of molecular clusters for: (a) pure naphthalene containing 5 molecules; (b) pure naphthalene containing 17 molecules; (C) pure naphthalene containing 57 molecules;

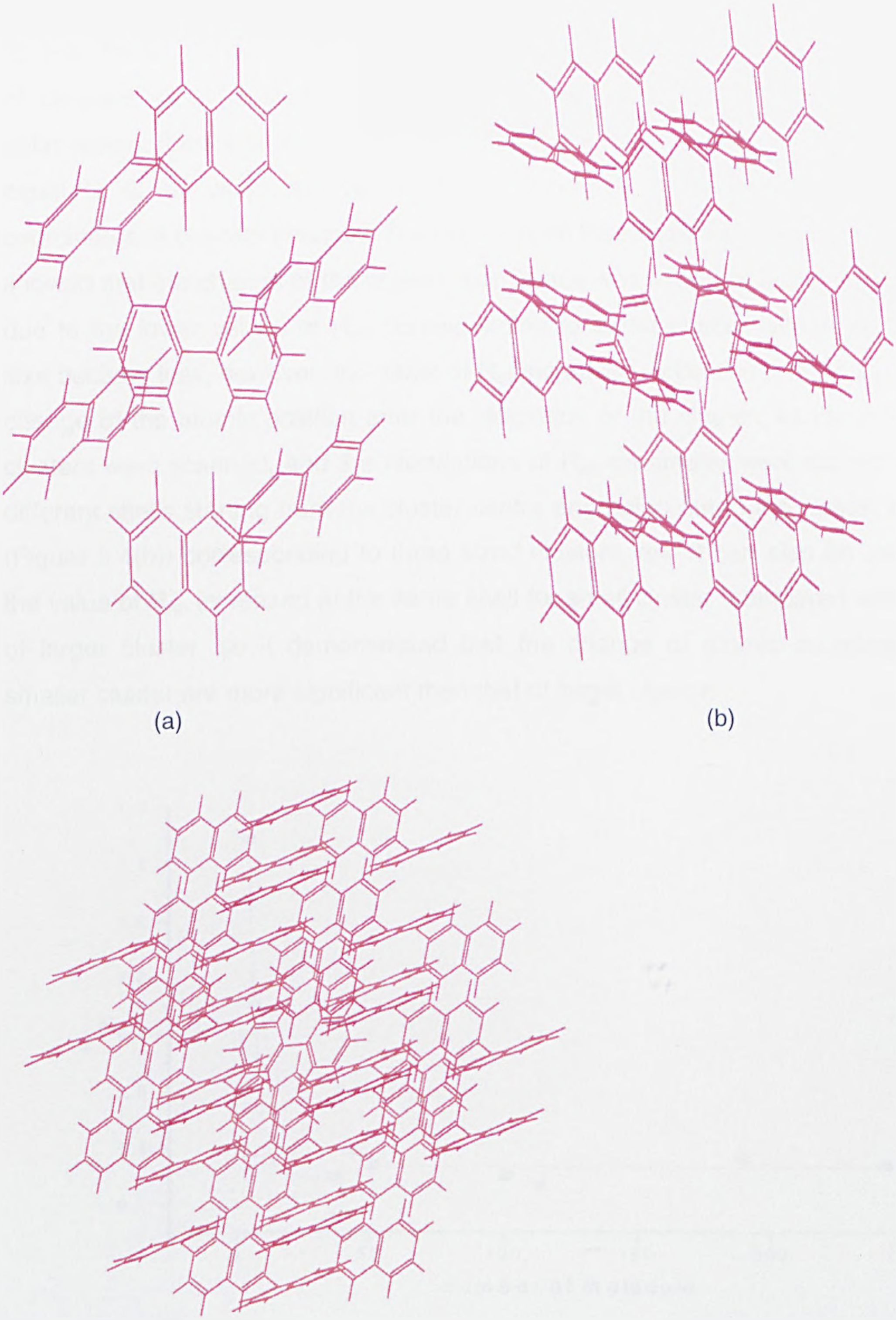

(a)

(b)

(c)

Figure 5.4: Conformations of molecular clusters for: (a) naphthalene with biphenyl in the centre of the cluster containing 5 molecules; (b) naphthalene with biphenyl in the centre of the cluster containing 17 molecules; (c) naphthalene with biphenyl in the centre of the cluster containing 45 molecules.

An R_{wp} parameter was calculated using Equation (4-7). This parameter reveals how far from the original crystallographic positions the coordinates of the cluster atoms of different sized clusters of naphthalene have moved after cluster geometry optimization. If there is no change in the atomic coordinates, the value of R_{wp} will be equal to 0, so when the value of R_{wp} increases, it means that the atomic coordinates of clusters change. The results from these calculations (Figure 5.4 (a)) showed that the change of the atomic coordinates was minor for large cluster sizes due to the lower values of R_{wp} corresponding to larger cluster. When the cluster size became less, however, the value of R_{wp} increased, reflecting a more significant change of the atomic position after the relaxation of the cluster. All the molecular clusters were scanned, and the calculations of R_{wp} parameter were carried out for different shells starting from the cluster centre and going out to the cluster surface (Figure 5.4(b)) corresponding to three sized clusters, and it can also be seen that the value of R_{wp} increased at the same shell for small cluster compared with those of larger cluster, so it demonstrated that the change of atomic coordinates for smaller cluster are more significant than that of larger cluster.

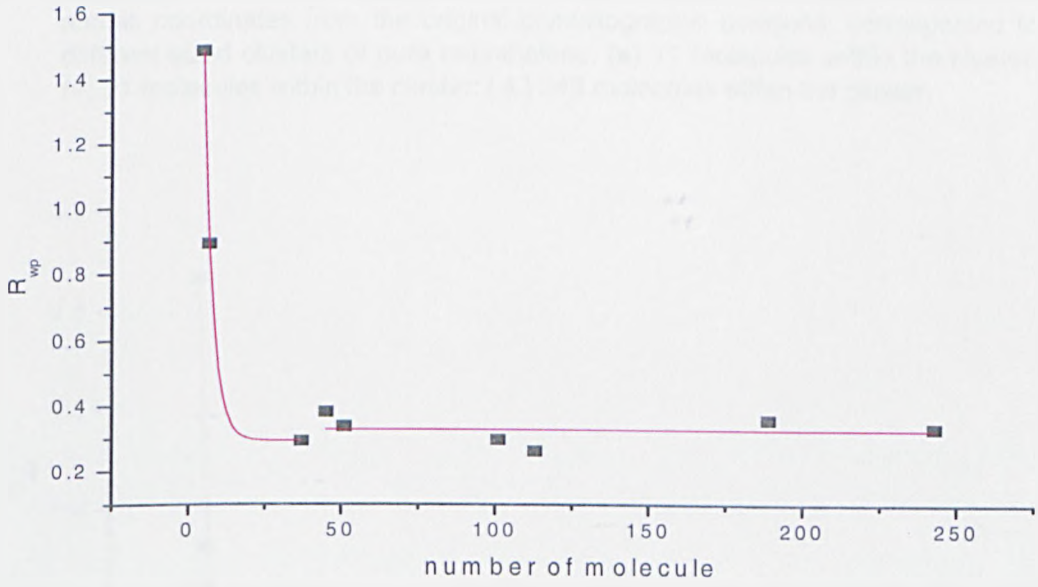

(a)

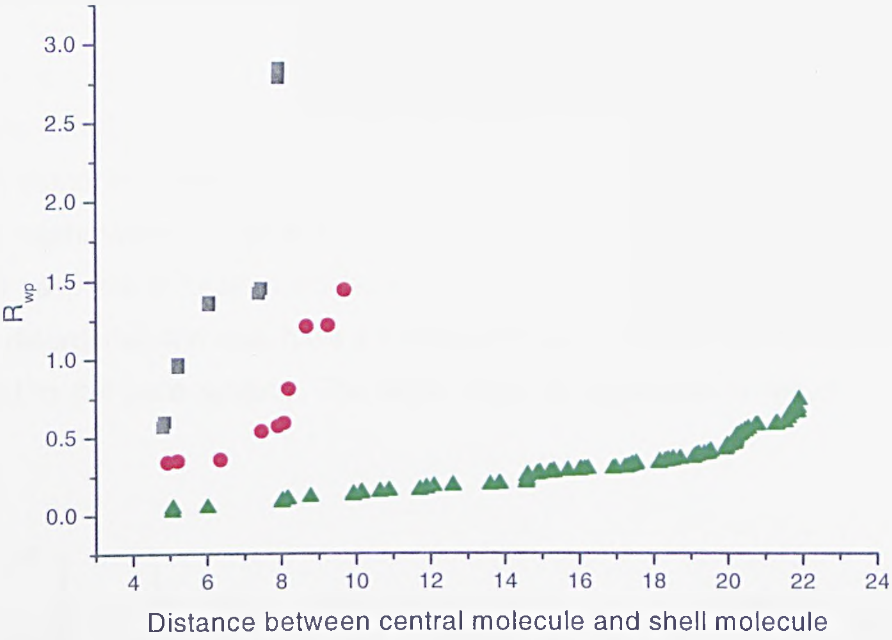

(b)

Figure 5.5: R_{wp} parameter, calculated as a function of cluster size (a), and of the number of step-shifts from the molecular cluster centre (b) reflects the change of the cluster atomic coordinates from the original crystallographic positions, corresponind to different sized clusters of pure naphthalene: (■) 11 molecules within the cluster; (●) 21 molecules within the cluster; (▲) 243 molecules within the cluster.

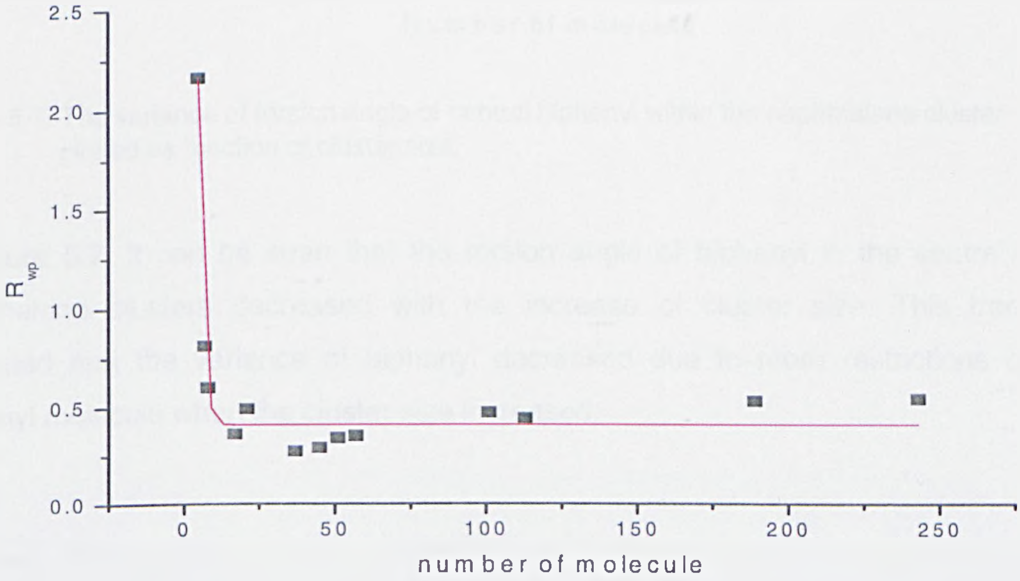

Figure 5.6: Rwp parameter, calculated as a function of cluster size reflects the change of the cluster atomic coordinates from the original crystallographic positions for naphthalene doped by biphenyl.

The value of an R_{wp} parameter is calculated to evaluate the change of atomic coordinates after the addition of biphenyl compared with a pure naphthalene cluster of the same size. The trend of the R_{wp} parameter of naphthalene with biphenyl decreased with the increase of cluster size, the same with that of pure naphthalene and pure biphenyl shown in Figure 5.6, and the values are larger than the results for pure naphthalene clusters through the comparison of R_{wp} corresponding to values of base line in Figures 5.5 (a) and 5.6. This indicates that the doped system is more disordered and may have a higher energetic barrier to crystallization when compared to the pure system. The latter might be expected to result in a higher MSZW.

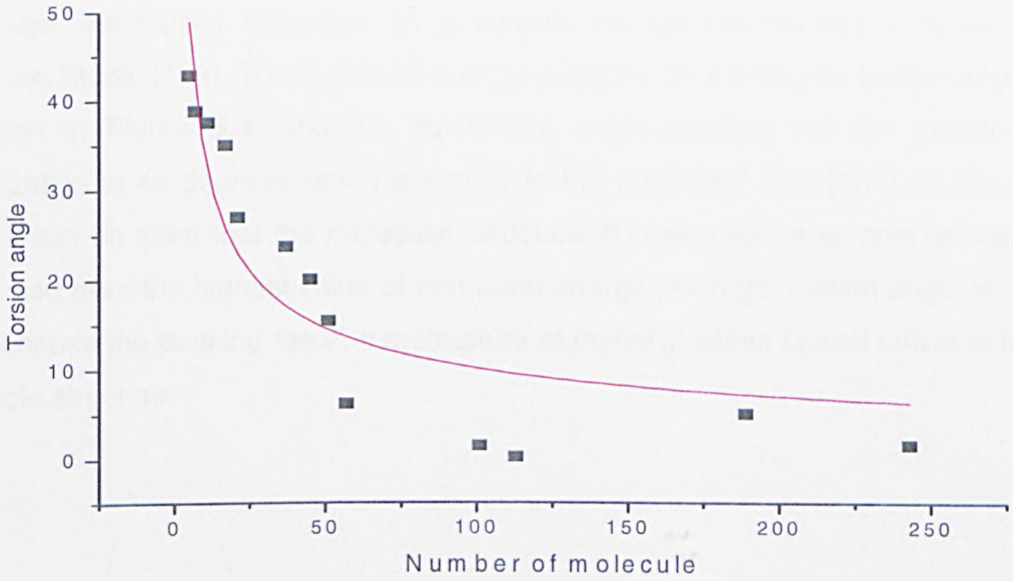

Figure 5.7: The variance of torsion angle of central biphenyl within the naphthalene cluster plotted as function of cluster size.

In Figure 5.7, it can be seen that the torsion angle of biphenyl in the centre of naphthalene clusters decreased with the increase of cluster size. This trend illustrated that the variance of biphenyl decreased due to more restrictions on biphenyl molecule when the cluster size increased.

5.2.2 Molecular modelling of pure biphenyl and biphenyl in the presence of naphthalene

5.2.2.1 Structural analysis and morphological prediction of biphenyl

Biphenyl is known as a flexible molecule due to the torsion angle within the molecule, and from Figure 5.8, it can be seen that the torsion angle changed from 0.113° to 47.522 °after the geometry optimization in which the total energy of the molecule decreased to its lowest value (see Figure 5.8). It demonstrated that the deformation happens when the geometry is changing, so the molecule of biphenyl is definitely flexible. The torsion angle was varied from -180 to 180 degrees with a step-size of 10 degrees and the torsion energy was calculated using the Dreiding molecular mechanics force-field in a module named Conformers program in Materials Studio [132]. The non-bond energy is highest at a 0 degree torsion angle, as seen in Figure 5.9, and the equilibrium angle carrying out the geometry optimization is 44 degrees which is similar to the published data [131]. In Figure 5.10, it can be seen that the molecular structure in crystal lattice is most unstable confirmed from the highest value of non-bond energy when the torsion angle is 0°. But because the packing force, the structure of biphenyl within crystal lattice is the unstable structure.

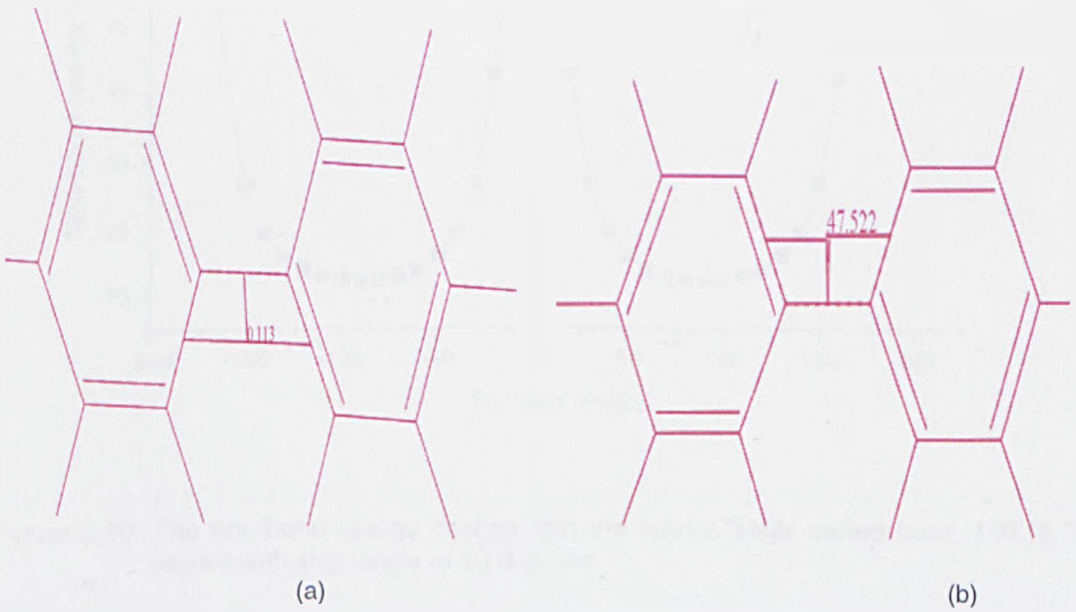

(a) (b)

Figure 5.8: Distance between hydrogen atoms in the molecule of biphenyl calculated with Material studio, (a) original molecule; (b) molecule after geometry optimization

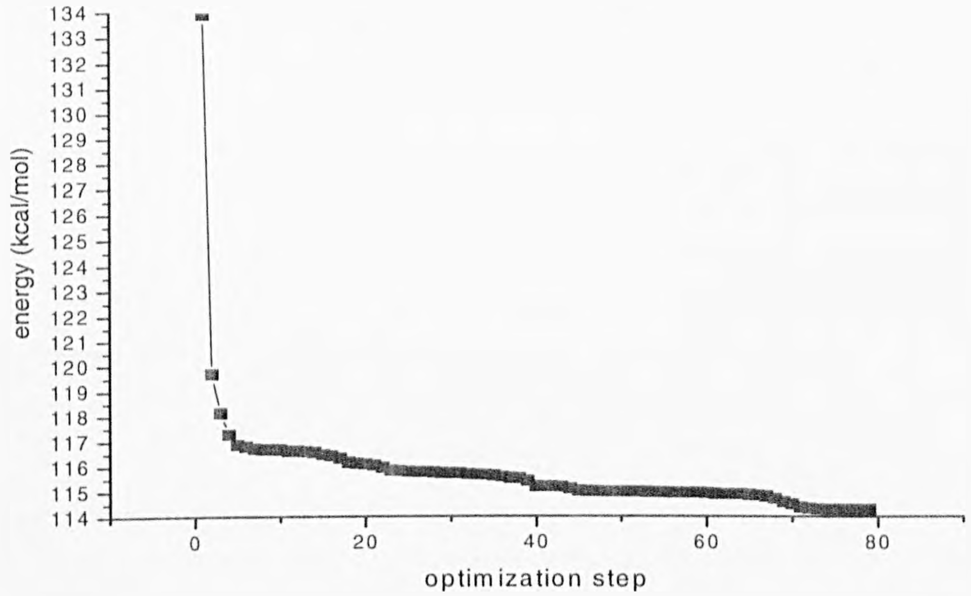

Figure 5.9: Energy minimization using the module of geometry optimization

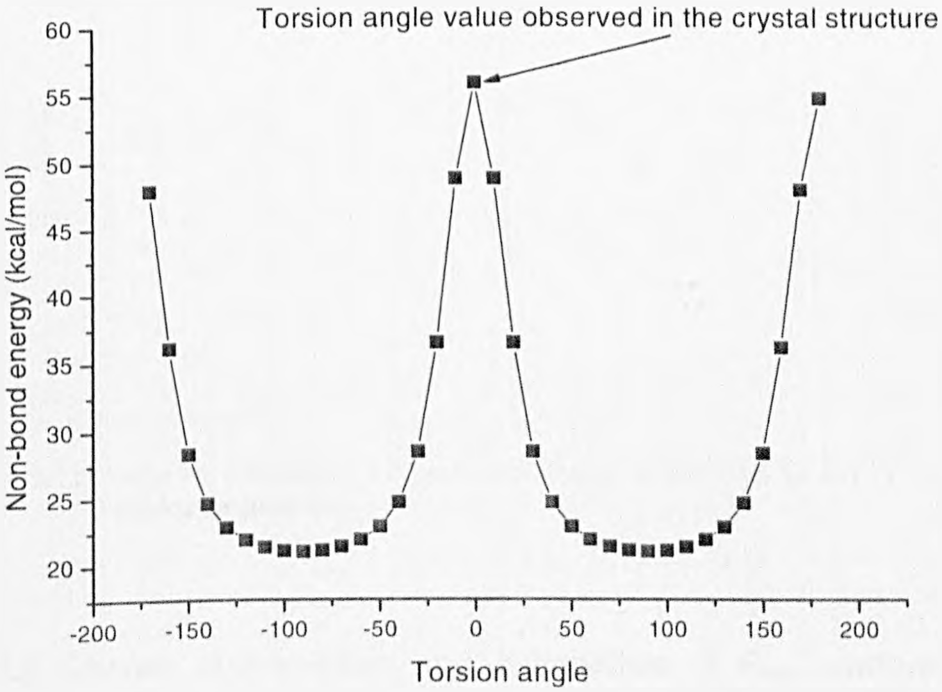

Figure 5.10: The non-bond energy change with the torsion angle varied from -180 to 180 degree with step-angle of 10 degrees.

The lattice energy of biphenyl, -19.31kcal mol^{-1}, calculated using Momany [136] force field parameters is very close to the values of experimental lattice energy, -20.7kcal mol^{-1}, from the literature reported [143]. The predicted crystal morphology using the attachment energy method revealed that (001) face with (110) face are the major side faces. These results are in agreement with the literature reporting predicted morphology and attachment energies [143].

Table 5.2 Slice energy and attachment energy for the important habit faces of biphenyl

Face	d_{hkl} (Å)	Slice energy (kcal/mol)	Attachment energy (kcal/mol)
(0 0 1)	9.43	-14.46	-4.85
(1 1 0)	4.63	-7.76	-11.55
(-1 1 1)	4.24	-6.48	-12.83
(2 0 0)	4.04	-5.71	-13.61
(-2 0 1)	3.85	-5.76	-13.55

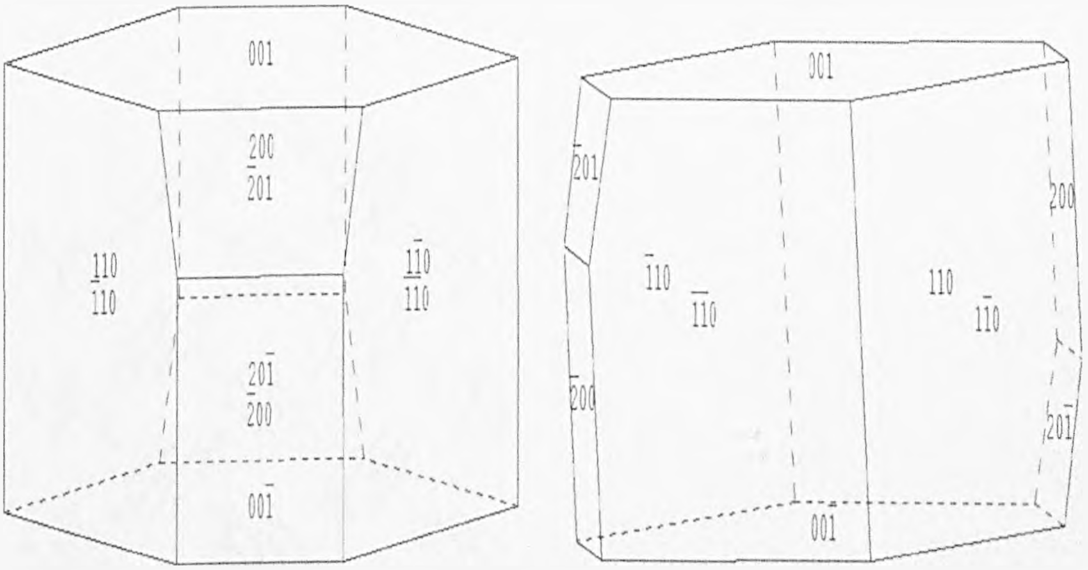

Figure 5.11: Different projections of predicted shape of biphenyl based on attachment energy calculations

5.2.2.2 Cluster construction and calculation of R_{wp} conformational variance

The molecular clusters of biphenyl and biphenyl doped by naphthalene constructed using HABIT98 as a function of cluster size, the molecular packings in three different sized clusters are shown in Figures 5.12 and 5.13.

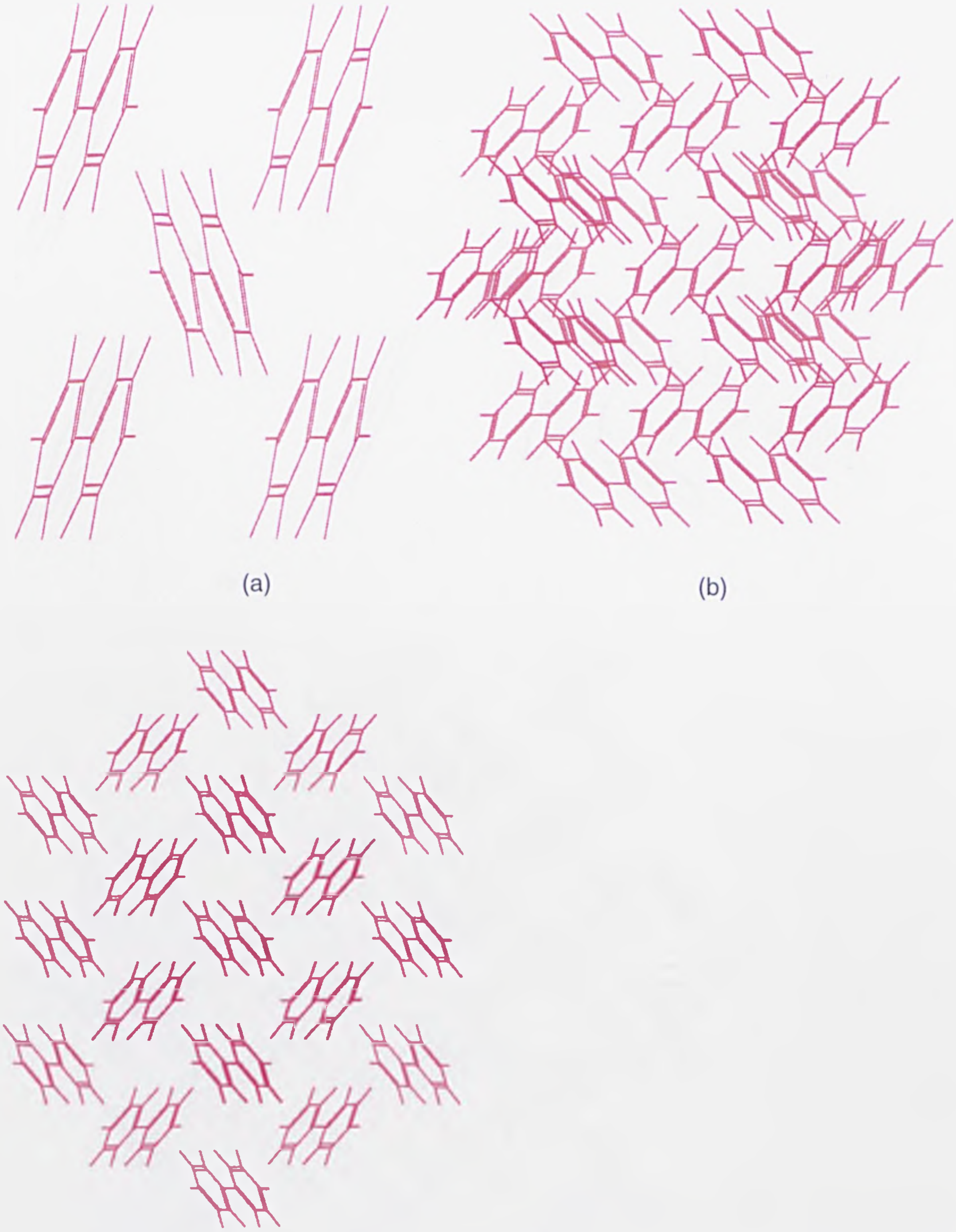

(a)

(b)

(c)

Figure 5.12: Conformations of molecular clusters for: (a) pure biphenyl containing 5 molecules; (b) pure biphenyl containing 23 molecules; (c) pure biphenyl containing 35 molecules.

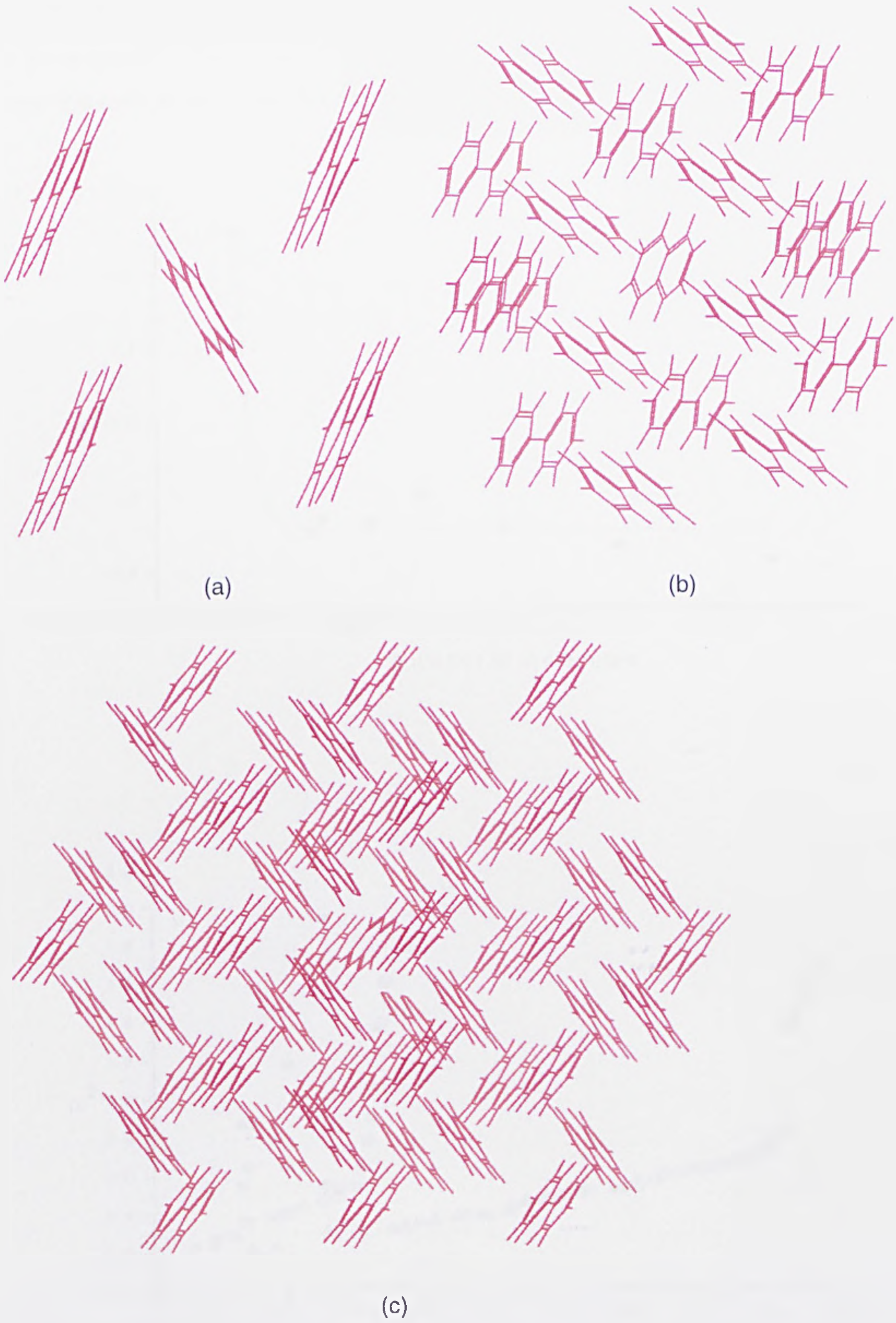

(a)

(b)

(c)

Figure 5.13: Conformations of molecular clusters for: (a) biphenyl with naphthalene in the centre of the cluster containing 5 molecules; (b) biphenyl with naphthalene in the centre of the cluster containing 23 molecules; (c) biphenyl with naphthalene in the centre of the cluster containing 57 molecules.

Compared with rigid molecules of naphthalene, biphenyl presented more significant change after relaxation through the comparison of the values of R_{wp} between pure naphthalene and biphenyl as illustrated by the higher base line variance compared to pure naphthalene; however the trend in the value of R_{wp} is similar to the results from the calculation of naphthalene.

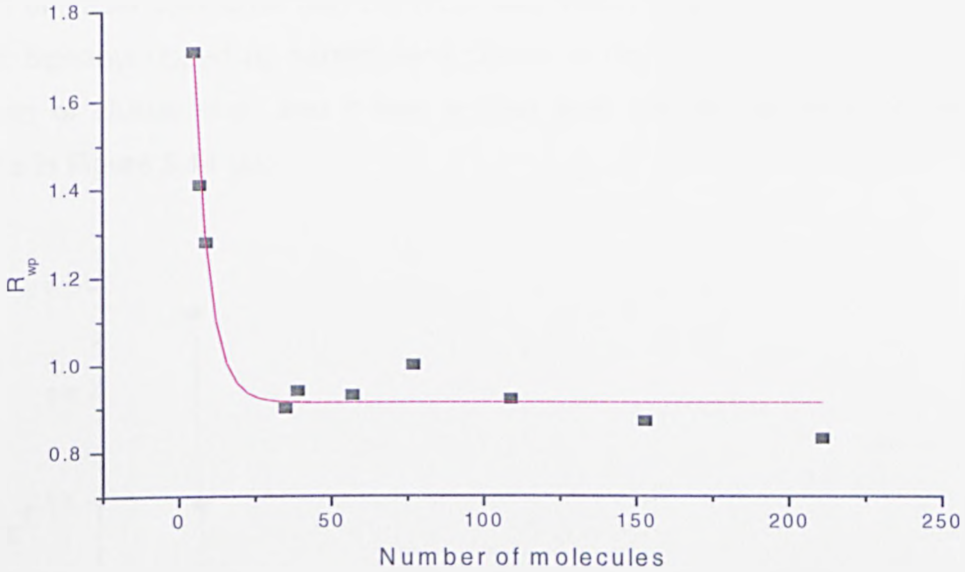

(a)

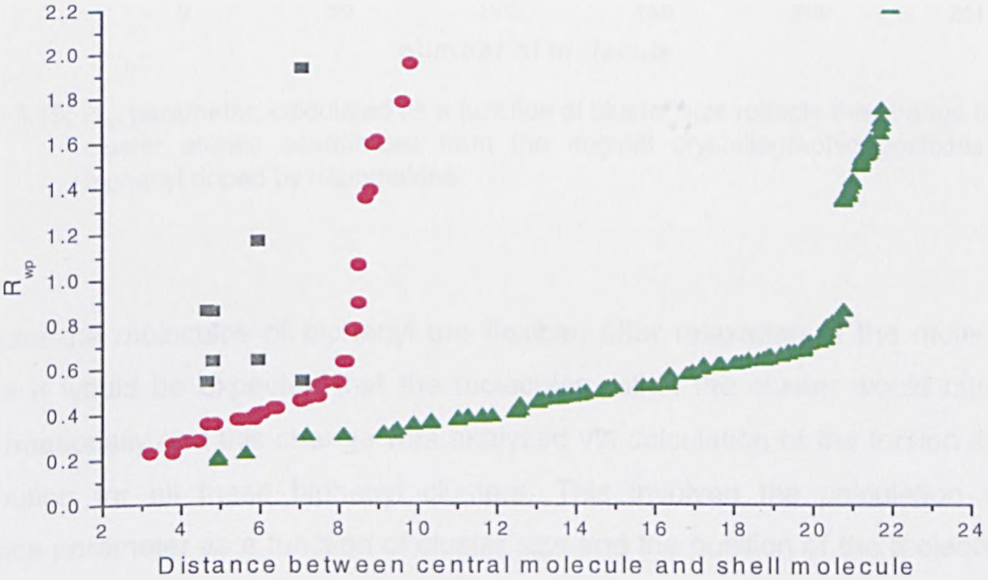

(b)

Figure 5.14: R_{wp} parameter, calculated as a function of cluster size (a), and of the number of step-shifts from the molecular cluster centre (b), reflects the change of the cluster atomic coordinates from the original crystallographic positions, corresponding to different sized clusters of pure biphenyl: (■) 9 molecules within the cluster; (●) 39 molecules within the cluster; (▲) 211 molecules within the cluster.

It can be found in Figure 5.14 (a) that the values of R_{wp} decreased with the increase of cluster size, and the values of R_{wp} at the same distance from central molecule for smaller cluster are larger compared with those of larger cluster shown in Figure 5.14 (b), so it was confirmed that the molecules within smaller cluster are always unstable compared with the molecules within larger cluster. The values of R_{wp} for biphenyl doped by naphthalene shown in Figure 5.15 decreased with the increase of cluster size, and it was smaller than the results for pure biphenyl clusters in Figure 5.14 (a).

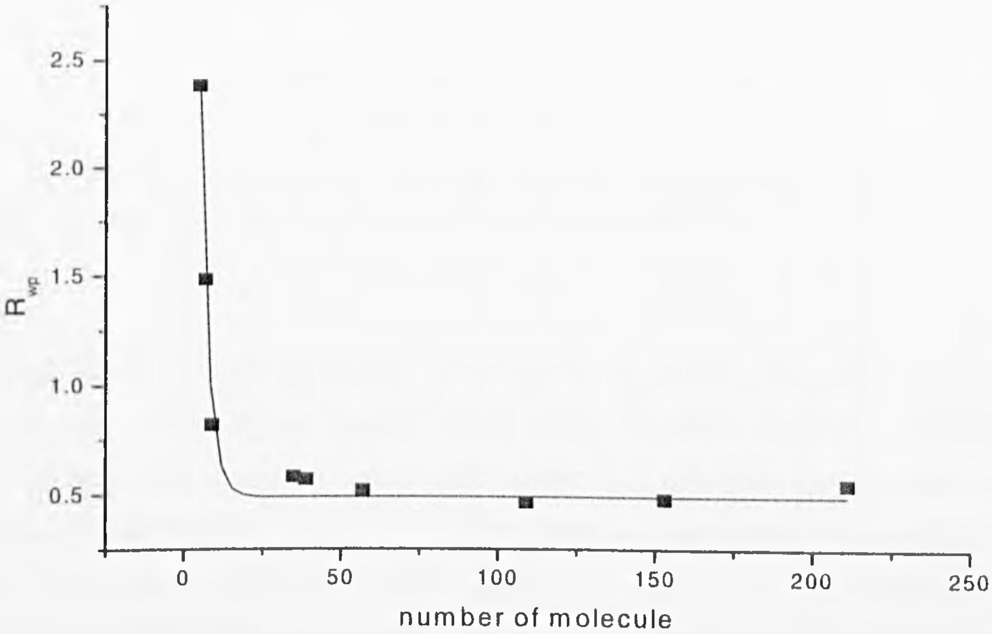

Figure 5.15: R_{wp} parameter, calculated as a function of cluster size reflects the change of the cluster atomic coordinates from the original crystallographic positions, for biphenyl doped by naphthalene.

Because the molecules of biphenyl are flexible, after relaxation of the molecular cluster it would be expected that the molecules within the cluster would change conformationally and this change was analyzed via calculation of the torsion angle distribution for all these biphenyl clusters. This involved the calculation of a variance parameter as a function of cluster size and the position of the molecule in the molecular cluster using Equation (4-7).

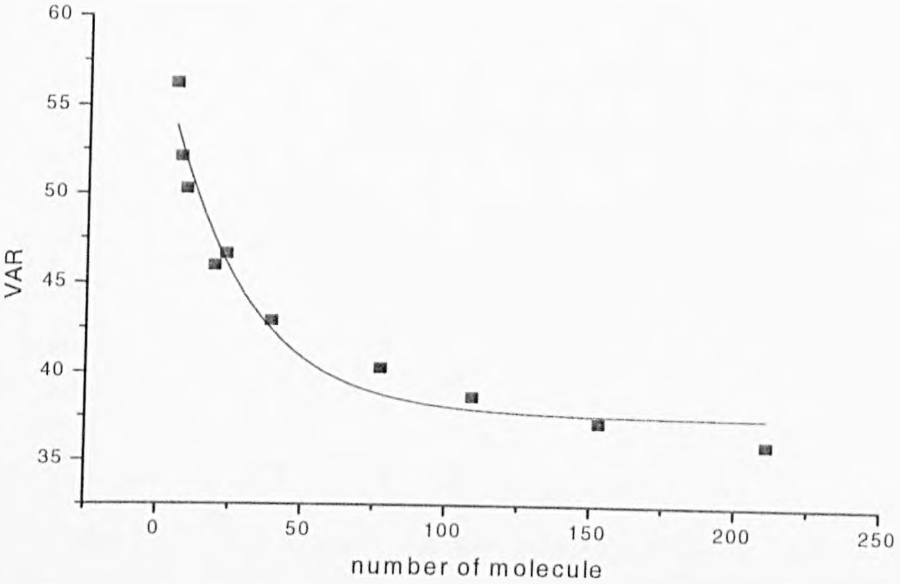

Figure 5.16: Torsion angle variance parameter within the molecular cluster of pure biphenyl correlated to cluster size calculated using Equation (4-7).

The conformational variance studied as a function of cluster size is shown in Figure 5.16, as expected, for bigger clusters the variation was less compared with smaller sized clusters. Because small cluster sizes allow for much more freedom within the molecular conformation as most of the molecules are exposed at the surface and hence, there are less inter-molecular bonds to restrain these molecules. The calculations revealed that when the cluster size increased, the cluster became less disordered, because the molecules dissolved in solution are more disordered than those in the crystal. Because the clusters are approximately spherical, so the average torsion angle at the same shell was plotted as a function of the radius of shell within one cluster shown in Figure 5.17. It can be seen that the torsion angle decreased when radius increased, because the interior of the cluster are restricted from moving freely due to the inter-molecular interactions holding the molecules together, and there was more freedom of molecule when the radius increased within one biphenyl cluster. It can also been that the average torsion angles of smaller cluster were larger than those of larger cluster at the same radius within the molecular clusters, and the torsion angle of biphenyl in crystal lattice is zero, so it reflected that the properties of cluster got close to those of real crystals when the size increased.

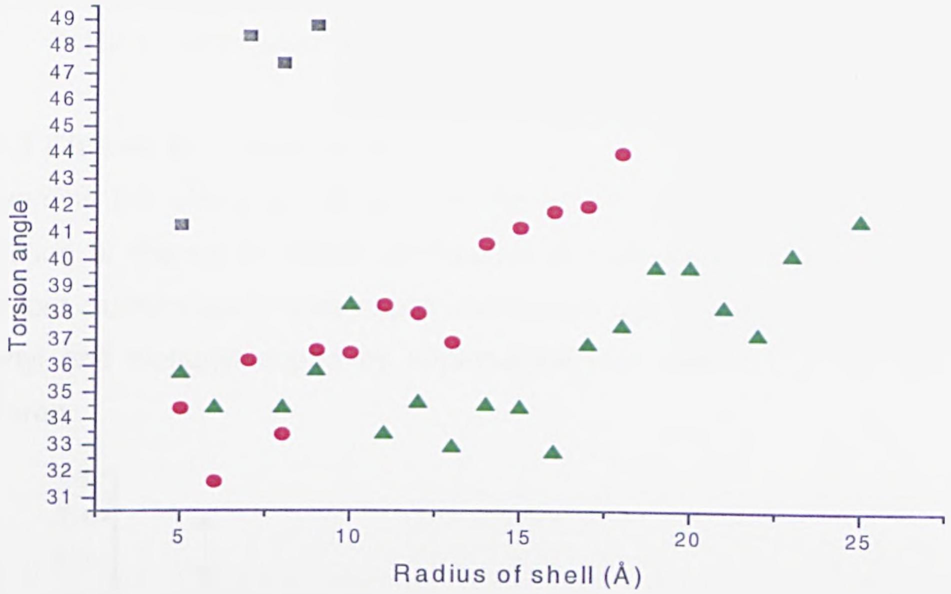

Figure 5.17: Average torsion angle distributions corresponding to the radius of shell from central molecule within a molecular cluster for pure biphenyl: (■) 19 molecules within the cluster with VAR=50.59; (●) 109 molecules within the cluster with VAR=38.66; (▲) 211 molecules within the cluster with VAR=36.08.

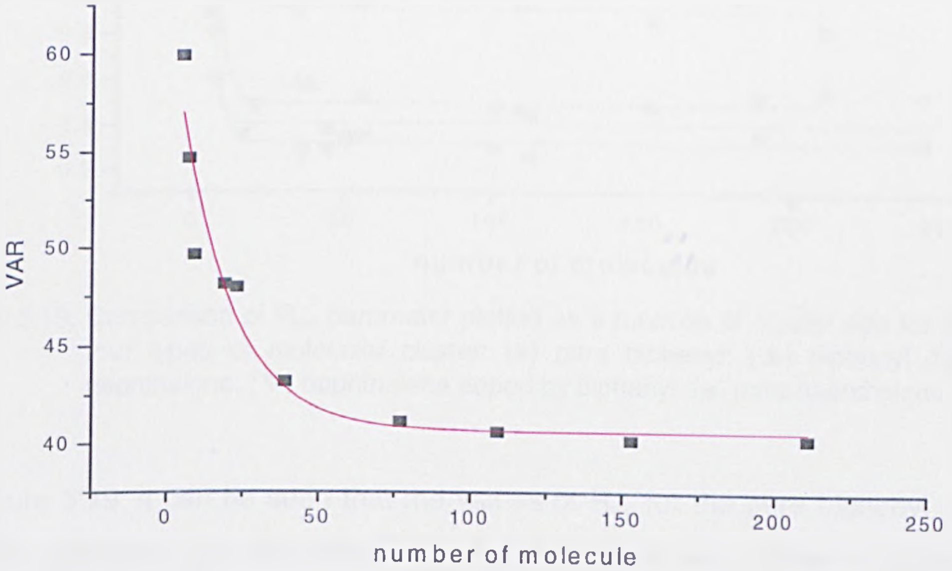

Figure 5.18: Torsion angle variance parameter within molecular cluster of biphenyl doped by naphthalene correlate to cluster size calculated using Equation (4-7).

The conformation variation of biphenyl with naphthalene shown in Figure 5.18, decreased with the increase of cluster size and showed the same trend with the value for the pure biphenyl cluster; however it was found that the variance became larger when the naphthalene was added to the centre of the naphthalene cluster.

5.2.3 Discussion: comparison of the change of atomic coordinates and torsion angles within molecular clusters

5.2.3.1 Cluster structural stability

To examine the effect of additives on the MSZW and solubility of solutes, the calculation of change in atomic coordinates and the conformational variation for these four clusters types: pure naphthalene, pure biphenyl, naphthalene doped by biphenyl and biphenyl doped by naphthalene was carried out and the results compared.

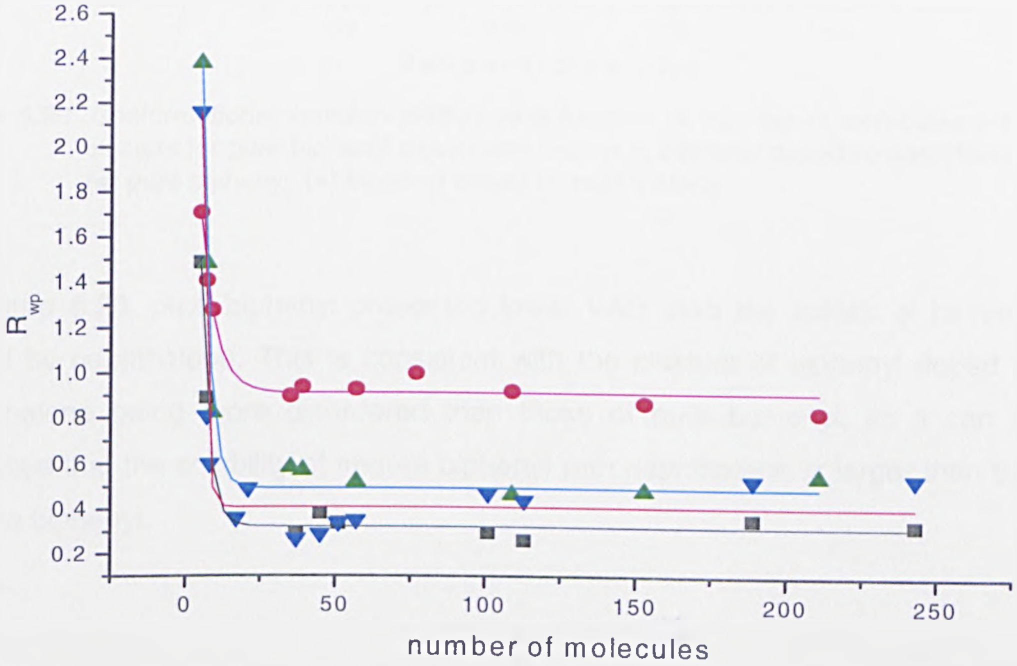

Figure 5.19: Comparison of R_{wp} parameter plotted as a function of cluster size for all these four types of molecular cluster: (●) pure biphenyl; (▲) biphenyl doped by naphthalene; (▼) naphthalene doped by biphenyl; (■) pure naphthalene .

In Figure 5.19, it can be seen that the values of R_{wp} for the pure biphenyl clusters are the greatest, and decreased when naphthalene was added to clusters of biphenyl. Compared with the values for pure biphenyl, the molecular clusters of pure naphthalene manifested the lowest values of R_{wp}, and R_{wp} increased with the addition of biphenyl to clusters of naphthalene.

5.2.3.2 Cluster disorder

The conformational variation within the clusters also relates to the disorder of cluster structure, so VAR can be used to qualify the degree of disorder in the solutions. It was known that the degree of disorder is measure of solubility in the solutions, so VAR can be used to investigate the change of solubility of biphenyl when naphthalene was added.

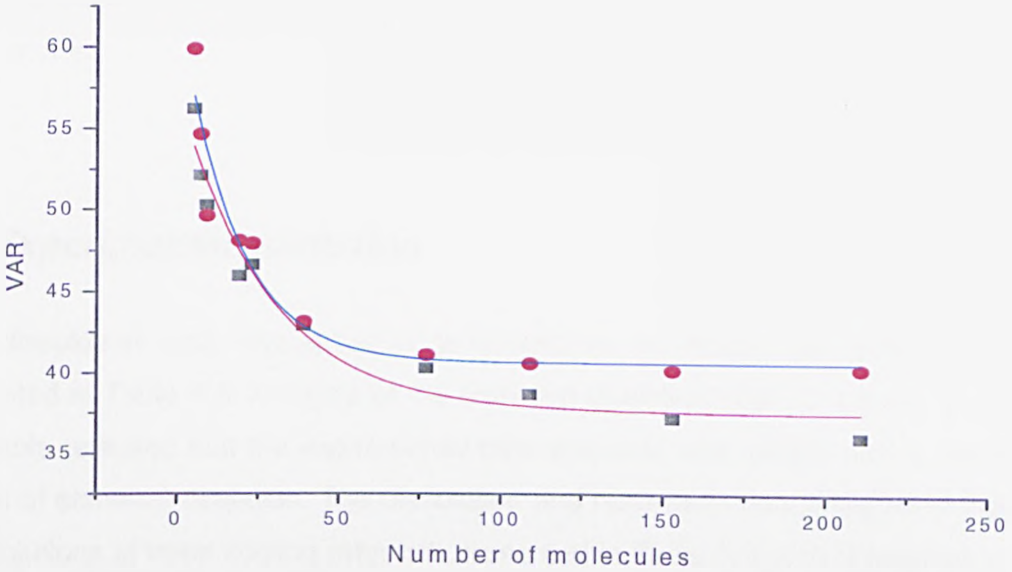

Figure 5.20: Conformational variation plotted as a function of number of molecules within clusters for pure biphenyl cluster and cluster of biphenyl doped by naphthalene: (■) pure biphenyl; (●) biphenyl doped by naphthalene.

In Figure 5.20, pure biphenyl presented lower VAR than the values of biphenyl doped by naphthalene. This is consistent with the clusters of biphenyl doped by naphthalene being more disordered than those of pure biphenyl, so it can be predicted that the solubility of impure biphenyl with naphthalene is larger than that of pure biphenyl.

5.2.3.3 Implication for crystallisation ability of compounds

From the definition of the R_{wp} parameter introduced before, it can be seen that the R_{wp} parameter characterizes the difference in the atomic coordinates of the molecular cluster before and after optimization, and can be used as a measure of crystallinity for the relaxed structure of clusters and to relate to the experimentally determined meta-stable zone width (MSZW). It is because the MSZW is the difference between the crystallization curve and solubility curve, and R_{wp} parameter reflects the change from an ordered structure to a disordered structure. From the comparison in Figure 5.19, it can be predicted that the MSZW of pure biphenyl will be largest, and MSZW of biphenyl doped by naphthalene will be the second largest one. Pure naphthalene's MSZW will be the smallest, and MSZW of naphthalene with biphenyl will be larger than that of pure naphthalene, however it will be lower than that of biphenyl doped by naphthalene. The simulation results of MSZW will be compared with the experimental results of MSZW from the slow cooling experiments.

5.3 Experimental validation

The dissolution and crystallization temperatures of these four solutions are presented in Table 5.3. Analysis of the standard deviations data in parentheses in the Table revealed that the experimental data are solid and reliable due to the low values of standard deviation. The dissolution and nucleation temperatures of these four solutions at three cooling rates are presented in Table 5.3, and dissolution and nucleation temperatures were extra plotted to 0 cooling rate. It can be seen that MSZW of pure biphenyl in toluene is the largest, and MSZW of pure naphthalene in toluene is the lowest. MSZW of biphenyl in toluene decreased when 1% of naphthalene was added, however MSZW of naphthalene increased when 1% of biphenyl was added. Compared with the MSZW predicted from simulation results of R_{wp} parameter, the trend of experimental MSZW is consistent with the simulation results (in Figure 5.19). It can also be seen from Table 5.3 that the dissolution temperature of biphenyl with 1% naphthalene is lower than that of pure biphenyl at 600g/l in toluene, so the solubility of impure biphenyl is larger than that of pure biphenyl in toluene. This result is in agreement with prediction of solubility determined from the calculation of conformational change (in Figure 5.20).

Table 5.3 Dissolution and nucleation with standard deviation (in brackets) onset temperatures and corresponding MSZW measurements for four solutes in toluene at 600g/l

Compound	Cooling rate (°C/min)	Crystallization Temperature (°C)	Dissolution Temperature (°C)	MSZW (°C)
Naphthalene	0	30.0	31.1	1.1
	0.1	29.5 (0.047)	31.0 (0.09)	1.5
	0.25	28.6 (0.54)	31.0 (0.08)	2.4
	0.5	27.3 (0.41)	30.8 (0.31)	3.5
1% Biphenyl in naphthalene	0	29.3	30.5	1.2
	0.1	29.1 (0.14)	30.5 (0.05)	1.4
	0.25	28.5 (0.26)	30.4 (0.04)	1.9
	0.5	28.0(0.35)	30.5 (0.14)	1.9
Biphenyl	0	15.9	18.3	2.4
	0.1	15.6 (0.38)	18.3 (0.49)	2.7
	0.25	14.6 (0.17)	18.0 (0.28)	3.4
	0.5	13.8 (0.25)	18.0 (0.50)	4.2
1% Naphthalene in Biphenyl	0	15.1	16.7	1.6
	0.1	14.8 (0.14)	16.8 (0.14)	2.0
	0.25	14.0 (0.10)	17.0 (0.20)	3.0
	0.5	13.2 (0.14)	17.2 (0.19)	4.0

From the analysis of experimental results of dissolution and nucleation temperatures for the model systems, the simulation work can be validated through the agreement with experimental results, so the cluster modelling work can be applied to predict MSZW for similar systems that do not exhibit hydrogen bonding and investigate the effect of additives, i.e. cold flow additives for methyl stearate, on MSZW and solubility.

5.4 Conclusions

This chapter details the molecular modelling work applied to predict MSZW and the effect of additives on MSZW for molecular clusters. Naphthalene and biphenyl are used as the model materials to examine the change of atomic coordinates and conformational structures. Molecular clusters of pure naphthalene, pure biphenyl, naphthalene doped by biphenyl and biphenyl doped by naphthalene were built as a function of cluster size using HABIT98, and the structural variability and conformational variance of these molecular clusters have been calculated, so the crystalisability of these four molecular clusters can be qualified through the comparison of structural variability and the effect of naphthalene on solubility of biphenyl can be predicted. The results of MSZW and solubility were determined from polythermal experiments for pure naphthalene, pure biphenyl, 1% naphthalene in biphenyl and 1% biphenyl in naphthalene in the solvent of toluene. The experimental data confirmed the effect of naphthalene on the crystalisability of biphenyl and vice versa in agreement with the predicted MSZW from molecular cluster modelling work. So the molecular cluster method was validated and can be applied to investigate the effect of additives on MSZW and solubility.

CHAPTER 6

Molecular Modelling of Crystal Structure, Morphology and Habit Modification

Summary:

The lattice energies, inter-molecular and inter-atomic interactions of both two polymorphs for methyl stearate together with predicted morphologies in vacuum were determined. The effects of solvents on crystal habit of methyl stearate were confirmed through the experimental observation and simulation.

6.1 Introduction

HABIT98 [15] is a computer program designed to aid in morphological investigations and bond analysis of the internal structure of molecular materials. This program can be used for predicting crystal morphology, investigating the effects of tailor-made additives on crystal morphology, calculating intermolecular interactions in crystals.

HABIT98 [15] operates in two modes: LATT, FULL. LATT mode is used for the calculation of lattice energy and FULL mode is used to predict the crystal morphology. The input files for the calculation are listed below:

- The cssr file including crystallography information, i.e. unit cell (a, b, c, alpha, beta and gamma), the coordinates of the atoms in one asymmetric unit.
- The charge file including the charges of each atom in the unit cell calculated with the computer program MOPAC [133].
- The symmetry file containing the symmetry operators to apply to approach asymmetric units in the unit cell.
- A growth face list generated using BFDH for which to calculated the slice and attachment energies and produce an attachment energy based model of crystal morphology.

The force field was selected based on the type of the materials and the intermolecular bonds, and in this work the Momany [136] force field was selected as Momany [136] since the model materials do not have any hydrogen bonding. The output file from the calculation was made up of attachment energy corresponding to the growth face. According to the attachment energy, the relative distance between the (hkl) planes in the crystal structure can be evaluated, and then the plot of crystal shape is obtained using SHAPE [16].

The bond analysis mode (formerly called debug mode) can be used to discover the strength and direction of the intermolecular bonds, the dominant forces contributing to the lattice energy, and important atom-atom interactions. If the first mode used, the intermolecular interactions between all possible central molecules in the unit cell and the surrounding molecules will be written to file. This allows each intermolecular interaction to be identified in terms of its position in the crystal. The bonds between the central molecule and a second molecule can be identified as the intermolecular distance. If the second mode used, a list of all important atom-

atom interactions in thee whole crystal sphere will be written to the output file. The output file from the second mode is useful in assessing which atoms dominate the crystal energetically, with the partition data providing additional information about which potential types are important.

HABIT98 was used to predict the crystal morphology and analyse the intermolecular interactions for methyl stearate, however there were no data reported in the literature with which to compare the results for methyl stearate, so the biphenyl and naphthalene were used as the test materials to validate the program and these validation studies were reported in Chapter 5.

6.2 Lattice energy and Intermolecular & Inter-atomic Bond Analysis for Methyl Stearate

It is known that methyl stearate has two polymorphs (see Table 4.1, Figure 4.1). Figure 6.1 shows the space group and the packing in the unit cell for two polymorphs of methyl stearate.

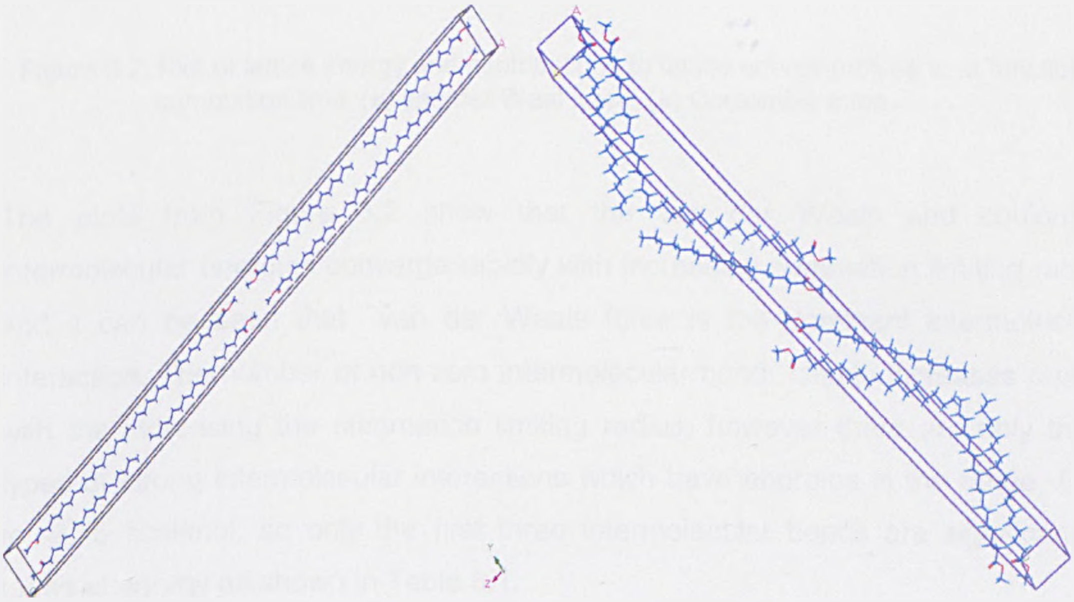

(a) (b)

Figure 6.1: Details of crystallographic unit cells for the two polymorphs of methyl stearate (a) A2/a; (b) Pnab

6.2.1 Monoclinic methyl stearate

6.2.1.1 Bond analysis

The calculated lattice energy for the monoclinic polymorph of methyl stearate is -35.12 kcal/mol, and shows excellent agreement with previously calculated values and the experimental sublimation enthalpy [144] (-37.79kcal/mol), which suggest that the force field selected in the simulation is appropriate.

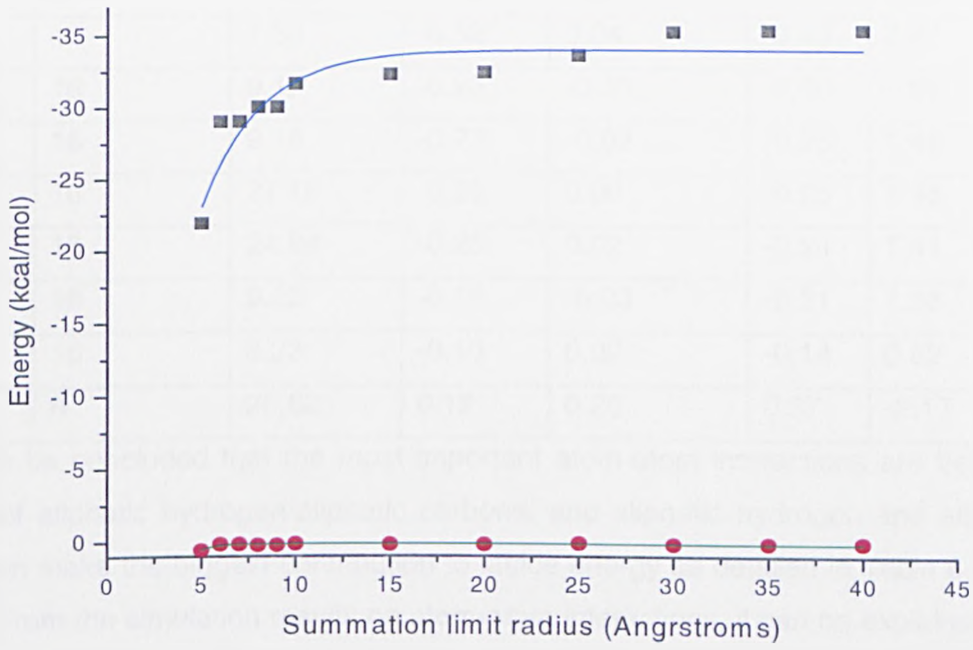

Figure 6.2: Plot of lattice energy and contributions to lattice energy profiles as a function of summation limit: (■) van der Waal force; (●) Coulombic force.

The plots from Figure 6.2 show that the van der Waals and coulombic intermolecular energies converge rapidly with increasing summation limiting radius and it can be seen that van der Waals force is the dominant intermolecular interaction. The number of non-zero intermolecular bond clearly increases rapidly with the increasing the summation limiting radius, however there are only three types of strong intermolecular interactions which have energies in the range -5.39 to -3.75 kcal/mol, so only the first three intermolecular bonds are significant in terms of energy as shown in Table 6.1.

Table 6.1 Intermolecular interaction strengths (kcal mol^{-1}) corresponding to the different molecular distance calculated using Habit98

Bond	Multiplicity	Distance [Å]	van der Waals	Coulumbic force	Total	Percentage (%)
a	16	4.63	-5.35	-0.04	-5.39	31.58
b	16	4.60	-5.60	0.32	-5.28	30.93
c	16	5.61	-3.55	-0.20	-3.75	21.97
d	8	23.58	-0.57	-0.12	-0.69	4.04
e	8	26.50	-0.49	0.00	-0.49	2.87
f	16	7.33	-0.52	0.04	-0.49	2.87
g	16	9.17	-0.23	-0.03	-0.26	1.52
h	16	9.18	-0.23	-0.02	-0.25	1.46
i	16	27.18	-0.25	0.00	-0.25	1.46
j	16	24.84	-0.25	0.02	-0.24	1.41
k	16	9.23	-0.19	-0.03	-0.21	1.23
l	16	9.23	-0.16	0.02	-0.14	0.82
m	8	25.82	0.12	0.25	0.37	-2.17

It can be concluded that the most important atom-atom interactions are between pair of aliphatic hydrogen-aliphatic carbons, and aliphatic hydrogen and aliphatic carbon make the biggest contribution to lattice energy as detailed in Table 6.3 and 6.4. From the simulation results on atom-atom interactions, it can be explained that the crystallization properties of methyl stearate are similar to those for long chain alkenes due to the fact that the largest contributions to lattice energy are from aliphatic hydrogen-aliphatic carbon, and aliphatic hydrogen and aliphatic carbon.

Table 6.2 Contributions of different types of atoms in the molecule of monoclinic methyl stearate to the lattice energy

Atom	Attractive energy (kcal/mol)	Repulsive energy (kcal/mol)	Coulombic (kcal/mol)	Total (kcal/mol)	Percentage
H	-19.87	10.13	-1.80	-11.54	54.05%
C1	-15.69	5.46	1.33	-8.90	41.67%
C2	-1.21	0.36	-0.78	-1.63	7.63%
O2	-1.33	0.67	1.52	0.86	-4.02%
O1	-0.50	0.07	0.28	-0.14	0.67%
Totals	-38.60	16.69	0.56	-21.35	100%

Note: H-aliphatic hydrogen, C1-aliphatic carbon, C2-carbonyl carbon, O2-carbonyl oxygen, O1 hydroxyl oxygen.

Table 6.3 Contributions of interactions between atoms in the molecule of monoclinic methyl stearate to lattice energy.

Type1	Type2	Attractive energy (kcal/mol)	Repulsive Energy (kcal/mol)	van der Waals (kcal/mol)	Percentage
H	H	-10.93	6.49	-4.44	20.23%
H	C1	-15.58	6.05	-9.53	43.42%
H	C2	-0.90	0.37	-0.53	2.41%
H	O2	-1.05	0.79	-0.26	1.18%
H	O1	-0.35	0.06	-0.29	1.32%
C1	C1	-7.00	2.14	-4.86	22.14%
C1	C2	-0.71	0.17	-0.54	2.46%
C1	O2	-0.81	0.36	-0.45	2.05%
C1	O1	-0.29	0.05	-0.24	1.09%
C2	C2	-0.16	0.02	-0.14	0.64%
C2	O2	-0.37	0.12	-0.25	1.14%
C2	O1	-0.14	0.01	-0.13	0.59%
O2	O2	-0.16	0.03	-0.13	0.59%
O2	O1	-0.12	0.01	-0.11	0.50%
O1	O1	-0.05	0.00	-0.05	0.22%
TOTALS		-38.62	16.67	-21.95	100%

6.2.2 Orthorhombic methyl stearate

6.2.2.1 Bond analysis

The lattice energy for orthorhombic methyl stearate is -34.25kcal/mol, in excellent agreement with previously calculated values and the experimental sublimation enthalpy [144] (-37.79kcal/mol). The results from Figure 6.3 show that the van der Waals and coulombic intermolecular energies converge rapidly with the increasing summation limiting radius for the orthorhombic form, and it can be seen that the van der Waals interactions are the dominant intermolecular interactions operating in the crystal lattice. Again three dominant types of intermolecular bonds which have energies in the range from -5.37 to -3.56 kcal/mol.

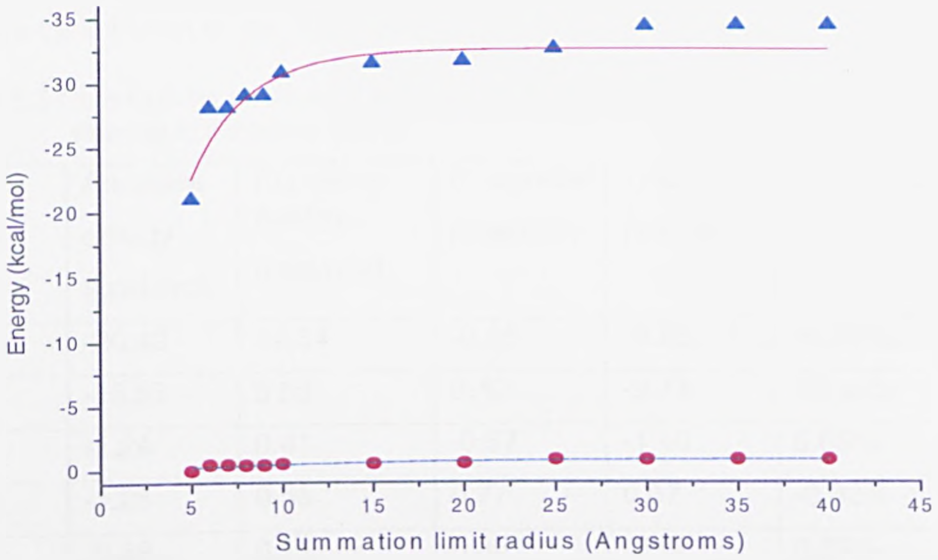

Figure 6.3: Plot of lattice energy and contributions to lattice energy profiles as a function of summation limit: (▲) van der Waal force; (●) Coulombic force.

Table 6.4 Intermolecular interaction strengths (kcal mol^{-1}) corresponding to the different molecular distance calculated using Habit98

Bond	Multiplicity	Distance [Å]	van der Waals	Coulombic	Total	Percentage (%)
a	16	4.64	-5.31	-0.06	-5.37	32.3
b	16	4.61	-5.22	0.10	-5.11	30.7
c	16	5.61	-3.22	-0.24	-3.56	21.4
d	16	7.35	-0.51	0.02	-0.49	2.95
e	8	24.93	-0.32	-0.03	-0.35	2.11
f	8	24.93	-0.28	-0.04	-0.32	1.93
g	16	25.26	-0.30	0.00	-0.30	1.81
h	16	9.18	-0.24	-0.02	-0.26	1.56
i	16	9.19	-0.24	-0.02	-0.26	1.56
j	16	25.37	-0.24	0.00	-0.24	1.44
k	16	9.25	-0.19	-0.02	-0.21	1.26
l	20	9.25	0.16	0.01	-0.15	0.9

It can be concluded that the most important atom-atom interactions are a pair of aliphatic hydrogen-aliphatic carbons, and aliphatic hydrogen and aliphatic carbon that make the greatest contribution to lattice energy as summarised in Tables 6.5 and 6.6. However, compared with the monoclinic form, the aliphatic carbon and the pair of aliphatic hydrogen-aliphatic carbons from the orthorhombic form make a greater contribution to the lattice energy.

Table 6.5 Contributions of different types of atoms in the molecule of orthorhombic methyl stearate to the lattice energy

Atom	Attractive energy (kcal/mol)	Repulsive energy (kcal/mol)	Coulombic (kcal/mol)	Total (kcal/mol)	percentage
H	-20.49	11.54	-0.88	-9.83	46.90%
C1	-15.65	5.50	0.40	-9.74	46.48%
C2	-1.24	0.41	-0.57	-1.40	6.65%
O2	-1.25	0.55	0.77	0.07	-0.32%
O1	-0.52	0.11	0.35	-0.06	0.29%
totals	-39.15	18.10	0.08	-20.97	100%

Note: H-aliphatic hydrogen, C1-aliphatic carbon, C2-carbonyl carbon, O2-carbonyl oxygen, O1-hydroxyl oxygen.

Table 6.6 Contributions of interactions between atoms in the molecule of orthorhombic methyl stearate to lattice energy

Type1	Type2	Attractive energy (kcal/mol)	Repulsive energy (kcal/mol)	van der Waals (kcal/mol)	Percentage
H	H	-11.43	7.75	-3.68	17.47%
H	C1	-15.74	6.32	-9.42	44.73%
H	C2	-0.97	0.48	-0.49	2.33%
H	O2	-0.99	0.63	-0.36	1.71%
H	O1	-0.42	0.14	-0.28	1.33%
C1	C1	-6.91	2.08	-4.83	22.93%
C1	C2	-0.70	0.18	-0.52	2.47%
C1	O2	-0.75	0.29	-0.46	2.18%
C1	O1	-0.28	0.05	-0.23	1.09%
C2	C2	-0.16	0.02	-0.14	0.67%
C2	O2	-0.37	0.12	-0.25	1.19%
C2	O1	-0.13	0.01	-0.12	0.57%
O2	O2	-0.15	0.02	-0.13	0.62%
O2	O1	-0.11	0.01	-0.1	0.48%
O1	O1	-0.05	0.00	-0.05	0.24%
TOTALS		-39.16	18.10	-21.06	100%

6.3 Polymorphic Cluster Stabilities for Methyl Stearate

A novel method of molecular cluster analysis has been validated through the experimental determination of MSZW for a number of model systems in chapter 5. The molecular clusters (in Figure 6.4) of methyl stearate were constructed using the same general approach as for clusters of naphthalene. The energies of the molecular clusters containing different numbers of molecules, created using HABIT98, were calculated by applying Dreiding force-field parameters using Materials Studio [132] and plotted as a function of the number of molecules within the cluster for both polymorphic form of methyl stearate. It can be seen that the monoclinic form would be predominant from smaller clusters to larger clusters (Figure 6.5), so it was confirmed that the monoclinic form should be the more stable structure than that of the orthorhombic form.

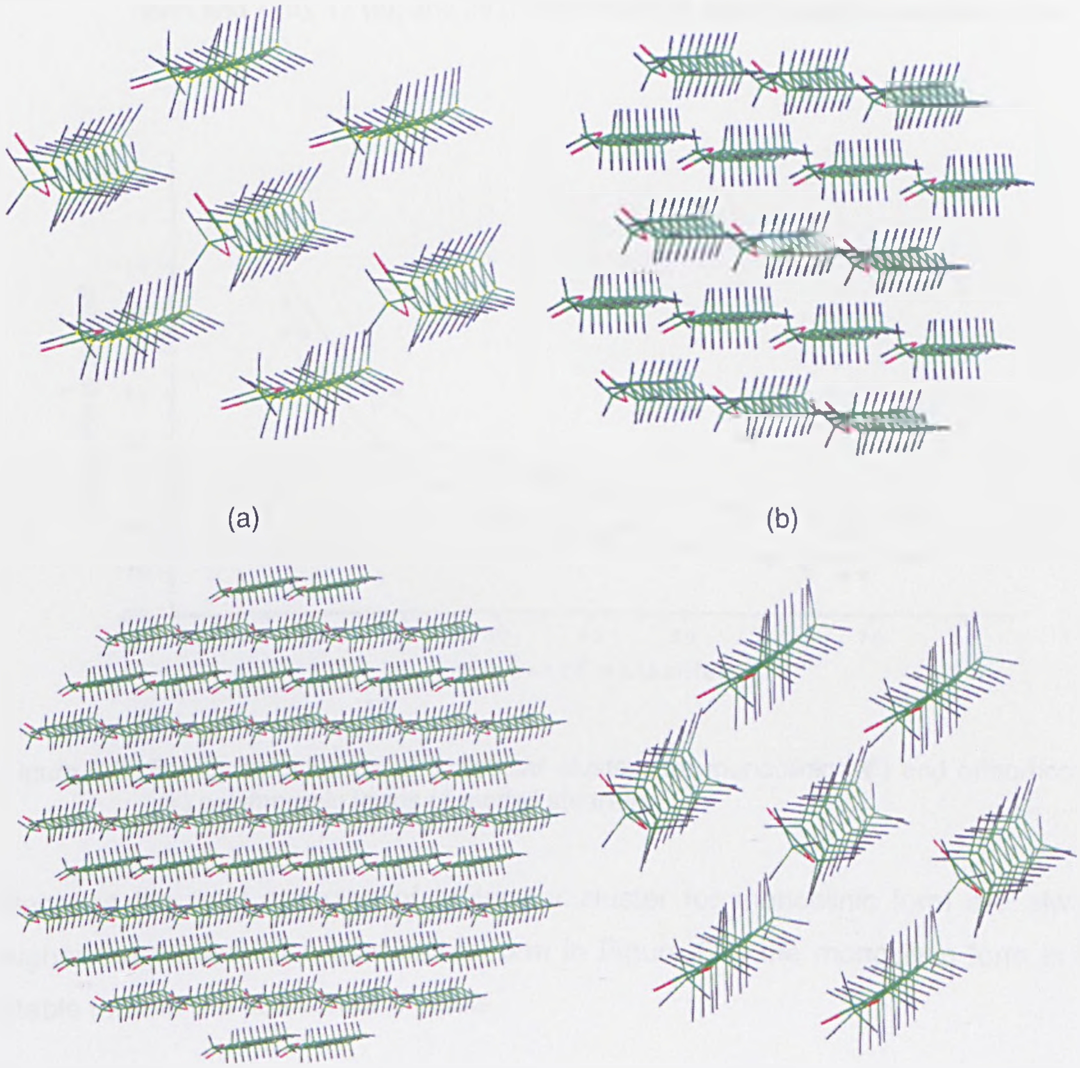

(a) (b)

(c) (d)

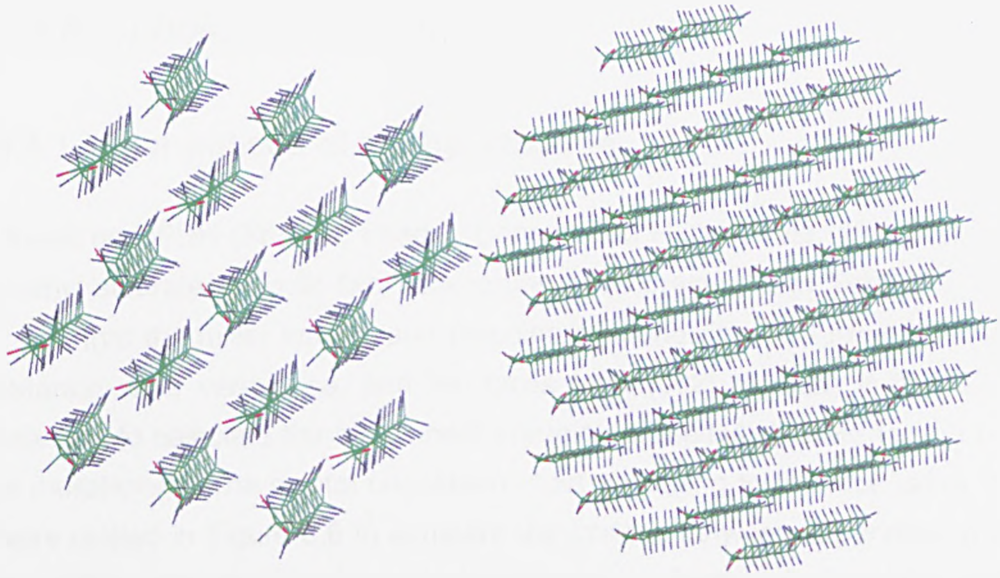

(e) (f)

Figure 6.4: Molecular clusters containing 7 (a), 17 (b), and 59 (c) molecules of monoclinic form and 7 (d), 17 (e), and 59 (f) orthorhombic form of methyl stearate created.

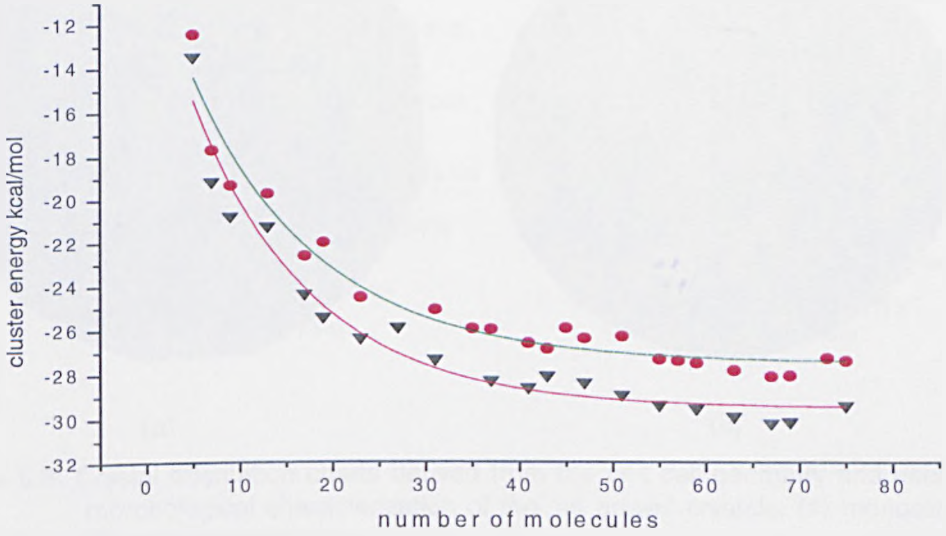

Figure 6.5: Energy calculations of molecular clusters for monoclinic (▼) and orthorhombic (●) polymorphic forms of methyl stearate.

Because the total energies of molecular cluster for monoclinic form are always higher than those for orthorhombic form in Figure 6.5, the monoclinic form is the stable form in the solution or crystals.

6.4 Morphological Prediction

6.4.1 Miller indices of methyl stearate

Based on BFDH (Bravais, Friedel, Donnay and Harker) rule, the miller indices of methyl stearate for both two polymorphs were presented in Table 6.7. It can be found that the miller indices and d-spcing of monoclinic and orthorhombic methyl stearate were very close, and the faces from (002) to (024) in Table 6.7 were selected to calculate the attachment energies of methyl stearate for the prediction of morphology. The crystal orientation chart according to the face list in Table 6.7 were plotted in Figure 6.6 to compare the images between experimental data and simulation results. From the crystal orientation in Figure 6.6, it can be found that it was difficult to identify the phase of methyl stearate because the faces were very similar.

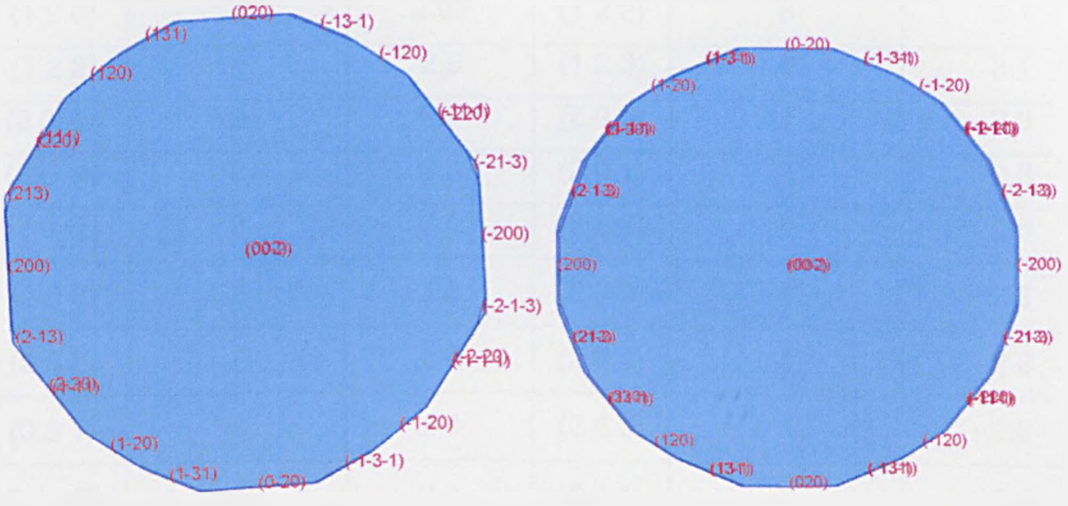

(a) (b)

Figure 6.6: Crystal orientation charts derived from the unit cell geometry and used for the morphological characterization of the 'as grown' crystals: (a) monoclinic form; (b) orthorhombic form.

Table 6.7 List of miller indices of methyl stearate based on BFDH rule

hkl	Multiplicity (monoclinic)	d_{hkl} (monoclinc) (Å)	hkl	Multiplicity (orthorhombic)	d_{hkl} (orthorhombi) (Å)
(0 0 2)	2	47.6	(0 0 2)	2	47.6
(0 1 1)	4	7.3	(0 1 1)	4	7.3
(0 1 3)	4	7.1	(0 1 3)	4	7.2
(1 1 -3)	4	4.3	(1 1 1)	8	4.5
(1 1 -1)	4	4.2	(1 1 2)	8	4.4
(1 1 1)	4	4.1	(1 1 3)	8	4.4
(1 1 3)	4	3.9	(0 2 0)	2	3.6
(0 2 0)	2	3.7	(0 2 4)	4	3.6
(0 2 4)	4	3.6	(1 2 0)	4	3.1
(1 2 -2)	4	3.0	(1 2 1)	8	3.1
(1 2 0)	4	2.96	(1 2 2)	8	3.1
(1 2 2)	4	2.9	(1 2 3)	8	3.1
(2 0 -6)	2	2.7	(2 0 0)	2	2.8
(2 0 -4)	2	2.6	(2 0 1)	4	2.8
(2 0 -2)	2	2.6	(2 0 2)	4	2.8
(2 0 0)	2	2.5	(2 0 3)	4	2.8
(2 0 2)	2	2.4	(2 0 4)	4	2.8
(0 3 1)	4	2.4	(2 0 6)	4	2.8
(2 1 -3)	4	2.4	(2 1 1)	8	2.6
(2 1 -1)	4	2.4	(2 1 2)	8	2.6
(2 0 4)	2	2.4	(2 1 3)	8	2.6
(2 1 1)	4	2.3	(0 3 1)	4	2.5
(2 0 6)	2	2.3	(1 3 1)	8	2.2
(2 1 3)	4	2.3	(1 3 2)	8	2.2
(1 3 -3)	4	2.2	(1 3 3)	8	2.2
(1 3 -1)	4	2.2	(2 2 0)	4	2.2
(1 3 1)	4	2.2	(2 2 1)	8	2.2
(1 3 3)	4	2.2	(2 2 3)	8	2.2
(2 2 -4)	4	2.1			
(2 2 0)	4	2.1			

6.4.2 Monoclinic methyl stearate

The slice energies and attachment energies corresponding to individual face for monoclinic methyl stearate were calculated using Equation (4-4), and the results were presented in table 6.8. The predicted morphology of monoclinic methyl stearate are plotted in Figure 6.7.

Table 6.8 Slice energies and attachment energies for the growth faces of methyl stearate

Growth direction	Multiplicity	d_{hkl} (Å)	Slice energy (kcal/mol)	Attachment energy (kcal/mol)
(0 0 2)	2	47.6	-33.53	-1.59
(0 1 1)	4	7.3	-20.61	-14.51
(1 -1 -1)	4	4.5	-12.86	-22.26
(0 2 0)	2	3.7	-8.85	-26.27
(0 2 4)	4	3.6	-8.32	-26.80

Table 6.9 Assignments of the bonds to slice energy or attachment energy for particular face of methyl stearate crystal

Face	a		b		c	
	(SL)	(ATT)	(SL)	(ATT)	(SL)	(ATT)
(002)	16	0	16	0	16	0
(011)	0	16	16	0	16	0
(111)	8	8	8	8	0	16
(020)	0	16	0	16	16	0
(024)	0	16	0	16	16	0
(12-2)	0	16	8	8	0	16

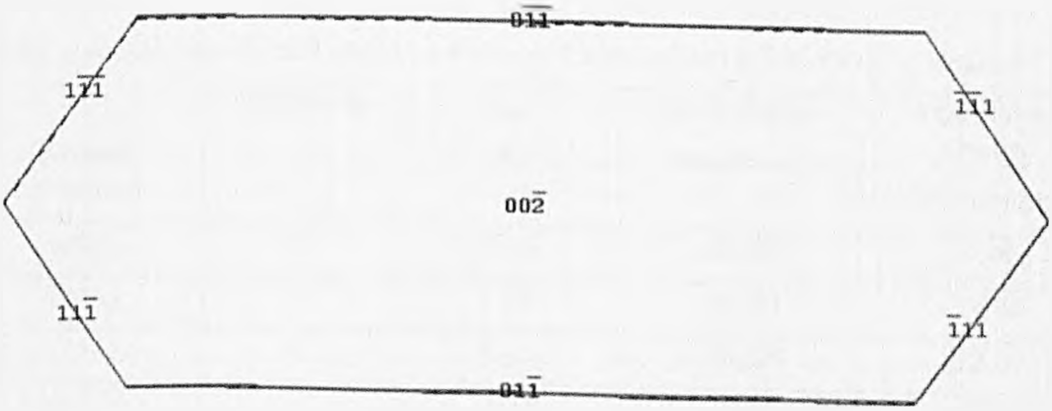

(a)

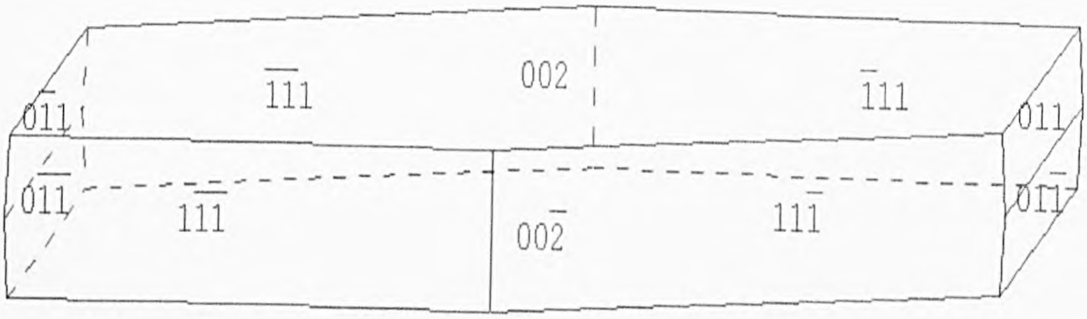

(b)

Figure 6.7: Different projections of predicted shape of methyl stearate (monoclinic) based on attachment energy calculations: (a) from the z-axis, (b) from the b-axis.

The values of attachment energies in Table 6.8 revealed that the attachment energy of (002) face is lowest, so the (002) face is the dominant face according to the relationship between attachment energy and growth rate. The number of intermolecular-bond contributions to the slice energy reflects the morphological importance in Table 6.9, and it can be seen that the (002) face is the most important face. The results from the morphological prediction in Figure 6.6 revealed that (002) is the most important face and much bigger than other faces, and the crystal shape is thin and plate-like.

6.4.3 Orthorhombic methyl stearate

The slice energies and attachment energies corresponding to individual face for orthorhombic methyl stearate were presented in table 6.10. The predicted morphology of monoclinic methyl stearate are plotted in Figure 6.8.

Table 6.10 Slice energy and attachment energy for the growth faces of methyl stearate

Growth direction	Multiplicity	d_{hkl} (Å)	Slice energy (kcal/mol)	Attachment energy (kcal/mol)
(002)	2	47.57	-32.80	-1.45
(011)	4	7.33	-19.60	-14.66
(111)	8	4.45	-11.58	-22.67
(0 2 0)	2	3.68	-8.01	-26.25
(0 2 4)	4	3.08	-8.13	-26.13

Table 6.11 Assignment of the bonds to slice energy or attachment energy for particular faces of methyl stearate crystal.

Face	a		b		c	
	(SL)	(ATT)	(SL)	(ATT)	(SL)	(ATT)
(002)	16	0	16	0	16	0
(011)	0	16	16	0	16	0
(111)	8	8	8	8	0	16
(020)	0	16	0	16	16	0
(024)	0	16	0	16	16	0
(120)	0	16	8	8	0	16
(121)	0	16	8	8	0	16

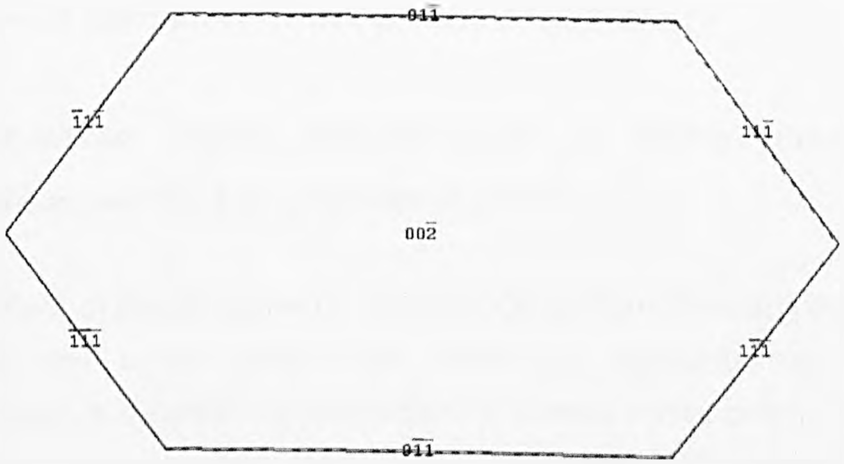

(a)

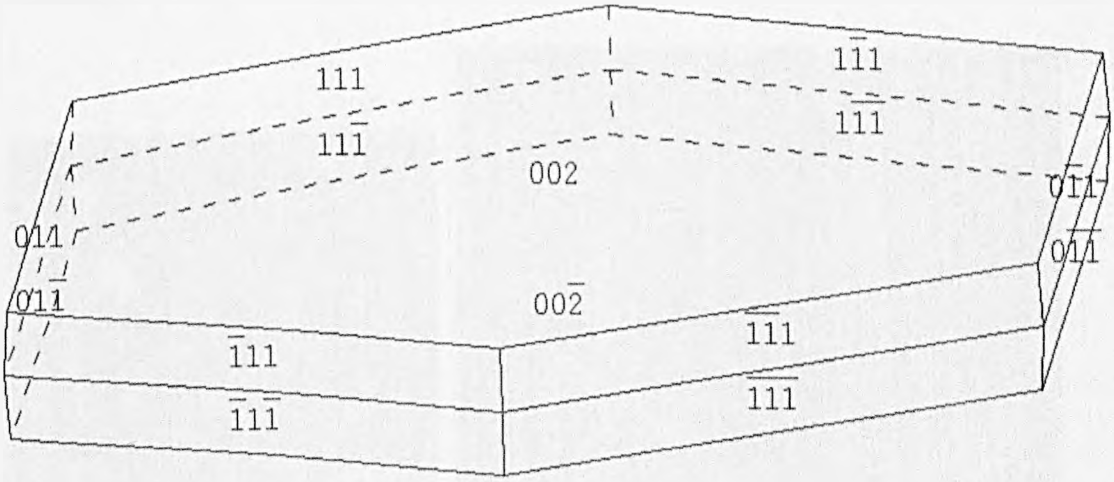

(b)

Figure 6.8: Different projections of predicted shape of methyl stearate (orthorhombic) based on attachment energy calculations: (a) from the z-axis, (b) from the b-axis.

The values of attachment energies in Table 6.10 revealed that the (002) face is dominant for the crystal of orthorhombic methyl stearate. The number of intermolecular-bond contributions to the slice energy in Table 6.11 reflects the morphological importance, because these values confirmed that the attachment energy of (002) was lowest. It can be seen from Figure 6.7 that the most important face is the (002) face, and the shape of orthorhombic methyl stearate is plate-like as well. Although there are two polymorphs for methyl stearate, the crystal shape of the monoclinic form is close to the orthorhombic form, and the only difference is the multiplicity of the (111) face. It may be because the structures of the two polymorphs are similar, the predicted morphologies for both two polymorphs are close.

6.5 Solvent-Mediated Effect on the Morphology

6.5.1 Observed crystal morphologies of methyl stearate as observed through cold room studies

6.5.1.1 Effect of temperature on habit modification of methyl stearate

Nucleation and crystal growth are driven by supersaturation, and the supersaturation is controlled by temperature in cooling crystallization. The crystal size is determined by nucleation and crystal habit is decided by crystal growth, so the temperature has a significant effect on the size and morphology of methyl stearate.

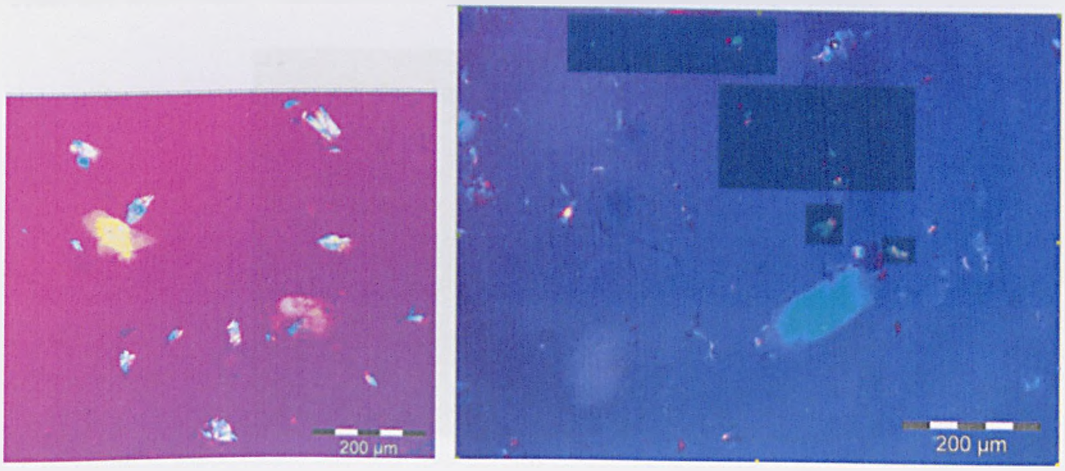

(a) (b)

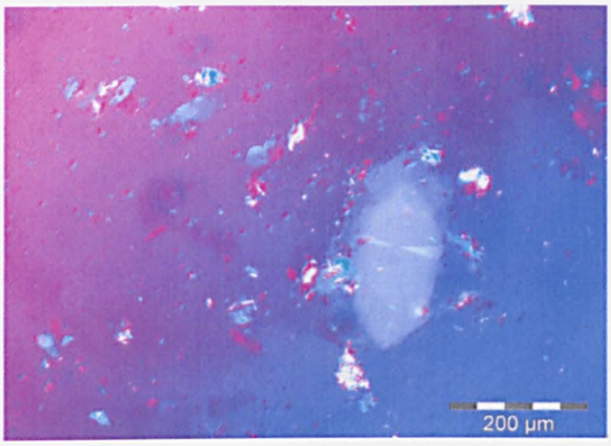

(c)

Figure 6.9: The images of methyl stearate in methyl oleate at different temperatures, (a) 2.5% methyl stearate in methyl oleate at 0°C; (b) 2.5% methyl stearate in methyl oleate at -1°C; (c) 2.5% methyl stearate in methyl oleate at -2°C.

The crystal habits displayed in Figure 6.9 showed the effect of temperature on crystal morphology and size of methyl stearate crystals in methyl oleate. It can be found that the number of crystals in solution increased, however only a few crystals grew, so the nucleation played an important role during the crystallization process. Because nucleation was the most important, the morphology didn't change too much.

6.5.1.2 Effect of solvent on habit modification of methyl stearate

Due to the different solubility and crystallization temperatures of methyl stearate in methyl oleate, dodecane and toluene, the variety of supersaturation of methyl stearate in different solvents will lead to different nucleation rates.

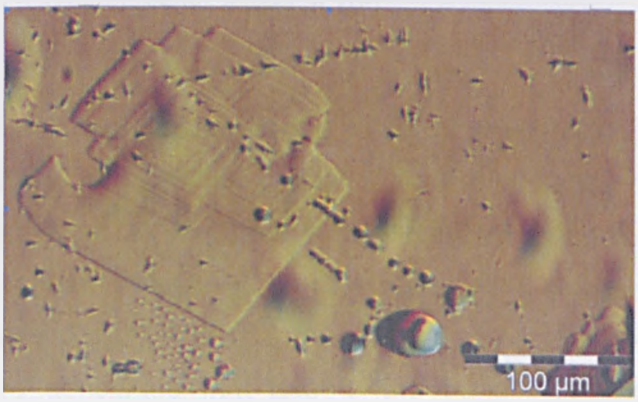

(a)

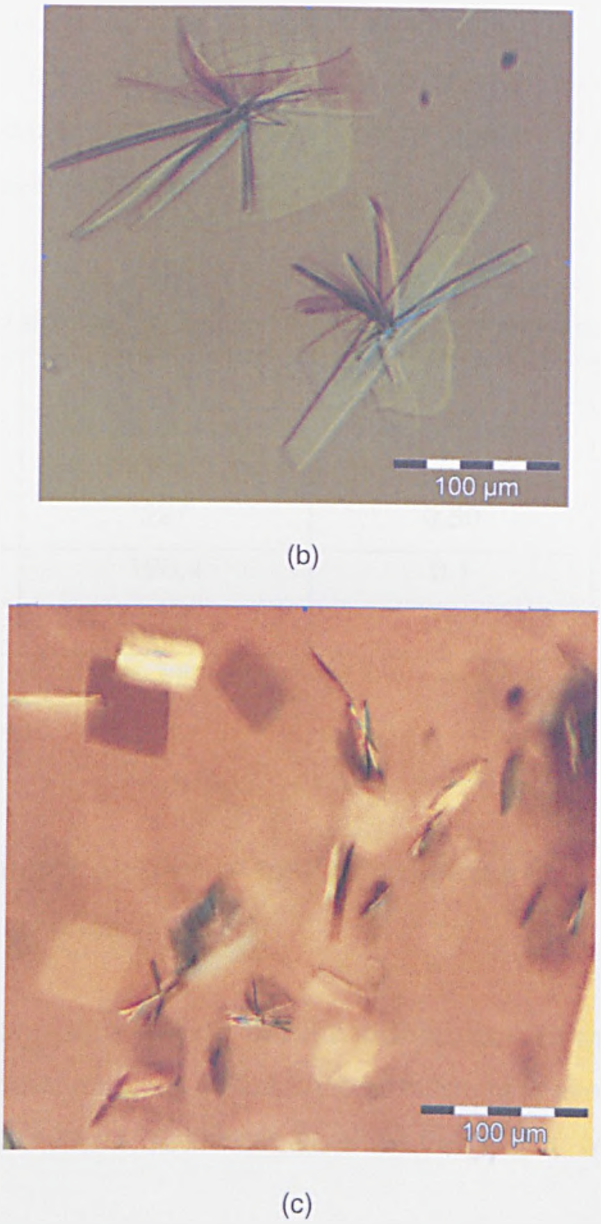

Figure 6.10: Images of methyl stearate crystallizing from different solvents: (a) 30% methyl stearate in toluene at 3°C; (b) 10% methyl stearate in dodecane at 5°C; (c) 10% methyl stearate in methyl oleate at 10°C.

The images in Figure 6.10 presented the effect of solvents on crystal habit and size, and the effect of solvents on crystal size, aspect ratio and thickness was assessed through the results in Table 6.12. It can be found that the crystals in toluene were larger than those in dodecane and methyl oleate, and thicker than those in dodecane and methyl oleate because the crystals in toluene were more optical. It can be concluded that due to the huge difference of molecular structures between toluene and methyl stearate, the nucleation of methyl stearate were depressed by toluene. Compared with the number of crystals in dodecane, there were more crystals in methyl oleate due to the high solubility of methyl steare in methyl oleate, and the supersaturation of methyl stearare in methyl oleate was higher. The high supersaturation of methyl stearate in methyl oleate led to high nucleation rates, so the growth rates of methyl stearate in methyl oleate was lower than those in dodecane, and the shapes of methyl stearate in methyl oleate will be smaller than shapes in dodecane.

Table 6.12 Crystal size, aspect ratio and thickness of methyl stearate in three solvents

Solvents	In-plane dimensions		Crystal thickness
	Largest dimension (μm)	Aspect ratio	1-5
Toluene	227	0.59	4
Dodecane	198.4	0.1	3
Methyl oleate	72.6	0.67	1

Note: The thickness of crystals were expressed by: 1 smallest; 2 smaller; 3 medium; 4 thicker; 5 thickest.

6.5.2 Observed morphologies of methyl palmitate observed through the cold room studies

6.5.2.1 Effect of temperature on habit modification of methyl palmitate

The effects of temperature work on the shapes of methyl palmitate as well. It can be found that the size of palmitate crystals decreases with a decrease in temperature.

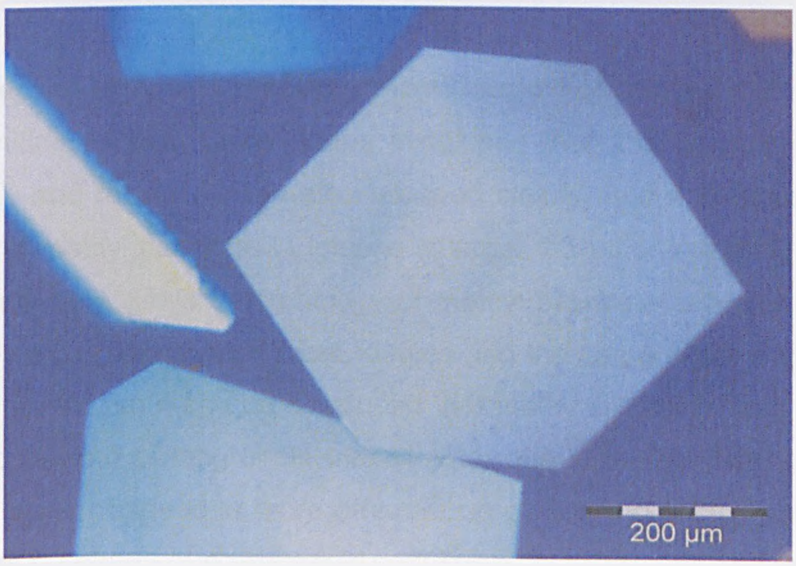

(a)

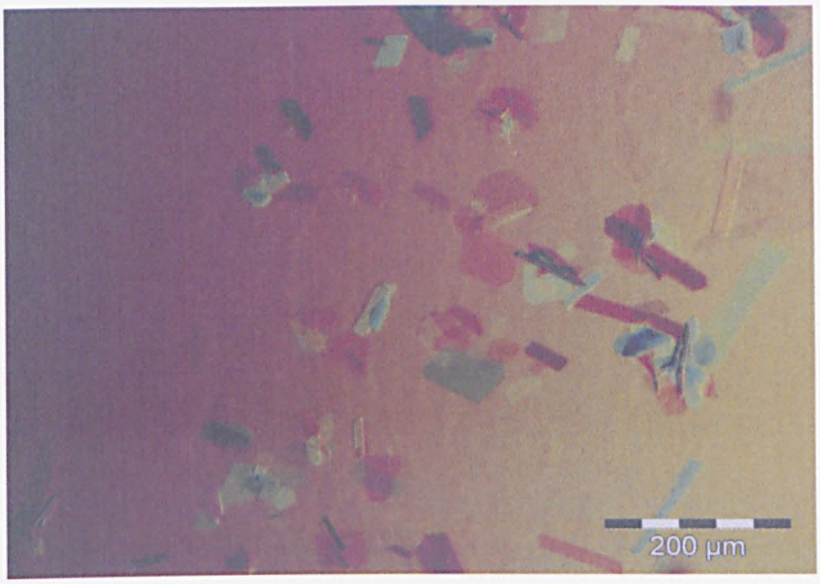

(b)

Figure 6.11: Images of methyl palmitate in toluene at different temperatures: (a) 30% methyl palmitate in toluene at -7°C; (b) 20% methyl palmitate in toluene at -11°C.

Although there is no big change in the shapes of methyl palmitate with the decrease of temperature of solution, the size of methyl palmitate was modified significantly and the number of crystals increased obviously at from -7°C to -11°C. From the analysis of the effect of temperature on crystal size of methyl stearate and methyl palmitate, it can be seen that the control of temperature is very key to nucleation, and it can be found that nucleation played an important in the crystallization process of methyl palmitate as well.

6.5.2.2 Effect of solvents on habit modification of methyl palmitate

Methyl palmitate exhibits better shape in toluene than that in methyl oleate (in Figure 6.11), and the spiral can also be seen clearly, and it is obvious that the crystal size of methyl palmitate in toluene is larger than that in methyl oleate. The effect of toluene on growth morphology of methyl palmitate is better than methyl palmitate in methyl oleate from these images and the same effect was also found for methyl stearate, so it can be concluded that methyl oleate is more effective on nucleation behaviour of long chain methyl ester due to the similarity of molecular structure. However toluene is more effective on growth morphology of long chain methyl esters.

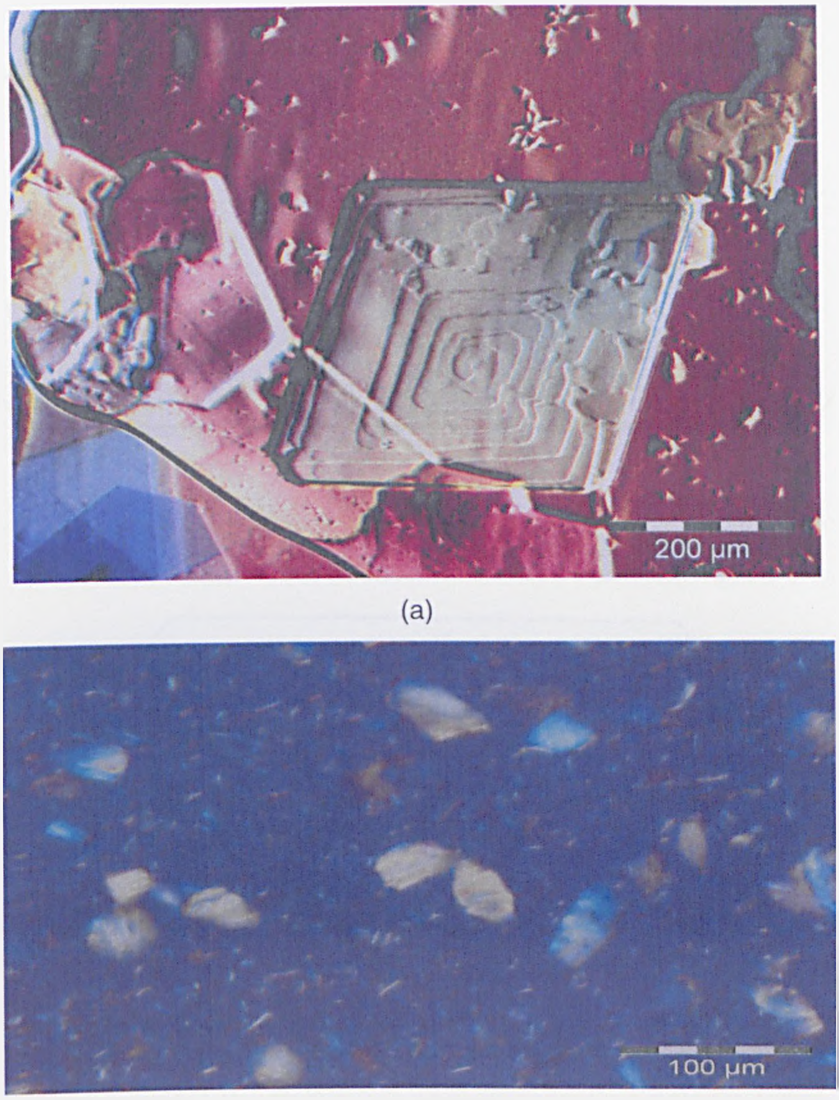

(a)

(b)

Figure 6.12: Images of methyl palmitate crystallizing from different solvents: (a) 30% methyl palmitate in toluene at -7°C; (b) 2.5% methyl palmitate in methyl oleate at -9°C.

6.5.3 Habit comparison between experimental and simulated data

The dominant faces were both calculated to be (002) face in the predicted crystal shapes of two polymorphs of methyl stearate with smaller (011) and (111) shown in Figure 6.13 (a), (b), and the map of in-plane faces based on BFDH was shown in Figure 6.13 (c).

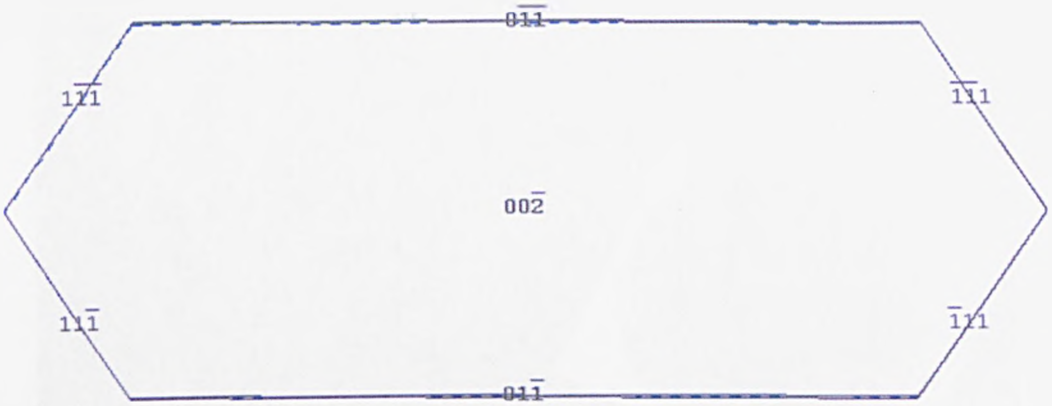
$0\bar{1}\bar{1}$
$1\bar{1}1$
$\bar{1}\bar{1}1$
$00\bar{2}$
$11\bar{1}$
$\bar{1}11$
$01\bar{1}$

(a)

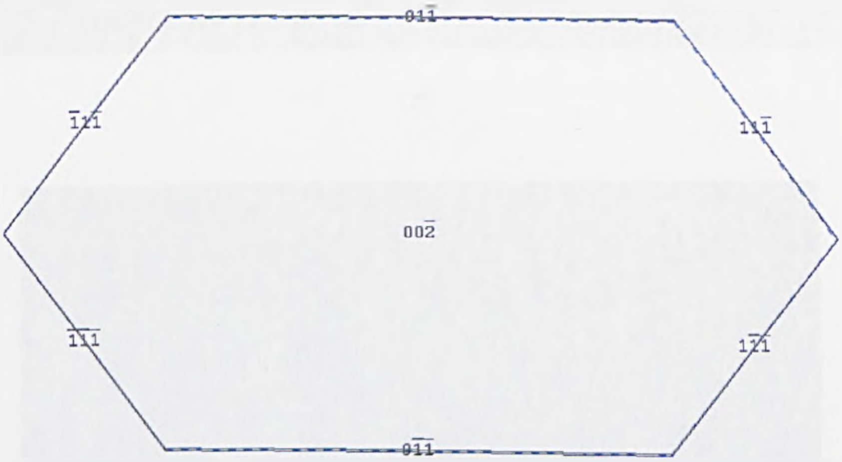
$01\bar{1}$
$\bar{1}1\bar{1}$
$11\bar{1}$
$00\bar{2}$
$\bar{1}\bar{1}\bar{1}$
$1\bar{1}\bar{1}$
$0\bar{1}1$

(b)

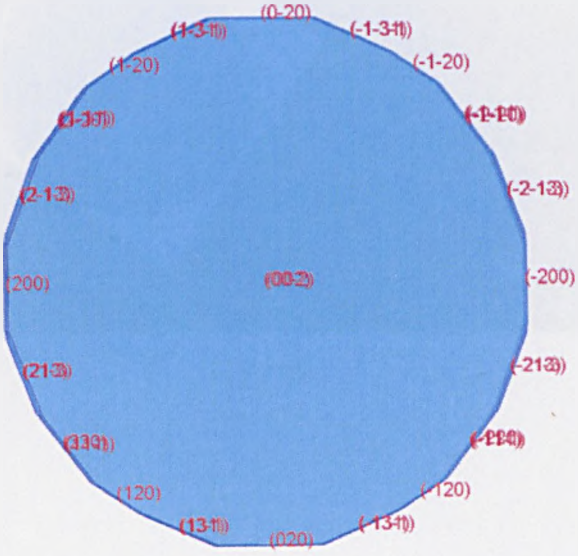
(0-20)
(1-3-1)
(-1-3-1)
(1-20)
(-1-20)
(2-13)
(-2-13)
(200)
(00-2)
(-200)
(21-3)
(-21-3)
(120)
(-120)
(13-1)
(-13-1)
(020)

(c)

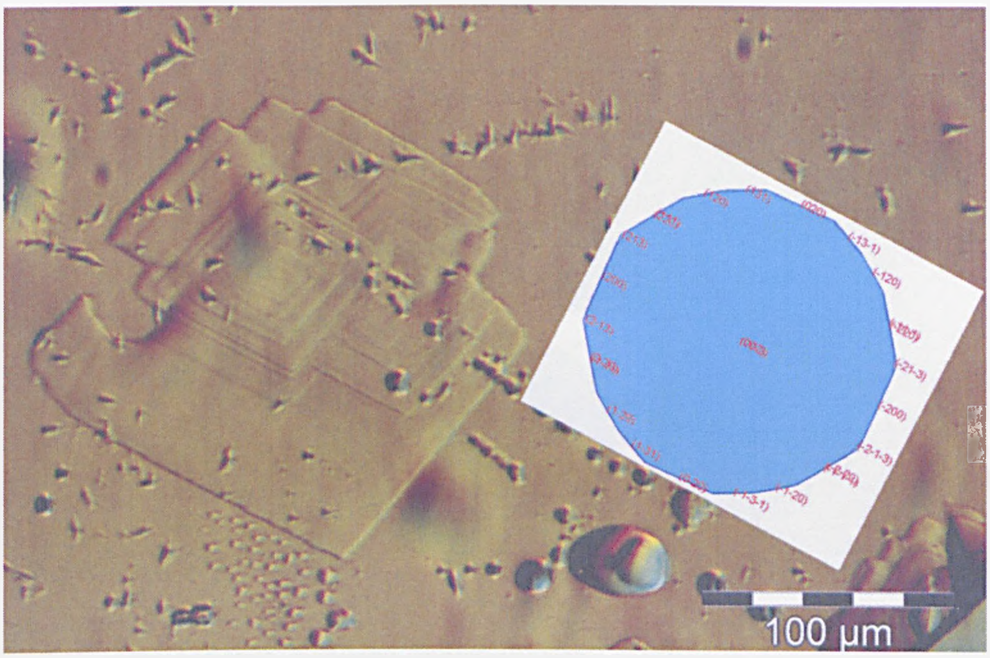

(d)

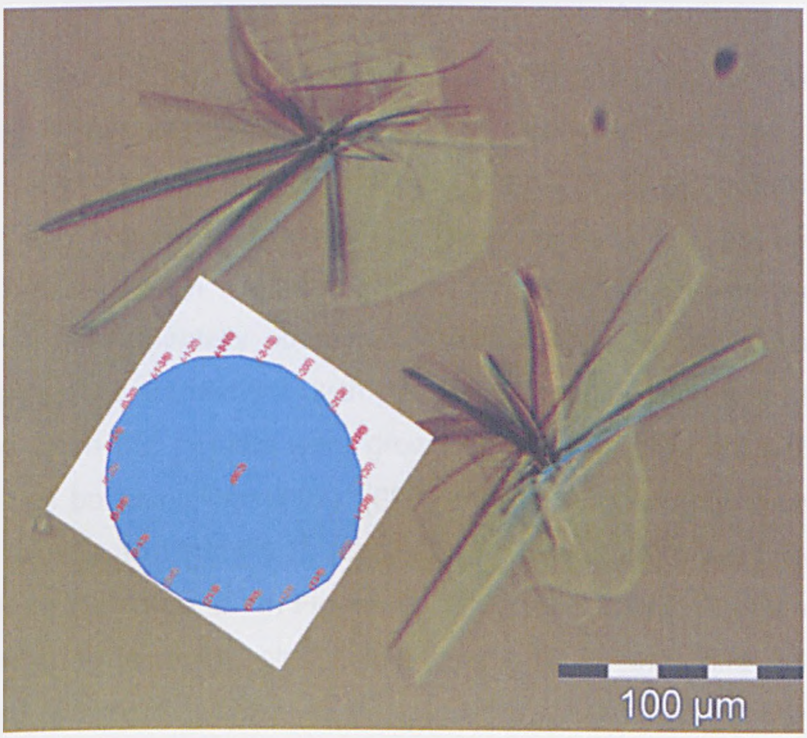

(e)

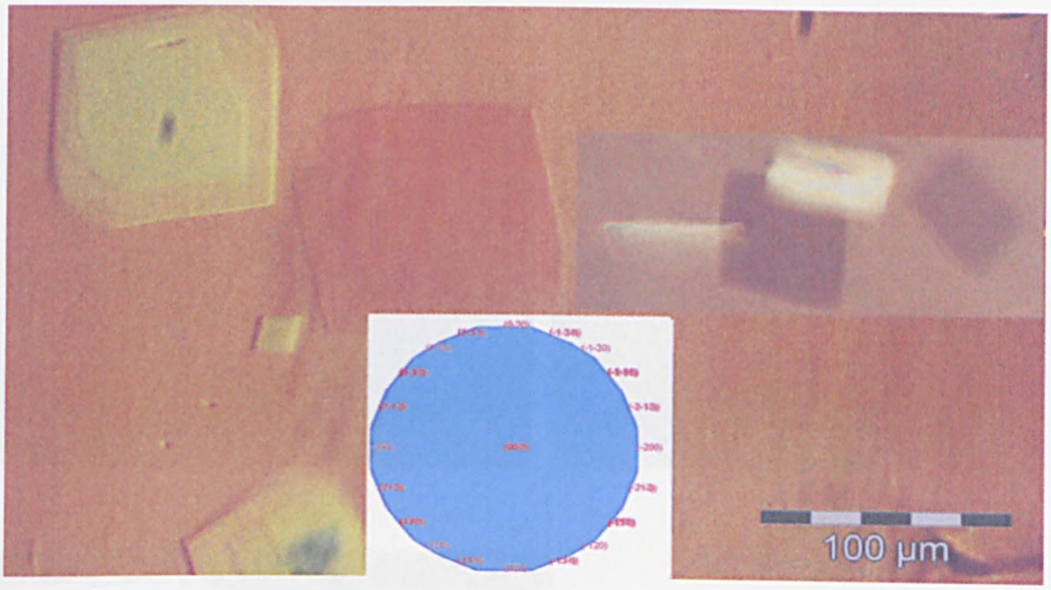

(f)

Figure 6.13: Comparisons between morphorlogical predictions for monoclinic (a) and orthorhombic (b) methyl stearate and experimentally observed crystal shapes grown from toluene (d), dodecane (e) and methyl oleate (f). Crystal orientation chart of monoclinic methyl stearate (c).

In Figure 6.13 (a) and (b) , the angle between (011) and (111) for monoclinic and orthorhombic methyl stearate is 126° and 128° respectively, and this difference is caused by lower aspect ratio between (011) and (111) for monoclinic methyl stearate. In the images of experimental observation, it can be seen that the dominante face of methyl stearate grown from different solvents was still (002) face, and the experimentally obersered crystal shapes of methyl stearate were plate-like shape in agreement with simulated results, however some faces disappeared when the crystals were grown from these three solvents. In Figure 6.13 (d), it can be found that (002), (020) and (213) were main faces of methyl stearate in toluene. In Figure 6.13 (e), (002), (020) and (200) were main faces of methyl stearate in dodecane. In Figure (f), (002), (020) and (111) were main faces of methyl stearate in methyl oleate. In Figure 6.13 (d) the spiral on the crystal surface were observed clearly, so the growth mechanism of methyl stearate is birth and spread.

6.5.4 Comparison of morphology between methyl stearate and methyl palmitate

Compared with the predicted morphologies of methyl stearate, the observed habits of methyl palmitate in toluene were very close to the results of simulation shown in Figure 6.14.

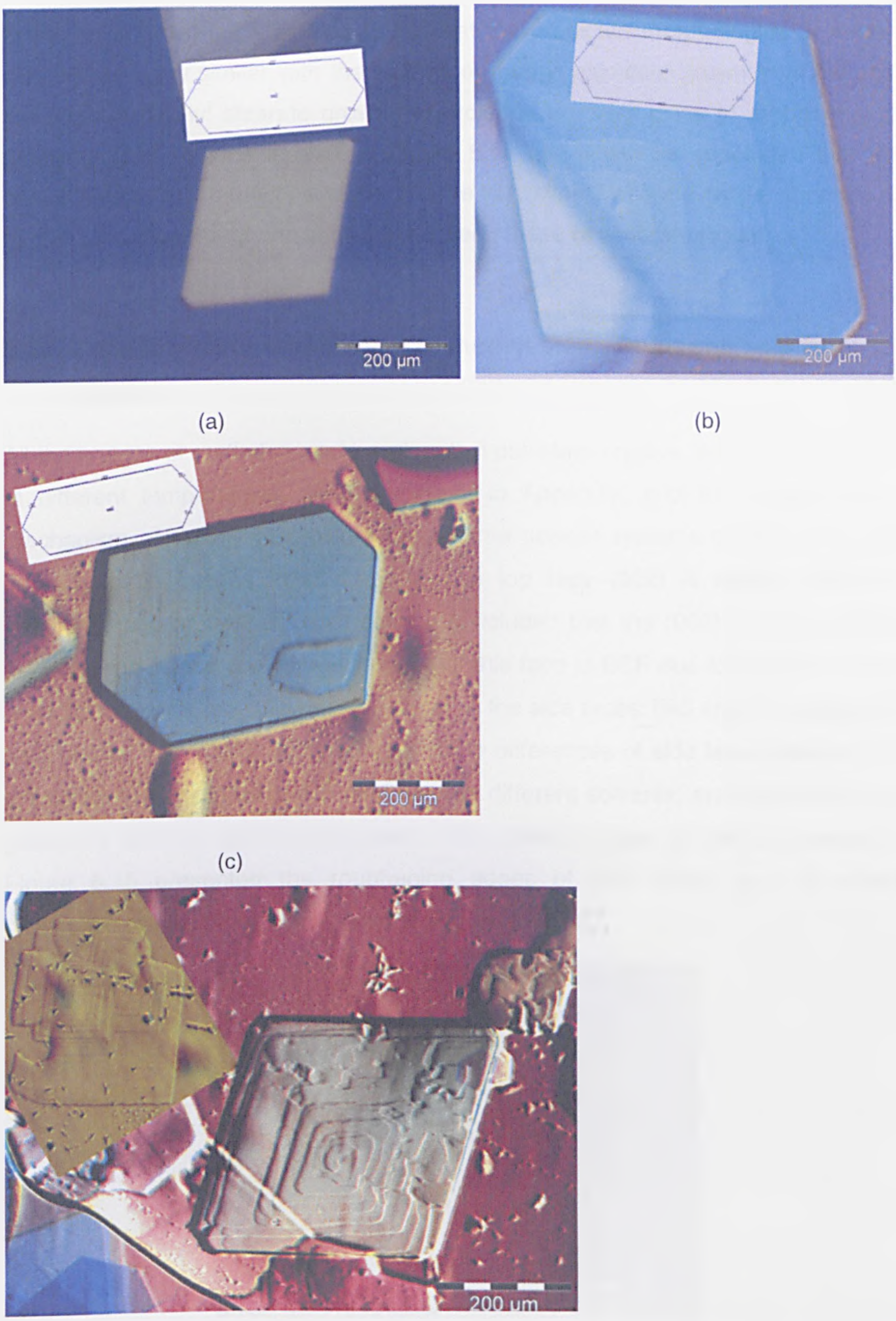

(a) (b)

(c)

(d)

Figure 6.14: Comparison between predicted morphologies of methyl stearate and habits of methyl palmitate grown from toluene: (a)-(c); comparison between morphologies of methyl stearate and methyl palmitate both grown from toluene (d).

In Figure 6.14 (a)-(c), it can be found that the predicted morphologies of methyl stearate are very similar with the shapes of methyl palmitate grown from toluene, the habit of methyl stearate grown from toluene are very close to that of methyl palmitate from toluene as well in Figure 6.14 (d). It can be concluded that the crystal structure of methyl palmitate may be very similar with the crystal structure of methyl stearate through the similarity between these two morphologies.

6.5.5 Crystal growth mechanism of methyl stearate crystallized from solution

All the images of methyl stearate and methyl palmitate crystals in different solvents at different temperatures were presented in Appendix, and the crystal growth mechanism of methyl stearate in these three solvent systems can be assessed through these images in cold room. The top face (002) is always the most important face of crystals, so it can be concluded that the (002) is slow growing face and the crystal growth mechanism of this face is BCF due to the clear screw dislocation on this face. The growth rates of the side faces: hk0 and hkl faces were much faster than (002), so there were some differences of side faces between the predicted morphologies and crystal habit in different solvents, and the faces were grown by BCF or continuous growth. The crystal images of methyl stearate in Figure 6.15 presented the roughening edges of side faces, and the screw dislocation of side faces were shown in Figure 6.10 (a).

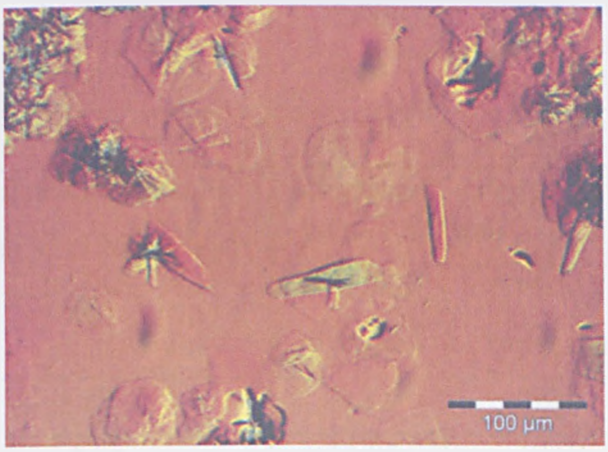

Figure 6.15: Crystal images of 10% methyl stearate in dodecane at 10°C showing the roughening edges of side faces and agglomeration of crystals

Due to different supsaturation in different solvents, the growth mechanism of side faces of methyl stearate may be BCF growth in large crystals or continuous growth in small crystals.

6.5.6 Modelling solvent effect on crystal habit

From the observation of crystal habit of methyl stearate and methyl palmitate in different solvents in the cold room, the effects of solvents on growth morphology were presented. A rough analysis of these effects was carried out using the SYSTEM SEARCH program, and the interactions between the molecular pairs of methyl stearate and toluene, methyl stearate and dodecane are calculated. Table 6.13 summarized the calculated results from simulations and the interaction energies and modified attachment energies are presented. In Table 6.13, it can be seen that the attachment energies of methyl stearate with respect to the three major faces were reduced due to the interaction energy of solvent, and had the biggest effect on the (002) face. The predicted morphologies of methyl stearate in different solvent systems were plotted, and it can be seen that there is no significant change of habit from Figure 6.14, except the thickness of crystals.

Table 6.13 Calculated attachment energies for dominant crystal habit faces of monoclinic methyl stearate together with recalculated attachment energies from solvent-mediated surface energies in 80% toluene solvent, 50% toluene solvent and 90% dodecane solvent.

Face	Calculated attachment energy in vacuum (kJ mol^{-1})	Interaction energy (kJ mol^{-1})		
		20% MS (toluene)	50% MS (toluene)	10% MS (dodecane)
(0 0 2)	-1.59	-3.00	-3.16	-3.53
(0 1 1)	-14.51	-2.64	-2.79	-2.91
(1 1 1)	-23.32	-2.58	-2.76	-3.01

Face	Calculated attachment energy in vacuum (kJ mol^{-1})	Attachment energy in different solvent systems (kJ mol^{-1})		
		20% MS (toluene)	50% MS (toluene)	10% MS (dodecane)
(0 0 2)	-1.59	-0.84	-0.80	-0.71
(0 1 1)	-14.51	-13.85	-13.81	-12.78
(1 1 1)	-23.32	-22.68	-22.63	-22.56

The morphologies of methyl stearate in Figure 6.16 are very similar to those predicted from morphology in a vacuum; however it had been found that the thickness of habit is changing with the change of solvent system. The predicted morphologies of methyl stearate were plotted from the same orientation, and the aspect ratio in Table 6.14 show that the thickness of crystal in vacuum is largest. The aspect ratio is ration between (002) and (011), so the higher value of aspect ratio means the crystal becomes thinner. The increase of methyl stearate in toluene led to the decrease of thickness of crystals, and the addition of dodecane led to the decrease of thickness of crystals compared with the thickness of crystals in vacuum.

Table 6.14 Aspect ratio of face (002) and (011) for morphologies of methyl stearate simulated in different solvents

Aspect ratio	Morphology in vacuum	Morphology in toluene (20%MS)	Morphology in toluene (50%MS)	Morphology in dodecane (10%MS)
	9.12	16.49	17.26	18.00

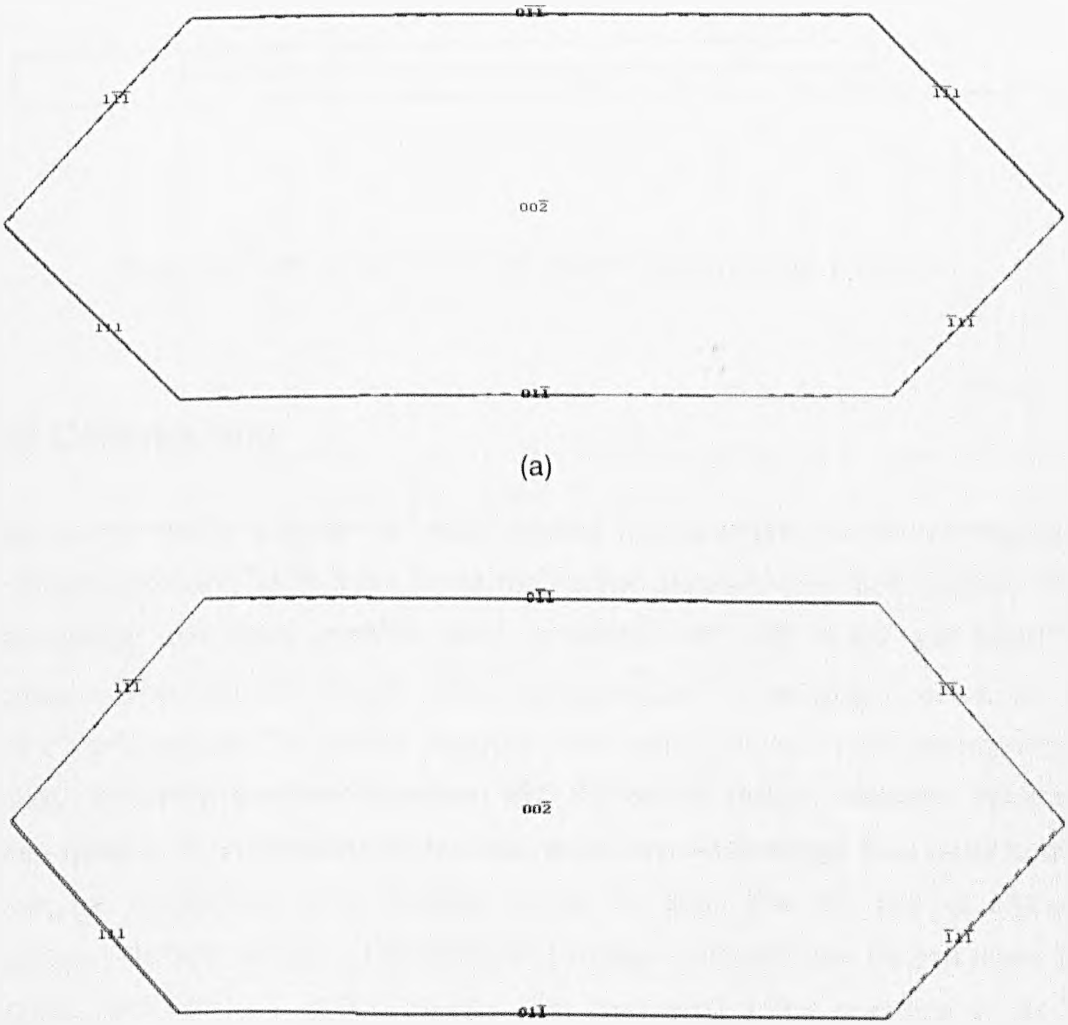

(a)

(b)

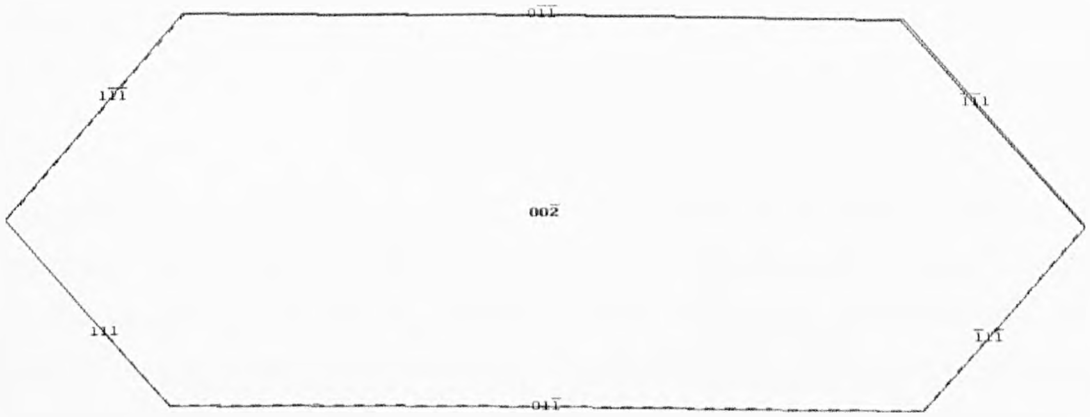

(c)

Figure 6.16: Predicted morphologies modified by solvent-mediated: (a) 20% methyl stearate in toluene; (b) 50% methyl stearate in toluene; (c) 10% methyl stearate in dodecane.

Figure 6.17: Morphology of methyl stearate observed from y direction.

6.6 Conclusions

This report details a modeling study applied to investigate the morphology and intermolecular and atom-atom bond for methyl stearate (two polymorphs). The morphology and bond analysis were calculated with AE mode and HABIT98 software. The van der Waals force, increasing with the limited radius, is the dominant interaction for methyl stearate. The number of non-zero intermolecular bonds for methyl stearate increased with the limited radius; however, there are three types of intermolecular interactions which are much bigger than other bonds. From the atom-atom bond analysis, it can be seen that the pair of aliphatic hydrogen-aliphatic carbons, and aliphatic hydrogen and aliphatic carbon make the biggest contribution to lattice energy. The calculated lattice energies of methyl stearate are close to the experimental sublimation enthalpies from the literature. The calculations of total cluster energies for both two polymorphs revealed that the monoclinic form are stable form. The predicted morphologies for two polymorphs are nearly the same, and it may be caused by the huge d-spacing of the (002) face.

This chapter provided photographs of methyl stearate and methyl palmitate in different solvent systems and different temperatures from the cold room laboratory, and the experiment observation validates the morphological prediction that the shape of methyl stearate is a plate-like. The effects of solvents and temperatures on crystal habit and crystal size of methyl stearate and methyl palmitate were examined from the results of image analysis.

The system search method provided rough analysis on the solvent-mediated effect on morphologies of methyl stearate.

CHAPTER 7

Crystallization Kinetics Studies Using Turbidmetric Detection

Summary:

The nucleation kinetics of methyl stearate without and with additives in methyl oleate were examined involving measurements of the solubility, meta-stable zone width and induction times.

7.1 Introduction

The nucleation process is important for the crystallization behaviour of methyl stearate in methyl oleate, and the aim of this chapter is to repeat investigations of the effect of additives on the nucleation process of methyl stearate crystallising in methyl oleate. One traditional way of describing the nucleation process is an empirical relationship derived by Nyvlt [59] relating the measured metastable zone width (MSZW) to the solution cooling and heating rate. A series of important nucleation parameters such as nucleation order and nucleation constant can be derived from this relationship. The MSZW is a key characteristic of the nucleation process, and it can be obtained from the experiment carried out using the polythermal mode. Induction time to nucleation is inversely proportional to the rate of nucleation, and it can be measured from crash cooling experiments from which classical homogeneous nucleation theory can be used to estimate the interfacial tension between the crystalline nucleus and solution, from which the critical nucleus size can be calculated using classical nucleation theory.

Hence, this chapter will provide the results from slow and fast cool crystallization of methyl stearate in methyl oleate. The slow cool experimental results were associated with the empirical relationship to determine MSZW, and the MSZW of methyl stearate in the presence of 8 additives was also determined. The effects of additives on the crystal nucleation rate of methyl stearate in methyl oleate were assessed from the induction time obtained from the crash cool experiments.

7.2 Study of Polythermal Crystallization for Methyl Stearate Crystallizing from Methyl Oleate Solutions

7.2.1 Experimental results

Figure 7.1 shows the optical turbidity profile for methyl stearate in the solution of 100g/l methyl oleate carried out using the turbidity probe. The region at which there is a vertical line on the left represents a drop in turbidity at crystallisation temperatures corresponding to the cooling process, whereas the single vertical line represents an increase in turbidity at the dissolution temperature corresponding to

the heating phase of the operation. The distance in between the two regions represents the MSZW.

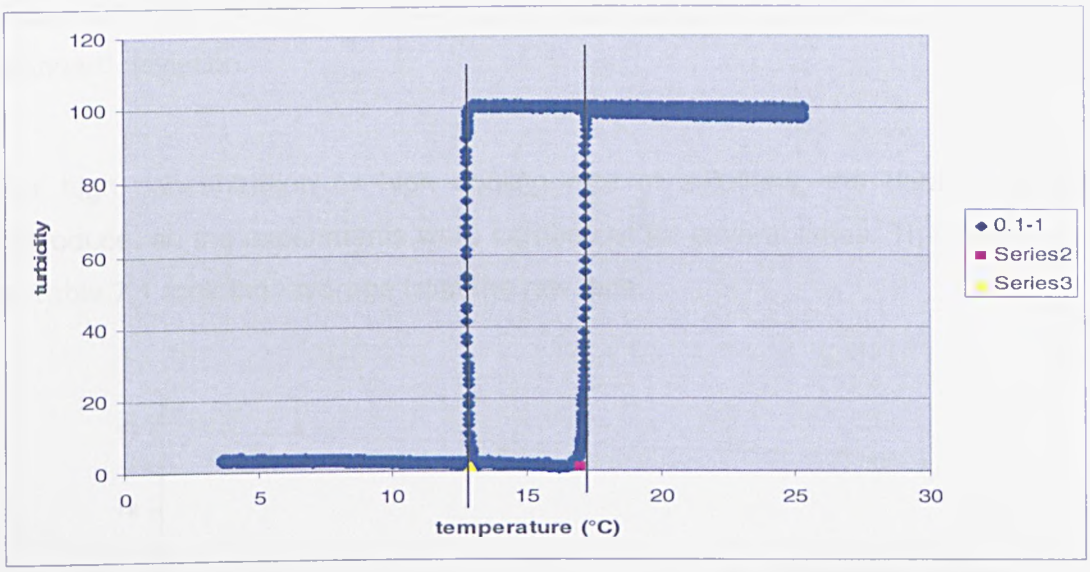

Figure 7.1: Sample turbidimetric profile for polythermal cooling crystallization of 100g/l methyl stearate in methyl oleate: function of temperature vs turbidity

Table 7.1 Dissolution and nucleation with standard deviation in the bracket onset temperatures and corresponding MSZW measurements for methyl stearate in methyl oleate.

Concentration (g/l)	Cooling rate	Nucleation temperature (°C)	Dissolution temperature (°C)	MSZW (°C)
100	0.1	12.8 (0.15)	17.0 (0.04)	4.2
	0.25	12.2 (0.12)	16.7 (0.11)	4.5
	0.5	11.7 (0.15)	16.7 (0.17)	5.0
150	0.1	16.2 (0.00)	19.6 (0.08)	3.4
	0.25	15.6 (0.11)	19.6 (0.08)	4.0
	0.5	15.1 (0.12)	19.5 (0.15)	4.4
200	0.1	18.2 (0.09)	21.7 (0.06)	3.5
	0.25	17.9 (0.11)	21.7 (0.04)	3.8
	0.5	17.5 (0.18)	21.7 (0.09)	4.2
250	0.1	20.3 (0.14)	23.6 (0.05)	3.3
	0.25	19.9 (0.21)	23.6 (0.17)	3.7
	0.5	19.5 (0.05)	23.5 (0.16)	4.0

The MSZW was measured at four concentrations and 3 cooling rates are listed in Table 7.1, the dissolution and nucleation temperature at 0°C/min are shown in Figure 7.2. To avoid the error during the experimental process, the slow cooling experiments were repeated more than three times, the standard deviation of nucleation and dissolution temperatures were calculated and shown in brackets in Table 7.1 this revealed that the experimental data are reliable due to the low standard deviation.

For high concentration or high cooling rate of solutions, the data is hard to reproduce, so the experiments were carried out for several times. The data shown in Table 7.1 took the average from the raw data.

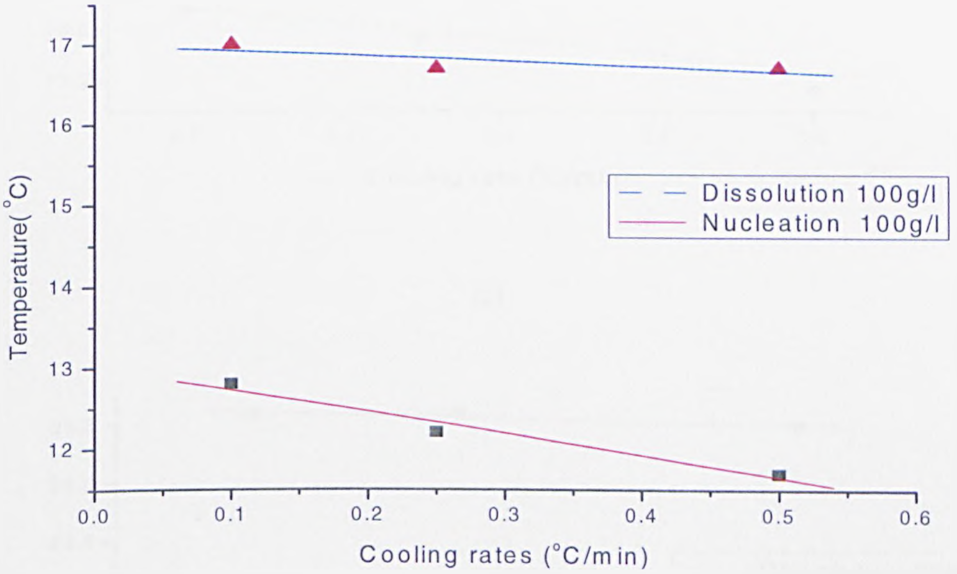

(a)

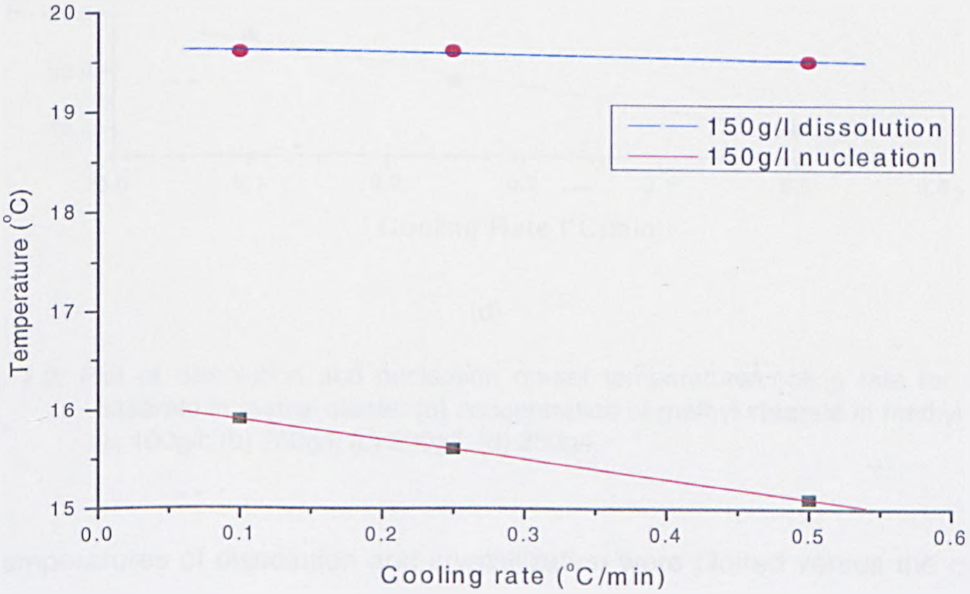

(b)

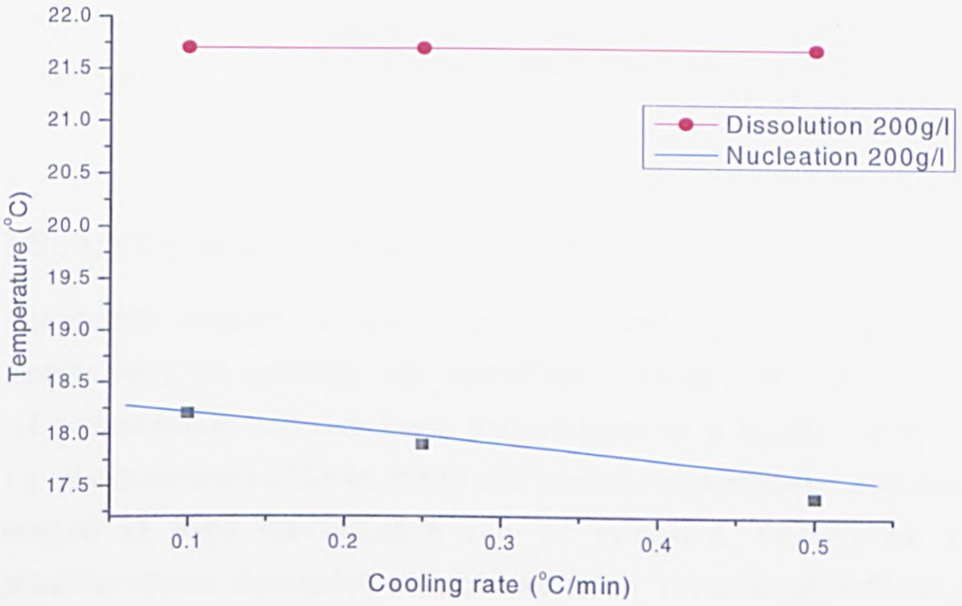

(c)

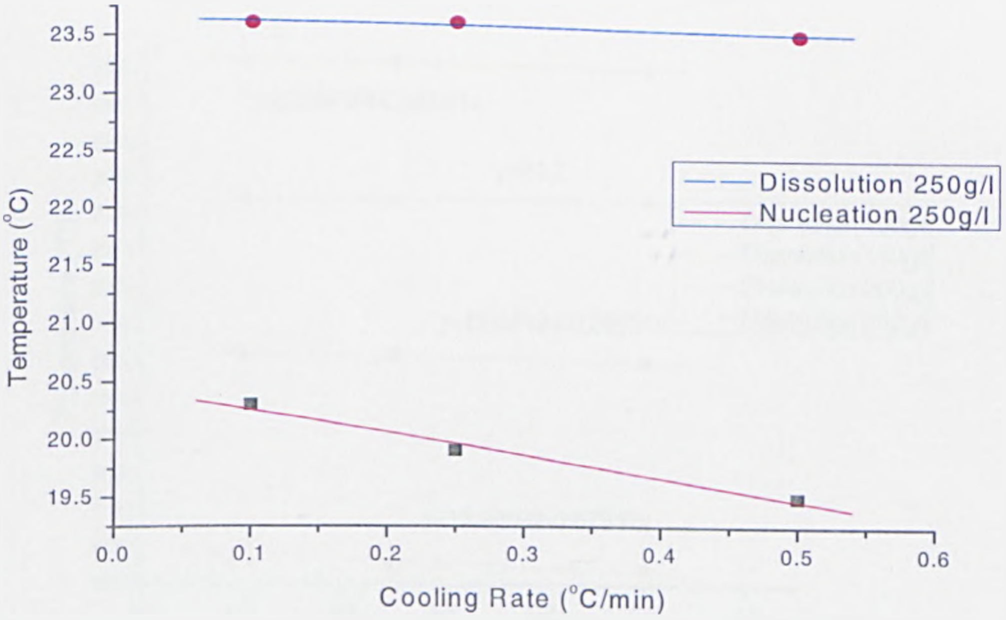

(d)

Figure 7.2: Plot of dissolution and nucleation on-set temperature/cooling rate for methyl stearate in methyl oleate: (a) concentration of methyl stearate in methyl oleate is 100g/l; (b) 150g/l; (c) 200g/l; (d) 250g/l.

The temperatures of dissolution and crystallization were plotted versus the cooling rates in Figure 7.2. It was found that the crystallization temperatures scatter more considerably compared to dissolution temperatures, which is expected as the dissolution temperature is a thermodynamic parameter, whilst the crystallization temperature is influenced by the kinetics. The MSZW for methyl stearate in methyl oleate can be seen to increase with the higher cooling rate and decrease with the higher concentration.

7.2.2 Solubility and crystallization curves

The relationship between solution concentration and MSZW can be established from constructing the solubility and crystallization curves. After extrapolation the plots of crystallization and dissolution temperatures as a function of the cooling rate, i.e. at extrapolated 0°C/min, the kinetic limits for crystallization and dissolution temperature at each concentration can be evaluated. Plotting the solution concentration versus dissolution temperature at an extrapolated 0°C/min cooling rate gives the solution solubility curve at the system kinetic limit, the same with the plot of solution concentration versus nucleation temperature. For methyl stearate in methyl oleate solution the graphical analysis is given below:

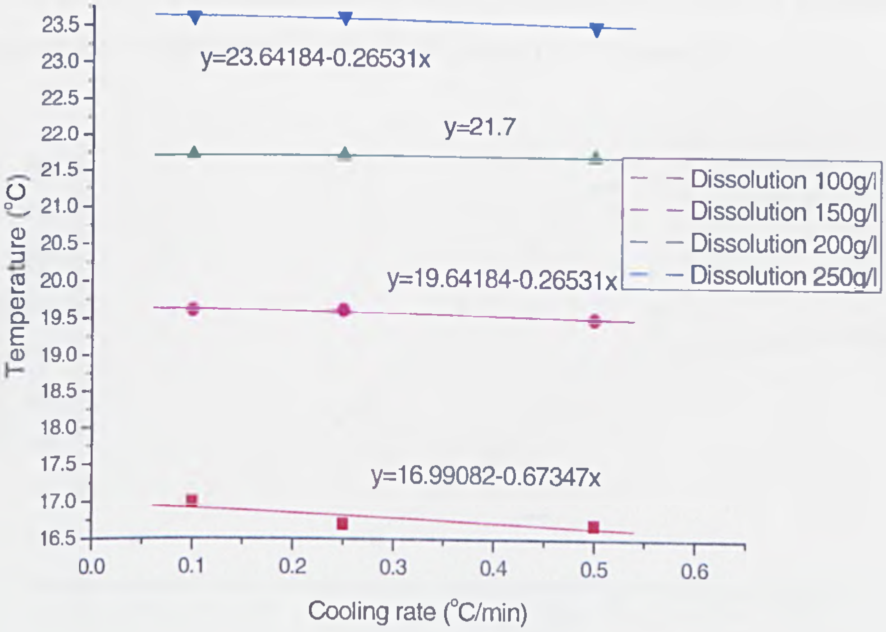

Figure 7.3: Plot of dissolution on-set temperature/cooling rate for methyl stearate in methyl oleate solution showing gradient equations

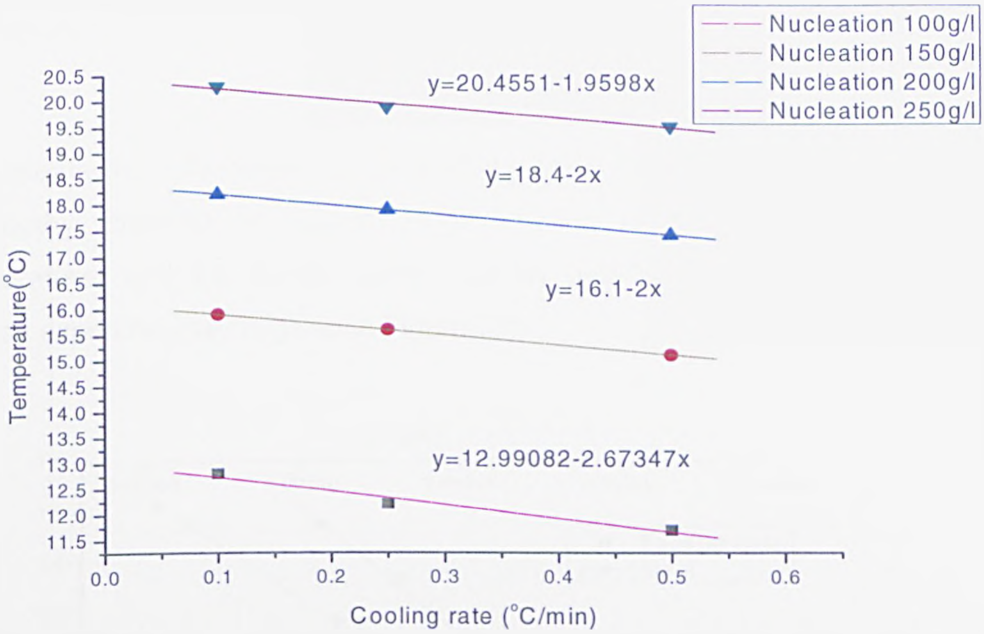

Figure 7.4: Plot of nucleation on-set temperature/cooling rate for methyl stearate in methyl oleate solution showing gradient equations

From the y intercepts taken from the equations of the interpolation lines shown in Figures 7.3 and 7.4 the solubility and the crystallisation curves at the kinetic limit (extrapolated 0°C cooling rate) have been plotted in Figures 7.5:

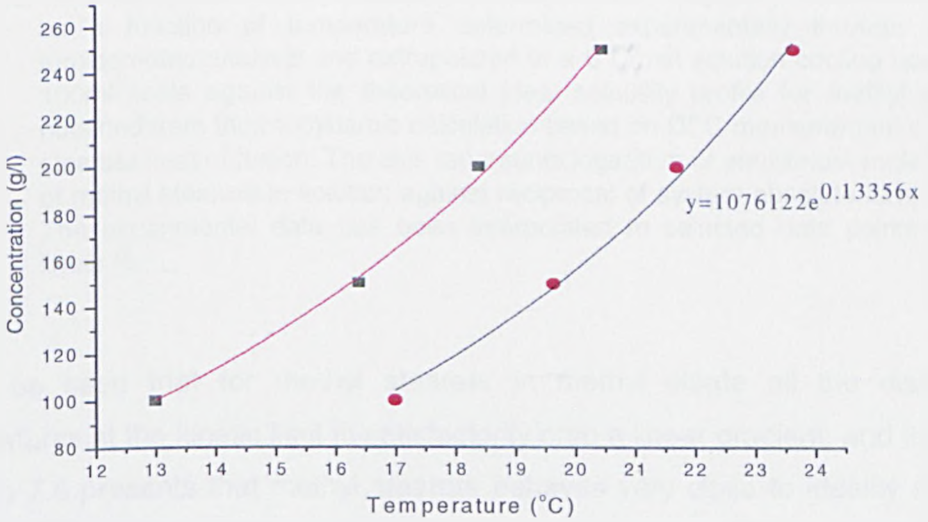

Figure 7.5: Solubility (●)and crystallization (■)curves for methyl stearate in methyl oleate at an extrapolated 0°C/min cooling rate.

The distance between the two curves represents the meta-stable zone width at the kinetic limit. The trend of MSZW for methyl stearate in methyl oleate solutions at kinetic limit is the same as that from the plot of dissolution/ nucleation versus cooling rates, MSZW decrease at higher concentration.

To evaluate the solution ideality of methyl oleate studied the ideal solubility profile for methyl stearate is plotted as a function of temperature (reciprocal of temperature) and the experimental solubility plot for the methyl oleate solution studied experimentally is given in Figure 7.6

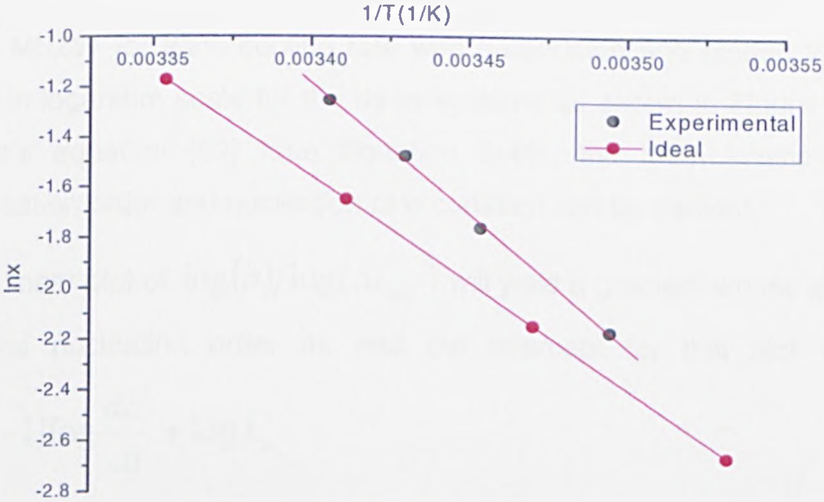

Figure 7.6: Van't Hoff plot for methyl stearate in methyl oleate comparing the solubility profile as a function of temperature determined experimentally through solution turbidometric analysis and extrapolated to a 0°C/min solution cooling rate at the 100ml scale against the theoretical ideal solubility profile for methyl stearate obtained from thermodynamic calculation based on DSC measurement of methyl stearate heat of fusion. The axis represents logarithm of equilibrium mole fraction of methyl stearate in solution against reciprocal of system absolute temperature. The experimental data has been interpolated to selected data points of best linear fit.

It can be seen that for methyl stearate in methyl oleate all the dissolution temperatures at the kinetic limit fit satisfactorily onto a linear gradient, and the trend in figure 7.6 presents that methyl stearate behaves very close to ideality and it is demonstrated that methyl stearate may behave slightly greater than ideal, i.e. at a given temperature the equilibrium concentration of methyl stearate in methyl oleate may be slightly higher than that predicted by the ideal solubility model. This suggests that methyl stearate solute-solute interactions are slightly weaker than the solute-solvent interactions that methyl stearate form with methyl oleate. Base on the Equation (2-18), the slope ($\frac{\Delta H_{diss}}{R}$) and intercept ($\frac{\Delta S_{diss}}{R}$) of the plot of $\ln x$ versus T^{-1} can be experimentally derived solubility data. So the value of $\Delta H_{diss}/\Delta S_{diss}$ is 0.00329.

7.2.3 Nucleation order and nucleation rate constant as a function of concentration

The MSZW for each cooling rate was determined and plotted versus the cooling rate in logarithm scale for the three systems as shown in Figure 7.7. According to Nyvlt's equation [59] (see Equation 2-48), the main kinetic parameters, the nucleation order and nucleation rate constant can be derived.

The linear plot of $\log(b)/\log(\Delta t_{\max})$ will yield a gradient whose slope will be equal to the nucleation order m, and the intercept for this plot will be equal to

$$(m-1)\log\frac{dc^*}{dt}+\log k_n. \tag{7-1}$$

Thus this term can be rearranged to obtain the nucleation constant k_n, but the $\frac{dc^*}{dt}$ term should be calculated first. The slope of the solubility curve can be evaluated from the fit equation of the curve, and the slope is approxiomated at each concentration via employing the following formula:

$$slope=\frac{y(x+h)-y(x)}{h} \tag{7-2}$$

where: h is a small increment, set at 0.1°C, y(x+h) is the equilibrium concentration at 0.1 0.1°C above the nucleation temperature, y(x) is the nucleation concentration (c*).

The nucleation order decreases with increasing the concentration but it does not have very high values generally for the four concentrations of methyl stearate in methyl oleate studied, which determines high rate dependency of the MSZW. The nucleation rate constant increases with the increase of the concentration:

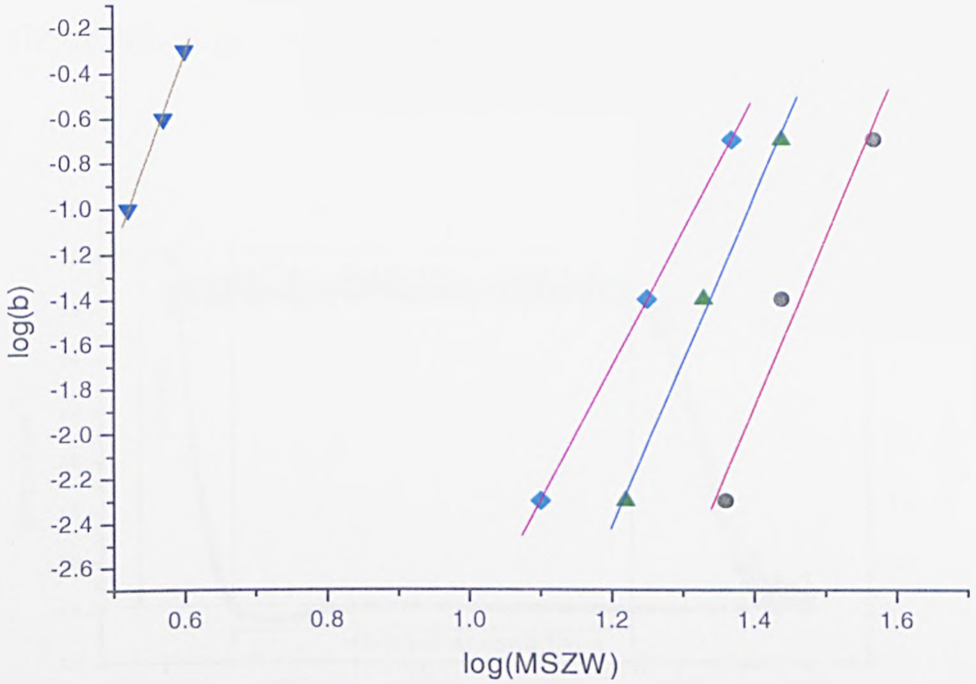

Figure 7.7: The kinetic parameters corresponding to different concentrations of nucleation can be determined using the Nyvlt method as the MSZW was plotted vs the cooling rate in logarithmic coordinates. The order of nucleation was determined as the slope of the linear plot: (●) 100 g/l methyl stearate in methyl oleate; (▲) 150g/l methyl stearate in methyl oleate; (■) 200g/l methyl stearate in methyl oleate; (▼) 250 g/l methyl stearate in methyl oleate.

Table 7.2 The order of nucleation was determined for four concentrations of methyl stearate in methyl oleate solution as the slope of the linear relationship log (MSZW) vs. log (b) and the error of the least square fit was shown

Concentration (g/l)	Linear plot relationship	Error of the fit
100	Y=-12.25119+7.40356X	0.97
150	Y=-11.13939+7.27273X	0.99
200	Y=-8.81858+5.92896X	0.99
250	Y=-8.82807+6.30977X	0.99

Table 7.3 Nucleation order and nucleation rate constant for methyl stearate in methyl oleate

Concentration (g/l)	$\frac{dc^*}{dt}$ (g/l/°C)	Nucleation order (min^{-1})	Nucleation rate constant
100	15.5	7.40	1.14E-13
150	23.3	7.27	3.84E-14
200	31.1	5.93	6.49E-12
250	38.8	6.04	1.43E-12

7.3 Study of Isothermal Crystallization for Methyl Stearate Crystallizing from Methyl Oleate Solutions

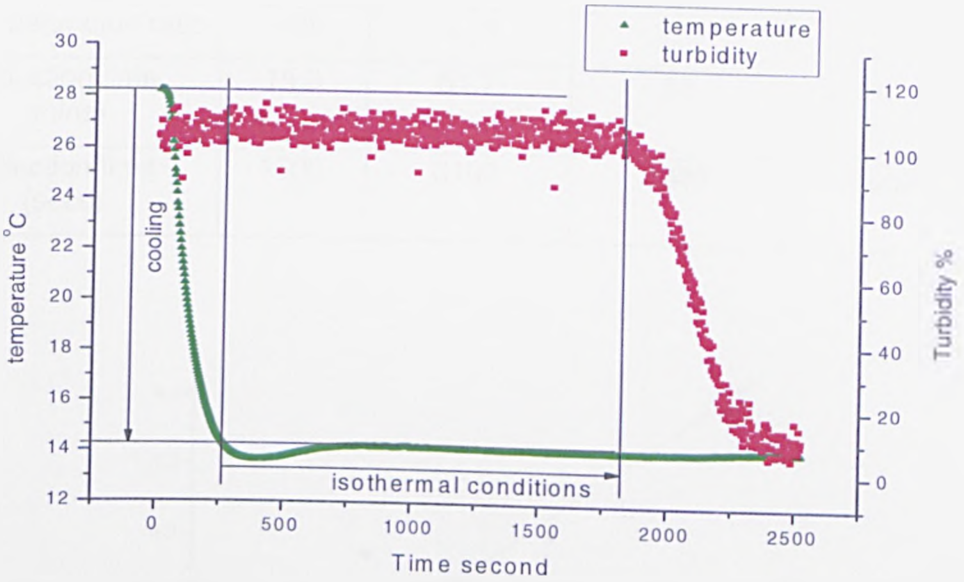

Figure 7.8: Induction time is the time between reaching constant supersaturation and appearance of first nuclei of methyl stearate.

The saturated solution of methyl stearate in methyl oleate prepared in advance was rapidly (crash) cooled (cooling rate >1) to a given temperature within the MSZW which was determined using a new turbidity probe and maintained at isothermal conditions until the turbidity rose quickly indicating the onset of crystallization.

The relationshipe between induction time and supersaturation was used to calculate the interfacial tension using Equation (2-48). In Equation (2-48), the molecular volume of methyl stearate, equal to 490Å^3. The data ln(τ) vs. $\frac{1}{T^3(\ln\sigma)^2}$ were fitted with a straight line, as shown in Figure 7.9 and from its slope the interfacial tension can be derived to $1.79\times10^{-3}\ J/m^2$ for concentration 100g/l, and then the determined interfacial energies were used to calculate the size of the critical nucleus shown in table 7.5 at one concentration using Equation (2-36). It can be seen that the critical nucleus size increase with the decrease of supersaturation.

Table 7.4 Induction time of 100g/l methyl stearate in methyl oleate for two bottom temperatures

	Concentration 100g/l			
Bottom temperature (°C)	13.70	14.25	14.70	15.00
Supersaturation ratio	1.88	1.73	1.61	1.53
Induction time (mins)	18.3	51.7	55	80
Induction time (secs)	1500	3100	3300	4800

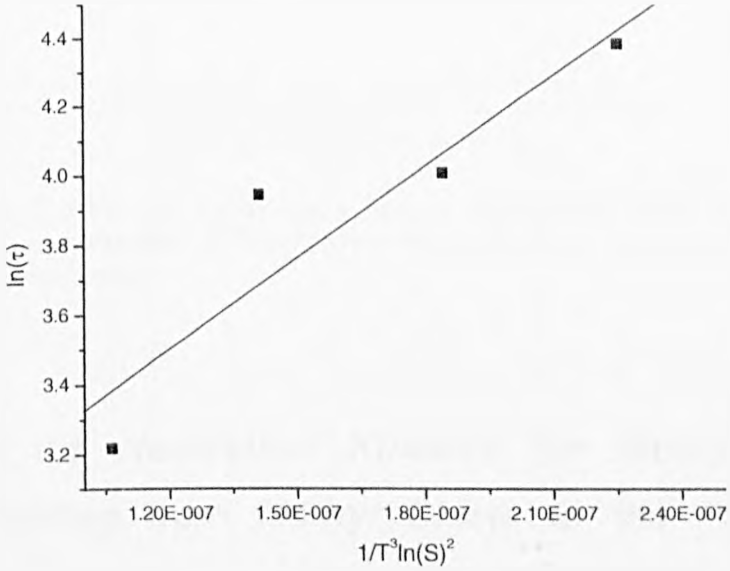

Figure 7.9: Interfacial tension was calculated from the slope of the line induction time vs supersaturation for two different concentrations

Table 7.5 Critical nucleus size in terms of spherical radius in the crystal nucleus were calculated as a function of temperature and supersaturation at the concentration of 100g/l

Temperature (°C)	Supersaturation	Critical nucleus size radius, Å
		100g/l
13.70	1.88	14.12
14.25	1.73	16.23
14.70	1.61	18.66
15.00	1.53	20.87

The result shows, as expected, that high critical nucleus size will be associated with high temperature and low supersaturation (Figure 7.18).

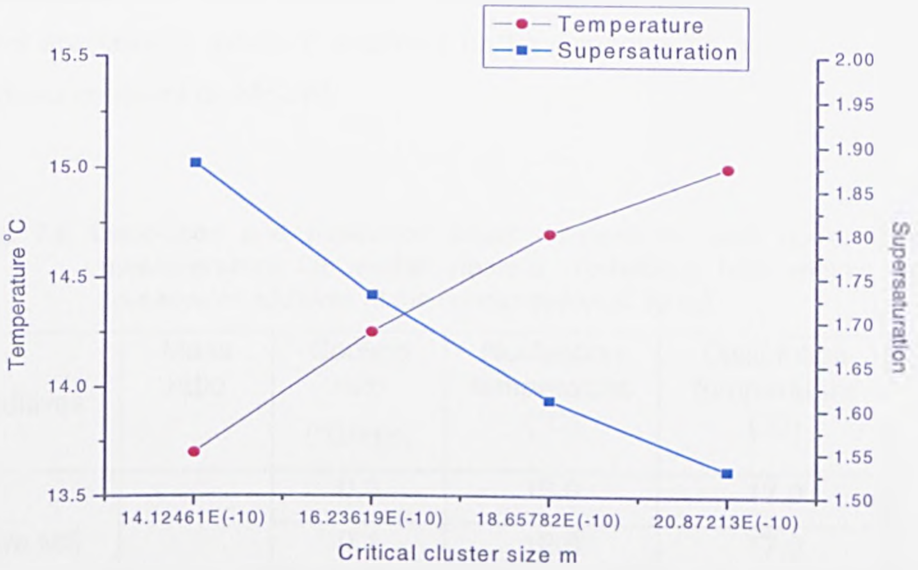

Figure 7.10: Size of the critical nucleus as a function of temperature and supersaturation at the concentration of 100g/l reveal to be high at high temperature and low supersaturation

7.4 Study of Nucleation Kinetics for Methyl Stearate Crystallizing from Methyl Oleate in the Presence of Additives

Eight additives were used to assess the effect on MSZW and nucleation temperature in this study. Besides two simple additives: ethyl stearate and monostearin (Figures 4.3 and 4.4). There are six types of industrial additives from Infineum:

- 16A16
- 16A18
- 18A18
- 16B16
- 16B18
- 18B18

7.4.1 Experimental results

The results from slow cooling experiments in the presence of eight additives at a concentration of 100g/l of methyl stearate in methyl oleate are shown in Table 7.6. There are several kinds of additives in the experiments qualifying the effects of additives contents on MSZW.

Table 7.6 Dissolution and nucleation onset temperatures and corresponding MSZW measurements for methyl stearate crystallizing from methyl oleate in the presence of additives at the concentration of 100g/l

Additives	Mass ratio	Cooling rate (°C/min)	Nucleation temperature (°C)	Dissolution temperature (°C)	MSZW (°C)
Pure MS		0.0	13.0	17.0	4.0
		0.1	12.8	17.0	4.2
		0.25	12.2	16.7	4.5
		0.5	11.7	16.7	5.0
18A18	0.5%	0.0	12.7	17.1	4.4
		0.1	12.5	17.0	4.5
		0.25	11.9	17.1	5.2
		0.5	11.3	16.8	5.5
	1.0%	0.0	11.3	17.1	5.8
		0.1	11.0	17.0	6.0
		0.25	10.4	17.1	6.7
		0.5	9.7	16.8	7.1
	1.5%	0.0	9.4	17.2	7.8
		0.1	9.2	17.0	8.0
		0.25	8.7	17.0	8.3
		0.5	8.2	16.6	8.4
	2.0%	0.0	9.3	17.0	7.7
		0.1	9.1	17.0	7.9
		0.25	8.5	17.0	8.5
		0.5	8.1	16.9	8.8
16A16	1.3%	0.0	13.3	17.2	3.9
		0.1	13.0	17.0	4.0
		0.25	12.1	16.7	4.6
		0.5	11.3	16.2	4.9
		0.0	13.5	17.1	3.6

	2.0%	0.1	13.2	17.0	3.8
		0.25	12.4	16.8	4.4
		0.5	11.7	16.5	4.8
	5.0%	0.0	13.5	17.3	3.8
		0.1	13.1	17.0	3.9
		0.25	12.4	17.0	4.6
		0.5	11.3	16.2	4.9
16B18	0.5%	0.0	10.7	17.6	6.9
		0.1	10.5	17.3	6.8
		0.25	10.1	17.5	7.4
		0.5	9.5	16.9	7.4
	1.0%	0.0	10.1	17.4	7.3
		0.1	10.1	17.2	7.1
		0.25	9.5	17.2	7.7
		0.5	9.45	16.7	7.3
16A18	0.5%	0.0	12.2	16.9	4.7
		0.1	12.0	16.9	4.9
		0.25	11.7	16.8	5.1
		0.5	11.3	16.7	5.4
	1.0%	0.0	11.8	17.0	5.2
		0.1	11.6	16.9	5.4
		0.25	11.2	16.8	5.6
		0.5	10.8	16.5	5.7
	2.0%	0.0	10.0	17.1	7.1
		0.1	10.0	17.0	7.0
		0.25	9.6	17.0	7.4
		0.5	9.4	16.8	7.4
	5.0%	0.0	7.9	17.2	9.3
		0.1	7.7	17.0	9.3
		0.25	7.2	17.0	9.8
		0.5	6.8	16.5	9.7
16B16	0.5%	0.0	10.7	16.1	5.4
		0.1	10.5	16.1	5.6
		0.25	10.1	15.9	5.8
		0.5	9.5	15.9	6.4
	1.0%	0.0	9.6	16.7	7.1
		0.1	9.4	16.5	7.1

		0.25	9.0	16.7	7.5
		0.5	8.4	16.3	7.9
	2.0%	0.0	7.4	16.8	9.4
		0.1	7.4	16.7	9.3
		0.25	7.2	16.5	9.4
		0.5	7.1	16.2	9.1
18B18	0.5%	0.0	11.4	18.2	6.8
		0.1	11.2	18.2	7.0
		0.25	10.7	18.2	7.5
		0.5	10.3	18.1	7.8
Ethyl stearate	10.0%	0.0	13.2	17.2	4.0
		0.1	13.1	17.1	4.0
		0.25	12.3	17.0	4.7
		0.5	12.1	16.8	4.7
Mono stearin	0.1%	0.0	14.0	17.4	3.4
		0.1	13.7	17.3	3.6
		0.25	13.1	16.9	3.8
		0.5	12.5	16.7	4.2
	1.0%	0.0	13.7	17.1	3.4
		0.1	13.4	17.1	3.7
		0.25	12.9	16.8	3.9
		0.5	12.2	16.7	4.5

From Table 7.6, it can be seen that the effect of additives is determined by the types and contents of additives in the solution and it is apparent that 16A16, ethyl stearate and mono stearin did not substantially change the MSZW of methyl stearate. This difference would be caused by the function group of additives and ethyl stearate and mono stearin are obviously small compared with other additives increasing MSZW. Although these five additives affect MSZW and the crystallization temperature of methyl stearate in methyl oleate, the degrees of MSZW increased are varied due to different molecular structures of additives, so two factors on the additives effect will be explored.

7.4.2 Factors of the additives effect on MSZW and crystallization temperature

7.4.2.1 Concentration of additives

As can been seen from Table 7.6 the concentration of additives in methyl stearate plays an important role on the effect on MSZW revealing MSZW to increase with the increase of additives from 0.5%. The relationship between MSZW and the concentration of additives for 18A18, 16A18, 18B18, 16B16 and 16B18 are shown in Figure 7.11. Because there is a significant effect of the additive concentration on the MSZW, these studies can be very important for the application of biodiesel to determine the optimized concentration in the solute.

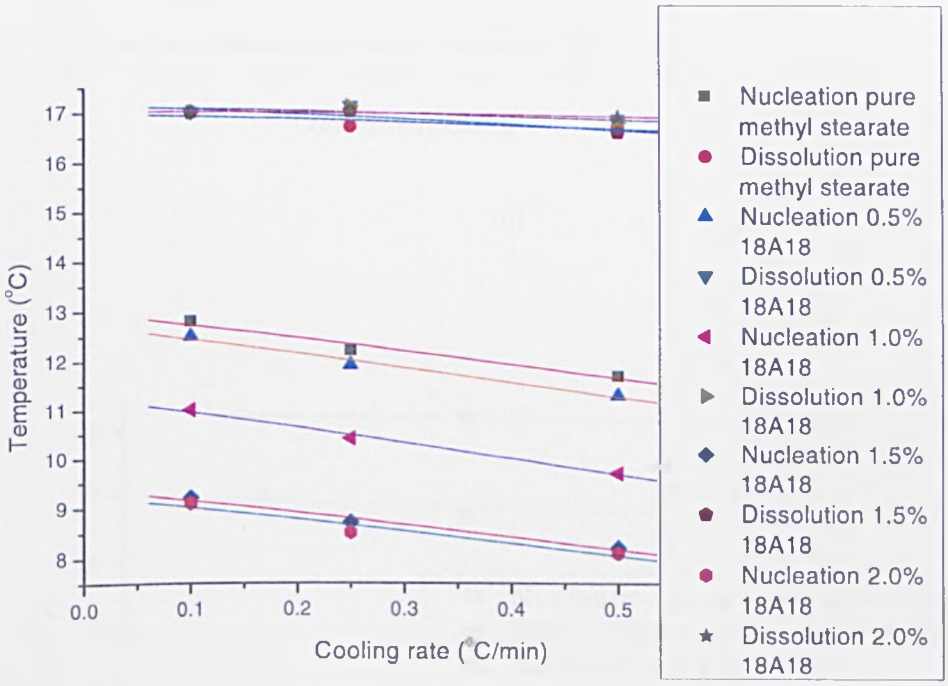

(a)

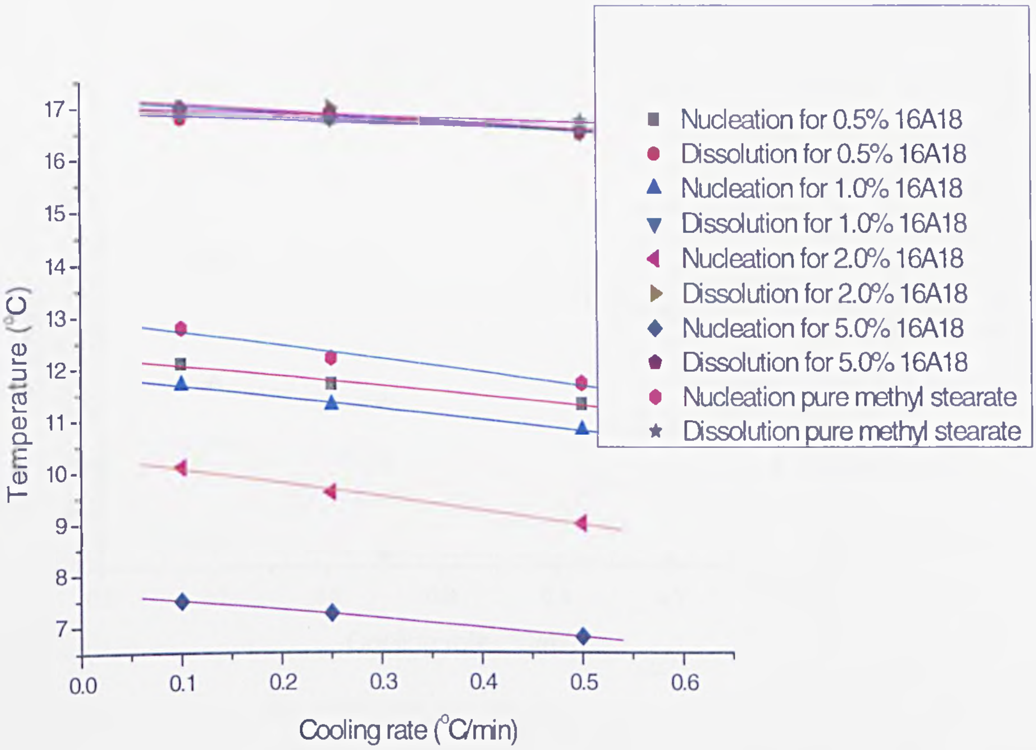
Temperature (°C)
17
16
15
14
13
12
11
10
9
8
7
0.0
0.1
0.2
0.3
0.4
0.5
0.6
Cooling rate (°C/min)
■ Nucleation for 0.5% 16A18
● Dissolution for 0.5% 16A18
▲ Nucleation for 1.0% 16A18
▼ Dissolution for 1.0% 16A18
◀ Nucleation for 2.0% 16A18
▶ Dissolution for 2.0% 16A18
◆ Nucleation for 5.0% 16A18
⬟ Dissolution for 5.0% 16A18
⬢ Nucleation pure methyl stearate
★ Dissolution pure methyl stearate

(b)

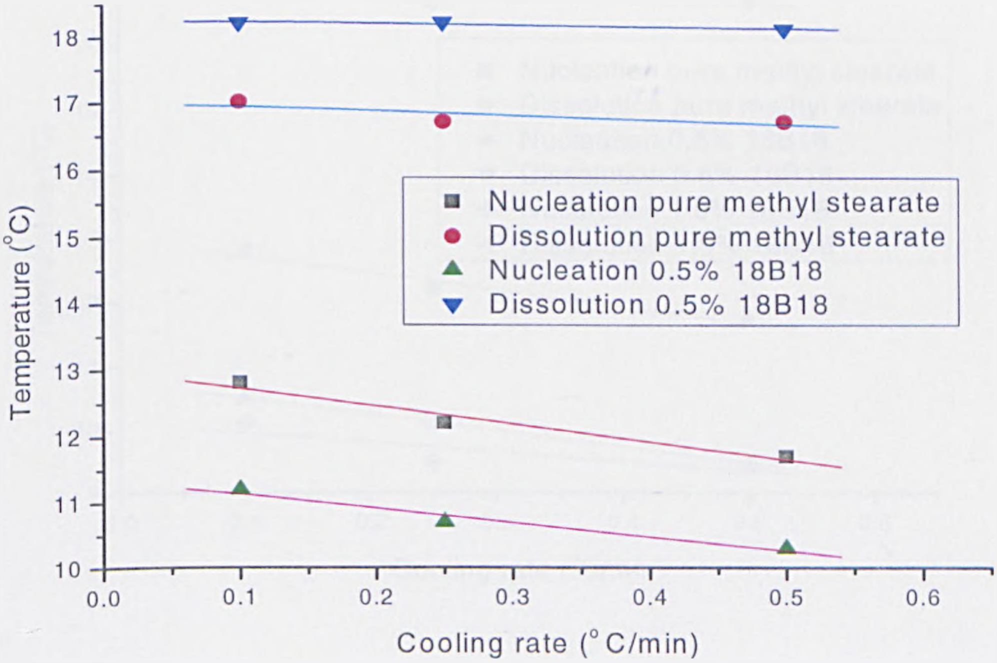
Temperature (°C)
18
17
16
15
14
13
12
11
10
0.0
0.1
0.2
0.3
0.4
0.5
0.6
Cooling rate (° C/min)
■ Nucleation pure methyl stearate
● Dissolution pure methyl stearate
▲ Nucleation 0.5% 18B18
▼ Dissolution 0.5% 18B18

(c)

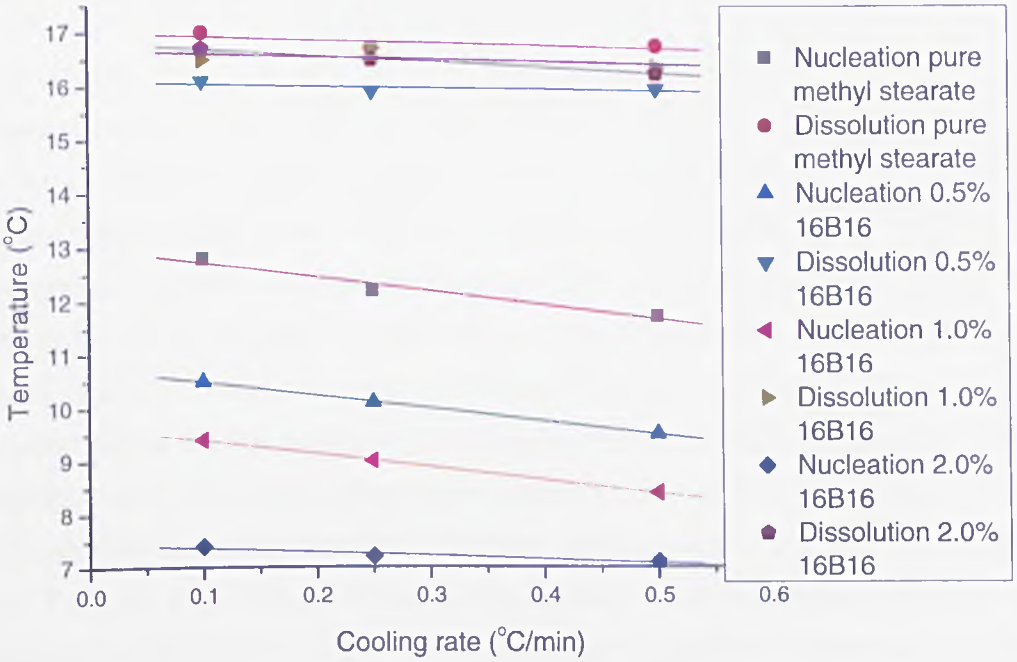

(d)

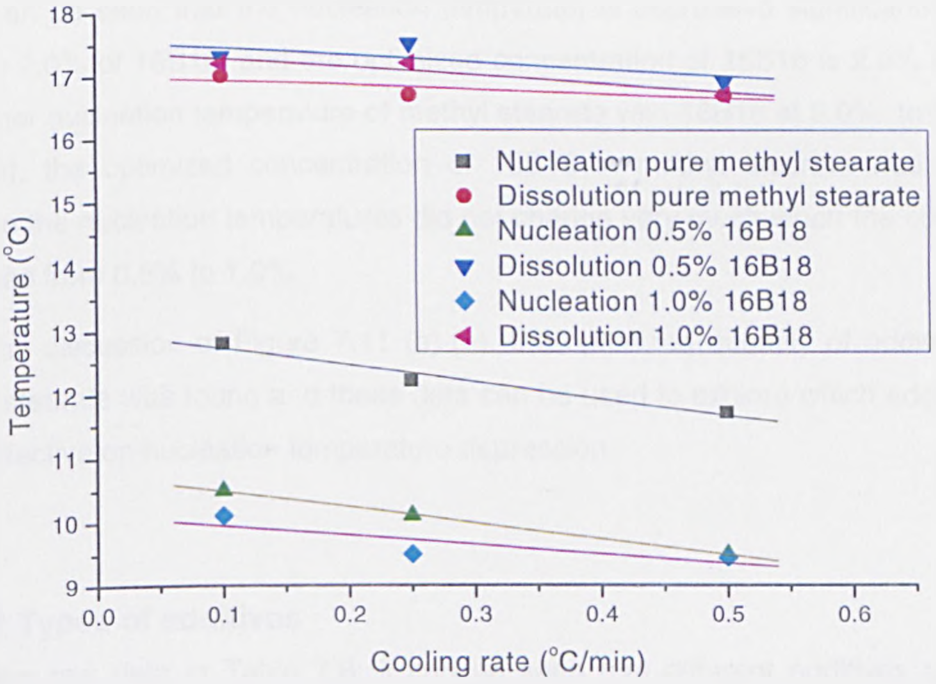

(e)

Figure 7.11: Plot of dissolution and nucleation on-set temperature/cooling rate for additives at different concentrations: (a) 18A18, (b) 16A18, (c) 18B18, (d) 16B16, (e) 16B18.

The effects of the concentration of additives on MSZW are presented in Figure 7.11, and these effects vary due to their abilities increasing MSZW and solubility in methyl oleate. In Figure 7.11 (a), nucleation temperatures of methyl stearate decrease from with the increase of 18A18 from 0.5% to 1.5%, however MSZW did not change with the increase of concentration from 1.5% to 2.0%, so 1.5% can be seen as the optimized concentration of 18A18 in methyl stearate. This optimized concentration can be used as the reference data of 18A18 used as the cold flow additives of methyl stearate. In Figure 7.11 (b), nucleation temperatures of methyl stearate did not change too much adding 0.5% and 1.0% 16A18. However, the nucleation temperatures decreased significantly when the concentration of 16A18 increased from 2.0% to 5.0%. The limited concentration of 16A18 was set as 5.0%, so the optimized concentration of cold flow additive was 5.0% for 16A18. From Figure 7.11 (c), it can be seen that both nucleation and dissolution temperatures change at the contents of 0.5% 18B18, although nucleation temperature did not decrease too much, MSZW was enlarged due to the increase of dissolution temperature. Due to the poor solubility of 18B18 in methyl oleate, the nucleation temperature did not change too much when the contents of 18B18 was more than 0.5%, so it is not a very effective additive for cold flow improvement. In Figure 7.11 (d), it can be seen that the nucleation temperatures decreased significantly from 0.5% to 2.0% of 16B16, and the optimized concentration of 16B16 is 2.0% due to the higher nucleation temperature of methyl stearate with 16B16 at 5.0%. In Figure 7.11 (e), the optimized concentration of 16B18 in methyl stearate was 0.5%, because the nucleation temperatures did not change very much when the contents increased from 0.5% to 1.0%.

From the discussion of Figure 7.11 (a)-(e), the optimized quantity of additives in methyl stearate was found and these data can be used to explore which additive is most effective on nucleation temperature depression.

7.4.2.2 Types of additives

From the raw data in Table 7.6, it can be seen that different additives present different effects on nucleation and dissolution temperatures of methyl stearate. First, ethyl stearate, monostearin and 16A16 can't be used as the cold flow additives decreasing nucleation temperatures, because the MSZW of methyl stearate didn't change significantly in the presence of these three additives. Second, 18A18, 16A18 and 16B16 can work on nucleation temperatures significantly at different contents. Third, the nucleation temperatures of methyl stearate did not decrease very much in the presence of 18B18 or 16B18 at lower contents and the nucleation temperatures did not change with the increase of additives in methyl stearate.

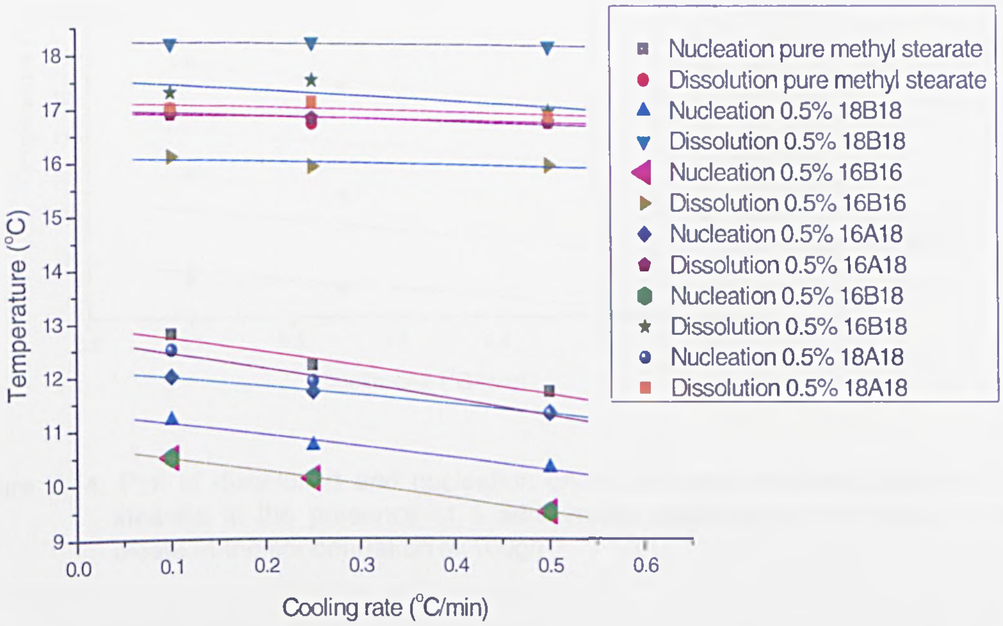

Figure 7.12: Plot of dissolution and nucleation on-set temperature/cooling rate for methyl stearate in the presence of 5 additives at 0.5% in methyl oleate at the concentration of 100g/l

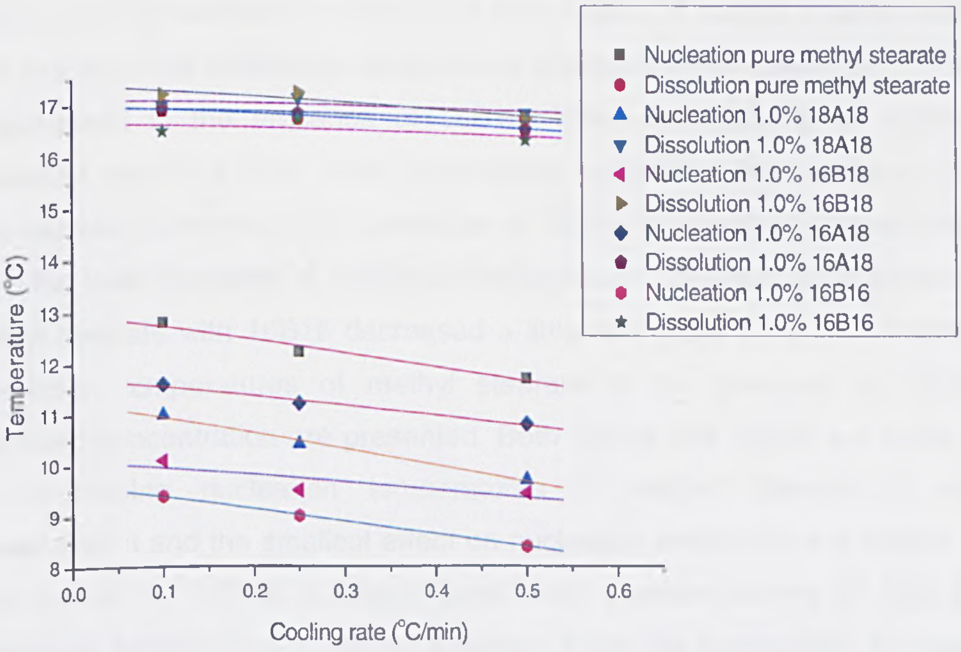

Figure 7.13: Plot of dissolution and nucleation on-set temperature/cooling rate for methyl stearate in the presence of 5 additives at 1.0% in methyl oleate at the concentration of 100g/l

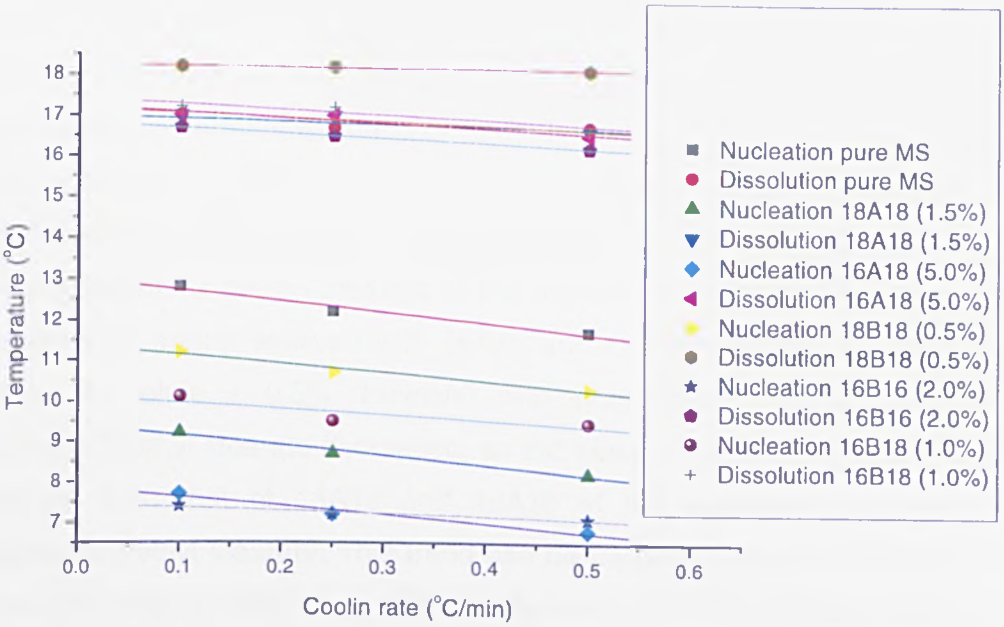

Figure 7.14: Plot of dissolution and nucleation on-set temperature/cooling rate for methyl stearate in the presence of 5 additives at optimized concentration in methyl oleate at the concentration of 100g/l

Figures 7.12, 7.13 and 7.14 present the comparisons of the effects of 5 additives of different contents on nucleation and dissolution temperatures of methyl stearate in methyl oleate. When the contents of additives in methyl stearate are 0.5% shown in Figure 7.12, the lowest nucleation temperature of methyl stearate was caused by 16B18, and the decrease of nucleation temperature of methyl stearate with 18A18 was smallest. The dissolution temperature increased in the presence of 18B18 and it decreased in the presence of 16B16. When the quantity of additives was increased from 0.5% to 1.0%, the lowest nucleation temperatures of methyl stearate was confirmed in the presence of 16B16, and methyl stearate with 16A18 have the least decrease of nucleation temperature. The dissolution temperature of methyl stearate with 16B16 decreased a little. In Figure 7.14, the nucleation and dissolution temperatures of methyl stearate in the presence of additives at optimized concentration are presented. Both 16A18 and 16B16 are most effective for decreasing nucleation temperatures of methyl stearate at optimized concentration and the smallest effect on nucleation temperature of methyl stearate was caused by 18B18, however there were greatest effects of 18B18 on the dissolution temperature of methyl stearate. From the comparison in Figure 7.14, the best additives (16A18 and 16B16) improving cold flow properties of methyl stearate in methyl oleate are found, and the optimized concentration of additives are confirmed. From the difference of molecular structure between methyl stearate and additives, it can be found that the increase of chain length of alkyl group was useful for nucleation depression especially for the dialkyl additives compared with monostearin and ethyl stearate due to C18 alkyl group in methyl stearate. The solvation played an important role on nucleation and dissolution temperature of methyl stearate, it can be seen that the changes of nucleation temperature were more significant for methyl stearate in the presence of 16B16, 18B18 and 16B18 than those for methyl stearate with 16A18 and 18A18 when the concentration of additives in solute is 0.5%. However with increase of salt link additives, the solubility of methyl stearate decreased, so the effect of 16B18 and 18B18 was less significant than that of 18A18 and 16A18 at the optimized concentration of additives in methyl stearate. This trend can be caused by the interaction between solute and additives molecules, different inter-molecular interactions resulted in the difference of nucleation temperature decrease, so the investigation of inter-molecular interactions between solute and additives should be done through molecular modelling methods, i.e. cluster modelling methods.

7.4.2.3 Effect of excessive additives on nucleation and dissolution temperatures

As mentioned above, there is an optimized concentration for the use of additives, this means that nucleation temperatures will increase or decrease a little when the quantity is higher than the optimized concentration.

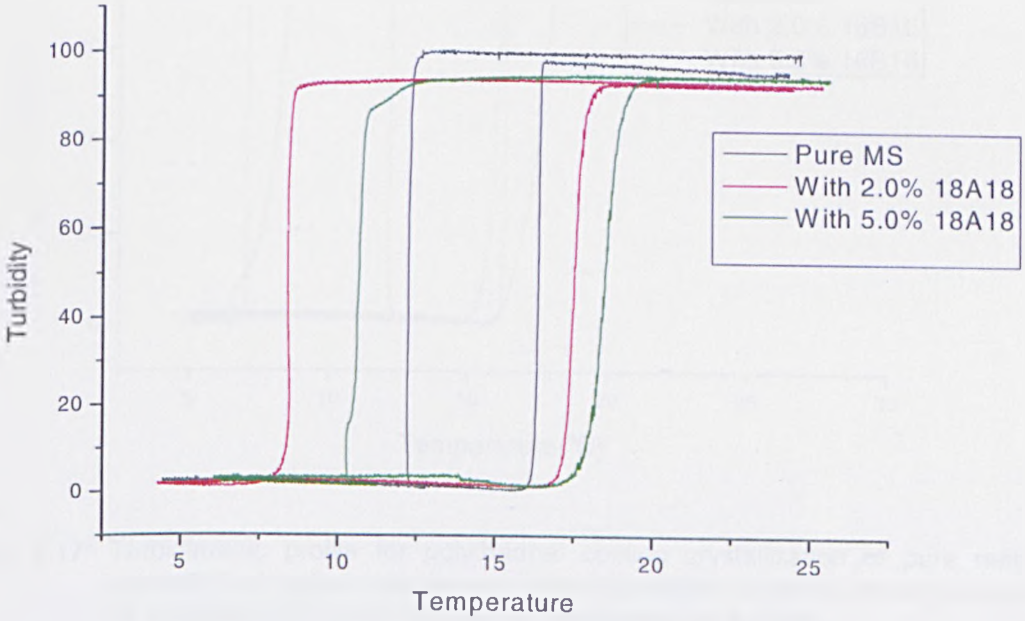

Figure 7.15: Turbidimetric profile for polythermal cooling crystallization of pure methyl stearate and methyl stearate with 18A18 in methyl oleate at the concentration of 100g/l at 0.25°C/min: function of temperature vs turbidity

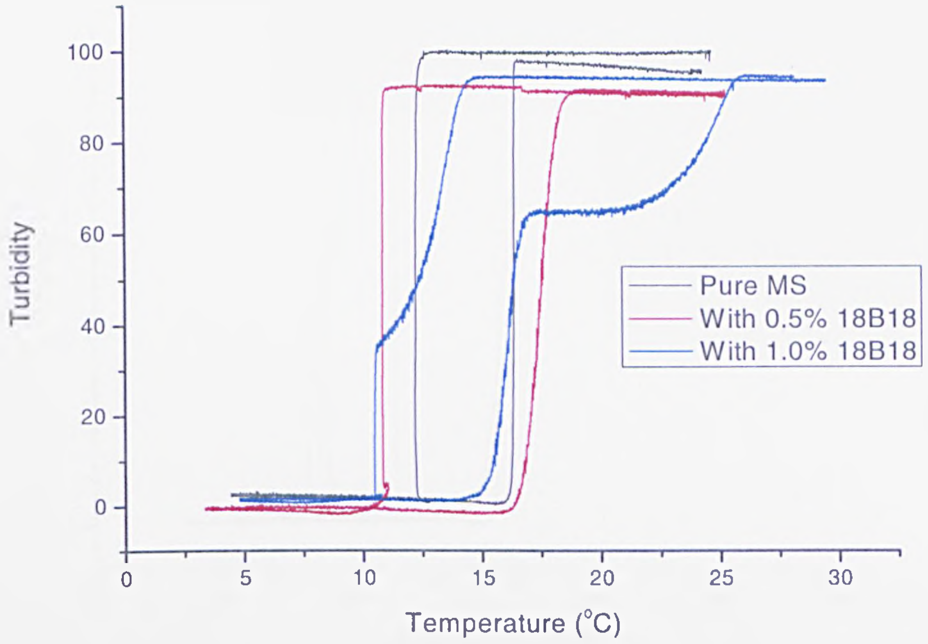

Figure 7.16: Turbidimetric profile for polythermal cooling crystallization of pure methyl stearate and methyl stearate with 18B18 in methyl oleate at the concentration of 100g/l at 0.25°C/min: function of temperature vs turbidity

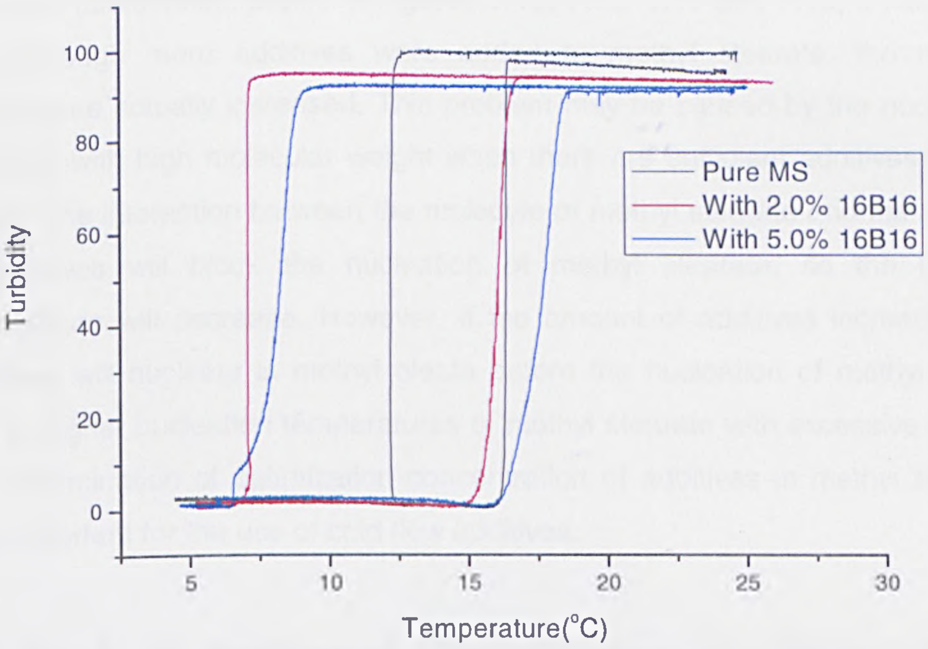

Figure 7.17: Turbidimetric profile for polythermal cooling crystallization of pure methyl stearate and methyl stearate with 16B16 in methyl oleate at the concentration of 100g/l at 0.25°C/min: function of temperature vs turbidity

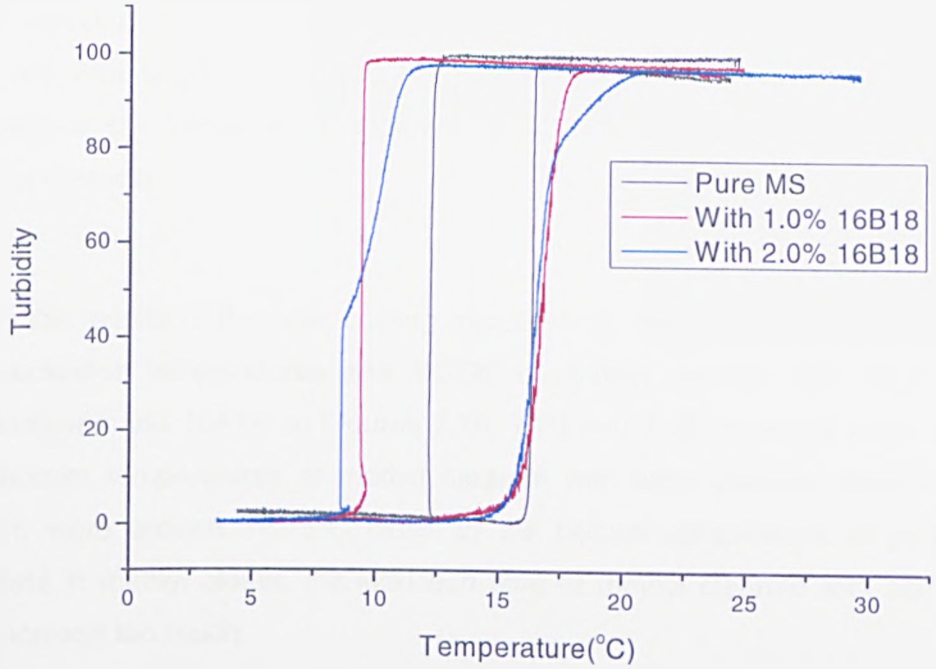

Figure 7.18: Turbidimetric profile for polythermal cooling crystallization of pure methyl stearate and methyl stearate with 16B18methyl oleate at the concentration of 100g/l at 0.25°C/min: function of temperature vs turbidity

From the turbidimetric profile in Figures 7.15, 7.16, 7.17 and 7.18, it can be seen that although more additives were added to methyl stearate, the nucleation temperature actually increased. This problem may be caused by the nucleation of additives with high molecular weight when there are sufficient additives in methyl oleate. The interaction between the molecule of methyl stearate and the molecules of additives will block the nucleation of methyl stearate, so the nucleation temperature will decrease. However, if the amount of additives increases, these additives will nucleate in methyl oleate before the nucleation of methyl stearate. Due to higher nucleation temperatures of methyl stearate with excessive additives, the determination of optimization concentration of additives in methyl stearate is very important for the use of cold flow additives.

7.5 Study of Isothermal Crystallization for Methyl Stearate Crystallizing from Methyl Oleate Solutions in the Presence of Additives

In the previous nucleation study of methyl stearate with 8 additives, it can be concluded that ethyl stearate, monostearin and 16A16 can't affect the nucleation temperature and MSZW of methyl stearate and the other 5 additives can influence the nucleation temperatures. The measurements of induction period of methyl stearate with 8 additives in methyl stearate at the concentration of 100g/l will investigate the influence of additives on induction time and nucleation rate of methyl stearate.

From the results of the slow cooling experiments, there were no significant effect on nucleation temperatures and MSZW of methyl stearate with ethyl stearate, monostearin and 16A16. In Figures 7.19, 7.20 and 7.22, it can be seen that when the bottom temperatures of methyl stearate with ethyl stearate, monotearin and 16A16 were around 14.25°C close to the bottom temperature of pure methyl stearate in methyl oleate, the induction time of methyl stearate with additives did not increase too much.

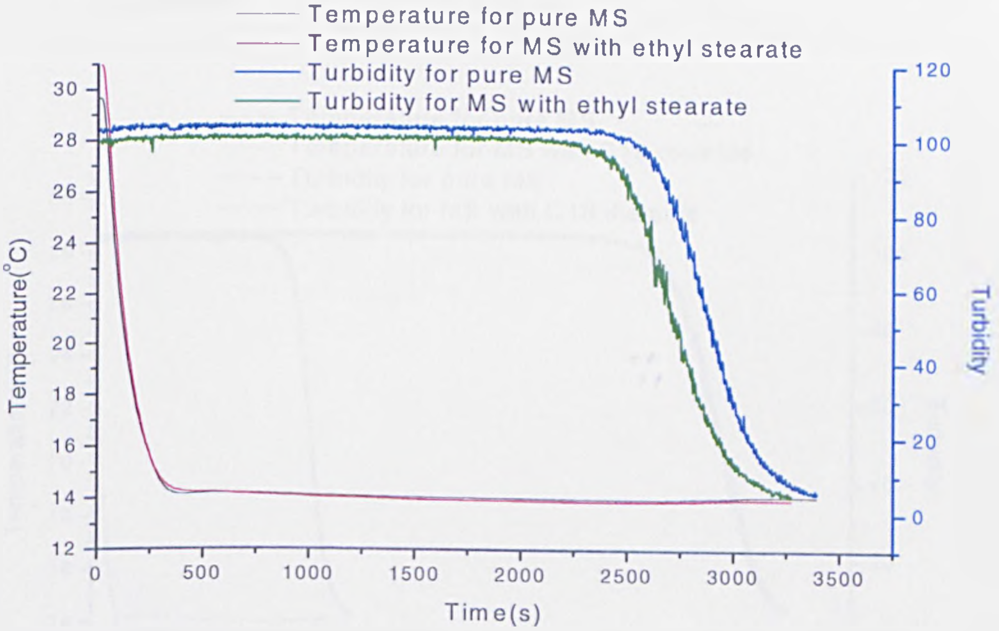

Figure 7.19: Comparison of induction time for pure methyl stearate, methyl stearate with 1% ethyl stearate

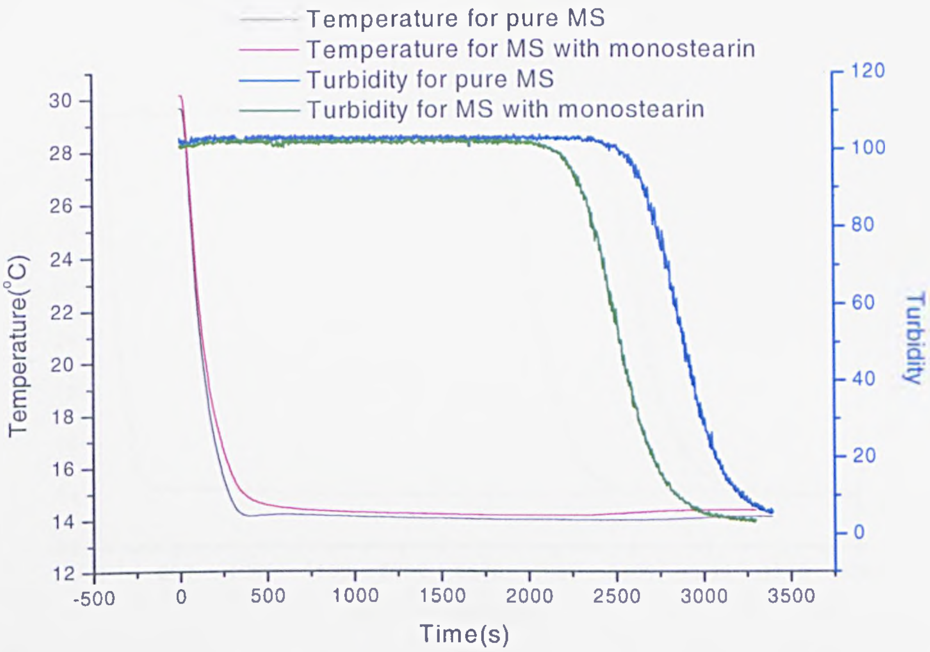

Figure 7.20: Comparison of induction time for pure methyl stearate, methyl stearate with 1% monostearin

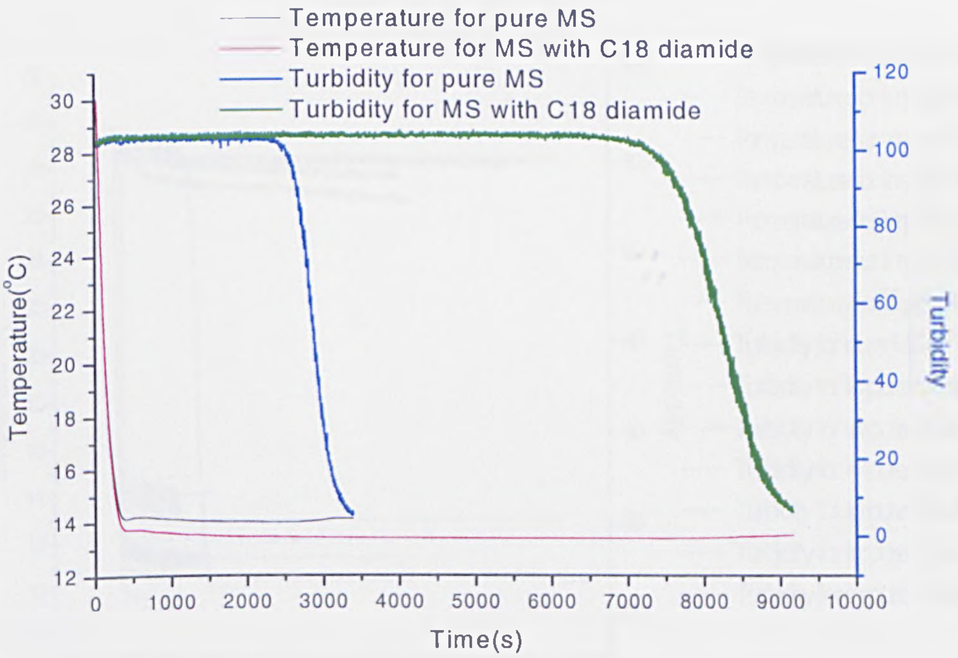

Figure 7.21: Comparison of induction time for pure methyl stearate, methyl stearate with 1.5% 18A18

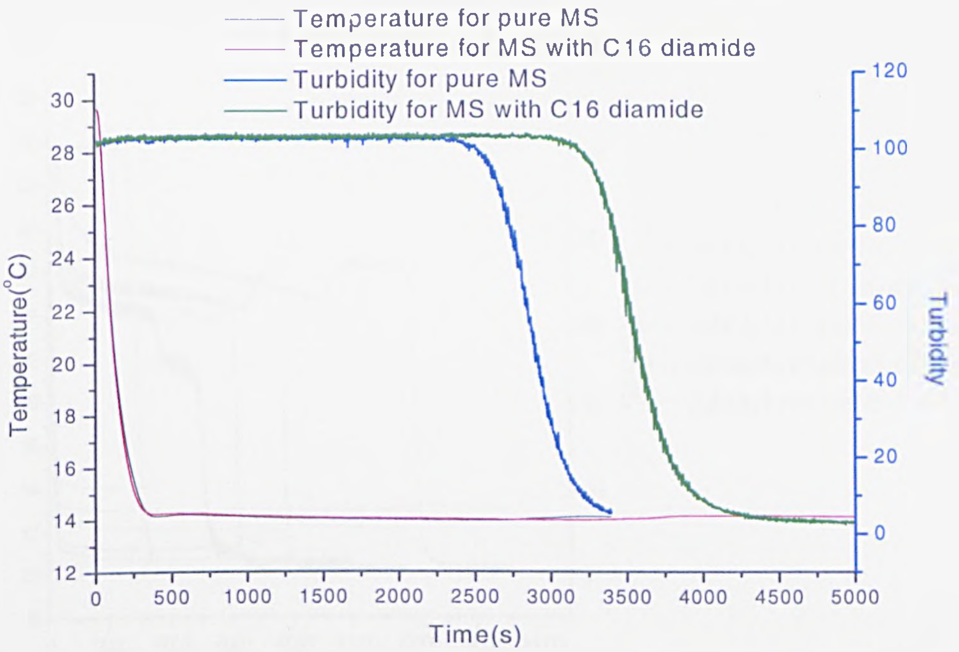

Figure 7.22: Comparison of induction time for pure methyl stearate, methyl stearate with 2% 16A16.

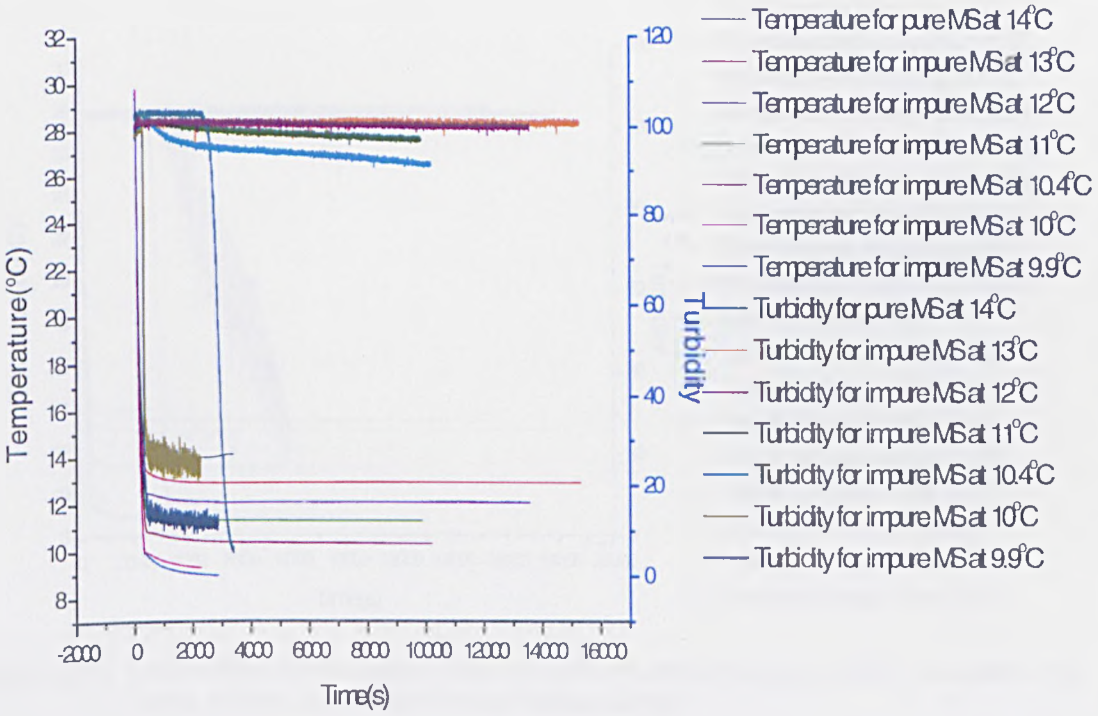

Figure 7.23: Comparison of induction time for pure methyl stearate, methyl stearate with 5% 16A18 at different bottom temperatures

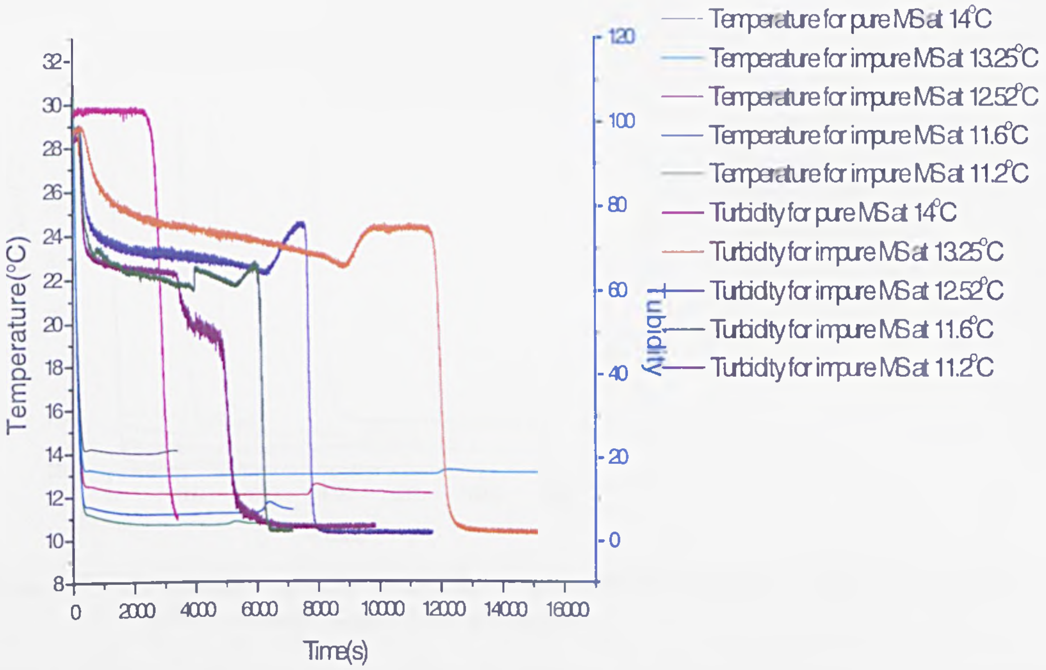

Figure 7.24: Comparison of induction time for pure methyl stearate, methyl stearate with 1% 18B18 at different bottom temperatures

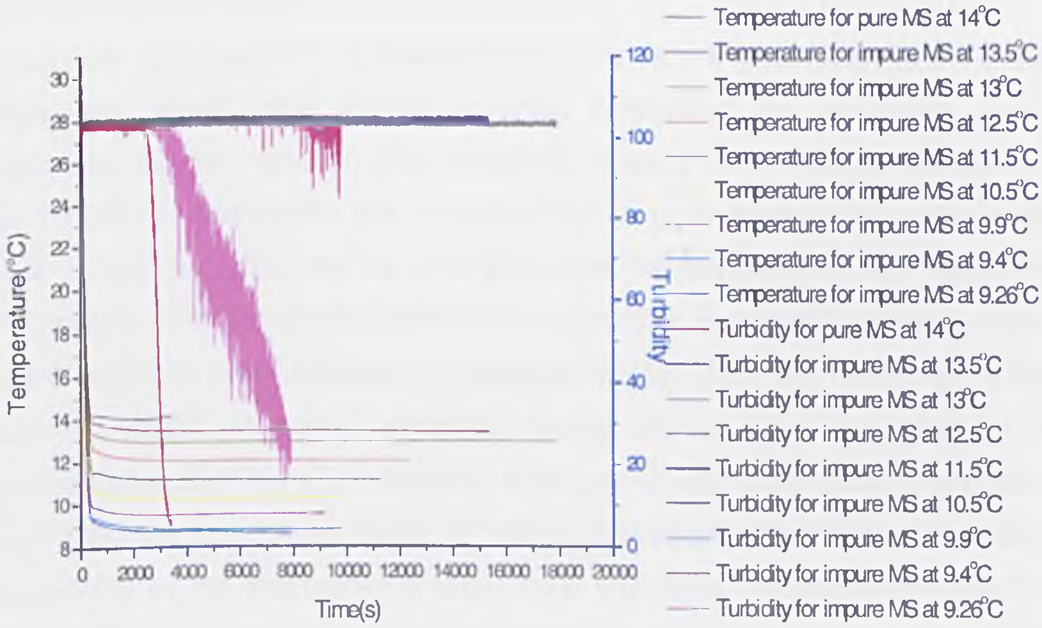

Figure 7.25: Comparison of induction time for pure methyl stearate, methyl stearate with 1.5% 16B16 at different bottom temperatures

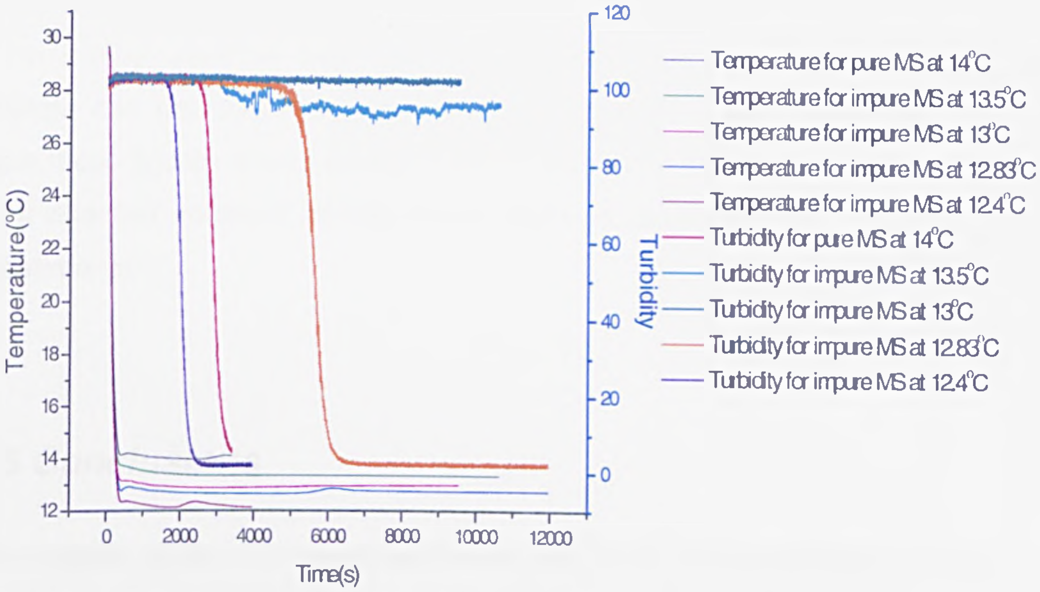

Figure 7.26: Comparison of induction time for pure methyl stearate, methyl stearate with 1% 16B18at different bottom temperatures

The optimized quantity of additives has been confirmed previously, so the quantity of additives added in methyl stearate is the optimized concentration for the measurements of induction time. From Figures 7.21, 7.23, 7.24, 7.25 and 7.26, it can be seen that only methyl stearate with 1.5% 18A18 crystallized at the bottom temperature which pure methyl stearate crystallized in the crash cooling experiment, but the induction time of methyl stearate with 18A18 increased more than 1 hour compared with the induction time of pure methyl stearate in methyl oleate. In Figure 7.23, it can be seen that when the temperature was higher than 10°C, methyl stearate with 5% 16A18 can't crystallize. But when the temperature is at 10°C or 9.9°C, methyl stearate crystallized rapidly. Because 16A18 has a great effect on MSZW of methyl stearate, methyl stearate can crystallize at low supersaturation and this will be helpful for the growth of methyl stearate crystals. In Figure 7.24, the turbidimetric value of methyl stearate with 1% 18B18 decreased to around 70% in the isothermal process then this value decreased sharply. This result could be caused by the low solubility of 18B18 in methyl oleate, 18B18 crystallized first. But due to the low quantity of 18B18, there were not too many crystals in the solution, the turbidimetric value can't decrease to 0% then methyl stearate crystallized. The results from the crash cooling experiments fit those from the slow cooling experiments, showing 18B18 is not a good additive for methyl stearate in methyl oleate due to the low solubility of 18B18 in methyl oleate. In Figure 7.25, 16B16 presented similar effects on induction time of methyl stearate as 16A18. Methyl stearate with 1.5% 16B16 did not crystallize when the bottom temperature was higher than 9.26°C. In Figure 7.26, the bottom temperature at which methyl stearate with 1% 16B18 crystallised was 12.83°C, and methyl stearate can not crystallise when bottom temperature was higher than 12.83°C. From these figures shown above, it can be seen that 16A18 and 16B16 are still the most effective additives inhibiting nucleation as discovered from the slow cooling experiments.

7.6 Conclusions

This chapter details the results from slow and crash cool crystallization runs. There are two aims for slow cool experiments, one is to study the kinetics of the nucleation process by calculating the order of nucleation and nucleation constant using the Nyvlt relationship and MSZW for pure methyl stearate in methyl oleate and the other is to examine the effect of 8 additives on MSZW and crystallization temperatures of methyl stearate. It has been found from the slow cool experiments that the MSZW, nucleations order decrease and nucleation constant increases with the increase of the solute concentration. The effects of additives on nucleation behaviour of methyl stearate in methyl oleate are detailed from two aspects: content of additives in methyl stearate and types of additives. It has been discovered that 16B16 and 16A18 are most effective on decreasing nucleation temperatures of methyl stearate at optimized concentration, and the chain length of alkyl group and salvation are very important to the actions of additives on nucleation dissolution temperatures of methyl stearate. Compared with the effects of polymer additives reviewed in Chapter 3, it can be found that the effects of polymer additives are more significant than monomer additives, however monomer additives are better than polymer additives through the aspects of economy and environmental protection. The crash cool experimental results revealed values for the interfacial tension and critical nucleus size at 100 g/l at different bottom temperatures and the effect of additives on induction are evaluated. From the experimental data of induction, it can be found that 16A18 and 16B16 are still the most effective additives inhibiting nucleation in agreement with the findings from the slow cool experiments. The real case has been studied in this chapter, and the great impact of additives on the use of biodiesel has been found. As mentioned in chapter 1, the limitation of the use of biodiesel is poor cold flow property of biodiesel, however it has been found that the depression of nucleation temperature by cold flow additives can enlarge the use of biodiesel. Through the experiment data and assess of 8 additives, the structure and amounts of additives in methyl stearate are very critical to nucleation temperatures of methyl stearate in methyl oleate, the amount control of additives should be carefully. The indication of the selection of additives has been revealed in this study, and the experimental data can also be used to validate the molecular cluster work on pure and impure methyl stearate system.

The real case has been studied in this chapter, and the great impact of additives on the use of biodiesel has been found. As mentioned in chapter 1, the limitation of the use of biodiesel is poor cold flow property of biodiesel, however it has been found that the depression of nucleation temperature by cold flow additives can enlarge the use of biodiesel. Through the experiment data and assess of 8 additives, the structure and amounts of additives in methyl stearate are very critical to nucleation temperatures of methyl stearate in methyl oleate, the amount control of additives should be carefully. The indication of the selection of additives has been revealed in this study, and the experimental data can also be used to validate the molecular cluster work on pure and impure methyl stearate system.

CHAPTER 8

Conclusions and Suggestions for Future Work

Summary:

This chapter summarizes all the findings and outcomes from the research together with suggestions for future work

8.1 Conclusions Arising from this Study

This PhD project aims at providing a new molecular method to study the nucleation behavior of materials through the information of crystallography, and the evaluation of effects of additives on nucleation properties of methyl stearate together with the prediction and experimental observation of morphologies of methyl stearate.

8.1.1 Modelling of molecular clusters

Examination of molecular clusters of different sizes for naphthalene, biphenyl, naphthalene doped by biphenyl and biphenyl doped by naphthalene was carried out. The calculation of structural variability and the conformational variance revealed the comparison of crystallisability and solubility. From this analysis, it can be found that MSZW of biphenyl are the greatest, and the MSZW of naphthalene is smaller than that of biphenyl. The influence of naphthalene on the crystallisability of biphenyl and vice versa was determined from the analysis of structural variability. From the comparison of conformational variance of biphenyl and biphenyl doped by naphthalene, it was predicted that the solubility of biphenyl was increased in the presence of naphthalene due to an increase in the degree of disorder. The simulation results were demonstrated from the slow cool experiments of pure naphthalene, pure biphenyl, 1% biphenyl in naphthalene and 1% naphthalene in biphenyl in the solvent of toluene at 600g/l, so the molecular cluster work was validated.

The molecular clusters of methyl stearate for two polymorphs were also constructed as a function of cluster size, and the monoclinic methyl stearate was regarded to be more stable than the orthorhombic methyl stearate from the calculation of cluster energies of clusters of different sizes.

8.1.2 Morphological prediction and investigation of observed habit and solvent-mediated effect on habit

The van der Waals force, increasing with the limited radius, is the dominant interaction for methyl stearate. The number of non-zero intermolecular bonds for methyl stearate increased with the limited radius, however there are three types of intermolecular interactions which are much bigger than other bonds and this result is totally different from naphthalene. From the atom-atom bond analysis, it can be seen that the pair of aliphatic hydrogen-aliphatic carbons, and aliphatic hydrogen and aliphatic carbon make the greatest contribution to lattice energy. The calculated lattice energies of methyl stearate are close to the experimental sublimation enthalpies from the literature. The predicted morphologies for two polymorphs are almost the same, and it may caused by the huge d-spacing of the (002) face. The experimental observation of methyl stearate in the cold room validated the morphological prediction that the shape of methyl stearate is plate-like.

The influences of solvents and concentration of solution on crystal habit and sizes of methyl stearate and methyl palmitate were determined from the image analysis of the crystal photographs taken in the cold room. The system search method was applied to investigate the effect of solvent on the morphology of methyl stearate and it was found that crystals of methyl stearate became thinner in the presence of toluene and dodecane compared with the predicted morphology of methyl stearate in a vacuum.

8.1.3 Nucleation study of pure methyl stearate and with 8 additives

The slow cool experiments were aimed at studying the kinetics of the nucleation process by deriving the order of nucleation and nucleation constant using the Nyvlt relationship and MSZW. It has been found from the slow cooling experiments that the MSZW nucleation order decreased and nucleation constant increased with the increase of the solute concentration. The MSZW can also increase with the increase of cooling rate at the constant concentration. It can be found that methyl stearate solute-solute interactions are slightly weaker than the solute-solvent interactions that methyl stearate form with methyl oleate through the comparison of ideal solubility from van der Hoff equation and experimental solubility.

The data from the slow cool crystallization of methyl stearate with 8 additives in methyl oleate revealed that most of the additives reduced the crystallization temperatures of methyl stearate except ethyl stearate, monostearin and 16A16.

The main reason for this difference is possibly that the large and complex alcohol group of the other 5 additves will block the nucleation of the cluster of methyl stearate in methyl oleate. The deep discussion on the influence of the other 5 additives on nucleation and dissolution temperatures of methyl stearate in methyl oleate was carried out, and it was summarized that there were two factors, the content and types of additives in methyl stearate, changing the nucleation behaviour of methyl stearate. Finally, it was found that 16B16 and 18A18 are most effective on decreasing nucleation temperatures of methyl stearate at optimized concentration, and the chain length of alkyl group and salvation are very important to the actions of additives on nucleation dissolution temperatures of methyl stearate. The crash cool experimental results revealed values for the interfacial tension and critical nucleus size at 100g/l at different bottom temperature, and the effect of additives on induction were evaluated. From the experimental data of induction, it can be found that 16A18 and 16B16 are still the most effective additives inhibiting nucleation in agreement with the findings from the slow cool experiments.

8.2 Recommendation for future work

A new molecular modelling method has been developed in this PhD project, however it still needs the application of synthonic engineering and the investigation of effects of additives on crystallization nucleation properties of methyl stearate and methyl palmitate. The synthonic work will be applied to molecular clusters of naphthalene and biphenyl and the intermolecular interactions within clusters can be viewed and defined. The molecule of effective additives will be built and inserted into the centre of a molecular cluster of methyl stearate and methyl palmitate and the relationship between structural variability and crystallisability will be investigated.

A rough analysis of solvent-mediate effect on crystal habit of methyl stearate and methyl palmitate has been carried out, however the effect of solvents on thickness and size of individual face still needs to be explored. The effect of additives on morphology of methyl stearate and methyl palmitate needs to be investigated through experimental work and grid search program.

Reference

1. Paolo, B., *The Biodiesel Handbook. By Gerhard Knothe, Jon Van Gerpen and Jürgen Krahl (Eds.)*. 2007. p. 1571-1572.
2. Lee, I., L. Johnson, and E. Hammond, *Reducing the crystallization temperature of biodiesel by winterizing methyl soyate*. Journal of the American Oil Chemists' Society, 1996. **73**(5): p. 631-636.
3. D. S. Shrestha, J.V.G., J. Thompson, A. Zawadzki *Cold flow properties of biodiesel and effect of commercial additives*. 2005
4. Knott, G., J.H. Schulman, and A.F. Wells, *On the Structure of Multilayers. Part I.* Proceedings of the Royal Society of London. Series A, Mathematical and Physical Sciences (1934-1990), 1940. **176**(967): p. 534-542.
5. Coumoulos, G.D. and E.K. Rideal, *On the Electron Diffraction of Multilayers of Esters of Fatty Acids. II. The Structure of Multilayers of the Esters.* Proceedings of the Royal Society of London. Series A, Mathematical and Physical Sciences (1934-1990), 1941. **178**(975): p. 421-428.
6. Firestone, D., *Physical and Chemical Characteristics of Oils, Fats, and Waxes, 2nd edition*. 2nd ed. 2006: Amer Oil Chemists Society. 237.
7. Jon Harlan Van Gerpen, R.P., Davis Clements, Brent Shanks, *Building a Successful Biodiesel Business: Technology Considerations, Developing the Business, Analytical Methodologies*. 2nd ed. 2006: Biodiesel Basics. 277.
8. Paul, R.S., *The effects of phospholipids on crystallisation and crystal habit in triglycerides*. 2000. p. 122-127.
9. Broadhurst, M.G. and E.R. Fitzgerald, *Dielectric Behavior and Crystal Structure of Ethyl and Vinyl Stearate*. The Journal of Chemical Physics, 1960. **33**(1): p. 210-220.
10. Goosen, R., *Feedstock Characteristics and Effect on Biodiesel Quality*, in *APEC Workshop on Biodiesel Standards*. 2007: Bangkok Thailand.
11. Alan D. Randolph, M.A.L., *Theory of Particulate Processes*. 1972: Academic Press Inc.,. 251.
12. Rauls, M.R., M., K. Bartosch, M. Kind, S. Kuch, R. Lacmann, and A. Mersmann, *The influence of impurities on crystallization kinetics - a case study on ammonium sulfate*. Journal of Crystal Growth, 2000. **213**(1-2): p. 116-128.

13. Chianese, A., M. Karel, and B. Mazzarotta, *Crystal-Growth Kinetics of Pentaerythritol.* Chemical Engineering Journal and the Biochemical Engineering Journal, 1995. **58**(3): p. 215-221.

14. S. Z. Erhan, R.O.D.G.K.B.R.M., *Fuel Properties and Performance of Biodiesel*, in *Biocatalysis and Bioenergy*, J.-F.S. Ching T. Hou, Editor. 2008. p. 1-57.

15. Clydesdale, G., R. Docherty, and K.J. Roberts, *HABIT - a program for predicting the morphology of molecular crystals.* Computer Physics Communications, 1991. **64**(2): p. 311-328.

16. Dowty, E., *Computing and drawing crystal shapes.* 1980. p. 465-471.

17. Hammond, R., *Application of systematic search methods to studies of the structures urea-dihydroxy benzene co-crystals.* . Journal of Physical Chemistry B, 2003. **107**: p. 11820.

18. Myerson, A.S., *Molecular Modeling Applications in Crystallization* 1999, Cambridge Cambridge University Press.

19. Tilley, R.J.D., *Crystals and Crystal Structures.* First ed. 2006, Chichester: John Wiely& Sons Ltd.

20. C. S. Barrett, T.B.M., *Structure of Metals* 3ed. Vol. 35. 1980: Elsevier Science & Technology Books.

21. Mullin, J.W., *Crystallization.* fourth ed. 2001, Oxford: A division of Reed Educational and Professional pu.

22. Laudise.R.A, *The growth of single crystal.* 1970. 12-13.

23. Myerson, A., *Handbook of Industrial Crystallization.* 2001: Butterworth-Heinemann.

24. Pearson, W.B., *The crystal chemistry and physics of metals and alloys* 1972: John Wiley & Sons Inc

25. Evans, R.C., *Introduction to Crystal Chemistry* 1964: Cambridge University Press.

26. Brittain, H.G., *Vibrational Spectroscopic Studies of Cocrystals and Salts. 2. The Benzylamine−Benzoic Acid System.* 2009.

27. Morissette, S.L., Ö. Almarsson, M.L. Peterson, J.F. Remenar, M.J. Read, A.V. Lemmo, S. Ellis, M.J. Cima, and C.R. Gardner, *High-throughput crystallization: polymorphs, salts, co-crystals and solvates of pharmaceutical solids.* Advanced Drug Delivery Reviews, 2004. **56**(3): p. 275-300.

28. Mutaftschiev, B., *The Atomistic Nature of Crystal Growth.* 2001: Springer.

29. D.Elwell, H.J.S., *Crystal Growth from High-temperature Solutions.* 1975, London: Academic Press Inc.Ltd.

30. M. Broul, J.N., O. Sohnel,, *Solubility in Inorganic Two-Component Systems.* Physical Sciences Data, 1981. **6**.

31. Ostwald, W., *Studien uber die Bildung und Umwandlung fester Korper.* Z. Phys. Chem., 1897. **22:**: p. 289.

32. Hook, A.V., *Crystallization: Theory and Practice.* 1961: Reinhold Publishing Corporatio.

33. Mersmann, A., *Crystallization Technology Handbook.* 2nd ed. 2001, New York: Routledge.

34. Gibbs, J.W., *Collected works.* Vol. 1. 1928, New York: Longmans Green.

35. Alan D.R andolph, M.A.L., *Theory of particulate processes* 2nd ed. 1988, New York: Academic Press.

36. M. Volmer, A.W., *Keimbildung in u¨ bersa¨ ttigten Lo¨ sungen.* Z. Phys. Chem., 1926. **119**: p. 277.

37. Wagner, C., *Kinetik der Phasenbildung. Von Prof. Dr. M. Volmer. (Bd. IV der Sammlung „Die chemische Reaktion”, herausgegeben von K. F. Bonhoeffer.) XII und 220 S. Verlag Th. Steinkopff, Dresden und Leipzig 1939. Preis geh. RM. 19, - , geb. RM. 20, -* 1939. p. 503-504.

38. R. Becker, W.D., *Kinetische Behandlung der Keimbildung in übersättigten Dämpfen.* 1935. p. 719-752.

39. Farkas, L., *Keimbildungsgeschwindigkeit in u¨ bersa¨ ttigten Da¨ mpfen.* Z. Phys. Chem., 1927. **A125**: p. 236.

40. Zeldovich, Y.B., *On the theory of new phase formation: Cavitation, Zhur. Eksper. Teor. Fiz.*, in *Chemical Physics and Hydrodynamics*, G.I.B. J. P. Osterik, and R. A. Sunayev, Editor. 1942, Princeton University Press: Princeton NJ.

41. Frenkel, J., *Kinetic Theory of Liquids.* 1955, New York: Dover Press.

42. Lacmann, R., *Volmersche Keimbildungstheorie, in Kinetik metallurgischer Vorga¨nge bei der Stahlherstellung.* 1972, Du¨ sseldorf: VerlagStahleisen.

43. A. Collet, M.J.B.a.J.J., *Optical resolution by direct crystallization of enantiomer mixture.* Chem. Rev, 1980. **80**: p. 215-230.

44. Boistelle, R. and J.P. Astier, *Crystallization mechanisms in solution.* Journal of Crystal Growth, 1988. **90**(1-3): p. 14-30.

45. J. W. Nieuwenhuijzen, *Resolutions with Families of Resolving Agents: Principles and Practice.* 2002, University of Groningen: The Netherland.

46. Roger J. Davey, J.G., *From Molecules to Crystallizers* 1st ed. 2001, Oxford: Oxford University Press. 96.

47. Schieber, M., *Kinetics and mechanism of crystallization--From the fluid phase and of the condensation and evaporation of liquids : by R.F. Strickland-Constable (Academic Press, London and New York, 1968) 346 pages, about 250 references. Price $ 14.50.* Journal of Crystal Growth, 1969. **5**(3): p. 225-226.

48. J. Estrin, M.L.W.G.R.Y., *Secondary nucleation due to fluid forces upon a polycrystalline mass of ice*. 1975. p. 392-395.

49. Nývlt, J., *Kinetics of nucleation in solutions.* Journal of Crystal Growth, 1968. **3-4**: p. 377-383.

50. Kashchiev, D., *Nucleation: Basic Theory with Applications* 2000, Oxford: Butterworth-Heinemann

51. D. Kashchiev, G.M.v.R., *Review: Nucleation in solutions revisited.* 2003. p. 555-574.

52. Basset, J.-M., *Surface organometallic chemistry: molecular approaches to surface catalysis : [proceedings of the NATO Advanced Research Workshop on Surface Organometallic Chemistry: Molecular Approaches to Surface Catalysis, LeRouret, ArdÃ¨che, France, May 26 - 30, 1986].* NATO ASI series, 231. 1988, Dordrecht [u.a.]: Kluwer.

53. W. Ostwald, Z., Phys. Chem, 1897(22): p. 289.

54. I. N. Stranski, D.T., Z, *Keimbildungsgeschwindigkeit und Ostwaldsche Stufenregel.* Phys. Chem, 1933(163): p. 399.

55. John Garside, R.J.D., *From Molecules to Crystallizers.* 2001: Oxford University Press.

56. M. Ohara, R.C.R., *Modeling crystal growth rates from solution.* 1973, Englewood Cliffs, N.J: Prentice-Hall

57. Frank, F.C. *Dislocation of crystal growth* in *Discussions Faraday Soc.* 1949. London.

58. Burton, W.K., N. Cabrera, and F.C. Frank, *The Growth of Crystals and the Equilibrium Structure of their Surfaces.* Philosophical Transactions of the Royal Society of London. Series A, Mathematical and Physical Sciences, 1951. **243**(866): p. 299-358.

59. Nývlt, J., *The Kinetics of industrial crystallization.* Chemical engineering monographs, v. 19. 1985, Amsterdam; New York; New York: Elsevier ; Elsevier Science Pub. Co., Inc. [distributor].

60. P. Bennema, J.B.C.v.L.G.H.G., *Confrontation of the BCF theory and computer simulation experiments with measured (R, sigma) curves.* 1973. p. 659-678.
61. Bennema, P., *Analysis of crystal growth models for slightly supersaturated solutions.* Journal of Crystal Growth, 1967. **1**(5): p. 278-286.
62. Bennema, P., *The importance of surface diffusion for crystal growth from solution.* Journal of Crystal Growth, 1969. **5**(1): p. 29-43.
63. Jones, A., *CRYSTALLIZATION PROCESS SYSTEMS.* 2002: BUTTERWORTH HEINEMANN.
64. NÃ½vlt, J., *The Kinetics of industrial crystallization.* Chemical engineering monographs, v. 19. 1985, Amsterdam; New York; New York: Elsevier ; Elsevier Science Pub. Co., Inc. [distributor].
65. Gibbs, J., J. Trans. Acad, 1875.
66. J.W.Gibbs, *On the equilibrium of the heterogeneous substances*, in *The Scientific Papers of J.W. Gibbs.* 1906, Longman Green: London.
67. P.Curie, *On the formation of crystals and on the capillary constant of their different faces.* J.Chem.Edcn, 1970(636): p. 7.
68. Emmett, P.H., *Structure and Properties of Solid Surfaces.* 1954. p. 4498-4499.
69. P.Kern, *The equilibrium form of a crystal*, in *Morphology of crystals Part A*, D. i.Sunagawa, D.Reidel, Editor. 1987.
70. Donnay, J.D.H., Barker, D., *A new law of crystal morphology extending the law of Bravais.* Am. Mineral., 1937(11): p. 466-467.
71. P.Hartman, *Modern PBC*, in *Mophology of Crystals PartA*, D. i.Sunagawa, D.Reidel, Editor. 1987. p. 269-319.
72. Bunn, C.W., *Crystal growth from solution. II. Concentration gradients and the rates of growth of crystals.* Discuss. Faraday Soc, 1949(5): p. 132 - 144.
73. Hartman, P. and P. Bennema, *The attachment energy as a habit controlling factor : I. Theoretical considerations.* Journal of Crystal Growth, 1980. **49**(1): p. 145-156.
74. Saska, M. and A.S. Myerson, *The theoretical shape of sucrose crystals from energy calculations.* Journal of Crystal Growth, 1983. **61**(3): p. 546-555.
75. Black, S.N. and R.J. Davey, *Crystallisation of amino acids.* Journal of Crystal Growth, 1988. **90**(1-3): p. 136-144.
76. Davey, R.J., *The effect of impurity adsorption on the kinetics of crystal growth from solution.* Journal of Crystal Growth, 1976. **34**(1): p. 109-119.

77. G. Bliznakov, E.K., *Der Einflub der Adsorption auf das Kristallwachstum.* Z. Phys. Chem, 1957(206): p. 271–280.

78. Goodman, J., *Chemical Applications of Molecular Modeling* 1ed. 1998, UK: Royal Society of Chemistry. 216.

79. Atkins, P.W., *Physical chemistry.* 1990, Oxford: Oxford University Press.

80. Olga Gliko, W.P., † Panagiotis Katsonis,† Nikolaus Neumaier,§ Oleg Galkin,†, Sevil Weinkauf,§ and Peter G. Vekilov*,†,‡, *Metastable Liquid Clusters in Super- and Undersaturated Protein Solutions.* J. Phys. Chem. B, 2007. **111**: p. 3106-3114.

81. Weichun Pan, O.G., Luis Filobelo, Ronald L. Nagel and Peter G. Vekilov, *Metastable Mesoscopic Clusters in Solutions of Sickle-Cell Hemoglobin.* Biophysical Journal, 2007. **92**: p. 267-277.

82. Stein, G.D.A., J. A., *Nucleation Experiments in Molecular Beams.* J. Chem. Phys., 1973. **58**.

83. Bartell, L.S., *Diffraction studies of clusters generated in supersonic flow.* 1986. p. 491-505.

84. Bartell, L.S., *Nucleation and Phase transitions in Molecular Clusters: Molecular Dynamics Simulation and Experiment*, in *Theoretical Aspects and Computer Modeling of the Molecular Solid State*, A. Gavezzotti, Editor. 1997, John Wily& Sons: Chichester.

85. R. J. Davey, K.A., N. Blagden, W. I. Cross, H. F. Lieberman, M. J. Quayle, S. Righini, L. Seton and G. J. T. Tiddy, *Crystal engineering – nucleation, the key step.* CrystEngComm, 2002. **4**.

86. Sciortino, F.M., S.; Zaccarelli,E; Tartaglia,P., *Equilibrium cluster phases and low-density arrested disorder states: the role of short-range attraction and long-range repulsion.* Phys. Rev.Lett, 2004. **93**: p. 055701.

87. Groenewold, J.K., W.K, *Anomalously large equlibrium cluster of colloids.* J.Phys.Chem.B, 2001. **105**: p. 11702.

88. Sear, R.P.C., S.-W.; Markovich, G.; Gelbart, W.M.; Heath, J.R., *Spontaneous patterning of quantum dots at the air-water interface.* Phys. Rev. E, 1999. **59**: p. R6255.

89. Larson, M.A. and J. Garside, *Solute clustering in supersaturated solutions.* Chemical Engineering Science, 1986. **41**(5): p. 1285-1289.

90. Weissbuch, I., M. Lahav, and L. Leiserowitz, *Toward Stereochemical Control, Monitoring, and Understanding of Crystal Nucleation.* 2003. p. 125-150.

91. Pencheva, K., *Modelling the Solid-State and Surface Properties of Organic Nano-size Molecular Culster*, in *Institute of Particle Science &Engineering*. 2006, University of Leeds: Leeds.

92. Ryūzō Ueda, J.B.M. *Crystal Growth and Characterization*. in *International Organization of Crystal Growth, International Union of Crystallography*. 1974: American Elsevier Pub. Co.

93. Moscosa-SantillÃ¡n, M., O. Bals, H. Fauduet, C. Porte, and A. Delacroix, *Study of batch crystallization and determination of an alternative temperature-time profile by on-line turbidity analysis â€" application to glycine crystallization*. Chemical Engineering Science, 2000. **55**(18): p. 3759-3770.

94. Brown, C.J. and X.-W. Ni, *Determination of metastable zone width, mean particle size and detectable number density using video imaging in an oscillatory baffled crystallizer*. CrystEngComm, 2012. **14**(8): p. 2944-2949.

95. Radenovic, N., W. van Enckevort, D. Kaminski, M. Heijna, and E. Vlieg, *Structure of the {111}NaCl crystal surface grown from solution in the presence of CdCl2*. Surface Science, 2005. **599**: p. 196-206.

96. Inoue, T. and K. Nishioka, *Effects of impurity upon the habit changes in NaBrO3 crystals grown from aqueous solution*. Journal of Crystal Growth, 2000. **212**(3-4): p. 507-511.

97. Bhagavannarayana, G., S.K. Kushwaha, S. Prathiban, G. Ajitha, and S. Meenakshisundaram, *Influence of inorganic and organic additives on the crystal growth, properties and crystalline perfection of tris(thiourea) copper(I) chloride (TCC) crystals*. Journal of Crystal Growth, 2008. **310**(10): p. 2575-2583.

98. Garnier, S., S. Petit, and G. Coquerel, *Influence of supersaturation and structurally related additives on the crystal growth of alpha-lactose monohydrate*. Journal of Crystal Growth, 2002. **234**(1): p. 207-219.

99. Thompson, C., M.C. Davies, C.J. Roberts, S.J.B. Tendler, and M.J. Wilkinson, *The effects of additives on the growth and morphology of paracetamol (acetaminophen) crystals*. International Journal of Pharmaceutics, 2004. **280**(1-2): p. 137-150.

100. Hendriksen, B.A., D.J.W. Grant, P. Meenan, and D.A. Green, *Crystallisation of paracetamol (acetaminophen) in the presence of structurally related substances*. Journal of Crystal Growth, 1998. **183**(4): p. 629-640.

101. Gordon, J.D., A.H.L. Chow, J. D. Gordon, and A. H.L. Chow, *Modification of phenytoin crystals. II. influence of 3-propanoyloxymethyl-5,5-*

diphenylhydantoin on solution-phase crystallization and related crystal properties. International Journal of Pharmaceutics, 1992. **79**(1-3): p. 171-181.

102. Sgualdino, G., D. Aquilano, R. Fioravanti, G. Vaccari, and L. Pastero, *Growth kinetics, adsorption and morphology of sucrose crystals from aqueous solutions in the presence of raffinose.* Crystal Research and Technology, 2005. **40**(10-11): p. 1087-1093.

103. Nokhodchi, A., N. Bolourtchian, and R. Dinarvand, *Dissolution and mechanical behaviors of recrystallized carbamazepine from alcohol solution in the presence of additives.* Journal of Crystal Growth, 2005. **274**(3-4): p. 573-584.

104. Chianese, A., M. Di Luozzo, and N. Kubota, *Effect of pyrogallol additive on the growth rate and the habit of hydroquinone crystals.* Crystal Growth & Design, 2003. **3**(3): p. 425-430.

105. Mukuta, T., A.Y. Lee, T. Kawakami, and A.S. Myerson, *Influence of impurities on the solution-mediated phase transformation of an active pharmaceutical ingredient.* Crystal Growth & Design, 2005. **5**(4): p. 1429-1436.

106. Fiebig, A., M.J. Jones, and J. Ulrich, *Predicting the effect of impurity adsorption on crystal morphology.* Crystal Growth & Design, 2007. **7**(9): p. 1623-1627.

107. S. R. Lebedev, R.M.B.a.Y.B.C., *Pour-depressant additives for diesel fuels* Chemistry and Technology of Fuels and Oils, 1975. **11**(10): p. 4.

108. Hennessy, A., A. Neville, and K.J. Roberts, *In-Situ SAXS/WAXS and Turbidity Studies of the Structure and Composition of Multihomologous n-Alkane Waxes Crystallized in the Absence and Presence of Flow Improving Additive Species.* 2004. p. 1069-1078.

109. Hutter, J.L., S. Hudson, C. Smith, A. Tetervak, and J.H. Zhang, *Banded crystallization of tricosane in the presence of kinetic inhibitors during directional solidification.* Journal of Crystal Growth, 2004. **273**(1-2): p. 292-302.

110. Duffy, D.M., C. Moon, and P.M. Rodger, *Computer-assisted design of oil additives: hydrate and wax inhibitors.* Molecular Physics, 2004. **102**(2): p. 203-210.

111. Marie, E., Y. Chevalier, F. Eydoux, L. Germanaud, and P. Flores, *Control of n-alkanes crystallization by ethylene-vinyl acetate copolymers.* Journal of Colloid and Interface Science, 2005. **290**(2): p. 406-418.

112. Nascimento, R.S.V., V.L.P. Soares, S. Albinante, and L.R. Barreto, *Effect of ester-additives on the crystallization temperature of methyl hexadecanoate.* Journal of Thermal Analysis and Calorimetry, 2005. **79**(2): p. 249-254.

113. Sern, C.H., C.Y. May, Z. Zakaria, R. Daik, and C.S. Foon, *The effect of polymers and surfactants on the pour point of palm oil methyl esters.* European Journal of Lipid Science and Technology, 2007. **109**(4): p. 440-444.

114. Ooi, T.L., Teoh, C. M., Yeong, S. K., Marmot, S., Salmiah, A., *Studies to imrpove the low temperature performance of palm oil products.* Journal of Oil Palm Research, 2005. **17**(1): p. 5.

115. Ann, M.V., *Pour point of heavy cut methyl esters via alkyl methacrylate copolymer.* 2001, The Procter & Gamble Company: Lovelan, OH. p. 11.

116. Auschra; Chemens, V.J., Boehmke; Uwe, Neusius; Michael, *Additives for biodiesel and biodiesel oils.* 2002, Rohmax Additives GmbH DE. p. 9.

117. Lewtas, K., *Additives for oils.* 1993: US.

118. L.M. Du Plessis, J.B.M.D.V.a.W.H.V.d.W., *Stability studies on methyl and ethyl fatty acid esters of sunflower oil.* J Am Oil Chem Soc, 1985. **62**.

119. Dunn, R.O., *Effect of oxidation under accelerated conditions on fuel properties of methyl soyate (biodiesel).* J. Am. Oil Chem. Soc, 2002. **79**.

120. Schober, M.M.a.S., *The influence of antioxidants on the oxidation stability of biodiesel* J Am Oil Chem Soc, 2003. **80**.

121. Sigurd Schober, M.M., *The impact of antioxidants on biodiesel oxidation stability.* 2004. p. 382-389.

122. Soriano, J.N.U., V.P. Migo, and M. Matsumura, *Ozonized vegetable oil as pour point depressant for neat biodiesel.* Fuel, 2006. **85**(1): p. 25-31.

123. Stig. Aleby, E.V.S., *The Crystal Stucture of Methyl Stearate.* Acta Cryst, 1960. **13**: p. 487.

124. MACGILLAVRY, C.H., *Crystal Structure of an Orthorhombie Modification of Methyl Stearate.* Acta Cryst, 1970. **B26 645**: p. 645.

125. Abrahams, S.C., J.M. Robertson, and J.G. White, *The crystal and molecular structure of naphthalene. I. X-ray measurements*, in *Acta Crystallographica.* 1949. p. 233-238.

126. Acree Jr, W.E., N.M. Pontikos, and C.L. Judy, *Solubility in binary solvent systems. 6. Prediction of naphthalene and biphenyl solubilities based on the*

Wilson model. International Journal of Pharmaceutics, 1986. **31**(3): p. 225-230.

127. Cruickshank, D.W.J., *A detailed refinement of the crystal and molecular structure of naphthalene.* Acta Cryst, 1957. **10**: p. 504-508.

128. Bennema, R.D.a.G.C.a.K.J.R.a.P., *Application of Bravais-Friedel-Donnay-Harker, attachment energy and Ising models to predicting and understanding the morphology of molecular crystals.* 1991. p. 89.

129. Clydesdale, G., K.J. Roberts, K. Lewtas, and R. Docherty, *Modelling the morphology of molecular crystals in the presence of blocking tailor-made additives.* Journal of Crystal Growth, 1994. **141**: p. 443-450.

130. Trotter, J., *The crystal and molecular structure of biphenyl*, in *Acta Crystallographica*. 1961. p. 1135-1140.

131. Almenningen, A., O. Bastiansen, L. Fernholt, B.r.N. Cyvin, S.J. Cyvin, and S. Samdal, *Structure and barrier of internal rotation of biphenyl derivatives in the gaseous state: Part 1. The molecular structure and normal coordinate analysis of normal biphenyl and pedeuterated biphenyl.* Journal of Molecular Structure, 1985. **128**: p. 59-76.

132. Accelrys, *Materials Studio.* 2002.

133. Hammond, R.B., K. Pencheva, V. Ramachandran, and K.J. Roberts, *Application of Grid-Based Molecular Methods for Modeling Solvent-Dependent Crystal Growth Morphology: Aspirin Crystallized from Aqueous Ethanolic Solution.* Crystal Growth & Design, 2007. **7**(9): p. 1571-1574.

134. Phillips, F., *Introduction to Crystallography.* 1955, Bristol: Longmans.

135. Busing, W., *Modeling the phase change in crystalline biphenyl by using a temperature-dependent potential*, in *Acta Crystallographica Section A.* 1983. p. 340-347.

136. Momany, F.A., L.M. Carruthers, R.F. McGuire, and H.A. Scheraga, *Intermolecular potentials from crystal data. III. Determination of empirical potentials and application to the packing configurations and lattice energies in crystals of hydrocarbons, carboxylic acids, amines, and amides.* The Journal of Physical Chemistry, 1974. **78**(16): p. 1595-1620.

137. Clydesdale, G., G. Tefler, K. Roberts, and D. Grant, *Modelling Crystal Morphology of alpha monohydrate.* Journal of Pharmaceutical Science., 1997. **86**: p. 135.

138. Clydesdale, G., R. Docherty, and K. Roberts, *Computational studies of the morphology of molecular crystals through solid-state intermolecular force*

calculation using atom-atom method, in *Controlled Particle, Droplet and Bubble Formation*, Wedlock D., Editor. 1994, Butterworth Heinemann: Oxford.

139. Bladon, P.B., R., *Interchem 6.1*, in *QCPE Bulletin*. 1994, Indiana University:Bloominton.

140. Young, R.A., *Introduction to the Rietveld method*, in *The Rietveld Method*, R.A. Young, Editor. 1993, Oxford University Press. p. 1-38.

141. Gelin, B., *Molecular modelling of polymer structures and properties*. 1994, Cambridge: Hanser Publishers.

142. Hammond, R.B., *Application of Grid-Based Molecular Methods for Modelling Solvent-Dependent Crystal Growth Morphology:Aspirin Crystallized from Aqueous Ethanolic Solution*. Crystal Growth & Design, 2007. **7**: p. 1571-1574.

143. Docherty, R. and K.J. Roberts, *Modelling the morphology of molecular crystals; application to anthracene, biphenyl and I^2-succinic acid*. Journal of Crystal Growth, 1988. **88**(2): p. 159-168.

144. Chickos, J.S., H. Zhao, and G. Nichols, *The vaporization enthalpies and vapor pressures of fatty acid methyl esters C18, C21 to C23, and C25 to C29 by correlation - gas chromatography*. Thermochimica Acta, 2004. **424**(1-2): p. 111-121.

Appendix

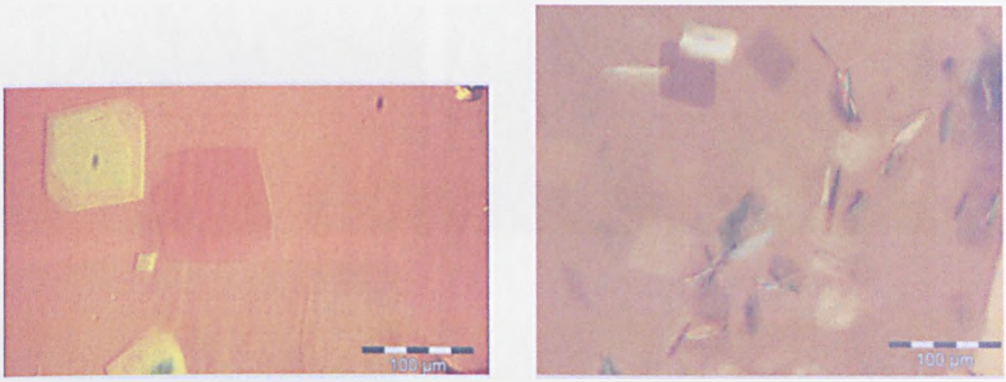

10% methyl stearate in methyl oleate at 10°C

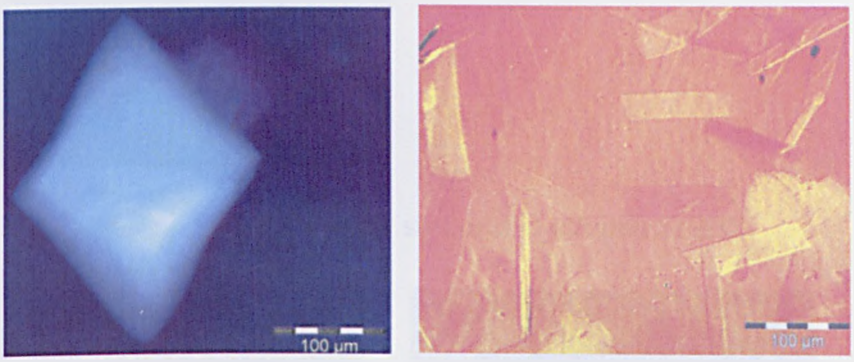

50% methyl stearate in toluene at 10°C

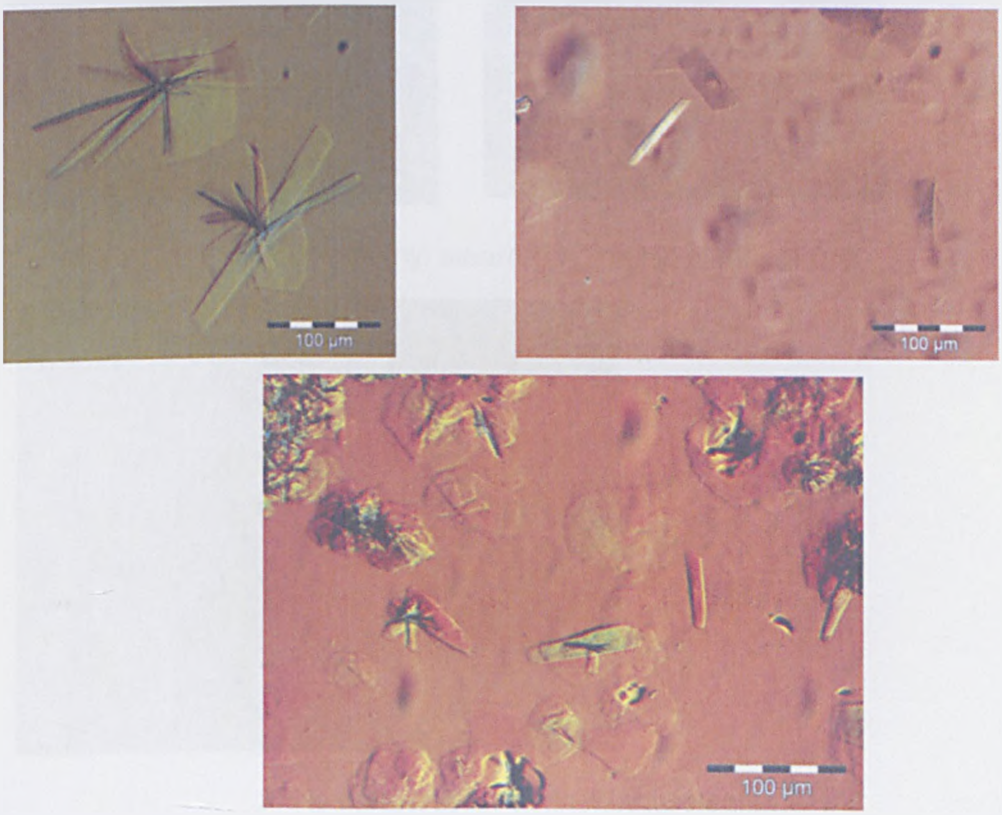

10% methyl stearate in dodecane at 5°C

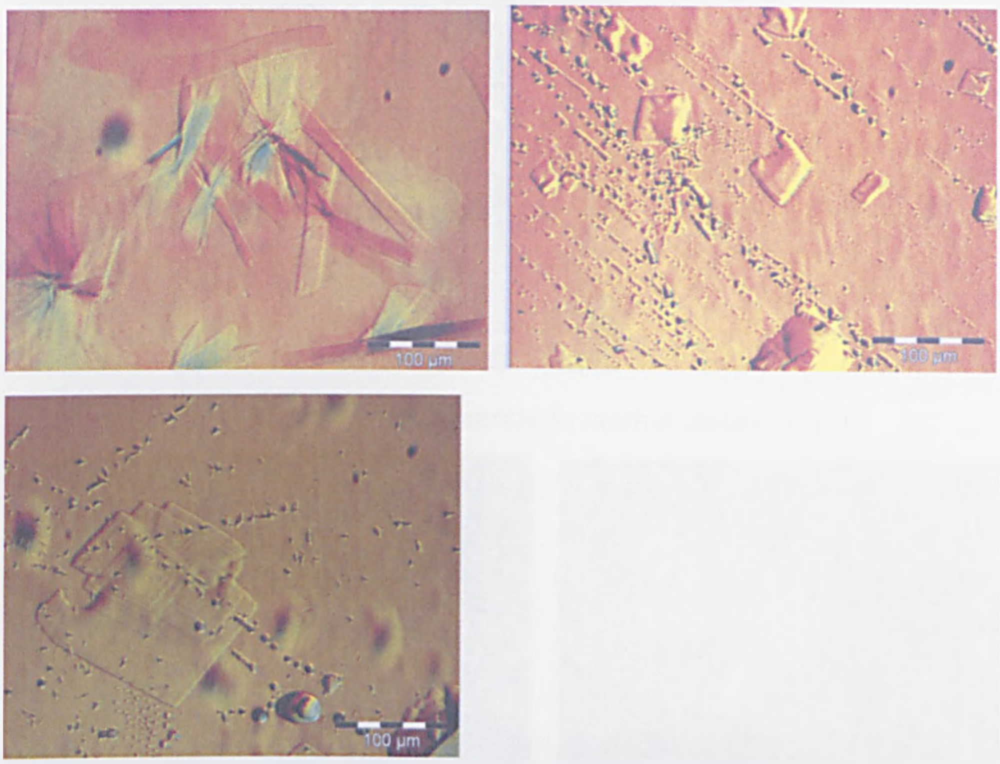

30% methyl stearate in toluene at 3°C

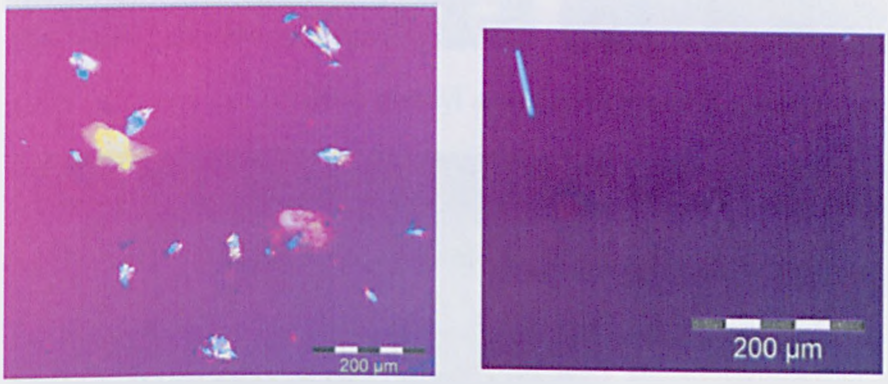

2.5% methyl stearate in methyl oleate at 0°C

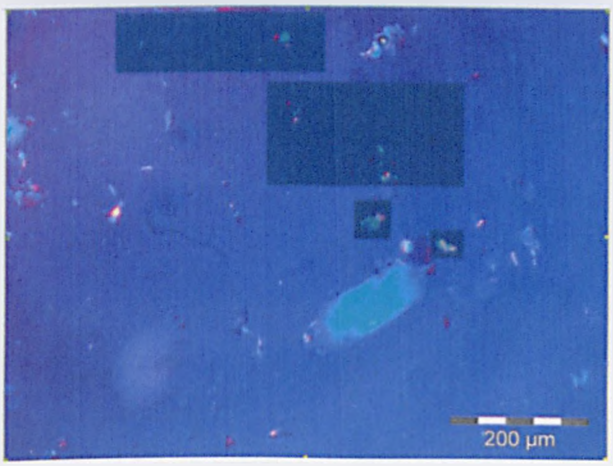

2.5% methyl stearate in methyl oleate at -1°C

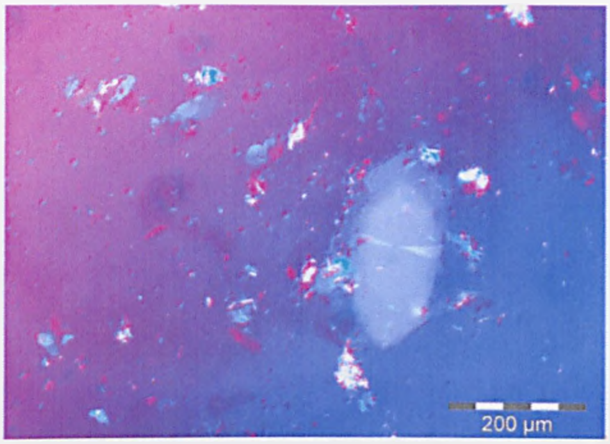

2.5% methyl stearate in methyl oleate at -2°C

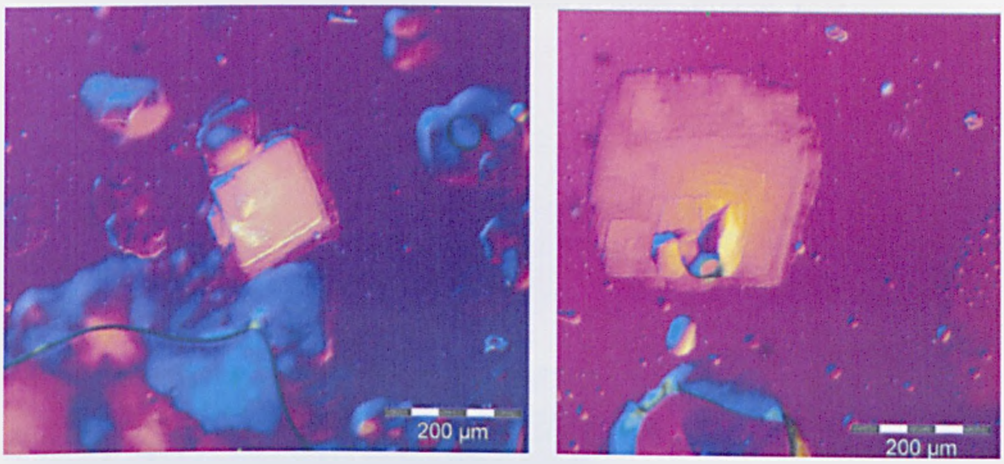

20% methyl stearate in toluene at -2°C

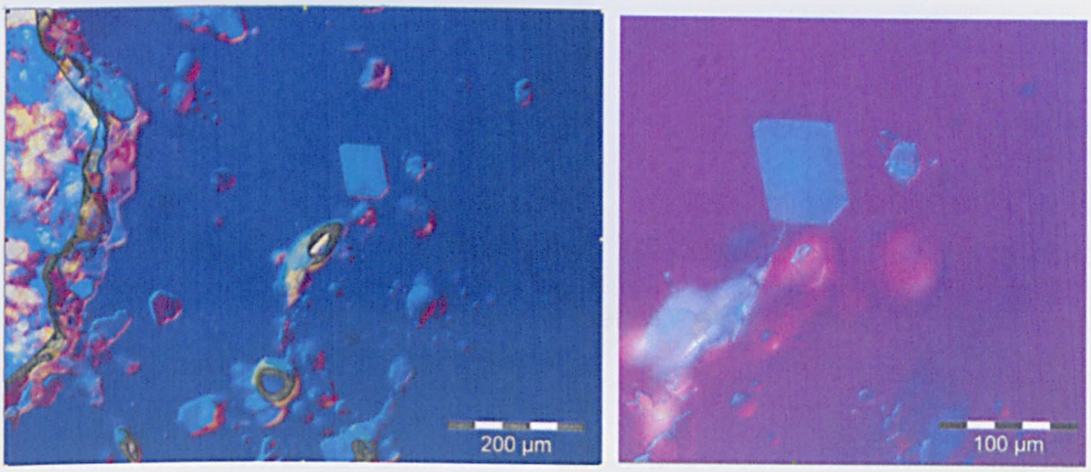

50% methyl palmitate in toluene at -1°C

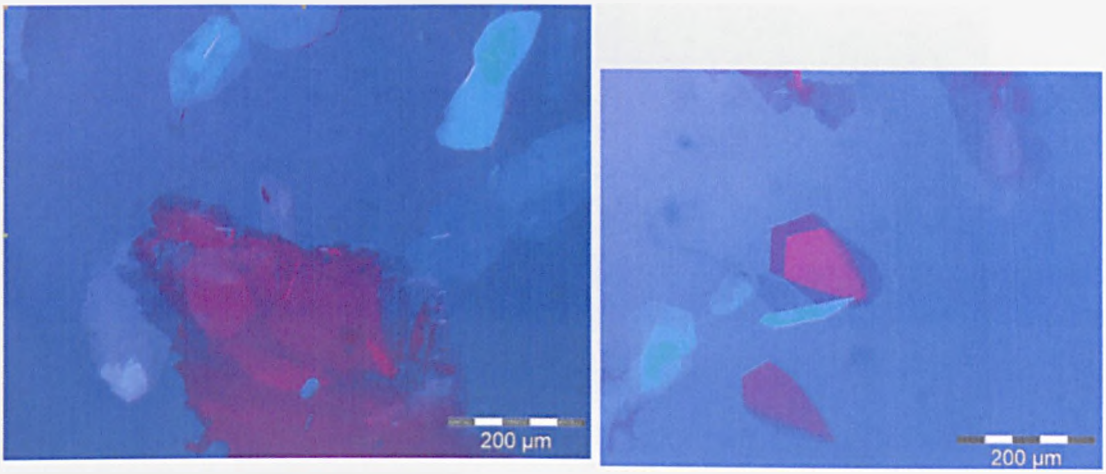

10% methyl palmitate in dodecane at -2°C

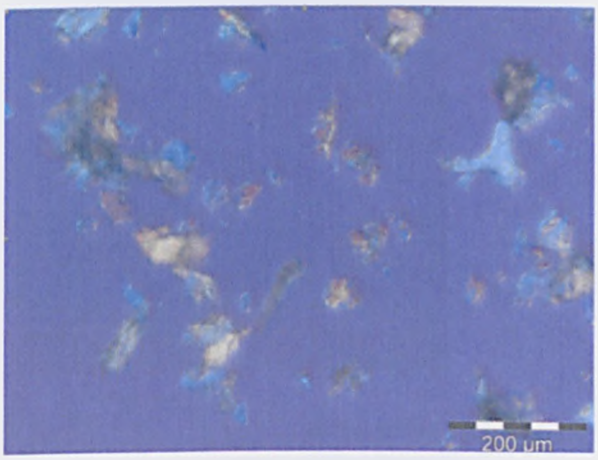

5% methyl palmitate in methyl oleate at -4°C

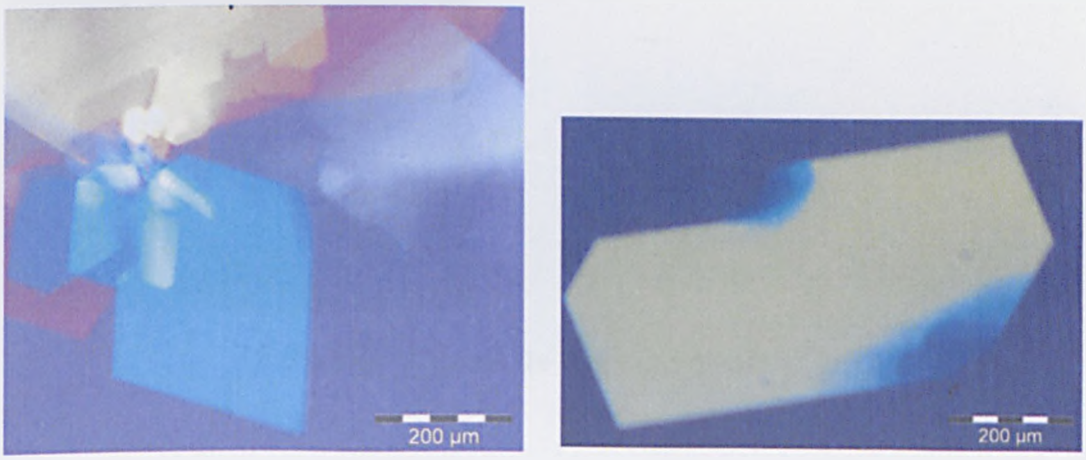

40% methyl palmitate in toluene at -6°C

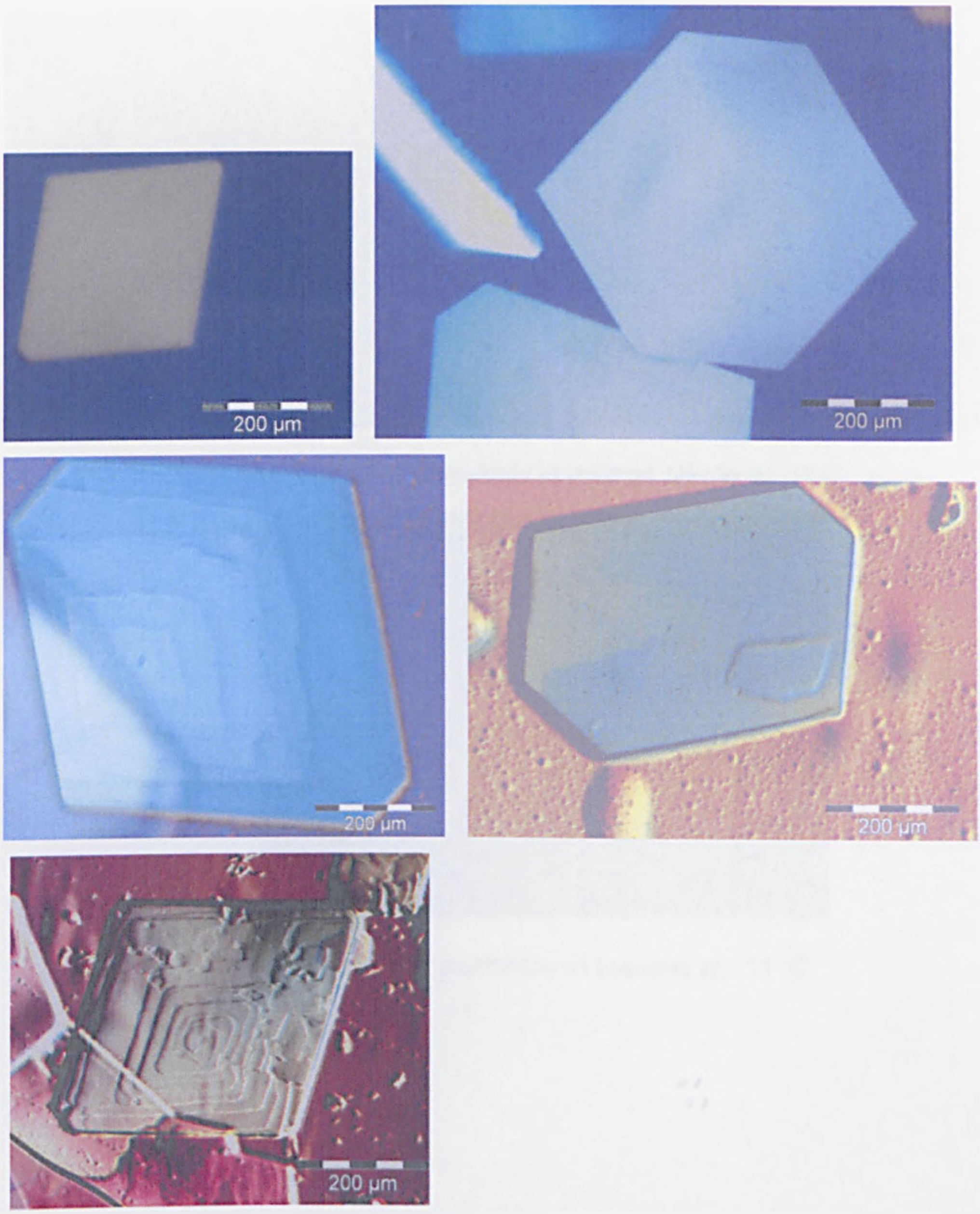

30% methyl palmitate in toluene at -7°C

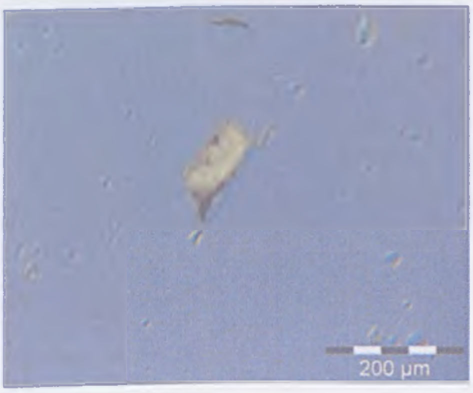

2.5% methyl palmitate in methyl oleate at -8°C

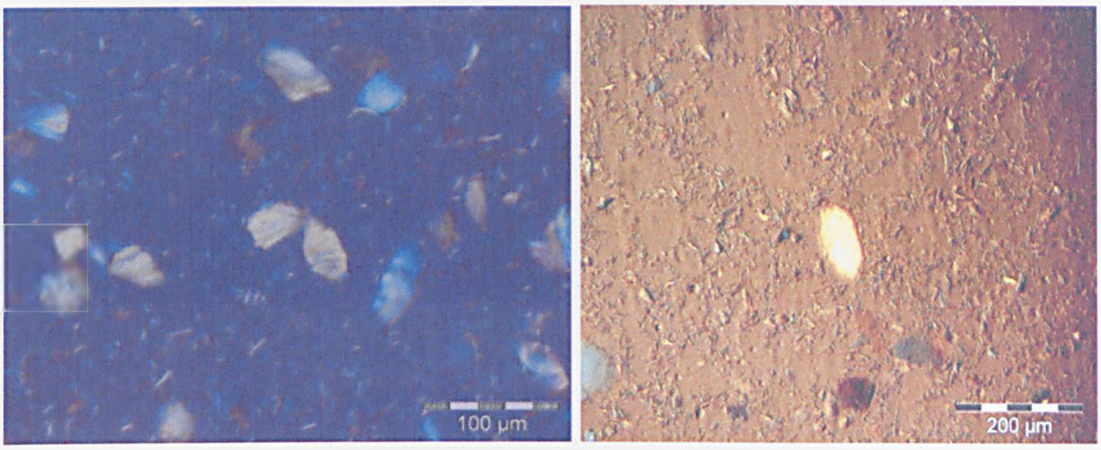

2.5% methyl palmitate in methyl oleate at -9°C

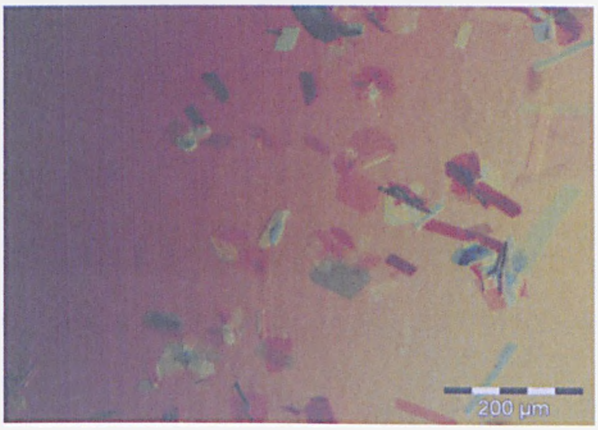

30% methyl palmitate in toluene at -11°C